UCONN LIBRARY

University of Connecticut
OpenCommons@UConn

Doctoral Dissertations | University of Connecticut Graduate School

1-13-2014

Microstructural Evolution in Lead Zirconate Titanate (PZT) Piezoelectric Ceramics

Ching-Chang Chung
University of Connecticut - Storrs, ching-chang.chung@uconn.edu

Follow this and additional works at: https://opencommons.uconn.edu/dissertations

Recommended Citation
Chung, Ching-Chang, "Microstructural Evolution in Lead Zirconate Titanate (PZT) Piezoelectric Ceramics" (2014). *Doctoral Dissertations*. 293.
https://opencommons.uconn.edu/dissertations/293

Microstructural Evolution in Lead Zirconate Titanate (PZT) Piezoelectric Ceramics

Ching-Chang Chung, Ph.D.

University of Connecticut, 2014

Solid solutions of lead zirconate titanate [$PbZr_{1-x}Ti_xO_3$ (PZT)] are extensively used in electromechanical transducers. A maximum in dielectric and piezoelectric response is observed near the morphotropic phase boundary (MPB) separating rhombohedral and tetragonal ferroelectric phases. The origin of the enhanced properties near the MPB remains controversial and has been variously attributed to coexisting rhombohedral and tetragonal ferroelectric phases, to the formation of nanodomains, and/or to lower symmetry monoclinic phases. Hence, the phase diagram of PZT in the region of the MPB remains open to debate.

In this work, dense polycrystalline PZT ceramics prepared by chemical methods were subjected to different time-temperature histories to investigate the origins of the two-phase coexistence and to determine the influence of thermal history on structure, microstructure and dielectric properties. Long annealing (240 hours) above the Curie temperature (*Tc*) revealed a slow relaxation process that was manifested in changes of structural properties. The changes in structural properties were accompanied by changes in the behavior of the paraelectric to ferroelectric phase transition, the domain structure, and the extrinsic contributions to dielectric permittivity. The changes in all these properties were found to show maxima near the MPB. The combined results showed that PZT ceramics made by a normal ceramic processing were not in their equilibrium state

near the MPB. However, no clear evidence of phase decomposition into an equilibrium mixture of tetragonal and rhombohedral phases was found. Instead, the changes in structural and dielectric properties observed on annealing were most consistent with a stress relief mechanism that provided for the coarsening of the domain structure and increased domain wall contributions to dielectric properties.

The results provide evidence that the domain structures and electromechanical properties of PZT compositions near the MPB can be controlled without dopants by processing using differing thermal histories. In addition, results obtained for un-annealed PZT ceramics were used to resolve the long controversial issue of tricritical behavior at the paraelectric to ferroelectric phase transition, to separate intrinsic and extrinsic contributions to the dielectric response, and to quantify reversible and irreversible domain wall motion.

Microstructural Evolution in Lead Zirconate Titanate (PZT) Piezoelectric Ceramics

Ching-Chang Chung

B.S., National Cheng Kung University, 2004

M.S., National Cheng Kung University, 2006

A Dissertation

Submitted in Partial Fulfillment of the

Requirements for the Degree of

Doctor of Philosophy

at the

University of Connecticut

2014

Copyright by

Ching-Chang Chung

2014

APPROVAL PAGE

Doctor of Philosophy Dissertation

Microstructural Evolution in Lead Zirconate Titanate (PZT) Piezoelectric Ceramics

Presented by

Ching-Chang Chung, B.S., M.S.

Major Advisor _____

George A. Rossetti, Jr.

Associate Advisor _____

S. Pamir Alpay

Associate Advisor _____

Pu-Xian Gao

University of Connecticut

2014

ACKNOWLEDGEMENTS

I would like to express my gratitude to Dr. George A. Rossetti, Jr. I could never have accomplished what I did over the last five years without his kind assistance, invaluable guidance, and support. I would also like to thank Dr. S. Pamir Alpay and Dr. Puxian Gao, my associate advisors, for their support, and constructive suggestions. I sincerely acknowledge the valuable feedback from my committee members Dr. Mark Aindow, Dr. Bryan D. Huey, and Dr. Harris L. Marcus. Also, I would like to thank Dr. Lichun Zhang for helping me with TEM measurements and data analysis. It has been an honor working with all of you.

I want to thank all the present and past members of Dr. George A. Rossetti's and Dr. S. Pamir Alpay's groups for their company and support- Richard, Nasser, Adam, Thevika, Jialan, Claire, Liang, Fu-Chang, Hamidreza and Tumerkan. Also, a special thank you also goes to my friends in the Institute of Materials Science (IMS) and the Taiwanese Student Association (TSA) at UCONN. I really enjoyed my time here.

I would like to thank the IMS and the Army Research Office (ARO) for their financial support. This work also benefited from the Office of Naval Research (ONR).

Lastly, I offer my most heartfelt thanks to my parents, Muyung and Chunming, aunt Meiyu, my brother Keen, my sister Carolina, my in-laws Melissa and Uri, and other family members for their unending encouragement and love throughout the years. Their unconditional support helped me to never lose optimism and motivation during my time at UCONN. Without them, this thesis would never have been written. I would like to dedicate this work to them.

TABLE OF CONTENTS

CHAPTER 10

LIST OF FIGURES

CHAPTER 1

CHAPTER 3

CHAPTER 4

CHAPTER 5

CHAPTER 6

CHAPTER 7

CHAPTER 8

CHAPTER 9

LIST OF TABLES

CHAPTER 1

CHAPTER 3

CHAPTER 4

CHAPTER 5

CHAPTER 6

CHAPTER 7

CHAPTER 8

CHAPTER 9

CHAPTER 1

TECHNICAL BACKGROUND

1.1 Ferroelectric Materials

The ferroelectricity was first discovered in Rochelle salt ($KNaC_4H_4O_6 \cdot 4H_2O$) by Valasek in 1921 [1, 2]. It is a phenomenon exists in certain materials that exhibit a spontaneous electric polarization, and this spontaneous electric polarization can be reversed by an applied electric field. Ferroelectricity only exists in the materials with certain structures. Twenty-one of thirty-two crystal classes are noncentrosymmetric, and twenty out of twenty-one of crystal classes with noncentrosymmetric can exhibit the piezoelectric effect (except the cubic 423). Among the twenty crystal systems that exhibit piezoelectricity, ten are polar (including 1, 2, m, mm2, 4, 4mm, 3, 3m, 6, and 6mm) and display pyroelectricity. Only some of these ten crystallographic classes exhibit ferroelectricity. It is because the electric field that required reorienting the polarization direction can be higher than the breakdown field of the sample. The relationship between piezoelectric, pyroelectric and ferroelectric is shown in Fig. 1.1. Therefore, all ferroelectrics must belong to pyroelectric and piezoelectric classes, but not vice versa.

Two decades after the discovery of ferroelectricity, barium titanate ($BaTiO_3$) was discovered during World War II in 1941 and 1944 in the United States [3], Russia [4], and Japan [5]. The discovery of ferroelectricity in $BaTiO_3$ ceramics was extremely important, as it was the first man-made ferroelectric ceramic without the hydrogen bond. This discovery seduces extensive investigations on ferroelectrics, and lead to several

critical findings to have a better understanding of ferroelectricity and piezoelectricity within a decade. These findings were (1) the electrical poling process that aligns the internal dipoles of the crystallites (domains) within the ceramic and make it to act similar to a single crystal was found by Gary in 1945 [6] (2) a phenomenological model of ferroelectrics on the basis of the electromechanical, structural and thermal properties of $BaTiO_3$ was developed by A.F. Devonshire in 1951 [7]. This approach was based on the earlier ideas of Landau and Ginzberg, and this Landau-Devonshire-Ginzberg Theory of ferroelectrics is still most widely used tool to understand ferroelectrics (3) Discovery of very strong and stable ferroelectric/piezoelectric effects in lead titanate zirconate ($PbZr_{1-x}Ti_xO_3$ or PZT) solid solution around 1952 [8]. Because of its outstanding properties, PZT with various additives has since become the dominant piezoelectric ceramic [9-12].

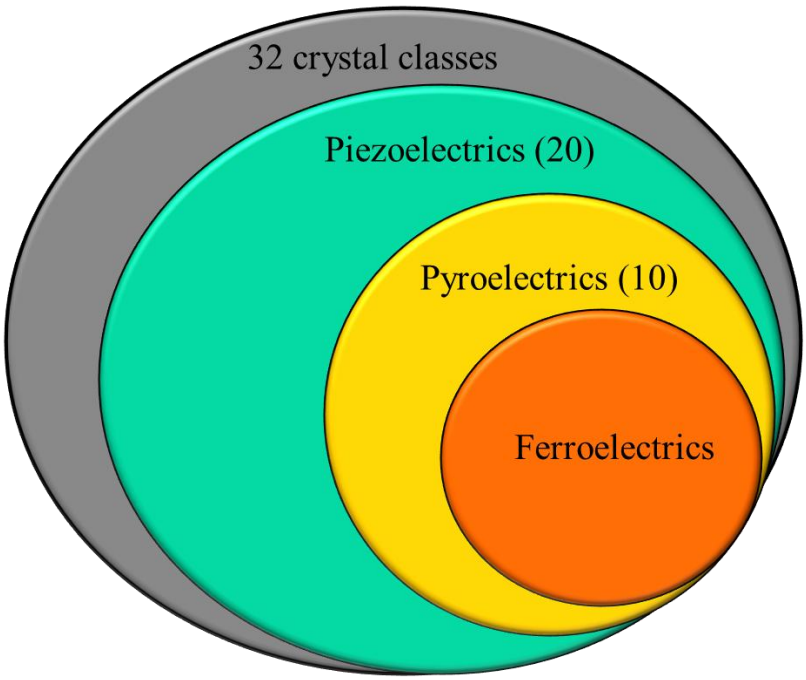

Figure 1.1 The relationship of piezoelectrics, pyroelectrics and ferroelectrics.

Both $BaTiO_3$ and PZT are the members of the perovskite family. The perovskite structure is by far the most important and useful structure in ferroelectrics. In fact, the majority of the applications utilize materials with the perovskite crystal structure. Most of the perovskite ferroelectrics have the general formula ABO_3 with the high symmetry m3m point group at high temperature. This structure can be described as a simple cubic with larger cations (A) occupied at the corner sites, the center site of the cubic cell is occupied by the smaller cation (B), and oxygen anions are located at the center sites of the faces [10]. In general, ferroelectric perovskites has a high symmetry cubic paraelectric phase at high temperature, and transit to a ferroelectric state with a lower symmetry where some of the atoms are slightly displaced when below the Curie temperature (Tc). Figure 1.2 shows a $PbTiO_3$ with perovskite structure at (a) above and (b) below Curie temperature. The $PbTiO_3$ shows a cubic paraelectric phase at the temperature above Tc. When cooled through Tc, the unit cell distorts by motion of the Ti atom along one of the <100> directions. The motion lead to the unit cell elongates in the direction parallel to the Ti displacement and form a tetragonal distortion of the unit cell.

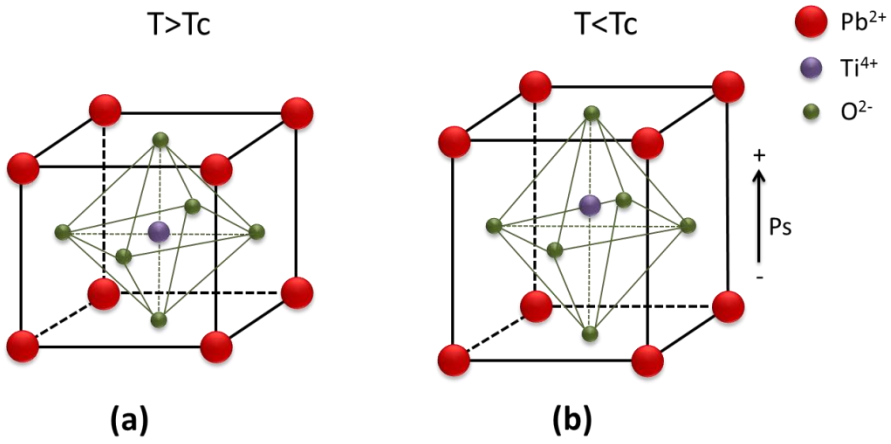

Figure 1. 2 The $PbTiO_3$ crystal structure (a) above and (b) below the phase transition between cubic and tetragonal

Another distinct feature of the ferroelectric behavior of a material is the polarization-electric field (P-E) hysteresis loop [10]. The polarization of a crystal is the summation of total dipole moments in each unit cell. In an un-poled ceramic, the total dipole moments with different directions were cancelled with each other. In a poled ceramic or a single domain crystal, there will be a net remnant polarization (P_r) [13]. There is lots valuable information that can be gained through P-E loop measurement, such as the saturation polarization (P_{sat}), the net remanent polarization (P_r), the spontaneous polarization (P_s), and the coercive field (E_C) of the ferroelectrics. The illustrations of the P-E hysteresis loop of (a) an ideal single crystal and (b) a polycrystalline ceramic were shown in Fig. 1. 3. The P_s is somewhat higher than P_r in ceramics, but is essentially the same as P_r in crystal [10].

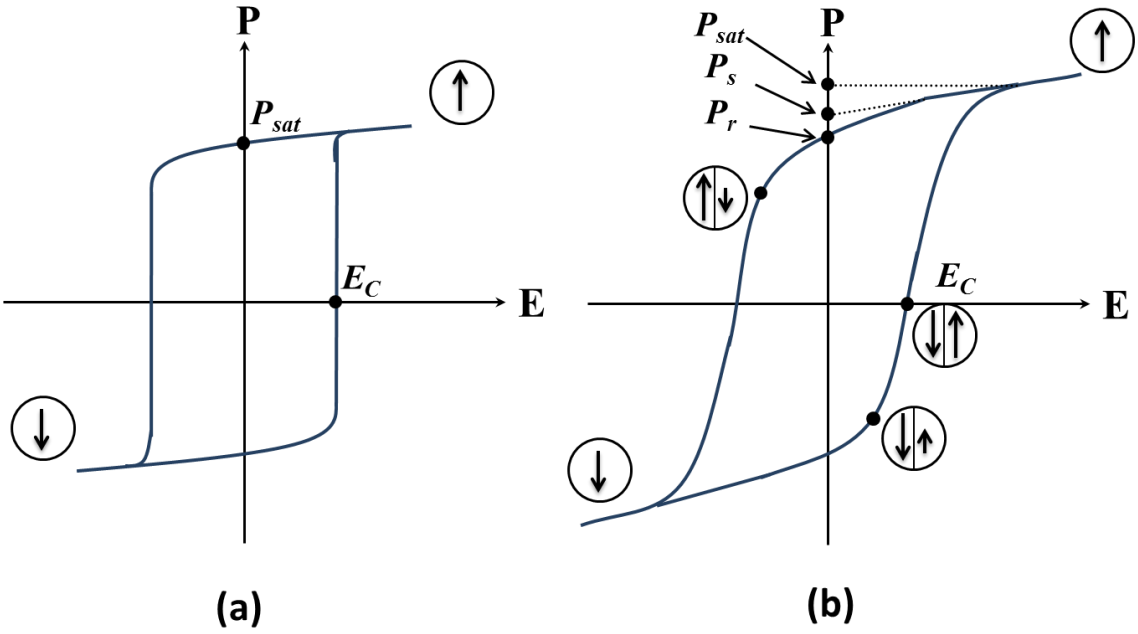

Figure 1. 3 The P-E hysteresis loop of (a) an ideal single crystal and (b) a polycrystalline ceramic

Ferroelectric ceramics are used in a wide range of functional ceramics and form the materials base for the majority of electronic applications. These applications can be classified into following categories based on the different properties in a ferroelectric ceramic [9, 14].

1. Dielectric property: Ferroelectrics which have high dielectric constant over a wide range of frequency and temperature are ideal for manufacturing commercial capacitors. In fact, the best product of the year in "Japan Electronic Industry" was a ferroelectric bypass capacitor for 2.3-GHz operation in mobile digital telephones [15-17].
2. Piezoelectric property: The piezoelectric property of the ferroelectrics is useful to apply on the sensors, transducers and actuators.
3. Pyroelectric property: Ferroelectrics can be cooled by applying an electric field to them under certain conditions is so-called "electrocaloric effect." This effect is useful in electrocaloric cooling for mainframes and microelectric motors [18-20].
4. Memory application: Chemically stable and relatively inert ferroelectric crystals are suitable for making electrically switchable memory devices. Such as ferroelectric random access memories (FeRAMs), dynamic random access memory (DRAM) capacitors [15, 21].
5. Electro-optic application: Since PLZT materials were discovered in late 1960s, ferroelectrics have been widely used in electro-optic devices such as electro-optic shutters, linear gate arrays, and color filters [9].
6. The others: The other potential applications based on the ferroelectric nanostructures, magnetoelectrics and self-assembly [15, 22, 23].

1.2 Ferroelectric Domains

In the ferroelectric materials, domain structures with uniformly oriented spontaneous polarization (P_s) are generated when pass through a paraelectric phase to a ferroelectric phase to minimize the total free energy in the system [24-26]. This energy is attributed from the electrostatic energy of depolarizing fields (E_d) and the elastic energy associated with mechanical constraints. The regions between different domains are the domain walls. The wall which separate two adjacent domains can be classified into two main categories: 180^o domain walls and non-180^o domain walls. The 180^o domain wall separate two domains with opposed spontaneous polarization direction, and those which separate the domains with polarization angle differ than 180° are called the non-180^o domain walls. Figure 1.4 shows the formation of 180^o and non-180^o (90^o) ferroelectric domain walls in a tetragonal perovskite ferroelectric, such as $PbTiO_3$ [26].

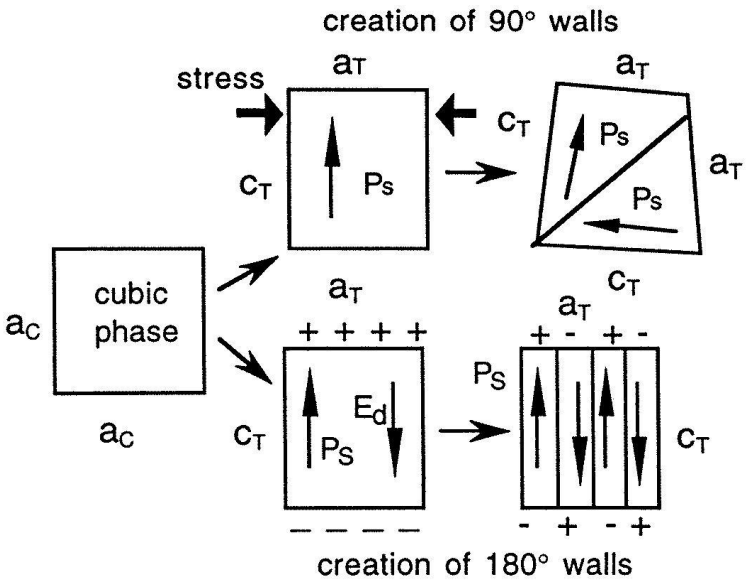

Figure 1. 4 Formation of 90^o and 180^o ferroelectric domain walls in a tetragonal $PbTiO_3$, after Damjanovic [26].

In general, the formation of the 180^{o} domain walls can reduce the electrostatic energy that created by depolarizing fields. Also, the 180^{o} domain walls are purely ferroelectrically active which means that they can only excited by electric fields and only contribute to the dielectric properties of the material [11, 27]. On the other hand, The formation of the non-180^{o} domain walls can reduce both electrostatic and elastic energies of the material[13, 28]. And the non-180^{o} domain walls are both ferroelectrically and ferroelastically active, which means that they can be excited by both electric field and mechanical force. Therefore, the non-180^{o} domain walls could contribute to both the piezoelectric and the dielectric properties.

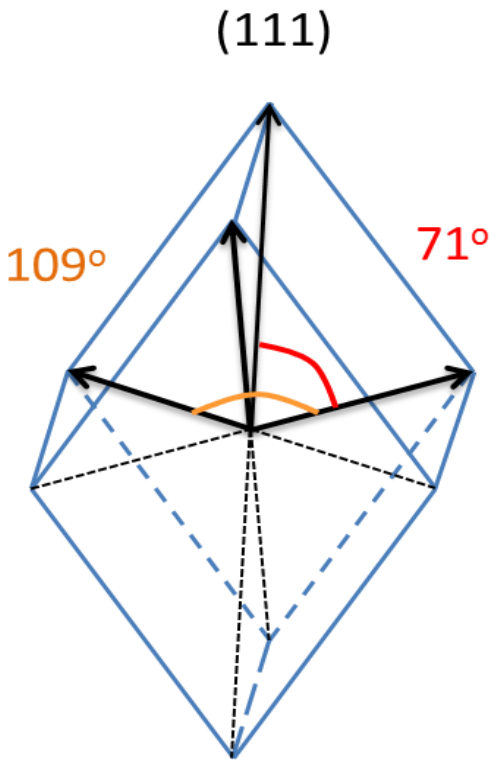

Figure 1. 5 Schematic representation of the available polarization directions in a rhombohedral crystal

The angle between the polarization directions of adjacent ferroelectric domains in a ferroelectric may vary with different crystal structures. For example, in a lead zirconate titanate ($PbZr_{1-x}Ti_xO_3$) with rhombohedral phase, the polarization develops along the (111) direction. This provides eight possible spontaneous polarization directions with 180º, 109º or 71º domain walls. Figure 1.5 shows simplified schematics of available polarization directions in a rhombohedral crystal. Similarly, 180º and 90º domain walls can be found in a lead zirconate titanate ($PbZr_{1-x}Ti_xO_3$) with tetragonal phase. The number and size of the domains were also depending on the external (temperature, electric and elastic) boundary conditions, local defects, crystal sizes, and sample history [13].

1.3 Intrinsic and Extrinsic Contribution to Dielectric Response

A ferroelectric ceramic is often subjected to high electric and/or high stress in electric devices, causing nonlinear dielectric and piezoelectric response. This thesis is focused on the dielectric nonlinearity [29]. Dielectric responses of ferroelectric ceramics are dependent on both intrinsic and extrinsic mechanisms. The Intrinsic contribution relates to the lattice, and is the average response of individual ferroelectric domains in the ceramic. The extrinsic contributions are the result of existence of the domain walls, the phase boundaries, and the defect dipoles [30, 31].

The domain structure of a ferroelectric ceramic has a great influence on its dielectric properties. In order to have a better understanding of domain structure and domain wall motions in a ferroelectric ceramics, it is important to distinguish between the intrinsic and extrinsic contributions. There are some common methods to separate out the

intrinsic properties and extrinsic contribution. These methods are the investigations of the field amplitude, frequency and temperature-dependent dielectric behavior, hydrostatic, and ageing time of the ferroelectric ceramic [29].

First method to separate out the intrinsic properties and extrinsic contribution is the frequency dependent dielectric behavior. This method is based on the fact that the extrinsic contribution cannot follow the external ac field at high frequencies and does not contribute to the dielectric/piezoelectric properties. The frequency dependence of dielectric properties in a ferroelectric ceramic often show a relaxation step at high frequency range (at around gigahertz frequencies ~10^9 Hz), which is considered to be related to the loss of contributions from domain wall vibrations and defects motions. This particular phenomenon was first mentioned in the early studies on $BaTiO_3$ by Von Hippel [32], and Poplavko *et al*. show that the dielectric permittivity relaxation step in a $BaTiO_3$ ceramic can be observed at around 4 GHz, as shown in Fig 1.6 [33]. The dielectric permittivity at frequencies higher than this relaxation step can be considered purely attributed by the intrinsic ionic and electronic response in the ferroelectric. Similar relaxation step of frequency dependence of dielectric permittivity in PZT-based ceramics were demonstrated by Kersten [34] and Böttger [35]. However, some authors showed the dielectric constant of BT single crystals also has a strong relaxation step at the temperature above Curie temperature. Therefore, the origin of the relaxation step has remained a subject of debates [36-38].

Besides the exact origin of the relaxation step is not clear, the greatest disadvantage of this method is the fact that the relaxation step in a ferroelectric ceramic

can be only observed at the very high frequency range. To measure the dielectric permittivity at gigahertz has some significant practical difficulties.

The second common method is investigating the temperature dependence of the dielectric properties in the ferroelectrics. The basic idea of this method is that the extrinsic contributions are frozen out when temperature closes to the 0K, and remaining dielectric permittivity only comes from the intrinsic part. It is because of the extrinsic contribution part (domain wall and defects motions) to dielectric permittivity is thermally activated, while intrinsic contribution part is almost temperature independent. Therefore, the intrinsic contribution can be determined exactly at absolute zero. Once the intrinsic contribution is determined, the value of the extrinsic contribution can be also derived at any temperatures.

This method has been used by several authors to distinguish the intrinsic and extrinsic contributions in ferroelectrics [28-31, 39-42]. A typical result obtained by Zhuang *et al*. using this method is shown in Fig. 1.7 [31]. The composition and temperature dependence of dielectric constants of pure PZT ceramics were measured from 4.2 to 300 K in this case, and the authors assumed the extrinsic domain wall and thermal defect motions freeze out at 4.2K. The low temperature dielectric data can be used to determine intrinsic contribution part and useful for determining coefficients in a phenomenological theory.

Another similar method was carried out to determine the intrinsic and extrinsic contributions to the ε_{33}, d_{33} and d_{31} coefficients of soft PZT ceramics by Zhang *et al.* [30]. This method was based on the hypothesis that domain wall motions (extrinsic part) do not

produce volumetric changes, and the intrinsic response does accompany with a change in the unit cell volume. It means that there will be no the extrinsic contribution to the piezoelectric hydrostatic coefficient d_h. In this case, the authors first measured the temperature dependence of the piezoelectric hydrostatic coefficient d_h. The intrinsic and extrinsic contributions to the ε_{33}, d_{33} and d_{31} coefficients were then calculated by utilizing the relationships between ε_{33}, d_{33}, d_{31} and d_h, via the electrostrictive coefficients Q_{11}, Q_{12} and Q_h. The calculated temperature dependence of the dielectric permittivity of a soft-PZT and a pure PZT were shown in Fig 1.8.

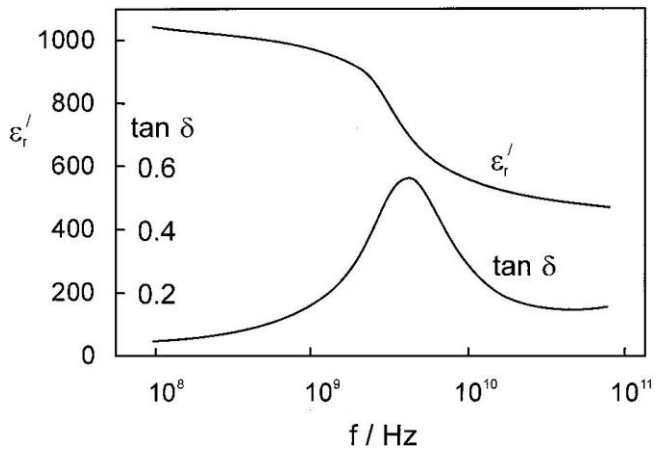

Figure 1. 6 Frequency dependence of dielectric properties of barium titanate ceramics, after Poplavko *et al*. [33].

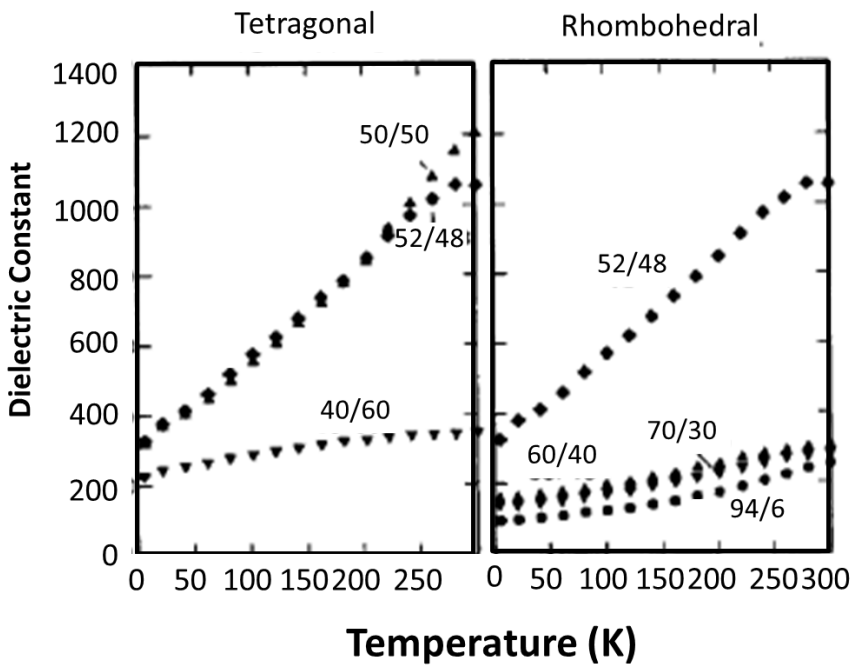

Figure 1. 7 Temperature dependence of the dielectric permittivity for (a) tetragonal and (b) rhombohedral PZT ceramics, after Zhuang *et al*. [31].

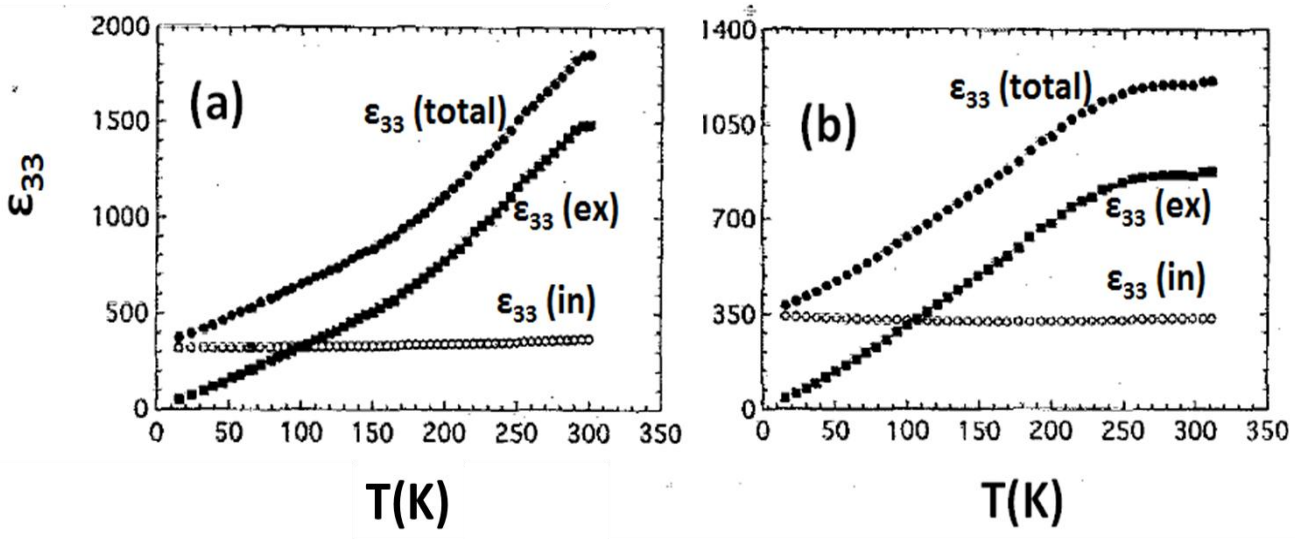

Figure 1. 8 The calculated intrinsic and extrinsic dielectric constant for (a) PZT-500 and (b) PZT 52/48, after Zhang *et al*. [30].

The aging effect of the ferroelectric ceramics is the dielectric, piezoelectric and elastic properties of a poled ferroelectric ceramics reduce gradually with time. It is known that the aging effect of ferroelectric ceramics is related to the defects reorientation under the influence of the local domain polarization, and lead to a reduction of non-180^{o} domain wall mobility. Therefore, the intrinsic contributions are assumed to be independent of the aging time based on this concept. The relation of the properties of the ferroelectrics with aging time can be written as in Equation 1.1:

$$\varepsilon'(\mathrm{t}) = \varepsilon'_{intrinsic} + \varepsilon'_{extrinsic}(t)\ ,\ \varepsilon''(\mathrm{t}) = \varepsilon''_{extrinsic}$$

$$\mathrm{d}'(\mathrm{t}) = \mathrm{d}'_{intrinsic} + \mathrm{d}'_{extrinsic}(t)\ ,\ \mathrm{d}''(\mathrm{t}) = \mathrm{d}''_{extrinsic} \qquad \text{Equation 1. 1}$$

where $\varepsilon'(t)$ and $d'(t)$ are the time real part, and $\varepsilon''(t)$ and $d''(t)$ are the imaginary part of the time dependence of dielectric and piezoelectric properties. It is clear in this equation that only the extrinsic contributions are the function of the aging time.

Arlt *et al*. developed a phenomenological model based on the aging time of the vibrating domain walls, which is related to the extrinsic contribution to dielectric, piezoelectric and elastic properties [43]. In this method, authors proposed that the ratio of the imaginary to the real parts of the dielectric should be constant and equal to the loss tangent ($\tan\delta_{dv}$) relate to the domain vibration mechanism. The relation can be expressed as in Equation 1.2:

$$\frac{\varepsilon'_{domain\ vibration}}{\varepsilon''_{domain\ vibration}} = \tan\delta_{domain\ vibration} \qquad \text{Equation 1. 2}$$

A linear relationship with a gradient of loss tangent ($\tan\delta_{dv}$) can be observed by plotting the real vs. imaginary parts of the time dependence dielectric properties, as Fig. 1.9. The intrinsic contributions to the properties can be obtained by extrapolated the line to the zero loss, and the extrinsic contribution to the properties can also be determined at any given aging time.

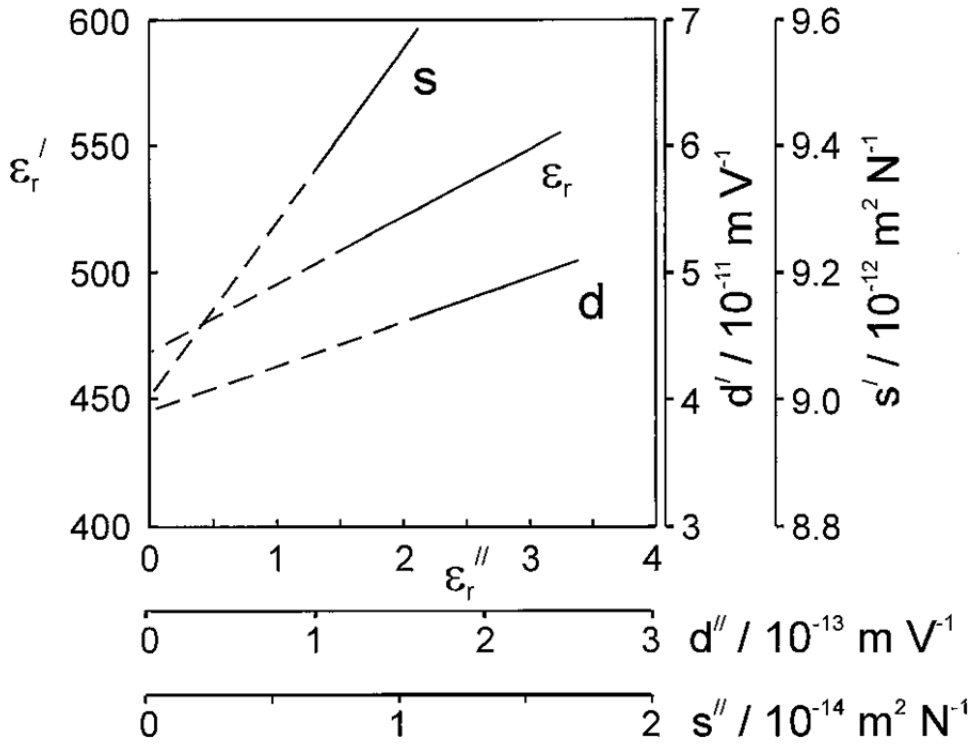

Figure 1. 9 Time dependence of ε'_r-ε''_r, *d'-d''* and *s'-s''* relationships for Fe doped hard PZT ceramics during ageing at 353K, after Arlt *et al*. [42].

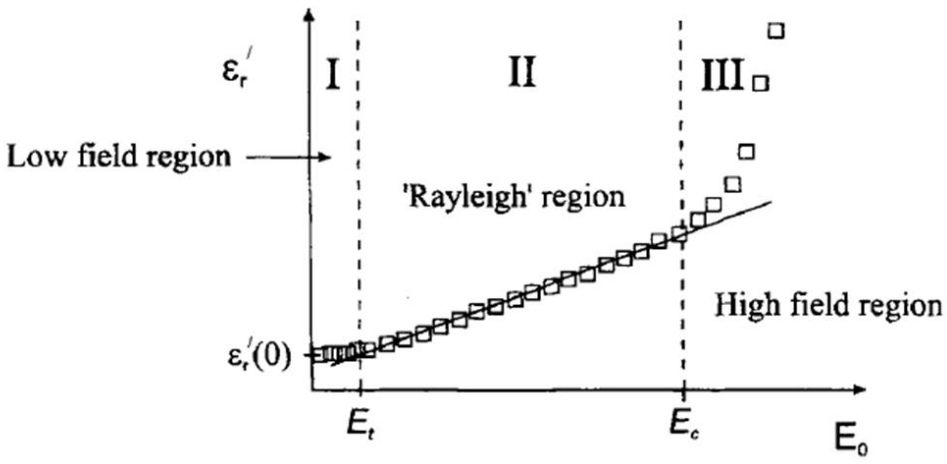

Figure 1. 10 Schematic view of field dependence of dielectric permittivity in ferroelectric ceramics, after Hall *et al*. [43].

1.4 Field Amplitude Dependence Dielectric Properties and Rayleigh Law

Another common method to separate the intrinsic and extrinsic contributions to the properties of a ferroelectric ceramic is the investigations of ac field amplitude dependence of the response. Fig 1.10 shows that three different types of dielectric behavior were identified, depending on the applied field amplitude [44]. At the low field region, the dielectric permittivity is independent or weakly dependent on the field amplitude when the applied field below the threshold field (E_t). A threshold field is usually defined as the field amplitude at which the dielectric permittivity is observed to increase 5% ($\Delta\varepsilon/\varepsilon_0 < 5\%$). The value of threshold field in ferroelectric ceramics can be considered as the onset point of measurable nonlinearity [45], and it is a function of composition, ageing time and temperature. The dielectric permittivity and loss were increased rapidly with field amplitude beyond the threshold field due to increasing of domain wall mobility or domain switching [29]. Therefore, the extrapolated value of

dielectric permittivity at zero electric field was attributed by both intrinsic ionic response and reversible domain wall vibration.

At an intermediate field values, which is beyond the threshold field (E_t) and below the high field region, as shown in the Fig. 10. The dielectric permittivity shows an almost linear increase with increasing field amplitude, and the ε-E relation can be applied by the Rayleigh law [29]. Rayleigh law was first developed for explaining quadratic relation between the magnetization M and the applied magnetic field H in ferromagnetic materials[46]. Later Damjanovic *et al.* show that an analogous law can be used to describe the dependence of the dielectric and piezoelectric on the field amplitude in the ferroelectric ceramics [26, 47-50].

Rayleigh analysis has been applied to a number of interesting ferroelectric ceramic systems at around MPB compositions. Observed variations in the Rayleigh coefficient (α) will be used to help explain role of crystal symmetry and domain wall mobility to total dielectric and piezoelectric response. The Rayleigh relations, as shown in Equations 1.3 and 1.4, can be used to quantify the irreversible extrinsic contributions to the dielectric properties of ferroelectrics.

$$\varepsilon_{33} = \varepsilon_{init} + \alpha E_0 \qquad \text{Equation 1. 3}$$

$$P_3 = \varepsilon_{init} E_0 + \alpha E_0^2 \qquad \text{Equation 1. 4}$$

where ε_{33} is the dielectric permittivity, ε_{init} is the deformation of the lattice and the intrinsic reversible domain wall contributions to the dielectric permittivity, α is the Rayleigh coefficient, P_3 is the polarization, and E_0 is the field amplitude. The first terms of both equations are the intrinsic part, and second terms are the extrinsic parts.

In 1942, Neèl proposed a theory to explain the physical origin of the Rayleigh law by analyzing displacements of a single domain wall in a medium containing defects[51]. This gives a better understanding of the definitions of reversible and irreversible domain wall motions, a schematic diagram of the potential energy of a domain wall as a function of position in a medium with a random and uniform distribution of potential energy barriers is shown in Fig. 1.11. The reversible domain wall motion refers to the domain wall moves around its original equilibrium position within a potential well surrounding.[52] The average depth of the potential well in the ceramic can be determined by the threshold field (E_t). The domain wall can overcome the energy barrier and moves to a new position when the external field is sufficiently large, which is so-called irreversible domain wall motion. The extrinsic irreversible domain wall motion contribution to the total dielectric permittivity can be determined by the ratio of the $\alpha E_0/\varepsilon_{33}$.

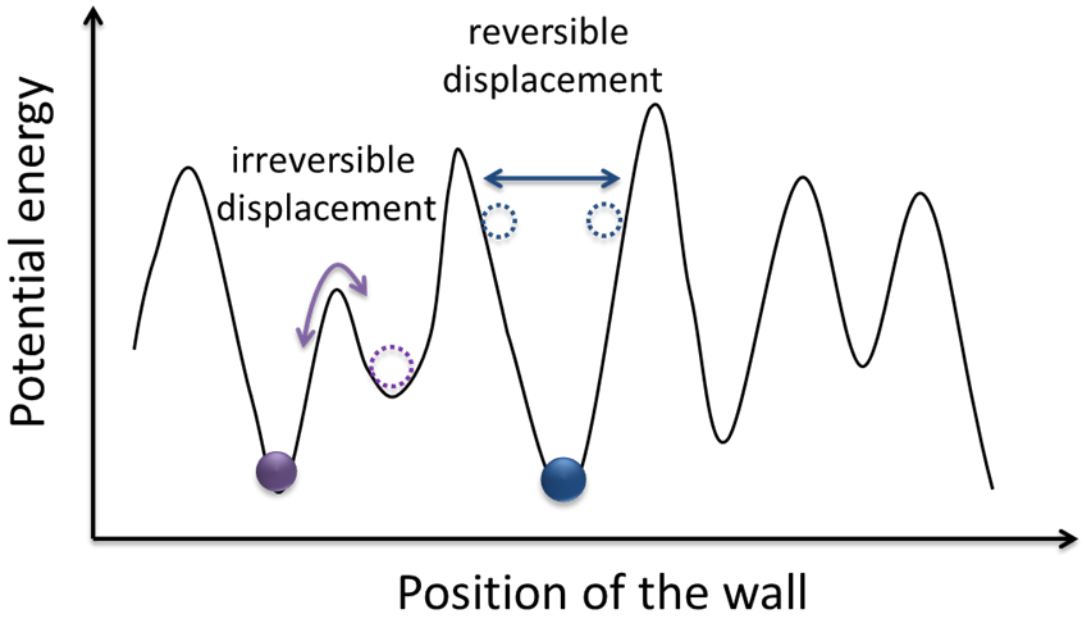

Figure 1. 11 Potential energy of the domain wall in a medium which contains randomly distributed defects, after Damjanovic [47].

The overall domain structure of a ferroelectric ceramic remains relatively stable in the remnant polarization state below the coercive field (*Ec*). The partial domain start switching and energy landscape is totally changed when the field amplitudes approach to the coercive field. Therefore, Rayleigh law is no longer suitable for applying on the ferroelectric ceramics at high field region in Fig 1. 10 [29].

1.5 Lead Titanate Zirconate (PZT)

Lead zirconate titanate, $PbZr_{1-x}Ti_xO_3$ (PZT), was discovered by Sawaguchi *et al.* [8, 53] around 1952. At room temperature, the solid solution between lead titanate, $PbTiO_3$ (PT), and lead zirconate, $PbZrO_3$ (PZ), presents three different regions. For $0.96 \leq x \leq 1$, PZT presents an orthorhombic antiferroelectric structure (A_O, Pbam), a tetragonal

phase (F_T, P4mm) is present in the titanium rich (Ti-rich) region of the pseudo-binary system, and two ferroelectric phases on the zirconium rich (Zr-rich) region, $F_{R(LT)}$ and $F_{R(HT)}$. Conventionally these phases are attributed to space groups *R3c* and *R3m*, respectively [54]. In the high-temperature region of the subsolidus phase diagram, it is believed that there is a complete single phase paraelectric cubic solid solution (P_c, Pm3m).

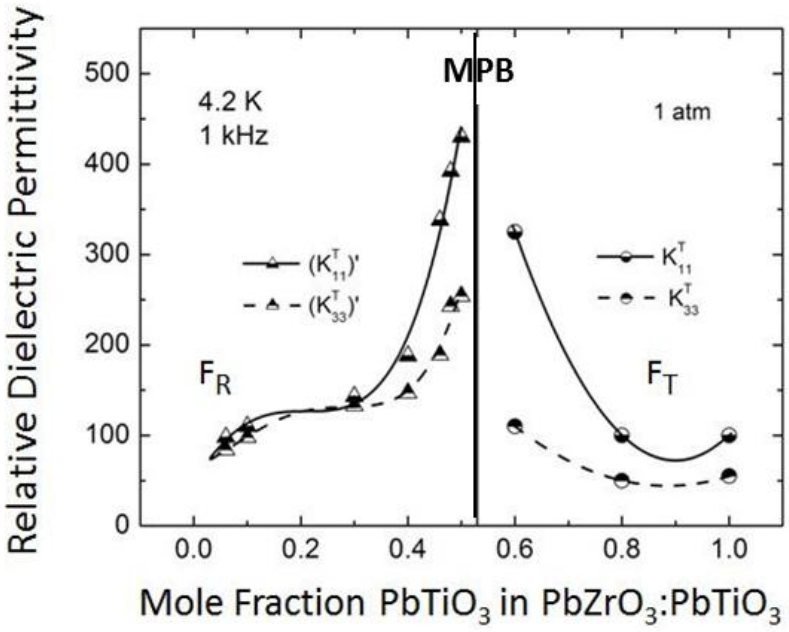

Figure 1. 12 The dielectric permittivity shows an extrma at MPB in PZT system, after Haun [55].

PZT ceramics are widely used in electro-active devices and in other technological applications due to the maximum in the piezoelectric, elastic, and dielectric properties that occur near the morphotropic phase boundary (MPB) where this solid solution changes structure as a function of the chemical composition (around x = 0.48) [10, 55]. The composition dependence of dielectric permittivity is shown in Fig. 1.12 [56]. It is

well known that the increased piezoelectric response and poling efficiency in PZT materials near the MPB is due to the increased number of allowable domain states (six in F_T, eight in F_R) near the MPB [57]. In addition, PZT-based solutions have other desirable characteristics as follows: mechanically strong, chemically inert, relatively inexpensive to manufacture, high operating temperature, high coupling coefficient, and they can be easily tailored by adjusting the Zr/Ti ratio, or by introducing dopants to meet the requirements of a specific application.

Pure PZT has good electromechanical properties for compositions near the MPB, but it is rarely used in commercial devices. It is always doped with either acceptor dopants (K^+, Na^+ and Fe^{3+}...etc.), which create oxygen (anion) vacancies and impede domain wall motion, or donor dopants (La^{3+}, W^{6+} and Nb^{5+}...etc.), which create metal (cation) vacancies and facilitate domain wall motion in the material [10, 58]. With different types of dopants, the domain mobility and properties of PZT-based materials can be controlled. Generally, the acceptor doping creates hard PZT while donor doping creates soft PZT. Hard PZT materials can be subjected to high electrical and mechanical stresses, and soft PZT materials are typically used when high coupling and/or high charge sensitivity are important. Table 1.1 shows the characteristics of pure, soft and hard PZTs. These modified PZT-based materials are widely used in sensors, actuators, and transducers [9].

Characteristics of Pure, Soft and Hard PZT Ceramics

Characteristic	Soft PZT	Hard PZT	Pure PZT
Examples	Donor-doped (La^{+3}, W^{+6}, Nb^{+5} or Sb^{+5})	Acceptor-doped (K^{+} Na^{+} Fe^{+3} Sc^{+3} or Mg^{+2})	$PbZr_{0.52}Ti_{0.48}O_3$
	PZT-5A, PZT-5H	PZT-4, PZT-8	
Piezoelectric Constants (pC/N)	Larger (~450-640)	Smaller (~225-300)	~223
Dielectric Constants	Larger (~1800-3400)	Smaller (~1000-1300)	~600-700
Dielectric Losses	Higher (~1.3-1.5%)	Lower (0.2-0.5%)	~0.4%
Electromechanical Coupling Factors	Larger (~0.62-0.68)	Smaller (~0.57-0.62)	0.52
Electrical Resistivity (Ω-m)	High ($>10^{10}$)	Lower ($>10^{8}$)	$>10^{9}$
Mechanical Quality Factors (Q)	Low (~65-100)	High (~800-1200)	500
Coercive Field (kV/cm)	low (~5-11)	Higher (14-18)	~30-40
Polarization / Depolarization	easier	more difficult	

Table 1. 1 Comparison of the properties of the pure PZT and modified-PZT

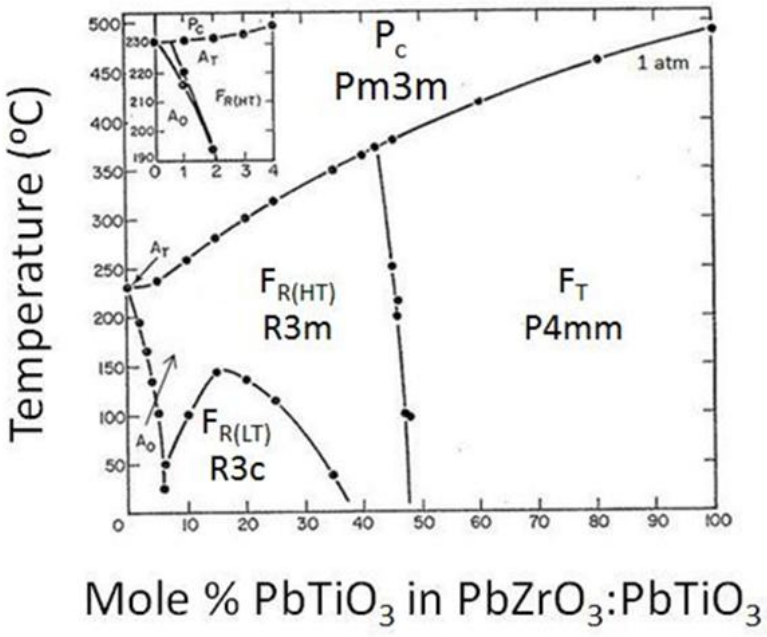

Figure 1. 13 Diffusionless phase diagram of PZT solid solutions [10]

1.6 Phase Coexistence in PZT

The temperature–composition phase diagram for PZT (shown in Fig. 1.13) was assembled by Jaffe *et al.* [10] in 1971. The MPB is represented as a nearly temperature-dependent (vertical) and one dimensional (line) boundary located at the composition x = 0.48 (48 mole % $PbTiO_3$). The observation of the vertical MPB line in this phase diagram immediately raised questions about how such a phase boundary could exist. The line boundary can be only observed when atomic diffusion is fully frozen and the transformation between phases is diffusionless. If diffusion is not totally frozen in, according to Gibbs phase rule, it is expected that the lines in this phase diagram should be replaced by a two-phase region [14]. Despite suggestions of the coexistence of phases at the MPB as early as 1970 by Isupov [57] and later by Ari-Gur and Benguigui [59, 60], this picture of the PZT phase diagram remained essentially unchallenged until 1999 when

a new monoclinic phase (C_m, M_A) was reported by Noheda *et al*. [61-64]. In their work, they found that the M_A phase is positioned between the F_T and F_R phase along the MPB at low temperatures (shown in Fig. 1.14). Thus the phase diagram remains a diffusionless diagram without phase coexistence around the MPB line.

Extensive new studies were undertaken after the discovery of the intermediate monoclinic structure by Noheda *et al*. in 1999. Prior to this, no ferroelectric phase of symmetry lower than orthorhombic had ever been observed in the perovskite oxides. Also the conventional Ginzburg-Landau-Devonshire theory of second and weak first order phase transitions could not account for the appearance of proper ferroelectric states with symmetries lower than orthorhombic. Proper ferroelectric phase of monoclinic symmetry are stabilized only when the Landau polynomial is expanded to terms of order eight [65]. This implies that special conditions are required for forming the monoclinic phase.

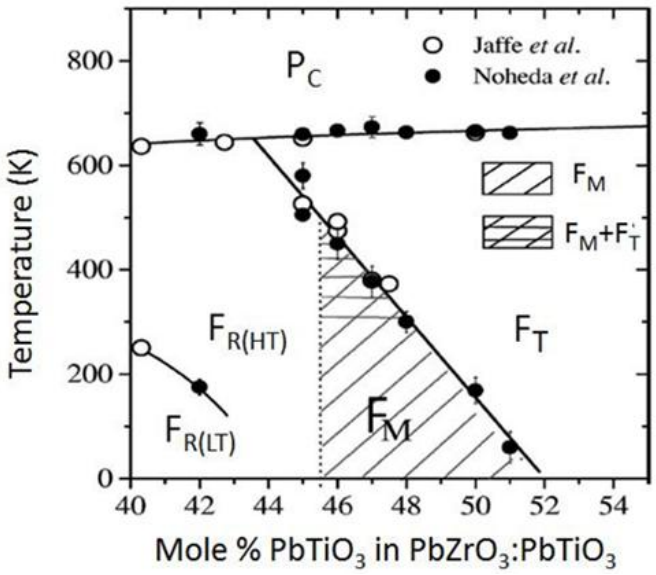

Figure 1. 14 New PZT phase diagram with a monoclinic phase (shaded area) around the MPB [63].

All of the proposed hypotheses of the last 40 years for phase coexistence in PZT have been classified into five categories: Diffusionless phase diagram, metastable coexistence, heterogeneity (composition fluctuation), thermal fluctuation (statistical distribution model), and equilibrium coexistence. Among these categories, the possible phase diagrams are illustrated for each case. The different cases can be described by how the unit volumes of the tetragonal and rhombohedral phases vary with composition. This provides a useful way to interpret experimental results regarding phase coexistence near the MPB.

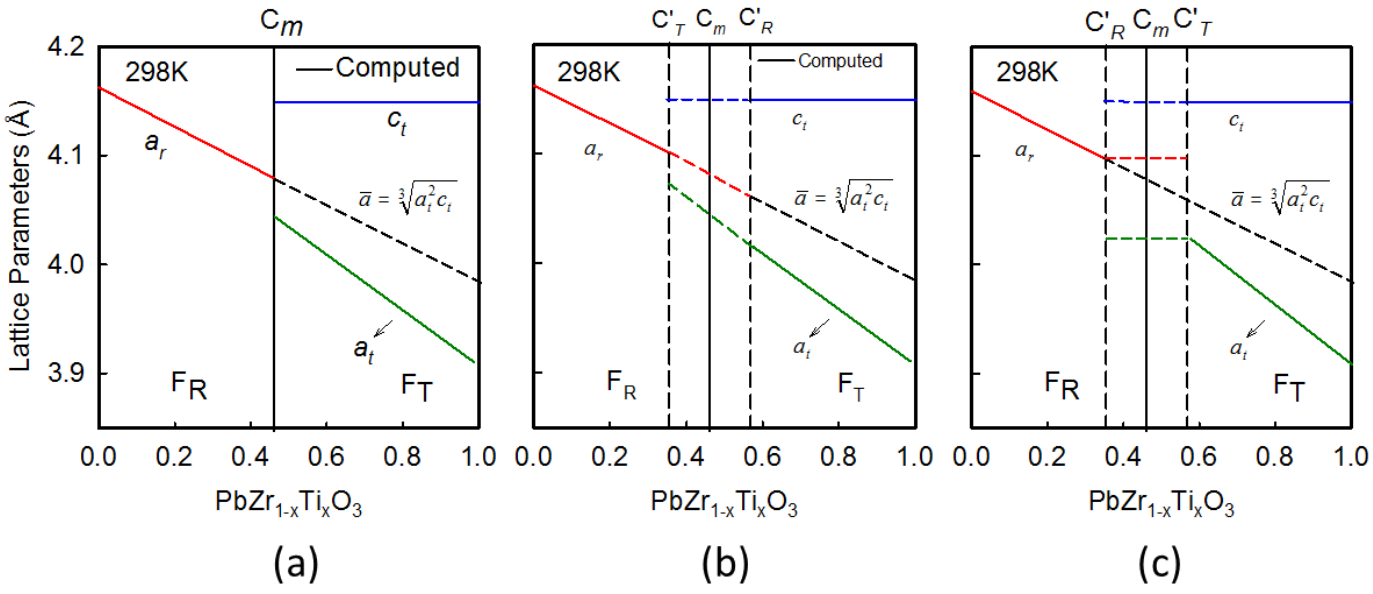

Figure 1. 15 PZT Lattice constant of (a) without phase coexist, (b) metastable coexistence and (c) equilibrium coexistence.

1.6.1 Conventional Diffusionless Phase Diagram

As mentioned above the traditional diffusionless phase diagram of PZT cannot be an equilibrium phase diagram. The variation of the lattice constants with composition according to this model is shown in Fig. 1.15(a). The phase transformation from rhombohedral to tetragonal occurs at $c_m \approx 0.48$. The volume of F_T phase on the MPB line is $V_T = a_t^2 c_t$, and the volume of F_R phase is $V_R \cong a_R^3$ (the rhombohedral angle $\alpha_R > 89.5°$). In the diffusionless phase diagram, the phase coexistence of F_T and F_R does not occur and the unit cell volume of the solid solution shows a linear composition dependence across the whole diagram, including in the MPB region [66]. The computed variation of the unit cell volume has been compared with selected experimental data [64, 67, 68]. Therefore, if the diffusional process is totally frozen, the volume of F_T phase and F_R phase can be the same depending on the thermal history.

1.6.2 Metastable Coexistence

A thermodynamic consideration of properties of the PZT ceramics at the MPB was carried out by Isupov in 1970 [57]. Later he published a series of papers related to phase coexistence in PZT MPB region and tried to state the conditions for that occurrence [69-75]. Isupov's analysis implied that the MPB in the phase diagram of PZT solid solutions represents a certain extended region with possible metastable coexistence of the T and R phases. The composition that corresponds to the phase transition is considered to be a first order transition. Under his assumption that the thermodynamic potentials of the T and R phases are equal to each other at a concentration $x = c_m$ (see Fig. 1.15(b)), the T phase is stable and the R phase is metastable at $x > c_m$. Conversely, the T phase is

metastable and the R phase is stable at $x < c_m$. This is also indicates that the stable and metastable phases can coexist over a rather wide range of concentrations. The range of the metastable phase regions is from $x = c'_T$ to $x = c'_R$. The illustration of the metastable coexistence phase diagram is shown in Fig. 1.15(a).

1.6.3 Equilibrium Coexistence

Benguigui *et al*. [59, 60, 76] and Barbulescu *et al*. [77] applied the classical thermodynamics to justify the existence of both F_T and F_R phases. Fig. 1.16(b) shows the phase diagram as an equilibrium system with the two-phase region between each single phase according Gibbs phase rule. In their opinion, the two-phase region observed around the MPB of PZT ceramics arises due to a solubility gap. From this model, the morphotropic phase change is a first-order transition. Inside the insolubility interval, the relative amount of each phase is expected to change according to the lever law, while the chemical composition, the lattice parameters and the physical properties (dielectric susceptibility, piezoelectric constants) of each phase are independent of the concentration x in the coexistence range (shown in Fig. 1.15(c)). Therefore, in the two-phase coexistence region the volume of the F_R phase is larger than that of the F_T phase ($V_R > V_T$), which is the inverse situation to that seen in the metastable equilibrium coexistence.

Later, Rossetti *et al*. [66, 78] calculated an equilibrium phase diagram satisfying the Gibbs phase rule for the PZT system from a low-order Landau expansion in the approximation of the theory of regular solutions. Miscibility gaps replace the MPB line and the paraelectric to ferroelectric transition lines of the diffusionless phase diagram. The width of the miscibility gap increases directly with the value of the mixing parameter. In their calculation, the PZT solid solution consists of two cubic phases (P_C and P'_C) in

the high temperature region when the interaction parameter (w) exceeds a critical value. Also, direct thermochemical studies of the equilibrium enthalpies of formation from the oxides have shown that the PZT system with a large positive mixing energy and exhibits a tendency towards phase decomposition [79].

1.6.4 Heterogeneity (Composition Fluctuation)

In 1977, Kakegawa *et al*. [80] claimed the single phase PZT can be obtained by a "wet-dry combination technique". By this processing, no coexistence of F_T and F_R phases was found in any composition range. They claimed that the phase coexistence observed when using other processing methods was simply due to the PZT system not reaching its homogeneous state since the diffusion rate of titanium is much higher than that of zirconium. This causes a change in composition of the perovskite phase and results in a certain range of compositional distribution. Later, they reported related results aimed at obtaining and determining the range of heterogeneity in PZT solid solutions [81-85]. The heterogeneity could be observed by the broadening of (200) peak in XRD which represents the lattice constant a_T as a series of different but close numbers instead of a constant (shown in Fig. 1.17). This broadened peak could be sharpened by applying a longer calcination time. Fig. 1.16(c) is a simple illustration of this model. The coexistence region is due to heterogeneity, and the distribution size of lattice constant a_T determines the range of the heterogeneity. However, the averaged lattice constant is equal to the one at MPB.

In this model, two-phase coexistence is not recognized. The lattice constant is a distribution range throughout the whole system. The average lattice constant is the same as the diffusionless model (see Fig. 1.15(a)), and the volumes of F_T and F_R at MPB are

equal (V_R=V_T). This model can be differentiated from diffusionless model by comparing the peak width of the x-ray diffraction reflections.

1.6.5 Thermal Fluctuation (Statistical Distribution Model)

In 1992, Cao and Cross developed a statistical distribution model to describe the molar fraction change in the region where both phases coexist [86-88]. They assumed the system had different structures but the same composition. This hypothesis indicates that the two phases occur due to thermal fluctuations that are quenched in during the cooling from the paraelectric to the ferroelectric states. The probability of attaining a particular low-temperature state on cooling from the fluctuating state is proportional to the different possible domain numbers of F_T and F_R. The illustration of the phase diagram for this model is shown in Fig. 1.18.

In this model, the composition considered remains the same but with different structures. The average lattice constant is the same as the metastable coexistence model. Therefore, the volumes of F_T and F_R at coexistence region are equal ($V_R < V_T$), it implies that this model is essentially the same as metastable coexistence model.

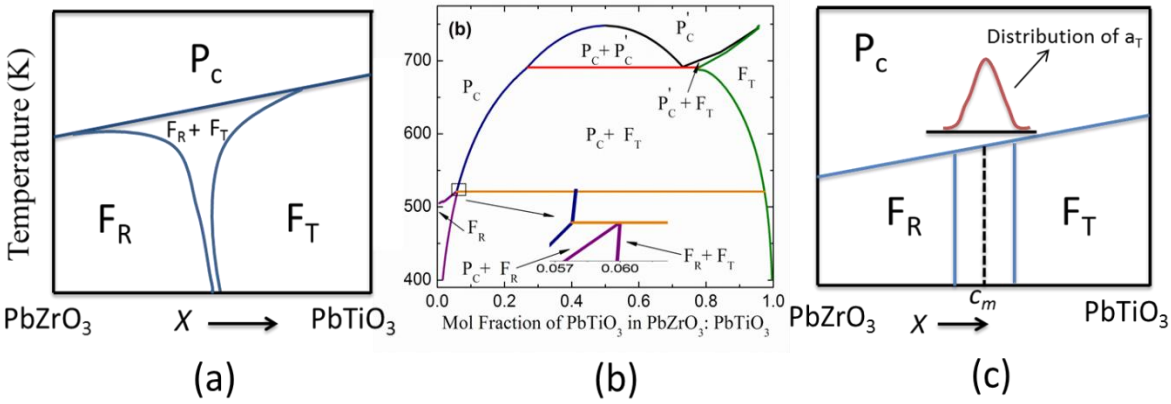

Figure 1. 16 . Illustrations of PZT (a) metastable coexistence, (b) equilibrium coexistence at interaction parameter w =4 [64], and (c) heterogeneity phase diagram.

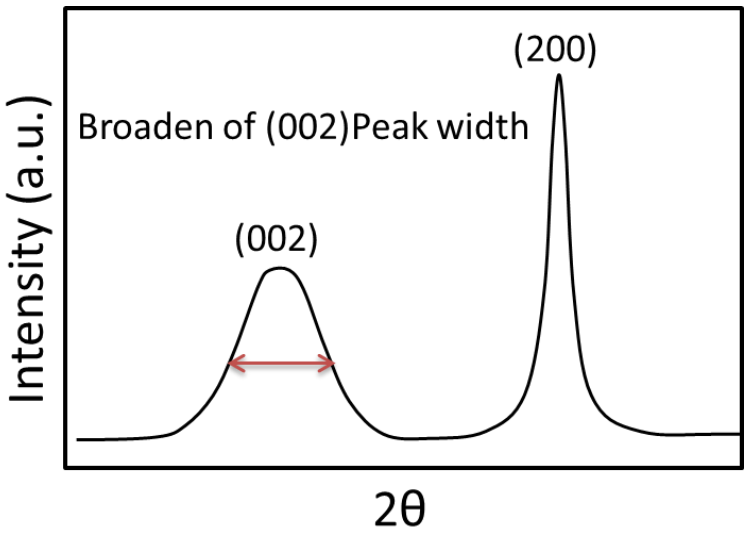

Figure 1. 17 Illustration of the peak broadening of (002) reflection due to compositional fluctuation.

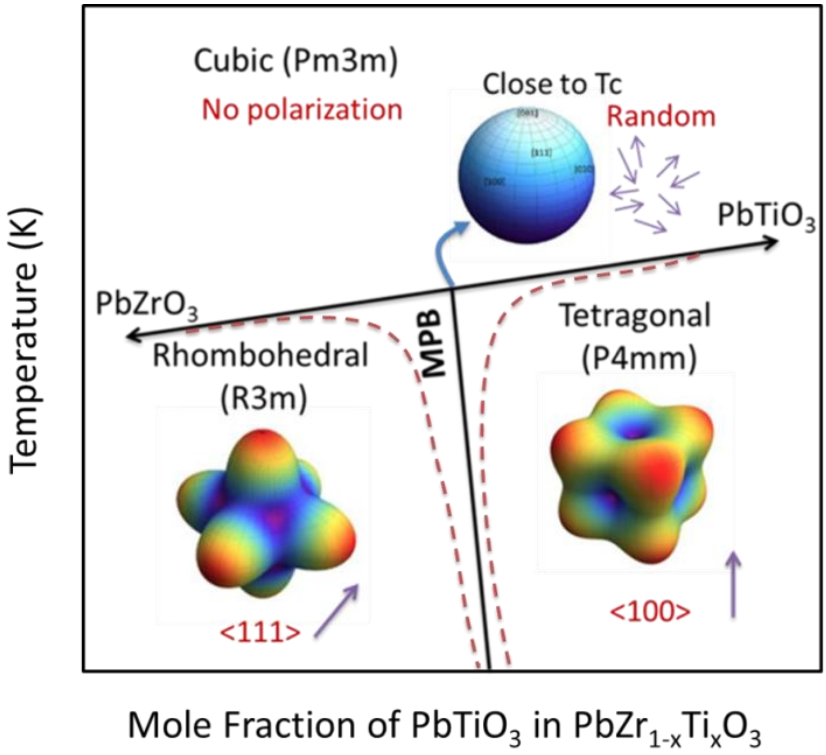

Figure 1. 18 Illustration of the phase diagram of the thermal fluctuation model.

A diffusionless phase diagram and the four phase coexistence models have been carefully assayed. The phase coexistence model of PZT solid solution can be determined by comparing the volumes between F_T and F_R phases. Among these models, an equilibrium coexistence model shows the most consistency with the experiment results. It makes the equilibrium coexistence model become the most suitable candidate for explaining phase coexistence phenomenon in PZT solid solution.

1.7 Kinetics of Forming PZT Solid Solution

The kinetics of forming PZT solid solutions by the mixed oxide or the sol-gel methods have been extensively studied since the 1960's. Table 1.2 shows four possible reaction sequences in PZT formation from mixed oxides [89-91]. The starting materials are lead oxide (PbO or P in short), zirconium oxide (ZrO_2 or Z) and titanium oxide (TiO_2 or T). From all of the studies, PbO reacted with TiO_2 to form lead titanate ($PbTiO_3$, PT in short) at around 723K, and then PZT was formed due to reaction of ZrO_2 with PT at around 923K. Single phase PZT was reached above 1273K. Other phases such as intermediate PZT composition (PZ_xT_{1-x}) and solid solution of PbO, ZrO_2 and $PbTiO_3$ (P(ss)) were observed during the PZT formation process. No lead zirconate ($PbZrO_3$) was observed during the reaction sequence. Among these studies, Biggers *et al*. observed the two-phase coexistence in the PZT formation by XRD analysis. The final PZT solid solution with composition x = 0.40 (PZT 60/40) was formed by the combination of two PZT solid solutions with different compositions, which were x = 0.50 and x = 0.40 (PZT 50/50 and PZT 60/40) [90, 91].

There are also many studies focused on the formation of PZT solid solution by sol-gel methods. Wilkinson *et al*. [92, 93] reported the crystallization kinetics in

alkoxide-derived PZT. Their studies showed that PZT exhibits a two-phase coexistence even under very carefully constrained experimental conditions. Furthermore, the tetragonal / rhombohedral ratio observed in alkoxide-derived PZT was very close to that of the mixed oxide-derived PZT. Hence, a two-phase coexistence in PZT with F_T and F_R phases with similar phase ratio was observed by both mixed oxide or sol-gel methods. In contrast, Kakegawa *et al.* [80, 82] claim that single phase PZT can be obtained by a "wet-dry method" and a "combination of thermal spray decomposition method with solid-phase reaction". However, these methods involve a special series of reactions in order to avoid forming the two-phase state. This indicates that the single phase state obtained by these special methods is metastable.

Mori	Matsuo	Speri	Biggers
P+Z+T	P+Z+T	P+Z+T	P+Z+T
↓	↓	↓	↓
(PT+Z)(ss)	PT+P+T+Z	PT+P+Z+T	PT+P+Z+T
↓	↓	↓	↓
PZT	PT+(PZ_xT_{1-x})	PT+P(ss)	PT+P(ss)
	↓	↓	↓
	PZT	PZT	PZT

P: othorhombic PbO, Z: monoclinic ZrO_2, T: tetragonal TiO_2, PT+Z(ss): solid solution of $PbTiO_3$ and ZrO_2, PT: tetragonal $PbTiO_3$, PZT: $PbZr_xTi_{1-x}O_3$, P(ss): solid solution of PbO, PbTiO3 and ZrO2: and (PZ_xT_{1-x}): intermediate PZT composition

Table 1. 2 Comparative list of reaction sequence in PZT formation from mixed oxide

1.8 Monoclinic Phase in PZT

Noheda *et al.* proposed a new monoclinic phase (C_m) exists in the MPB region at low temperature, which is acting like a bridge between the tetragonal (F_T) and rhombohedral (F_R) PZT phases. This observation was based on high resolution synchrotron x-ray and neutron diffractions measurements [61, 64]. Later, the Noheda *et al.* updated the stability for this monoclinic phase (*Cm*), which is stable at PZT $0.46 \leq x \leq 0.51$ [62]. The new phase diagram contains a monoclinic phase within MPB region at low temperature is shown in Fig. 1. 14.

There were extensive discussions , which including both experimentally and theoretically, on the phase transition mechanism, stability and phase coexistence of this new found phase in the past decades. These experimental approaches to study the monoclinic phase in PZT were high-resolution X-ray diffraction (XRD) with Rietveld analysis [68, 94], Raman-spectroscopy [68, 95], TEM [96, 97] and dielectric characterizations [98]. In theoretical approaches, first-principle calculations on the PZT solid solution have not only confirmed the presence of the monoclinic phases but have also shown that they are responsible for the maximum electromechanical response [99, 100]. The observation of an MPB immediately raised questions that list as follows,

1. The stability of monoclinic phase.
2. The coexistence of monoclinic phases and other phases, and the range of these coexistence phases.
3. There were several reports question if the monoclinic phase really exists in the PZT system, and the details will be discussed in the chapter 1.9.

Several authors have been reporting the existence range of a monoclinic phase in PZT. Ragini *et al.* were considered two monoclinic phases, *Cm* and *Cc*, exist at different temperature range at near the MPB region, and one of the monoclinic phases (*Cm*) coexists with tetragonal phase at the boundary of two phases. In their work, composition and temperature range of the PZT with monoclinic phase (*Cm*) was extended to $0.38 \leq x \leq 0.47$ at room temperature, which was previously considered as rhombohedral phase (*R3m*) [101]. In fact, there is a sharp boundary between monoclinic and tetragonal phases observed experimentally [64], but no such boundary has been reported between the monoclinic and rhombohedral phases. In the work of Singh *et al.*, they reported that monoclinic with space group *Cm* exist at the composition of $0.40 \leq x \leq 0.475$ at room temperature, with no coexistence of phases [102].

There were several interpretations of Rietveld analysis of the neutron powder data, which indicate that there are more than one monoclinic phases exist at around MPB. Another low temperature monoclinic phase (*Cc*) with a doubled cell characteristic of anti-phase tilting of the oxygen octahedral was first proposed by Ranjan and coworkers [94, 101, 103]. In addition, Frantti *et al*. concluded that the weak superlattice peaks observed in the neutron scattering should be attributed to the coexistence of a rhombohedral *R3c* phase and a monoclinic *Cm* phase [68]. However, this conclusion was disputed by other authors , Noheda *et al.* [104] and Ranjan *et al.* [105], who argue that the coexistence model of *Cm* and *Cc* phases was account for the superlattice peak positions. It is extremely difficult to have a definitive result from Rietveld analysis alone in these complicated piezoelectric systems. Because of the diffraction methods were unable to determine the true crystallographic symmetries of these phases due to the resolution limit

of the diffraction [106]. Cordero *et al.* also indicated that "it is still controversial whether superlattice reflections observed in diffraction spectra at liquid He temperatures are due to rotations of the octahedral, with the monoclinic phase passing from *Cm* to *Cc*, or instead to coexistence of the *Cm* and *R3c* structures [107, 108]".

Furthermore, structural difference between the samples prepared by different methods was observed in the literatures [106, 109]. Therefore, the structure of the PZT at around the MPB is rather confusing and without definitive result by far.

1.9 Domain Miniaturization around MPB

The existence of monoclinic phases in PZT, which are usually determined by high resolution x-ray or neutron powder diffractions, remains a topic of intense debate. Because of the diffraction results in this complicated PZT system can be easily affected by small domain sizes, internal stress, and multiple coexisting phases. Thus, it is difficult to determine lattice parameters and precise phases from the complicated diffraction patterns.

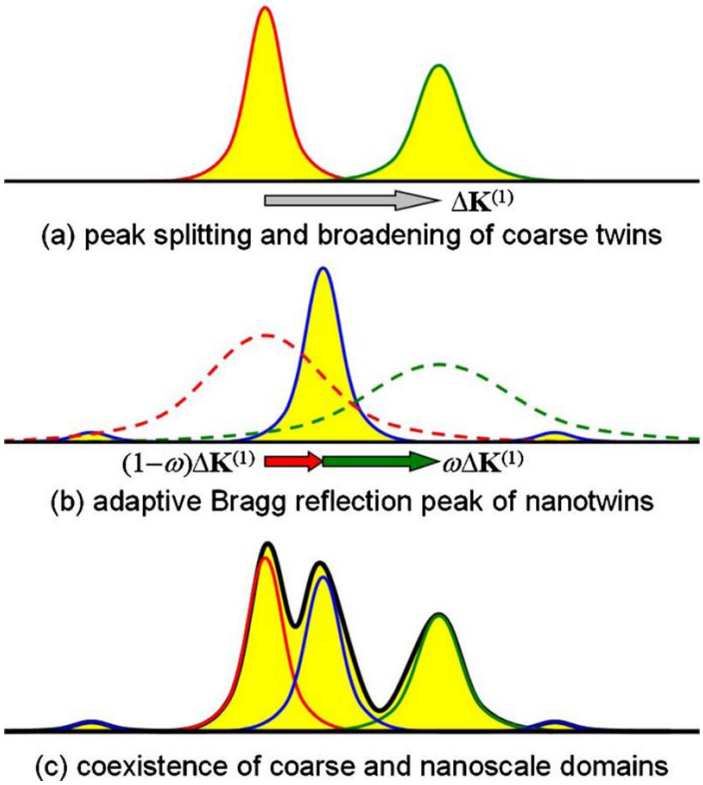

Figure 1. 19 Schematic illustrations of diffraction phenomena in the cases of (a) coarse twins, (b) nanotwins, and (c) coexistence of coarse and nanoscale domains, after Wang [113]. Where ω is twin variant volume fraction of tetragonal phase and ΔK(1) is the Bragg twin peak splitting vectors due to twinning deformation.

Jin *et al.* developed a theory of an adaptive ferroelectric phase to predict the microdomain-averaged crystal lattice parameters of this structurally inhomogeneous state [110, 111]. This theory was based on the adaptive phase model, which was originally applied to explain an adaptive phase formation a martensitic transformation [112]. An adaptive state in ferroelectrics is the ferroelectric phase transforms into an inhomogeneous microdomain state which is macroscopically homogeneous. Based on this theory, the authors stated that the lattice parameters of the monoclinic phase calculated using Rietveld refinement were made up of tetragonal nanotwins. In a similar approach, Wang *et al*. was able to develop a diffraction theory of nanotwin superlattices

with low symmetry phases [113, 114]. Wang indicates that "the nanotwin superlattices of rhombohedral phase with (001) and (110) twin planes diffract incident waves just like monoclinic M_A and M_B phases, respectively." It means that one or more extra diffraction peaks would be appeared when nanodomains coexist with coarse domains. Such a diffraction result can be easily misinterpreted as evidence of a new phase. Fig. 1.19 shows the schematic illustrations of diffraction phenomena in (a) coarse twins, (b) nanotwins, and (c) coexistence of both coarse and nanoscale domains.

In fact, the domains miniaturization due to very low domain wall energy (Υ) at MPB region in PZT system was experimentally observed by TEM [96, 97]. Fig. 1.20 shows TEM results of PZT with different compositions, and it clearly shows that the domain miniaturized at the MPB region.

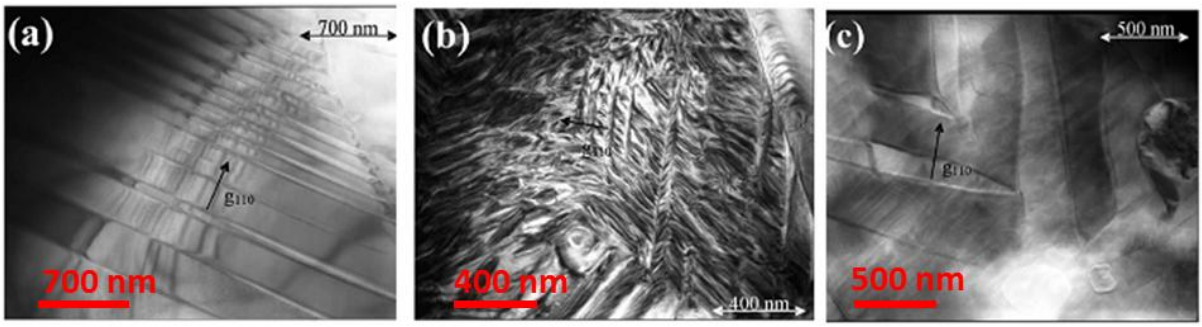

Figure 1. 20 TEM bright field images of typical domain structure of the PZT (a) x = 0.40, (b) x = 0.50, and (c) x = 0.60, after Woodward *et al.* [95].

1.10 References

1. J. Valasek, *Physical Review* **15**, 537 (1920)
2. J. Valasek, *Physical Review* **17**, 475 (1921)
3. A.V. Hippel, R.G. Breckenridge, F.G. Chesley, and L. Tisza, *Ind. Eng. Chem.* **38**, 1097 (1946)
4. B.M. Wul and I.M. Goldman, *Dokl. Akad. Nauk SSSR* **46**, 154 (1945)
5. S. Miyake and R. Ueda, *J. Phys. Soc. Jpn.* **1**, 32 (1946)
6. R.B. Gray, U.S. Patent No.2 486 560 (1949).
7. A.F. Devonshire, *Phil. Mag.* **42**, 1065 (1951)
8. E. Sawaguchi, *J Phys Soc Jpn* **5**, 615 (1953)
9. G.H. Haertling, *J Am Ceram Soc* **86**, 797 (1999)
10. B. Jaffe, W.R. Cook, and H.L. Jaffe, *Piezoelectric ceramics* 1971, London, New York,: Academic Press. 135.
11. L.E. Cross, *Ferroelectric ceramics: tutorial reviews, theory, processing, and applications* 1993, Basel, Switzerland: Birkhäuser. 1.
12. M.E. Lines and A.M. Glass, *Principles and Applications of Ferroelectrics and Related Materials* 1977, New York: Oxford University Press.
13. *IEEE Trans. Ultras. Ferro. Freq. Control* **50**, 1 (2003)
14. N. Bassiri-Gharb, *DIELECTRIC AND PIEZOELECTRIC NONLINEARITIES IN ORIENTED Pb(Yb1/2Nb1/2)O3-PbTiO3 THIN FILMS*, in *Mater Sci Eng*2005, The Pennsylvania State University.
15. J.F. Scott, *Science* **315**, 954 (2007)

16. L.M. Levinson, *Electronic Ceramics: Properties, Devices, and Applications* 1988: CRC Press.

17. A.K. Tagantsev, V.O. Sherman, K.F. Astafiev, J. Venkatesh, and N. Setter, *Journal of Electroceramics* **11**, 5 (2003)

18. G. Akcay, S.P. Alpay, G.A. Rossetti, and J.F. Scott, *J Appl Phys* **103**, 024104 (2008)

19. A.S. Mischenko, Q. Zhang, J.F. Scott, R.W. Whatmore, and N.D. Mathur, *Science* **311**, 1270 (2006)

20. A.S. Mischenko, Q. Zhang, R.W. Whatmore, J.F. Scott, and N.D. Mathur, *Appl Phys Lett* **89**, 242912 (2006)

21. J.F. Scott and C.A.P. Dearaujo, *Science* **246**, 1400 (1989)

22. I.I. Naumov, L. Bellaiche, and H.X. Fu, *Nature* **432**, 737 (2004)

23. Y.K. Jun, W.T. Moon, C.M. Chang, H.S. Kim, H.S. Ryu, J.W. Kim, K.H. Kim, and S.H. Hong, *Solid State Commun* **135**, 133 (2005)

24. J. Fousek and V. Janovec, *J Appl Phys* **40**, 135 (1969)

25. J. Sapriel, *Physical Review B* **12**, 5128 (1975)

26. D. Damjanovic, *Rep Prog Phys* **61**, 1267 (1998)

27. N. Bassiri-Gharb, I. Fujii, E. Hong, S. Trolier-McKinstry, D.V. Taylor, and D. Damjanovic, *Journal of Electroceramics* **19**, 47 (2007)

28. G. Arlt, H. Dederichs, and R. Herbiet, *Ferroelectrics* **74**, 37 (1987)

29. D.A. Hall, *J Mater Sci* **36**, 4575 (2001)

30. Q.M. Zhang, H. Wang, N. Kim, and L.E. Cross, *J Appl Phys* **75**, 454 (1994)

31. Z.Q. Zhuang, M.J. Haun, S.J. Jang, and L.E. Cross, *Ieee T Ultrason Ferr* **36**, 413 (1989)

32. A. von Hippel, *Reviews of Modern Physics* **22**, 221 (1950)

33. Y.M. Poplavko, V.G. Tsykalov, and V.I. Molchanov, *Sov. Phys. –Solid State* **10**, 2708 (1969)

34. O. Kersten, M. Hofmann, and G. Schmidt, *Ferroelectrics Lett* **6**, 75 (1986)

35. U. Bottger and G. Arlt, *Ferroelectrics* **127**, 95 (1992)

36. A.V. Turik and N.B. Shevchenko, *Phys Status Solidi B* **95**, 585 (1979)

37. G. Arlt, U. Bottger, and S. Witte, *Ann Phys-Leipzig* **3**, 578 (1994)

38. M. Maglione, R. Bohmer, A. Loidl, and U.T. Hochli, *Physical Review B* **40**, (1989)

39. X.L. Zhang, Z.X. Chen, L.E. Cross, and W.A. Schulze, *J Mater Sci* **18**, 968 (1983)

40. F. Xu, S. Trolier-McKinstry, W. Ren, B.M. Xu, Z.L. Xie, and K.J. Hemker, *J Appl Phys* **89**, 1336 (2001)

41. C. Ang and Z. Yu, *Appl Phys Lett* **85**, 3821 (2004)

42. C.A. Randall, N. Kim, J.P. Kucera, W.W. Cao, and T.R. Shrout, *J Am Ceram Soc* **81**, 677 (1998)

43. G. Arlt, *Ferroelectrics* **76**, 451 (1987)

44. D.A. Hall and P.J. Stevenson, *Ferroelectrics* **228**, 139 (1999)

45. S.P. Li, W.W. Cao, and L.E. Cross, *J Appl Phys* **69**, 7219 (1991)

46. L. Rayleigh, *Philos. Mag* **23**, 225 (1887)

47. D. Damjanovic and M. Demartin, *J Phys D Appl Phys* **29**, 2057 (1996)

48. D. Damjanovic, *J Appl Phys* **82**, 1788 (1997)

49. D.V. Taylor and D. Damjanovic, *J Appl Phys* **82**, 1973 (1997)

50. D. Damjanovic and M. Demartin, *J Phys-Condens Mat* **9**, 4943 (1997)

51. L. Néel, *Cahier de Physique* **12**, 1 (1942)

52. G. Arlt and N.A. Pertsev, *J Appl Phys* **70**, 2283 (1991)

53. G. Shirane, E. Sawaguchi, and Y. Takagi, *Physical Review* **84**, 476 (1951)

54. J.-M.M. Christian Michel, Gary D. Achenbach, Robert Gerson, W.J. James, *Solid State Commun* **7**, 865 (1969)

55. S.A. Mabud, *J Appl Crystallogr* **13**, 211 (1980)

56. M.J. Haun, Z.Q. Zhuang, E. Furman, S.J. Jang, and L.E. Cross, *Ferroelectrics* **99**, 45 (1989)

57. V.A. Isupov, *Soviet Physics - Solid States* **12**, 1084 (1970)

58. T. Frömling, A. Schintlmeister, H. Hutter, and J. Fleig, *J Am Ceram Soc* **94**, 1173 (2011)

59. P. Ari-gur and L. Benguigui, *Solid State Commun* **15**, 1077 (1974)

60. P. Arigur and L. Benguigui, *J Phys D Appl Phys* **8**, 1856 (1975)

61. B. Noheda, D.E. Cox, G. Shirane, J.A. Gonzalo, L.E. Cross, and S.E. Park, *Appl Phys Lett* **74**, 2059 (1999)

62. B. Noheda, D.E. Cox, G. Shirane, R. Guo, B. Jones, and L.E. Cross, *Physical Review B* **63**, 014103 (2000)

63. B. Noheda, J.A. Gonzalo, A.C. Caballero, C. Moure, D.E. Cox, and G. Shirane, *Ferroelectrics* **237**, 541 (2000)

64. B. Noheda, J.A. Gonzalo, L.E. Cross, R. Guo, S.E. Park, D.E. Cox, and G. Shirane, *Physical Review B* **61**, 8687 (2000)

65. I. Sergienko, Y. Gufan, and S. Urazhdin, *Physical Review B* **65**, 144104 (2002)

66. G.A. Rossetti, A.G. Khachaturyan, G. Akcay, and Y. Ni, *J Appl Phys* **103**, 114113 (2008)

67. D.L. Corker, A.M. Glazer, R.W. Whatmore, A. Stallard, and F. Fauthx, *Journal of Physics: Condensed Matter* **10**, 6251 (1998)

68. J. Frantti, S. Ivanov, S. Eriksson, H. Rundlöf, V. Lantto, J. Lappalainen, and M. Kakihana, *Physical Review B* **66**, 064108 (2002)

69. V.A. Isupov, *Solid State Commun* **17**, 1331 (1975)

70. V.A. Isupov, *Soviet Physics - Solid States* **18**, 529 (1975)

71. V.A. Isupov, *Soviet Physics - Solid States* **16**, 2103 (1975)

72. V.A. Isupov, *Soviet Physics - Solid States* **19**, 783 (1977)

73. V.A. Isupov, *Soviet Physics - Solid States* **22**, 172 (1980)

74. V.A. Isupov, *Physics of the Solid State* **43**, 2262 (2001)

75. V.A. Isupov, *Ferroelectrics* **266**, 427 (2002)

76. L. Benguigui, *Solid State Commun* **19**, 979 (1976)

77. A. Barbulescu, E. Barbulescu, and D. Barb, *Ferroelectrics* **47**, 221 (1983)

78. G.A. Rossetti, W. Zhang, and A.G. Khachaturyan, *Appl Phys Lett* **88**, 072912 (2006)

79. M.V. Rane, A. Navrotsky, and G.A. Rossetti, *J Solid State Chem* **161**, 402 (2001)

80. K. Kakegawa, J. Mohri, T. Takahashi, H. Yamamura, and S. Shirasaki, *Solid State Commun* **24**, 769 (1977)

81. K. Kakegawa, J. Mohri, S. Shirasaki, and K. Takahashi, *J Am Ceram Soc* **65**, 515 (1982)

82. K. Kakegawa, K. Arai, Y. Sasaki, and T. Tomizawa, *J Am Ceram Soc* **71**, C49 (1988)

83. K. Kakegawa, M. Kawakami, and Y. Sasaki, *J Am Ceram Soc* **71**, C444 (1988)

84. K. Kakegawa, O. Matsunaga, T. Kato, and Y. Sasaki, *J Am Ceram Soc* **78**, 1071 (1995)

85. K. Kakegawa, T. Kato, and Y. Sasaki, *J Eur Ceram Soc* **20**, 1599 (2000)

86. W.W. Cao and L.E. Cross, *Jpn J Appl Phys 1* **31**, 1399 (1992)

87. W. Cao and L. Cross, *Physical Review B* **47**, 4825 (1993)

88. W. Cao and L.E. Cross, *J Appl Phys* **73**, 3250 (1993)

89. Y. Matsuo and H. Sasaki, *Journal of the Amercan Ceramic Society* **48**, 289 (1965)

90. D.L. Hankey and J.V. Biggers, *Journal of the Amercan Ceramic Society*, C-172 (1981)

91. B.V. Hiremath, A.I. Kingon, and J.V. Biggers, *J Am Ceram Soc*, 790 (1983)

92. A.P. Wilkinson, J.S. Speck, and A.K. Cheetham, *Chemistry of Materials* **6**, 750 (1994)

93. A.P. Wilkinson, J. Xu, S. Pattanaik, and S.J.L. Billinge, *Chemistry of Materials* **10**, 3611 (1998)

94. R. Ranjan, Ragini, S. Mishra, D. Pandey, and B. Kennedy, *Physical Review B* **65**, 060102 (2002)

95. A.G. Souza, K.C.V. Lima, A.P. Ayala, I. Guedes, P.T.C. Freire, J. Mendes, E.B. Araujo, and J.A. Eiras, *Physical Review B* **61**, 14283 (2000)

96. D. Woodward, J. Knudsen, and I. Reaney, *Physical Review B* **72**, 104110 (2005)

97. K.A. Schönau, L.A. Schmitt, M. Knapp, H. Fuess, R.-A. Eichel, H. Kungl, and M.J. Hoffmann, *Physical Review B* **75**, 184117 (2007)

98. Ragini, S. Mishra, D. Pandey, H. Lemmens, and G. Tendeloo, *Physical Review B* **64**, (2001)

99. L. Bellaiche, A. García, and D. Vanderbilt, *Ferroelectrics* **266**, 41 (2002)

100. H.X. Fu and R.E. Cohen, *Nature* **403**, 281 (2000)

101. Ragini, R. Ranjan, S.K. Mishra, and D. Pandey, *J Appl Phys* **92**, 3266 (2002)

102. A.K. Singh, D. Pandey, S. Yoon, S. Baik, and N. Shin, *Appl Phys Lett* **91**, 192904 (2007)

103. D. Hatch, H. Stokes, R. Ranjan, Ragini, S. Mishra, D. Pandey, and B. Kennedy, *Physical Review B* **65**, (2002)

104. B. Noheda, L. Wu, and Y. Zhu, *Physical Review B* **66**, 060103 (2002)

105. R. Ranjan, A.K. Singh, Ragini, and D. Pandey, *Physical Review B* **71**, 092101 (2005)

106. H. Yokota, N. Zhang, A.E. Taylor, P.A. Thomas, and A.M. Glazer, *Physical Review B* **80**, 104109 (2009)

107. F. Cordero, F. Trequattrini, F. Craciun, and C. Galassi, *Journal of physics. Condensed matter : an Institute of Physics journal* **23**, 415901 (2011)

108. F. Cordero, F. Craciun, and C. Galassi, *Phys Rev Lett* **98**, 255701 (2007)

109. H. Yokota, N. Zhang, P.A. Thomas, and A.M. Glazer, *Ferroelectrics* **414**, 147 (2011)

110. Y.M. Jin, Y.U. Wang, A.G. Khachaturyan, J.F. Li, and D. Viehland, *J Appl Phys* **94**, 3629 (2003)

111. Y.M. Jin, Y.U. Wang, A.G. Khachaturyan, J.F. Li, and D. Viehland, *Phys Rev Lett* **91**, 197601 (2003)

112. A. Khachaturyan, S. Shapiro, and S. Semenovskaya, *Physical Review B* **43**, 10832 (1991)

113. Y. Wang, *Physical Review B* **74**, 104109 (2006)

114. Y. Wang, *Physical Review B* **76**, 024108 (2007)

Chapter 2

OBJECTIVES AND THESIS OVERVIEW

2.1 Statement of Problem and Objectives

Solid solutions of lead zirconate titanate [$PbZr_{1-x}Ti_xO_3$ (PZT)] are extensively used in electro-active devices and in other technological applications due to the maxima in piezoelectric, elastic, and dielectric properties that occur near the morphotropic phase boundary (MPB) where this solid solution changes structure as a function of the chemical composition (around x = 0.48) [1-5]. One of most commonly accepted reasons for the enhanced properties near the MPB is the rhombohedral (*R3m*) and tetragonal (*P4mm*) ferroelectric phases coexist at near the MPB and increases the number of possible spontaneous polarization directions [6-8]. Phase coexistence is commonly observed near the MPB in PZT at room temperature. However, the origin of the phase coexistence, the width of the two-phase region, and the average structure of PZT near the MPB are still controversial.

In the last 40 years, the origin of two low temperature phases coexists and near the MPB in the PZT ceramics has been variously attributed to the metastable coexistence [9, 10], to the heterogeneity and/or the composition fluctuation [11, 12], to the thermal fluctuation with a statistical distribution model [13, 14], and to equilibrium coexistence[15-18]. Besides, the coexistence of tetragonal and rhombohedral phases around the MPB could be also affected by internal stress [19, 20]. Among these hypotheses, an equilibrium PZT phase diagram with two-phase regions replacing the line boundaries in the traditional phase diagram was reported by Rossetti *et al.* [17, 18]. This

predicted equilibrium phase diagram can be obtained by considering PZT solutions as a regular solution and combines the conventional Landau-Ginzburg-Devonshire (LGD) free energy [21] function with a positive enthalpy of mixing [22]. It also suggests the decomposition occurs by a peritectoid reaction and the miscibility gaps can be extended to the cubic phase with a sufficient value of the atomic exchange interaction parameter. Based on this hypothesis, an equilibrium two-phase coexistence can be achieved with a normal material processing if the diffusional processes are sufficiently fast, and the ratio between two phases is determined by the lever law. Conversely, if diffusion processes are not sufficient fast enough, the ratio between the two ferroelectric phases would vary with different processing conditions and/or cooling rate.

In addition, a large tolerance (±20%) in piezoelectric and dielectric properties of the commercial PZT-based ceramic is usually observed. This, added to the fact that the ratio between two ferroelectric phases at near the MPB is not consistent with all literature data, would lead one to suspect that the PZT ceramics may not able to reach their equilibrium state after sintering at high-temperature and cooled by natural convection. A better understanding of the phase equilibria in the PZT ceramic is not only scientifically interesting, but also technically important. It could provide useful information for the processing, microstructure control, and structure-sensitive properties of PZT solid solutions.

In this work, an unusual annealing approach was used to investigate the influence of thermal history on crystal structure, microstructure, domain structures and the dielectric properties of un-doped PZT ceramics. Furthermore, it is of interest to see whether the equilibrium phase mixture can be established by accelerating the diffusional

processes by applying a higher temperature at above Curie temperature (*Tc*) to allow for the atomic redistributions.

The main objectives in this thesis study are:

I. To determine whether or not diffusional processes are fast enough to establish two phase equilibrium
II. To determine the influence of thermal history on the crystal structure, microstructure and domain structure
III. To determine the influence of thermal history on the energetic of paraelectric to ferroelectric phase transitions in the PZT ceramics.
IV. To determine the influence of the structural changes on the dielectric properties

2.2 Thesis Overview

The technical background and literature review (Chapter 1)

The concepts used in this thesis were described in Chapter 1. These are

1. Fundamental knowledge of ferroelectrics, ferroelectric domains and the introduction to PZT.
2. Different approaches to study and separate intrinsic and extrinsic contributions to the dielectric property.
3. Literature reviews of current proposed PZT phase diagrams and other conflicting subjects near at MPB region.

Preparation and structural characterization of PZT powder and sintered disks/ceramics (Chapter 3 and 4)

To accomplish the objectives in this work, PZT powders (x = 0.00, 1.00) and sintered disks ($0.10 \leq x \leq 0.80$) with different compositions were prepared using three different chemical routes. The structure of PZT powder and sintered disks were characterized by x-ray diffraction. The quality of the samples was determined by comparing the structural properties to the literature data.

The paraelectric to ferroelectric phase transitions behavior in the PZT ceramics (Chapter 5)

Temperature dependence of specific heat (C_p) of the PZT powders (x = 0.00, 1.00) and sintered disks ($0.10 \leq x \leq 0.80$) was used to study the paraelectric to ferroelectric phase transitions behavior in the PZT ceramics. The order of the phase transition was determined by first derivative of C_p curves, the transition enthalpies (ΔH_i), and transition entropies (ΔS_i). The order of the phase transition was then used to find the tricritical points in the PZT system.

Intrinsic and extrinsic contributions to dielectric constant of as-synthesized PZT ceramics (Chapter 6)

Intrinsic and extrinsic contributions to dielectric of PZT sintered disks ($0.30 \leq x \leq 0.70$) were studied in this thesis work. There were many reports of contribution mechanisms to dielectric constant and Rayleigh analysis on the PZT sintered disks and thin films in the past two decades. However, the composition dependence of Rayleigh coefficient of the un-doped PZT ceramics across whole system has not been reported so far.

Temperature dependence of dielectric property was applied to separate out the contribution mechanisms to dielectric properties in the un-doped PZT system. The extrinsic contribution to dielectric is highly related to the domain wall motions, and different types of the domain wall motions in the PZT system can be quantified by applying Rayleigh analysis on field dependence of the dielectric behavior. The composition dependence of Rayleigh coefficient of the un-doped PZT ceramics across whole system was reported in this thesis work.

Thermal-activated irreversible domain wall motion, which is one of the mechanisms in the extrinsic contribution to dielectric constant, can be quantified from the combined result of the dielectric properties at low field and high field.

Anneal experiment (Chapter 7)

PZT sintered disks ($0.10 \leq x \leq 0.80$) were anneal at 923K for 72h, 120h and 240h to not only determine whether or not diffusional processes are fast enough to establish two phase equilibrium, but also to determine the influence of thermal history to the properties of PZT ceramics.

Weight loss measurement was used to determine whether or not lead loss occurring during the anneal process. Field emission scanning electron microscope (FE-SEM) was applied to characterize the grain size of the PZT sintered disks ($0.10 \leq x \leq 0.80$) before and after anneal process.

Influence of thermal history on structure, domain structure, dielectric behavior, and the paraelectric to ferroelectric phase transitions behavior in the PZT ceramics (Chapter 8 and 9)

The structural, dielectric behavior, and the paraelectric to ferroelectric phase transitions behavior in the annealed PZT sintered disks ($0.10 \leq x \leq 0.80$) were compare to the properties before annealing process. Four categories were used to determine the influence of thermal history on structural properties, which are lattice parameters, spontaneous strain, phase coexistence, and peak width. Among these, influence of thermal history on phase coexistence phase provides useful information to determine whether the un-annealed PZT ceramic is in its equilibrium state, and to test whether the or not diffusional processes are fast enough to rearrange two phases in the MPB region.

The influence of thermal history on domain structure was characterized by transmission electron microscopy (TEM). Domain structure evolution by anneal process was reported in this thesis. The influence of the thermal history on the dielectric properties at low and high field was also reported. How anneal process effect on contribution mechanisms and Rayleigh coefficients were discussed.

Conclusion and future work (Chapter 10)

A conclusion of the performed work and basic achievements was reported. Some suggestions were made for future research to have a better knowledge about the processing-structural-property relation.

2.3 References

1. B. Jaffe, W.R. Cook, and H.L. Jaffe, *Piezoelectric ceramics* 1971, London, New York,: Academic Press. 135.
2. S.A. Mabud, *J Appl Crystallogr* 13, 211 (1980)
3. J.F. Scott and C.A.P. Dearaujo, *Science* 246, 1400 (1989)
4. J.F. Scott, *Science* 315, 954 (2007)
5. D. Damjanovic, *Rep Prog Phys* 61, 1267 (1998)
6. P. Arigur and L. Benguigui, *J Phys D Appl Phys* 8, 1856 (1975)
7. V.A. Isupov, *Soviet Physics - Solid States* 18, 529 (1975)
8. J. Rouquette, J. Haines, V. Bornand, M. Pintard, P. Papet, C. Bousquet, L. Konczewicz, F.A. Gorelli, and S. Hull, *Physical Review B* 70, (2004)
9. V.A. Isupov, *Soviet Physics - Solid States* 19, 783 (1977)
10. V.A. Isupov, *Physics of the Solid State* 43, 2262 (2001)
11. K. Kakegawa, J. Mohri, T. Takahashi, H. Yamamura, and S. Shirasaki, *Solid State Commun* 24, 769 (1977)
12. W. Wersing, *Ferroelectrics* 7, (1974)
13. W. Cao and L.E. Cross, *J Appl Phys* 73, 3250 (1993)
14. W.W. Cao and L.E. Cross, *Physical Review B* 47, 4825 (1993)
15. P. Ari-gur and L. Benguigui, *Solid State Commun* 15, 1077 (1974)
16. A. Barbulescu, E. Barbulescu, and D. Barb, *Ferroelectrics* 47, 221 (1983)
17. G.A. Rossetti, W. Zhang, and A.G. Khachaturyan, *Appl Phys Lett* 88, 072912 (2006)

18. G.A. Rossetti, A.G. Khachaturyan, G. Akcay, and Y. Ni, *J Appl Phys* 103, 114113 (2008)

19. V.A. Isupov, *Soviet Physics - Solid States* 22, 172 (1980)

20. T. Kala, *Phys Status Solidi A* 78, (1983)

21. A.F. Devonshire, *Phil. Mag.* 42, 1065 (1951)

22. M.V. Rane, A. Navrotsky, and G.A. Rossetti, *J Solid State Chem* 161, 402 (2001)

CHAPTER 3

SYNTHESIS OF PZT POWDER AND SAMPLE PREPARATION

Lead zirconate titanate (PZT) ceramics are chosen as the model system in this work for investigation of processing-structure-property correlations in piezoelectric ceramics. The solid solution of lead zirconate ($PbZrO_3$) and lead titanate ($PbTiO_3$) is a well-known ferroelectric system with wide technological applications. There were many different reports on synthesis PZT since it was discovered in early ’50s.

This work was attempted to explore the processing-structure-property correlations across the PZT solid solution. Therefore, the composition of the PZT specimen needs to be carefully determined, and high phase purity of specimen is also needed. To achieve these requirements, four different approaches to synthesis the PZT powders were carried out.

3.1 Synthesis of PZT Powder

There are two major routes for synthesis of the ferroelectric PZT ceramics. First one is the conventional mixed oxide method, which is usually proceeds through a series of solid state reaction, and reaches completion only at very high temperatures (~1473K). Although this method is most common process of manufacturing PZT-based materials in the industry, the high temperature calcination usually leads to inevitable particle coarsening, the large crystallite sizes, and increased diffusion length for redistribution of the Zr and Ti cations under low-temperature equilibrium conditions. To reduce the particle coarsening, multiple steps of ball milling and grinding are necessary to apply on

the calcined powder. To avoid this problem, wet-chemistry-based routes were used to prepare PZT powders in this work.

The sol-gel process has been widely acknowledged to be a promising method because of its uniformity at the molecular level and the low operating temperature requirement. These features could be potential advantages in this work. The lower processing temperature reduce the situation of PbO volatilization and the generation of product phases with smaller crystallite sizes and shorter diffusion distances facilitating the interchange of Zr and Ti atoms. However, the sol-gel process has obvious limitations when employed to prepare PZT ceramics in large quantities. There are many different sol-gel methods to prepare the PZT powder. In this work, author chose two of the most well-known methods, the alkoxide-derived [1-4] the acetate-derived methods [5, 6], to prepare the PZT samples. Also, these two methods are the most convenient for us to obtain the PZT samples in our current laboratory.

PZT powders with different compositions were obtained through three alkoxide-derived approaches, and one acetate-derived approach. These four different approaches are listed as follow,

1. Alkoxide-derived PZT powder from Yi's recipe [1]
2. Acetate-derived PZT powder
3. A commercial alkoxide-based $PbZr_{0.52}Ti_{0.48}O_3$ (Alfa-Aesar) solution
4. Alkoxide-derived PZT powder from Wilkinson's recipe [3, 4]

The experimental procedure of these three approaches is shown in Fig. 3.1. The starting materials in the first approach were lead (II) acetate trihydrate [$Pb(CH_3CO_2)_2 \cdot 3H_2O$], zirconium n-propoxide [$Zr(OCH_2CH_2CH_3)_4$], and titanium isopropoxide

$[Ti[OCH(CH_3)_2]_4]$, glacial acetic acid and methanol as the solvents. The starting materials in second approach were lead sub-acetate $[Pb(C_2H_3O_2)_2 \cdot 2Pb[OH]_2]$, zirconium acetate $[Zr(CH_3COO)_2)]$, and diisopropoxytitanium bis(acetylacetonate) also known as Tyzor® GBA $[(CH_3)_2CHO]_2Ti(C_5H_7O_2)_2]$. The starting materials in both methods are dissolved in the solvent in particular sequences. The PZT solutions were slowly dried at 383K until dry gels formed.

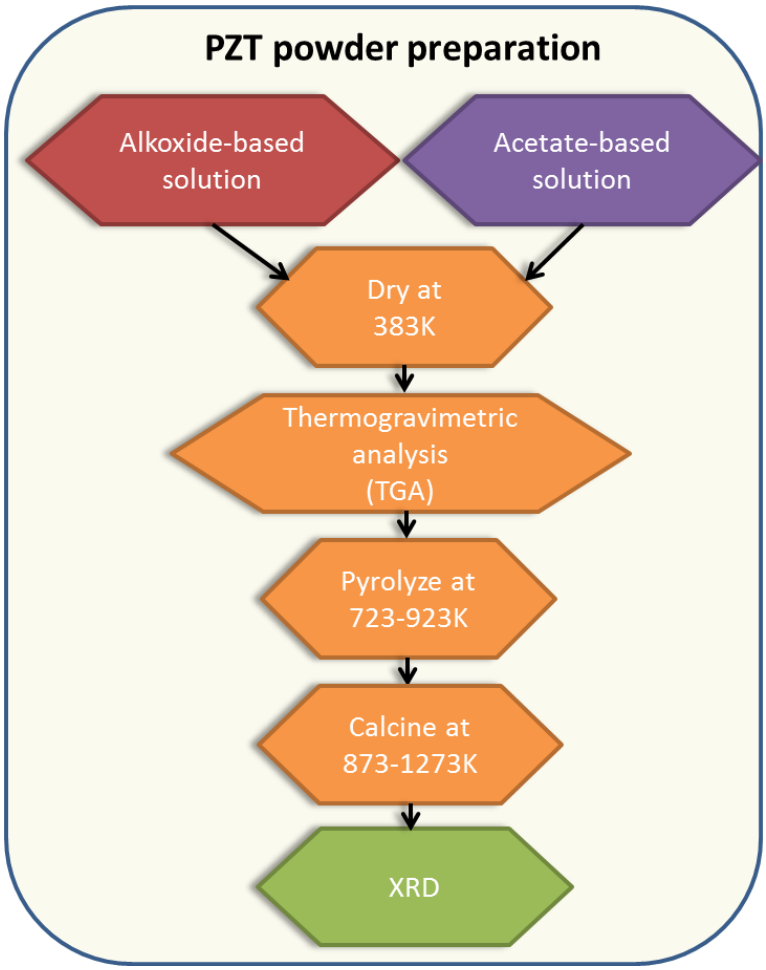

Figure 3. 1 Experimental flow of PZT powder synthesis

Prior to any further thermal treatments, a thermogravimetric analysis (TGA) measurement was carried out to identify the decomposition temperature of the precursors, to estimate the minimum temperature of product phase crystallization, and to determine the onset temperature of PbO volatilization. The measurements were carried out by using a TA Instruments Q500 instrument with 30 - 60 mg of the PZT dry gel. Dry gels were placed in an uncovered platinum pan and heated from 298 K to 1273 K in air with a heating rate of 10 K/min. The result of a dry PZT 50/50 (x = 0.50) gel is shown in Figure 3.2. The result suggest that 23.92% organic precursor in an acetate-derived PZT 50/50 dry gel was decomposed completely at 825K and volatilization of the PbO starts at around 1100K. After determined the pyrolysis and the calcination temperatures by the TGA measurement, the gels were then carefully pyrolyzed at temperatures in the range of 723K to 923K, and calcined at 873K to 1273K in the platinum crucibles. The PZT powder was obtained after the calcination process.

A commercial alkoxide based PZT solution with composition x = 0.48 (Alfa-Aesar) was used to obtained the PZT 52/48 powder at near the morphotropic phase boundary (MPB). The solution was processed into powder form by following the same procedure as above.

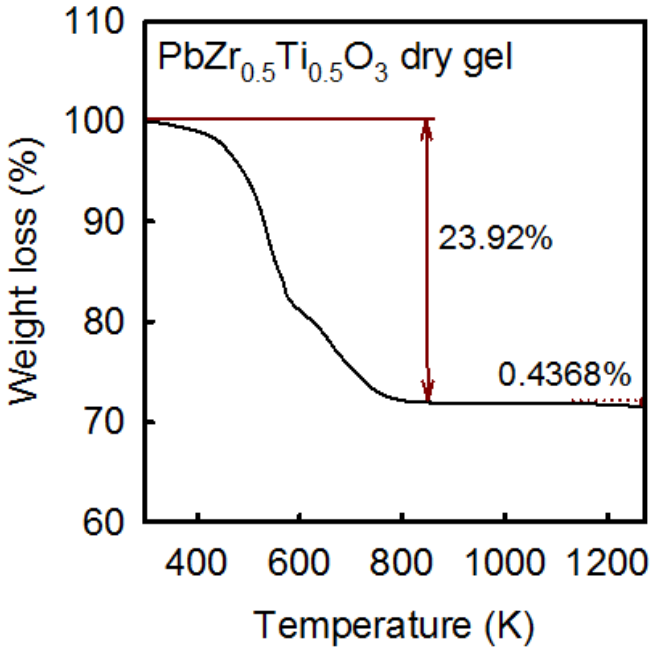

Figure 3. 2. Thermogravimetric analysis (TGA) of the PZT dry gel with composition $x = 0.50$.

Preparation of the alkoxide-derived PZT based on Wilkinson's recipe

$PbZr_{1-x}Ti_xO_3$ (x = 0.00, 0.10, 0.15, 0.20, 0.30, 0.40, 0.55, 0.70, 0.80 and 1.00) precursor solutions were prepared by an alkoxide-derived sol–gel method. The reagents consisted of lead (II) acetate trihydrate [$Pb(CH_3CO_2)_2 \cdot 3H_2O$], a 80 % solution of zirconium *n*-propoxide [$Zr(OCH_2CH_2CH_3)_4$] in *n*-butanol, titanium isopropoxide [$Ti[OCH(CH_3)_2]_4$] and anhydrous 2-methoxyethanol (2-MOE). These chemicals were obtained from Aldrich Chemical Company (Milwaukee, WI) and all manipulations of titanium and zirconium alkoxides were carried out using transfer syringes to avoid exposure to moisture.

The lead acetate trihydrate (approximately 0.02 mole) was added in about 60 mL of 2-methoxyethanol in a three neck flask. The solution was heated to 398K for

dissolution and dehydration of the lead acetate, and 20 mL of liquid was removed by distillation. After cooling the flask to 353K, proper amount of zirconium n-propoxide (~1.00 M in 2-methoxyethanol) and titanium isopropoxide (~1.00 M in 2-methoxyethanol) stock solutions were added to the solution in sequence. The solution was mixing overnight at room temperature then brief refluxed, and 40 mL of liquid was removed by distillation. A water and 2-methoxyethanol mixture solution (1:1; v:v) was used to hydrolyze the PZT solution.

The PZT solutions were slowly dried at 383K until orange dry gels formed. The calcination temperatures of dry gels were determined by thermogravimetric analysis (TGA). The gels were then carefully pyrolyzed at temperatures in the range of 723K to 923K, and PZT powder was obtained after calcining at 873K to 1273K in the platinum crucibles for two hours.

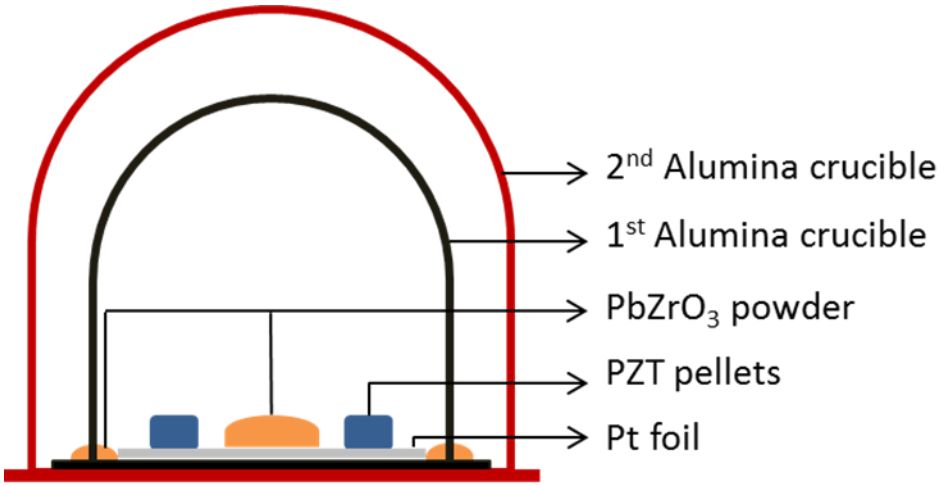

Figure 3. 3 Double crucibles setup for sintering dense PZT ceramic

3.2 Synthesis of Polycrystalline PZT Dense Pellets

The prepared alkoxide-derived PZT powders, based on the Wilkinson's recipe and a commercial solution, were mixed with 1 wt% PVA (Polyvinyl Alcohol) additive solution before made into pellets by applying $5x10^8$ N/m^2 to a 6mm die. These pellets were subsequently sintered in a double crucibles setup (shown in Fig 3. 3) at 1473K for 2 hours with a heating rate of 5K/min in a PbO-rich atmosphere by using $PbZrO_3$ powder as lead source. Densities of the PZT ceramics were list in table 3.1. The densities of all dense PZT ceramics in this study were larger than 95% theoretical density, except PZT 20/80. The reason of PZT 20/80 (x = 0.80) sintered disks have lower theoretical density was due to the fact that it has higher spontaneous strain (around 5% structural change in c direction between cubic to tetragonal phase transition).

Sample	x	Sample volume (mm^3)	Weight (mg)	Density (kg/m^3)	Theoretical density (kg/m^3)	% of theoretical density
1	**0.00**	-	-	-	-	-
2	**0.10**	21.85	137.18	7.69	7.97	96.54
3	**0.15**	21.85	153.54	7.69	7.97	96.54
4	**0.20**	21.85	168.09	7.69	7.97	96.54
5	**0.30**	22.08	169.25	7.67	7.98	96.07
6	**0.40**	21.31	163.41	7.67	7.99	96.04
7	**0.48**	16.18	126.08	7.79	7.98	97.62
8	**0.55**	19.17	148.07	7.72	7.98	96.77
9	**0.70**	21.03	161.82	7.69	7.99	96.28
10	**0.80**	19.81	145.47	7.34	7.99	91.94
11	**1.00**	-	-	-	-	-

Table 3. 1 Density of dense $PbZr_{1-x}Ti_xO_3$ sintered disks ($0.10 \leq x \leq 0.80$).

3.3 Phase Purity

Phase purity of the PZT samples was performed by X-ray diffraction (XRD). XRD patterns were acquired on a Bruker D5005 and a D8 Advance Bragg-Brentano diffractometer with CuKα radiation and a scan rate of 4^{o}/minute were employed to study the crystallographic properties of the as-made PZT powder and dense pellets. Generally, XRD patterns can be used to determine whether or not the undesirable pyrochlore phase exists in the PZT. Phase purity is an important factor to tell the quality of the samples. The existence of the pyrochlore phase is usually caused by off-stoichiometric precursor solution or the volatilization of PbO during the heating process. Therefore, the presence of the pyrochlore phase usually refers to the sample quality is poor and the actual composition maybe quite off to the desired composition.

3.3.1 Phase purity of PZT powder

Four different approaches, three alkoxide-derived methods and one acetate-derived method, were applied to synthesis the PZT powders in this study. The first approach in this work was focused on a parametric study of alkoxide-derived PZT powder by using Yi's recipe [1]. Different compositions of PZT powder were calcined at various times and temperatures. The XRD results are shown in Fig. 3. 4. It shows a pyrochlore phase (marked with red triangle) existing in four different compositions of alkoxide-derived PZT powder after calcining at 873K for 2 hours. Pyrochlore phase was also found in all PZT powders with composition x = 0.70 (PZT 30/70) calcined at 873K for two to 10 hours. A single phase PZT 30/70 powder was obtained after calcining at 1073K for 2 hours, and there is no pyrochlore phase PZT was obtained at around MPB

and Zr-rich regions by this method. This result matches with the reaction sequence in PZT formation study. All the researches were indicated that a PZT ceramic with single perovskite structure is easier to form at Ti-rich region than at Zr-rich region.

There are three possible reasons for an existing a second phase in PZT ceramic with compositions at the Zr-rich region: First is the starting materials are extremely sensitive to moisture and air, it is difficult to control the stoichiometry without operating in a dry box. Second is the volatilization of PbO during the calcination process, and third is the metastable nature of the PZT with compositions at the Zr-rich region, a higher calcination temperature may need to apply in this method. A list of alkoxide-derived PZT powders by using Yi's recipe is shown in Table 3.2.

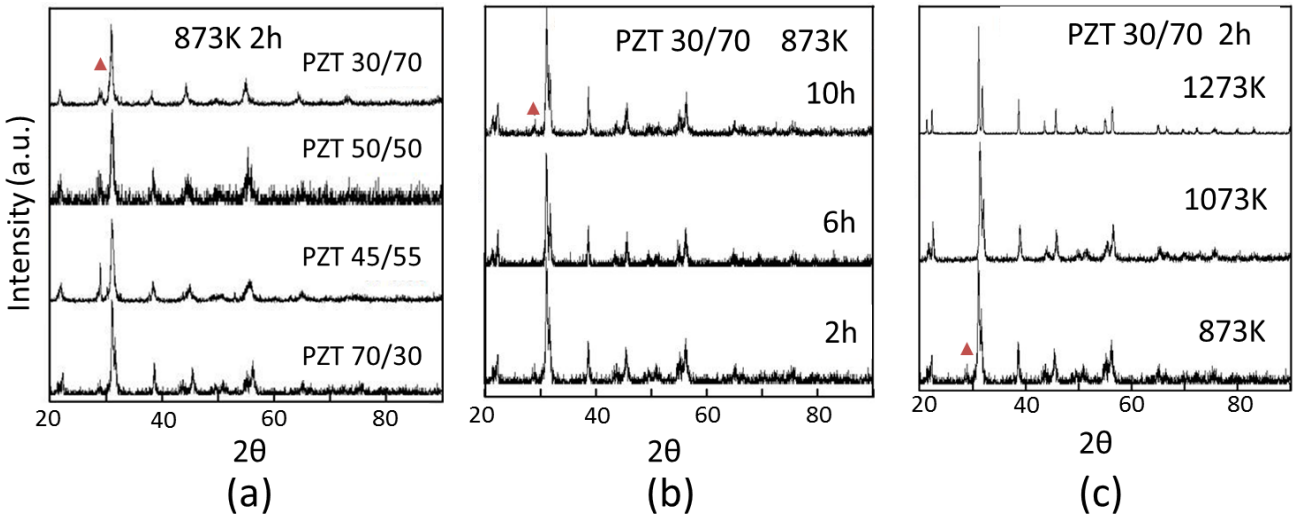

Figure 3.4 XRD patterns of (a) alkoxide-derived PZT powder with different compositions. (b) PZT 30/70 powders calcined at 873K with various time, and (c) PZT 30/70 powders calcined at different temperatures for 2 hours

Methods	Composition	Pyrolysis Temp (K)	Calcine Temp (K)	Calcine time (hr)	Anneal Temp (K)	Anneal time (hr)	Note
Alkoxide-derived (Yi's recipe)	30/70	873	873	2, 6 &10	N/A	N/A	pyrochlore
	30/70	923	1073	2 & 6	N/A	N/A	Pure phase
	30/70	923	1273	2 & 6	N/A	N/A	Pure phase
	45/55	873 & 923	873, 1073 & 1273	2, 6 & 10	648	72, 120 &240	pyrochlore
	50/50	873 & 923	873, 1073 & 1273	2, 6 & 10	623	72, 120 &240	pyrochlore
	70/30	873 & 923	873, 1073 & 1273	2, 6 & 10	N/A	N/A	pyrochlore

Table 3. 2 List of alkoxide-derived PZT powders by using Yi's recipe

However, the PZT powders near at the MPB region contain a pyrochlore phase, which are not suitable for this study. The PZT 30/70 powder shows a pure perovskite structure without pyrochlore phase. But PZT 30/70 is considered too far away from the MPB region and is not proper to use to investigate the redistribution of Zr and Ti atoms in the PZT solid solution. Therefore, it is necessary to use another method to obtain single phase PZT.

An acetate-derived method, which starting materials were less sensitive to moisture and air, was carried out to obtain pure single phase PZT in the second approach. Different from the first approach, all reagents were assayed by weight loss on ignition at 1073 K to determine the mass yield of their component metal oxides (PbO, TiO_2, and ZrO_2). In the procedure adopted, the as-received Tyzor GBA container was first sealed with a rubber septum. A quantity of the titanium reagent was then withdrawn by using a syringe, and its mass was determined after discharge into an Erlenmeyer flask containing a magnetic stir bar. The required mass of zirconium acetate solution was then calculated and this mass of solution was mixed with the Tyzor GBA. The mixed cation solution was diluted with methanol in the weight ratio 1:4 (reagent solution: methanol). After mixing, the required mass of lead subacetate was dissolved, and the solution was then dried at 383

K until a dry gel formed. The dry gel was carefully pyrolyzed and then calcined at 1273K for 2 hours in air. A commercial alkoxide-based PZT 52/48 (Alfa-Aesar) solution was used in the third approach. Fig. 3.5. shows (a) the commercial solution-derived PZT 52/48 and three acetate-derived PZT with compositions of (b) x = 0.50, (c) x = 0.60, and (d) x = 0.80 were calcined at 1273K for 2 hours. It shows a significant reduction of the second phase in the PZT powders derived from the acetate method and the commercial solution. This is due to the starting materials of this method are less insensitive to moisture and air, to the volatilization of PbO is not so severe, and/or to the PZT system can be stabilized at a lower temperature. These PZT powders were used to investigate the thermal effects on the properties in the PZT system and the origin of the phase coexistence at around the MPB region. The results of annealed PZT powders will be shown in the later chapters.

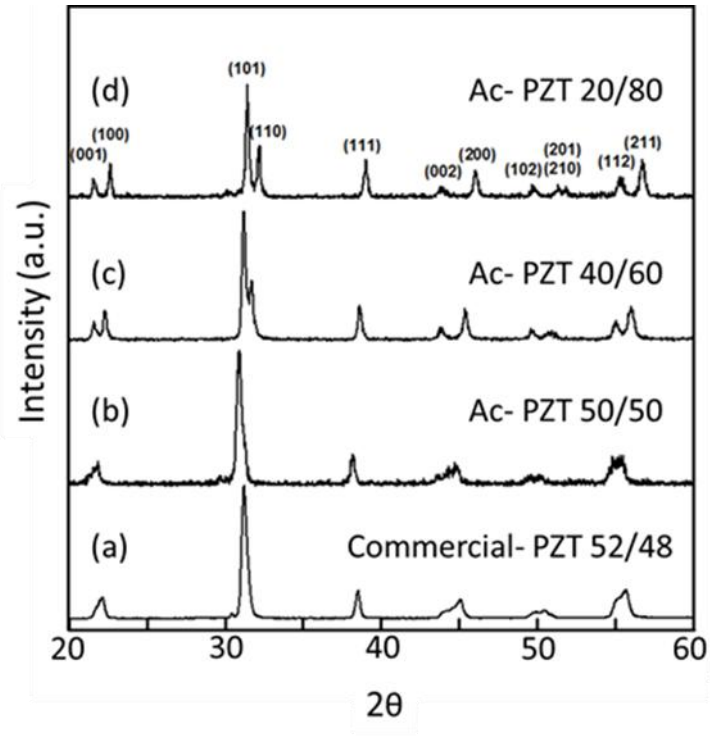

Figure 3. 5 (a) Commercial solution-derived PZT (x = 0.48), and acetate-derived PZT with (b) x = 0.50, (c) x = 0.60, and (d) x = 0.80 were calcined at 1273K for 2 h

An alkoxide-derived method developed by Wilkinson *et al.*[3, 4] was applied in the last approach to synthesis PZT powder. In this approach, the PZT stock solutions were carefully prepared in a three neck flask to prevent not necessary air/moisture contact. XRD results of the PZT powders prepared by Wilkinson's recipe were shown in Fig. 3.6. XRD results show that the PZT powders were pyrochlore phase free, and diffraction peaks match with the JCPDS database card of PZT. This means that the PZT powders with high phase purity can be obtained by this method.

According to the XRD patterns, the PZT powders prepared from this method were in a good quality. Therefore, this method is a good candid for further study in the thermal effects on structural, thermal and dielectric properties of the PZT solid solutions. In order to test the dielectric properties of the PZT solid solutions, all powders with different compositions were pressed into disk shape and sintered at 1473K to form the PZT sintered disks (or so-called ceramics) except two end members (PZ and PT) of the PZT system. The pure PT was extremely difficult to make into ceramic form due to its high spontaneous strain between ferroelectric tetragonal phase and paraelectric cubic phase. Some of PZ and PT powders were calcined at higher temperature of 1473K for 2 hours without making into dense ceramic form. In Fig. 3.8, the XRD results of these two end members show an orthorhombic structure for PZ powder and a tetragonal structure for PT powder, and their XRD reflections were match perfectly with JCPDS card.

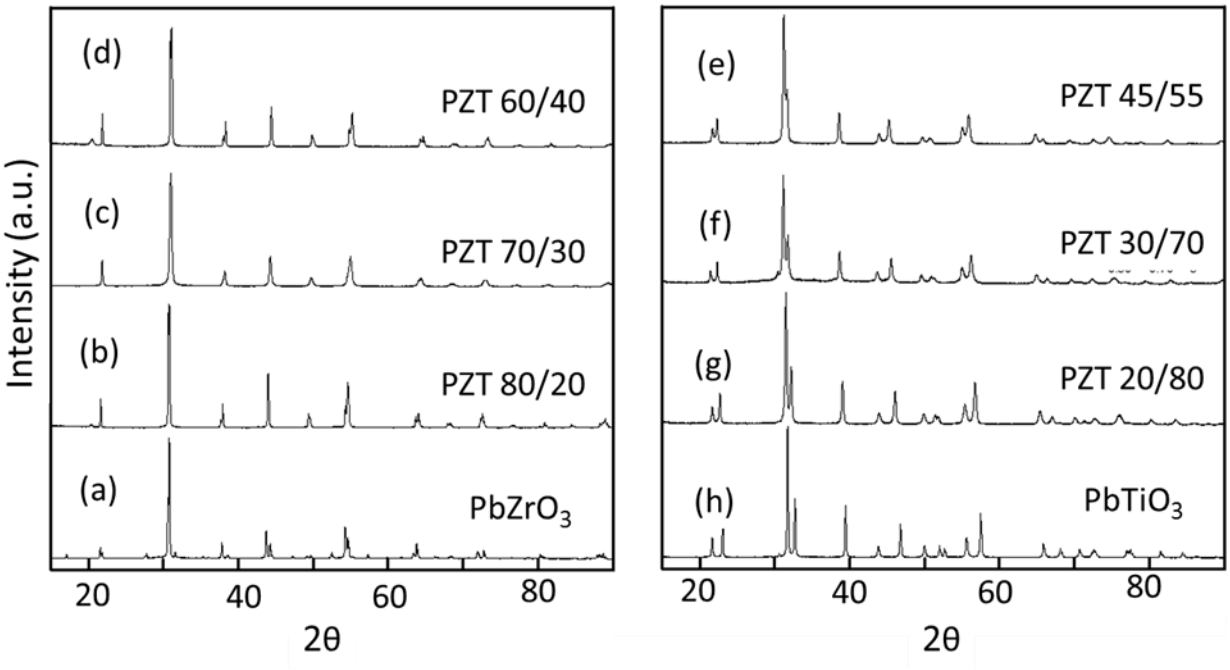

Figure 3. 6 (a)-(h) XRD patterns of alkoxide-derived PZT (x = 0.00 – 1.00) powders were calcined at 1273K for 2 h in air

Figure 3. 7 Diameter of a PZT sintered disk was measured by a caliper

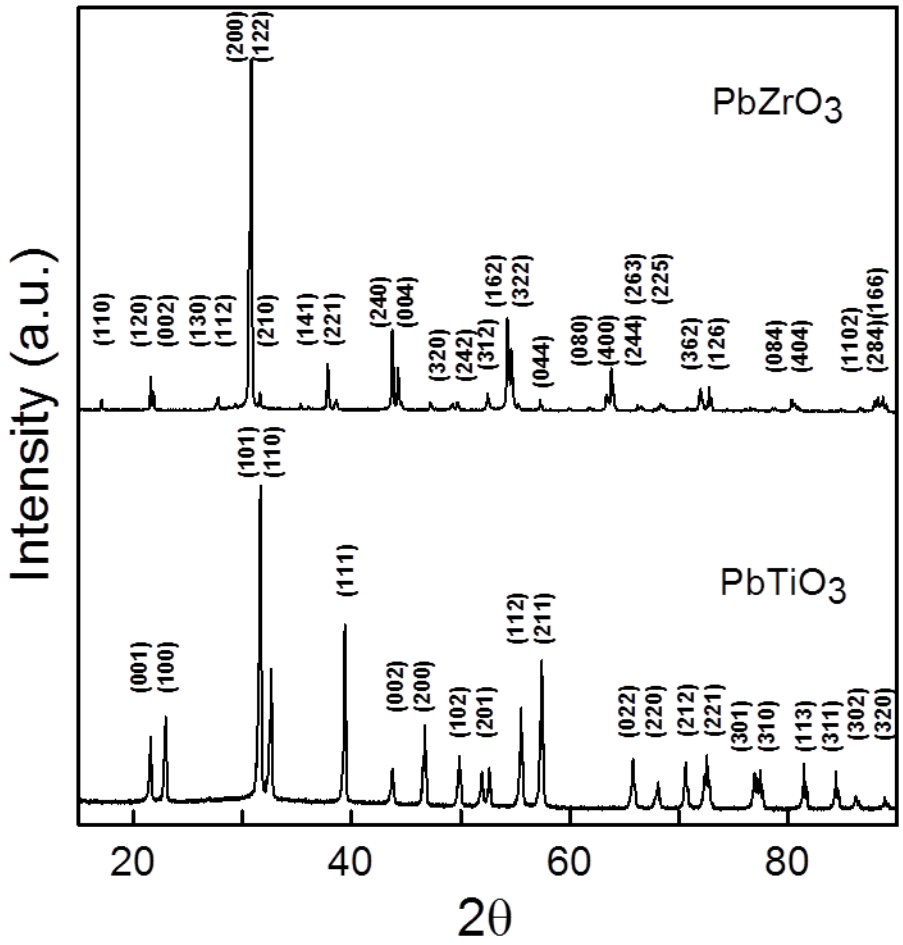

Figure 3. 8 XRD patterns of PZ and PT powders that were calcineded at 1473K for 2 hours.

3.3.2 Phase purity of dense PZT ceramics

The dense PZT ceramics were obtained after sintering at 1473K for 2 hours in a PbO abundant atmosphere. Picture of a PZT sintered disk (or so-called a dense PZT ceramic) is shown in Fig. 3.7. The XRD patterns of PZT sintered disks ($0.10 \leq x \leq 0.80$) were shown in Fig. 3.9. After sintering at 1473K for 2 hours, XRD patterns of the PZT ceramics show highly crystallized perovskite structure without pyrochlore in every composition. The structures at the Ti-rich side (x = 0.80 to x = 0.55) show a pure

ferroelectric tetragonal phase (F_T), and the structures at the Zr-rich side (x = 0.60 to x = 0.10) show a pure ferroelectric rhombohedral phase (F_R). The composition x = 0.52 which is near the MPB region shows a two phases mixture of tetragonal phase (F_T) and rhombohedral phase (F_R), and it is the direct evidence that two-phase coexistence at near the MPB region which will be discuss more at chapter 3.5.

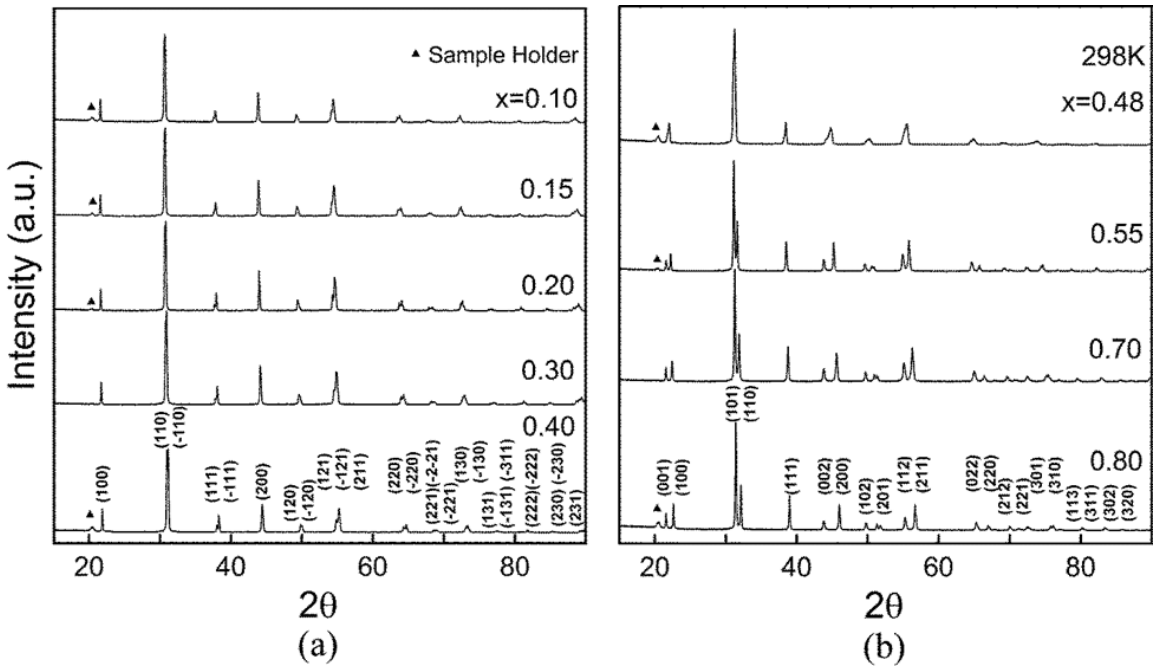

Figure 3. 9 Powder x-ray diffraction patterns collected on un-annealed sintered disks of PZT with varying composition (x) showing (a) the rhombohedral compositions with x = $0.10 \leq x \leq 0.40$ and (b) the tetragonal compositions with = $0.55 \leq x \leq 0.80$ and a two phase mixture of tetragonal and rhombohedral phases with x = 0.48. The indexing shown on the patterns in (a) and (b) is for the rhombohedral (R3m) and tetragonal (P4mm) symmetries, respectively.

3.4 Summary

Four different approaches, three alkoxide-derived methods and one acetate-derived method, were applied to synthesis the PZT powders in this thesis study. The phase purity of the PZT powders was examined by the x-ray diffraction measurement. The result shows that the PZT powders without the pyrochlore phase can be obtained reproducibly from an alkoxide-derived method, which was first developed by Wilkinson *et al.* [3, 4]. Another PZT powder without pyrochlore phase was obtained from a commercial alkoxide-based solution. However, this commercial solution can only provide one composition (x = 0.48, PZT 52/48), which is definitely not sufficient in this study. XRD results of the PZT powders obtained from another alkoxide-based method, which was built by Yi *et al.*, contain the pyrochlore phase in every composition. These PZT powders with pyrochlore phase are not suitable for this study. Although the pyrochlore phase was significantly reduce by using an acetate method, but the quality of the samples were not as good as the alkoxide-derived method that developed by Wilkinson *et al.*

Therefore, the alkoxide-derived method that developed by Wilkinson *et al.* was used to synthesis all the PZT powders in this study. In order to test their electrical properties, these PZT powders were then processed into dense ceramic form. XRD patterns show that the dense PZT ceramics were pyrochlore-free and highly crystallized. Also, the densities of all dense PZT ceramics in this study are larger than 95% theoretical density, except PZT 20/80.

3.5 References

1. G.H. Yi, Z. Wu, and M. Sayer, *J Appl Phys* **64**, 2717 (1988)
2. R.A. Assink and R.W. Schwartz, *Chemistry of Materials* **5**, 511 (1993)
3. A.P. Wilkinson, J.S. Speck, and A.K. Cheetham, *Chemistry of Materials* **6**, 750 (1994)
4. A.P. Wilkinson, J. Xu, S. Pattanaik, and S.J.L. Billinge, *Chemistry of Materials* **10**, 3611 (1998)
5. G.H. Haertling, *Ferroelectrics* **116**, 51 (1991)
6. W.D. Yang, *Ceram Int* **27**, 373 (2001)

CHAPTER 4

CHARACTERIZATION OF STRUCTURE, MICROSTRUCTURE AND DOMAIN STRUCTURE

4.1 Structural Characterization

The objectives of this thesis work are trying to investigate the processing-structure-property relation, and to have a better understand of the origin of two phase coexistence at near the MPB in the PZT system. To investigate the thermal history effect on structure properties of the PZT, the structure properties of un-annealed PZT samples need to be carefully assessed before applying any further heat treatments. The structural characterization of the un-annealed PZT samples in this study was focused on four main categories: (1) the lattice parameters, (2) the ferroelectric elastic strain, (3) the phase coexistence, and (4) the peak width of the PZT ceramics. Each category will be discussed in this chapter.

Crystal structure of the PZT powders and sintered disks at room temperature was characterized by the x-ray diffraction (XRD). The diffraction data were acquired at room temperature using a Bruker D8 Advance diffractometer (CuKα radiation) operating at a scan rate of 4^o/min in an auto-repeat mode that averaged the data from 4-6 scans in the range of $15^o - 90^o$ 2θ. Higher resolution data were acquired around selected reflections in step scans using a step size and count time of 0.02^o 2θ and 3s/step, respectively. To obtain more precise crystal details for the structural analyses, higher resolution data of the {111} and {200} reflections were acquired in the step scan mode by using a step size of 0.02° and a count time of 3 seconds per step. The {111} and {200} reflections were then

analyzed by the software "*Peakfit v.4.12*" using *Pearson VII* line profile shape functions to determine the peak positions, the peak intensities, and the peak widths.

4.1.1 Lattice Parameters

To determine lattice parameters of the dense PZT ceramics, the Si powder was used to calibrate the instrumental error. Reflection peak angle (2θ) of the Si powder was compared to the JCPDS card database, difference in the (220) peak positions of Si between JCPDS card data base and experimental data was used as the value of the instrumental error. After calibrating the instrumental error, the {111} and {200} reflections of the PZT samples were analyzed by the software "*Peakfit v.4.12*" using *Pearson VII* line profile shape functions to determine the peak positions (d-spacing), the x-ray profile peak breadth (FWHM) and the integrated intensities. *Pearson VII* distribution functions have been used for years to approximate the form of diffraction peaks for a variety of purposes [1-3]. It was found that satisfactory fits could be obtained without imposing constraints on the fitting parameters as judged by the fact that all *Pearson exponents* (shape factors) adopted a value of ~ 2. An example of the profile fitting results for a PZT 50/50 sample comprised of coexisting F_R and F_T phases is shown in the Fig. 4.1. In this figure, adequate deconvolution of the tetragonal (002)/ (200) and rhombohedral (200) peaks could be achieved at the resolution of the x-ray measurements. Peaks at either ends are the tetragonal (002) and the tetragonal (200), respectively. The center peak is the rhombohedral (200) peak.

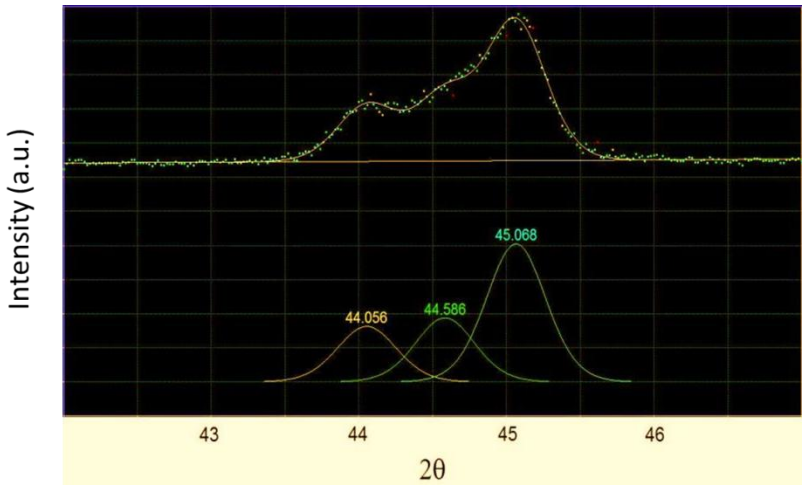

Figure 4.1 X-ray peak fitting results for PZT powder with composition x = 0.48 showing deconvolution of (002) and (200) reflections for coexisting tetragonal and rhombohedral phases.

After obtaining the peak positions of the XRD reflections, d-spacing of the PZT samples were calculated by the Bragg's Law.

$$\lambda = 2d\sin\theta \qquad \text{Equation 4. 1}$$

where λ is the wavelength of incident wave (In this study, the wave length of CuKα radiation is 0.15418 nm), d is the spacing between the planes in the atomic lattice, and θ is the angle between the incident ray and the scattering planes. The lattice parameters of PZT samples with different structures were then calculated according to the relationship between d-spacing and lattice constants:

$$Tetragonal: d_{hkl} = \left[\frac{h^2+k^2}{a^2} + \frac{l^2}{c^2}\right]^{-\frac{1}{2}} \qquad \text{Equation 4. 2}$$

$$R\,\text{hom}\,bohedral:$$

$$d_{hkl} = \left[\frac{1}{a^2}\frac{(h^2+k^2+l^2)\sin^2\alpha + 2(hk+kl+lh)(\cos^2\alpha-\cos\alpha)}{1-2\cos^3\alpha+3\cos^2\alpha}\right]^{-\frac{1}{2}} \qquad \text{Equation 4. 3}$$

where (*hkl*) is Miller indices of planes, and α is the angle of rhombohedral unit cell.

Fig. 4.2(a) shows composition dependence of the lattice parameters of the PZT powder (x = 1.00) and sintered disks ($0.10 \leq x \leq 0.80$) at 298 K. PZT went through a series of phase evolution with increasing titanium content at the room temperature, from an orthorhombic phase, to the rhombohedral phases, and to a tetragonal phase. Between the rhombohedral and the tetragonal phases, there is a two-phase coexistence region at near the MPB. Details of the lattice parameters were listed at table 4.1. In the Ti-rich region, lattice parameter *a* has increased with zirconium content from 3.90Å to 4.02Å (x = 1.00 to x = 0.55) while lattice parameter *c* remains a similar number (~4.14Å), and the lattice strain *c/a* ratio has decreased with zirconium content from 1.06 to 1.02. It should be noted that the pure lead titanate has the highest tetragonality, which makes it extremely difficult to make a pure lead Titanate dense ceramic. In the Zr-rich region, the lattice parameter *a* has decreased with zirconium content from 4.14Å to 4.07Å (x = 0.10 to x = 0.40). The unit-cell volume (Ω) has increased with zirconium content from around 63 $Å^3$ to 71 $Å^3$ and shows an essentially linear behavior with composition in the Fig. 4.1 (b). As seen in the figure, the unit cell volume (Ω) of this work match with the theoretically [4] and the experimentally observed continuity in unit cell volume across the MPB line. Values of the lattice parameters, the volume, and the rhombohedral angle α_R are in a good agreement with literature data [5-7]. It means that the compositions of samples in this work are very close to desired composition, the composition assessment will be discussed in the later chapter.

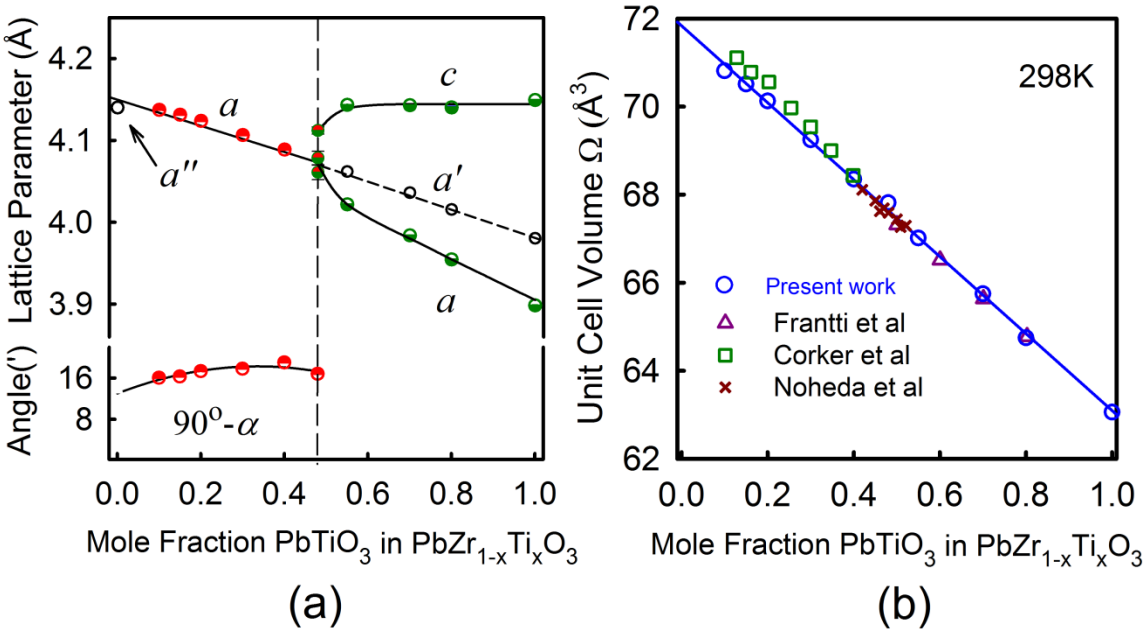

Figure 4. 2 (a) Crystal lattice parameters of un-annealed $PbZr_{1-x}Ti_xO_3$ powders (x = 0.00, 1.00) and sintered disks ($0.10 \leq x \leq 0.80$) *versus* composition at room temperature. The cube root of the primitive cell volume in the tetragonal (P4*mm*) phase ($a' = \sqrt[3]{a^2c}$) and the orthorhombic (P*bam*) phase ($a'' = \sqrt[3]{abc}/8$) are also shown. (b) Corresponding unit cell volume of the PZT powder (x =1.00) and sintered disks ($0.10 \leq x \leq 0.80$) at 298 K.

4.1.2 Ferroelastic spontaneous strain

Transition from a paraelectric phase into a ferroelectric phase in a ferroelectric material is usually leads to strong anomalies in dielectric, elastic, thermal, and other properties, and is accompanied with changes in the dimensions of the crystal unit cell. The strain correspond to this phenomenon is called the spontaneous strain, which represents the difference in the dimensions between the ferroelectric and paraelectric unit cells [8]. The spontaneous strain is also related to the spontaneous polarization, and can be calculated through electrostrictive coefficients [9, 10]. Composition dependence of the

spontaneous strain of the PZT ceramics is shown in Fig. 4. 3, and the corresponding values are also listed at the table 4.1.

The spontaneous strain [$(90^o-\alpha_R)/90^o$] of the PZT ceramics with rhombohedral phase (red hollow circle) is depending on the rhombohedral angle (α_R), which is increased slightly with decrease zirconium content from 0.0030 to 0.0035. In the tetragonal phase, the spontaneous strain [$(c/a)-1$] (green hollow circle) is depending on the tetragonal distortion (c/a), which is decreased linearly with increase zirconium content from 0.064 to 0.020. Spontaneous strain of the PZT ceramics with the tetragonal phase is an order larger than the ones with the rhombohedral phase due to the larger tetragonal distortion. In the MPB region, there are two different spontaneous strain systems due to the two phase coexistence of tetragonal and rhombohedral phases.

The same amount of non-180^o domain wall motion in a tetragonal phase would create a greater strain as compared with a rhombohedral phase [11]. In the other words, the domain wall motion is much difficult in the tetragonal phase than in the rhombohedral phase. Thus the dielectric constant decreases with increasing titanium content due to larger spontaneous strain impede the motion of the domain wall.

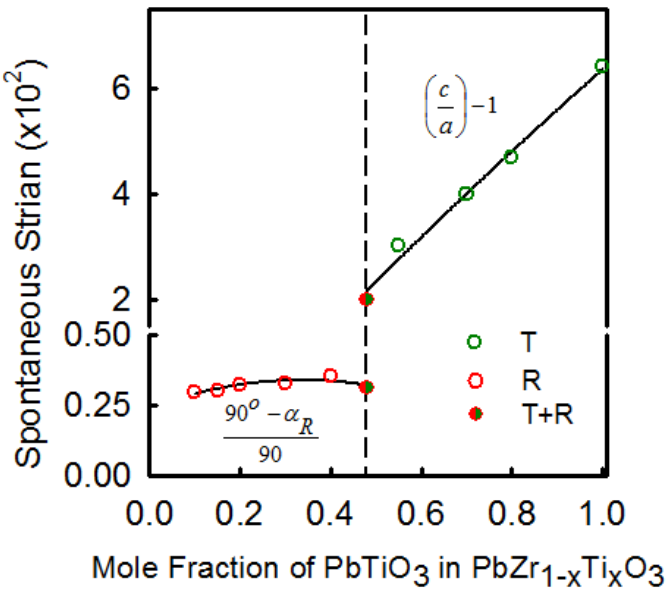

Figure 4.3 Composition dependence of spontaneous strains of un-annealed PZT powder (x = 1.00) and sintered disks ($0.10 \leq x \leq 0.80$) at room temperature

x	Phase	Form	a (Å)	b (Å) or α_R	c (Å)	Ω (Å^3)	$(c/a)-1$	$(90-\alpha_R)/90$
0.00	O [a]	P [b]	5.85	11.77	8.23	70.82(3) [c]	-	-
0.10	R	SD	4.14	89.73°	-	70.81(1)	-	0.003
0.15	R	SD	4.13	89.73°	-	70.51(1)	-	0.003
0.20	R	SD	4.12	89.71°	-	70.13(1)	-	0.0032
0.30	R	SD	4.11	89.70°	-	69.24(1)	-	0.0033
0.40	R	SD	4.09	89.70°	-	68.35(0)	-	0.0035
0.48	R +T	SD	4.08	89.72°	-	67.83(8)	-	0.0031
0.48	R +T	SD	4.06		4.11	67.83(8)	0.02	-
0.55	T	SD	4.02	-	4.14	67.01(1)	0.03	-
0.70	T	SD	3.98	-	4.14	65.75(1)	0.04	-
0.80	T	SD	3.95	-	4.14	64.75(3)	0.047	-
1.00	T	P	3.89	-	4.14	62.94(1)	0.064	-

[a] O: Orthorhombic (P*bam*), R: Rhombohedral (R3*m* /R3*c*), T: Tetragonal (P4*mm*)

[b] P: Powder, SD: Sintered disk

[d] Estimated uncertainty in the least significant digit

Table 4. 1 Crystal lattice parameters (a,b,c,α), unit cell volume, and spontaneous strains of un-annealed PZT powders (x = 0.00 and 1.00) and sintered disks ($0.10 \leq x \leq 0.80$).

4.1.3 Phase Coexistence

As discussed in the chapter 1. Based on the conventional diffusionless phase diagram, most authors claim the diffusional process cannot be fast enough to allow atomic redistribution to reach establish equilibrium with two phase mixtures of rhombohedral and tetragonal phases at compositions located near the MPB. The conventional diffusionless phase diagram with line boundaries cannot satisfies Gibbs phase rule, it is expected that the lines in this phase diagram should be replaced by two-phase coexisting regions[12]. The most direct evidence is that diffraction experiments frequently show the tetragonal and the rhombohedral phases coexisting in a finite composition range at around the MPB in PZT ceramics [13-16]. It has been reported that the MPB is not a narrow and vertically straight boundary but a region whose width depends on the thermal history and synthesis methods. However, there is no agreements on the definite range of two-phase coexistence region due to several obstacles were encountered in experimental studies of the phase coexistence in the PZT system. The width of coexistence region was reported from 1 mole% [17] up to 15 mole% [14].

X-ray diffraction is the most common and direct way to determine the phase coexistence in the PZT system. Fig. 4.4 exhibits the XRD profile fitting of (002) and (200) reflections of (a) the PZT 60/40, (b) the PZT 52/48, and (c) the PZT 45/55. 98% confidence intervals in the parameters of the fits were used as a measure of the relative errors. At the top of this figure, Zr-rich PZT 60/40 shows a single rhombohedral (200) reflection and the fitting result for rhombohedral (200) reflection was represented by a red curve. At the bottom of this figure, Ti-rich PZT 45/55 shows two reflections of tetragonal (002) / (200) and the fitting results of tetragonal (002) / (200) reflections were

shown as the green curve. In the middle of this figure, the (002) and (200) reflections of PZT 52/48 is clear shows the evidence of the F_T - F_R two-phase coexistence. As mentioned above in the earlier chapter, the coexistence of the two phases at around MPB was expected from the thermodynamical considerations.

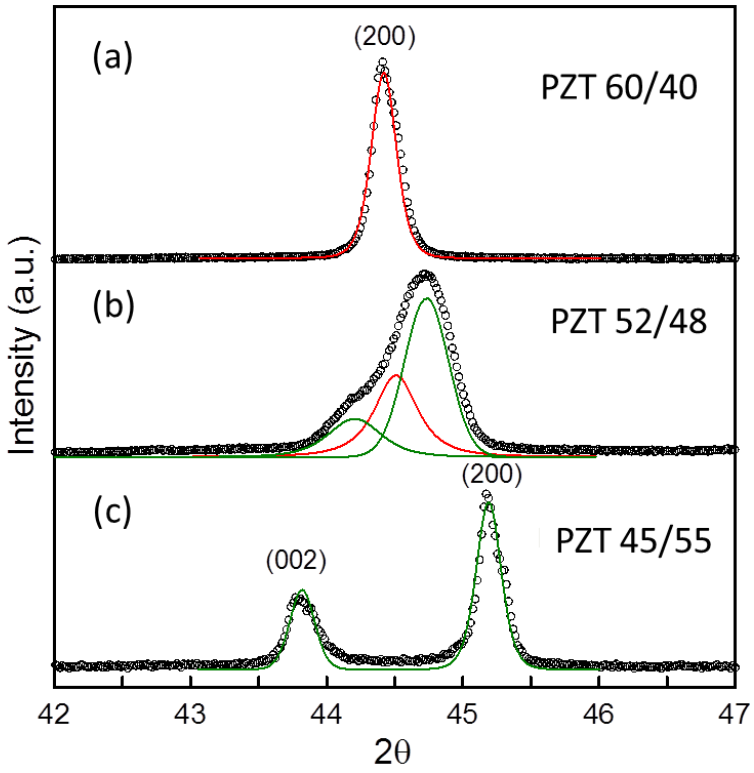

Figure 4.4. XRD profile fitting of {200} reflections of un-annealed $PbZr_{1-x}Ti_xO_3$ sintered disks with the compositions (a) x = 0.40, (b) x = 0.48, and (c) x = 0.55. Red sold lines and green sold lines are the best fit results by using a Pearson VII distribution functions for rhombohedral and tetragonal phases, respectively.

4.1.4 Peak Width

The peak width was defined by Full Width at Half Maximum (FWHM) of the (200) reflections. FWHM is the width of the diffraction peak, in radians, at a height half-way between background and the peak maximum [18]. There were many factors may

attribute to the observed peak profile. Such as the instrumental peak profile, the crystallite size, the different kind of micro-strains, and the temperature. In this study, all experimental conditions (scan speed, scan step and temperature) remain the same to reduce the effect of the instrumental and the temperature issues. Therefore, the reasons causing the peak broadening can be narrow down to the crystallite size and the different kind of micro-strains.

The peak broadening caused by crystallite size becomes obvious when the size is smaller than 100nm. However, above a certain size (~0.1 - 1 micron) this type of broadening is negligible [18]. The sources of non-uniform micro-strains in the PZT ceramics are mostly from the spontaneous strain caused by the phase transition between paraelectric and ferroelectric phases, vacancies, domain boundaries and grain surface relaxation. All these factors can lead to the broadening of the XRD peak.

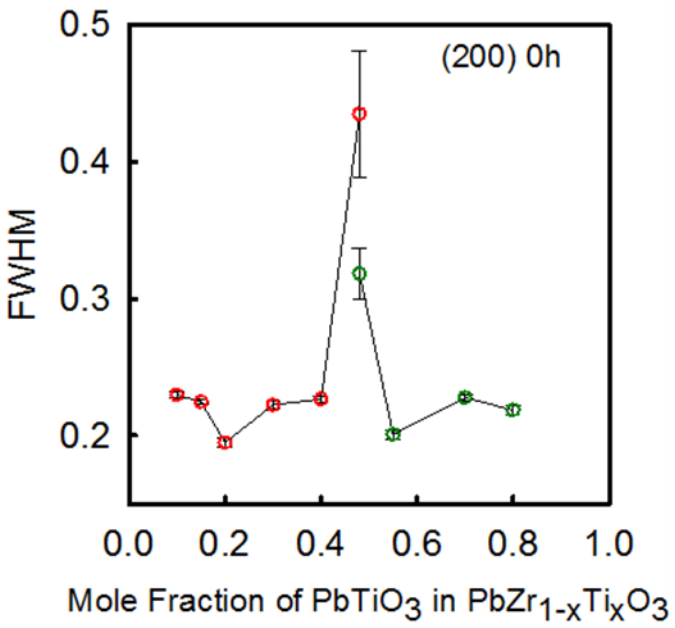

Figure 4.5 FWHM of (200) reflections of PZT sintered disks ($0.10 \leq x \leq 0.80$).

FWHM of the (200) reflections were shown in Fig. 4.5. The red circles represent the FWHM of (200) reflection of the PZT with rhombohedral phases, and the blue circles represent the FWHM of (200) reflection of the PZT with tetragonal phases. The sizes of the FWHM on the either side are similar, close to 0.23^{o}. The FWHM of (200) reflections show a jump at around MPB region due to the combination effects of crystallite size and micro-strains. The PZT at around MPB shows a two-phase coexistence characteristic, and lead to two spontaneous strains contribute to the PZT at around MPB. However, the volume fraction of two phases cannot be quantified precisely due to the resolution limits of the diffractometer at UCONN. The domain structure miniaturize to nano scale could be another reason to broaden the peak width. This combination effect of crystallite size, nano domains and micro-strains could be the reason that the FWHM at MPB is almost double the size than the rest of the compositions.

4.2 Grain Sizes of PZT Ceramics

Grain sizes of the PZT sintered disks were examined by using a JEOL 6335F Field Emission Scanning Electron Microscope (FE-SEM). A thin gold film was sputtered on the top of the PZT ceramics to increase the conductivity and reduce charging effects during the scans. The grain diameters were analyzed by measuring more than 90 grains in the plan-view SEM images. The grain size is reported as an average of these averages; the error bar gives the standard deviation.

Fig. 4.6 shows SEM images of the microstructure of PZT sintered disks as a function of the composition. The surface shows a dense and crackless morphology in every composition, and the Ti-rich PZTs show a larger averages grain size than the Zr-

rich PZTs. It may due to the Ti-rich compositions tend to react with the PbO-rich atmosphere during sintering result in better crystalline structure [19, 20]. The details of grain sizes were shown in Fig. 4.7 and listed at table 4.2. At Ti-rich, the grain size decreases with increased zirconium content from 4.38μm (x = 0.80) to 3.8μm (x = 0.55), and grain size dramatically dropped to 1.46μm at MPB (x = 0.48). The grain sizes of the Zr-rich PZTs are in the range from 1.01μm (x = 0.10) to 3.10μm (x = 0.40).

Many researches have been indicated that both mechanical and electrical properties are depending on the grain size [21-24]. It is worth noting that the most striking effects of the grain size, however, are on mechanical rather than electrical properties. Both flexural strength and Vickers hardness increase dramatically with the decrease of grain size[25].

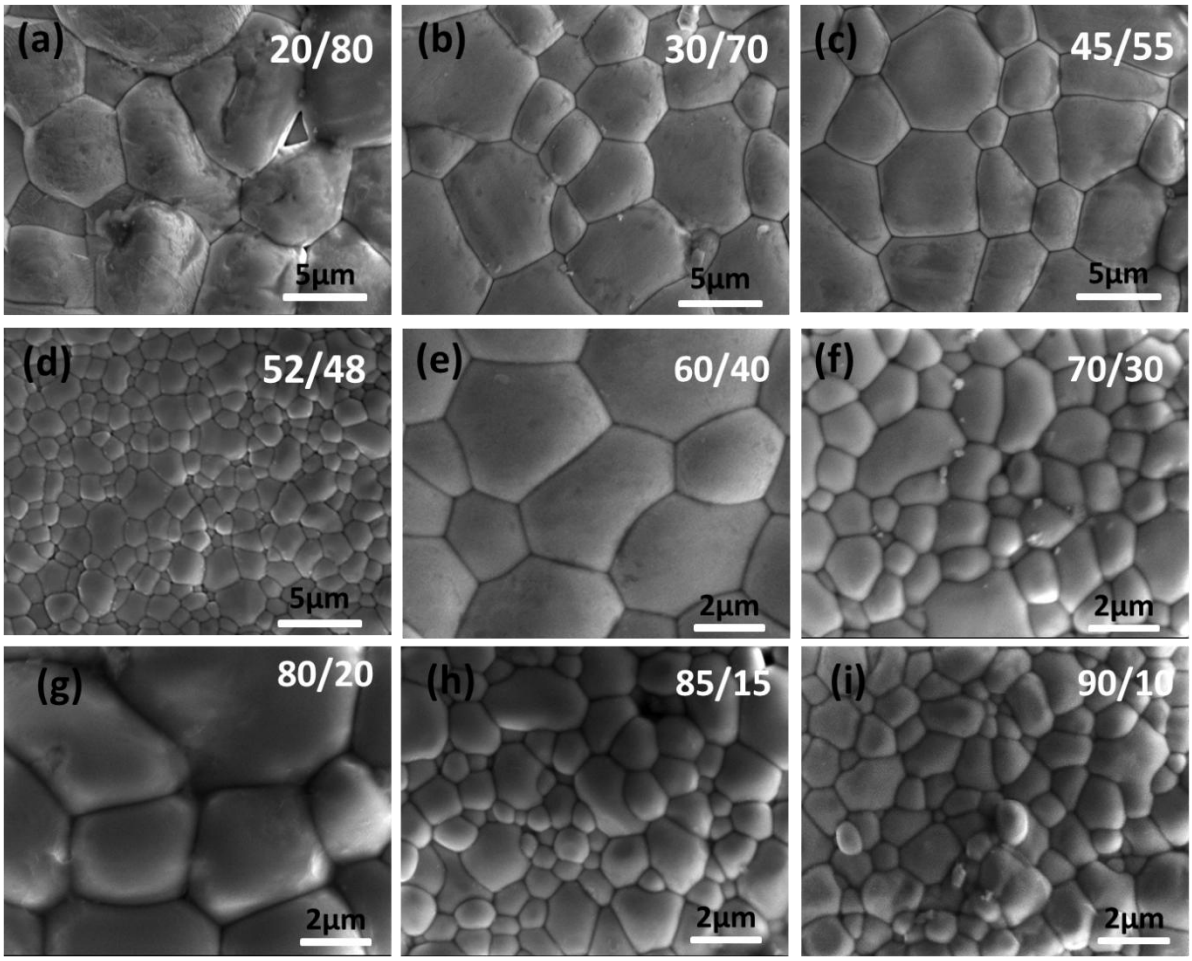

Figure 4.6 SEM images of PZT sintered disks with composition (a) $x = 0.80$ to (i) $x = 0.10$.

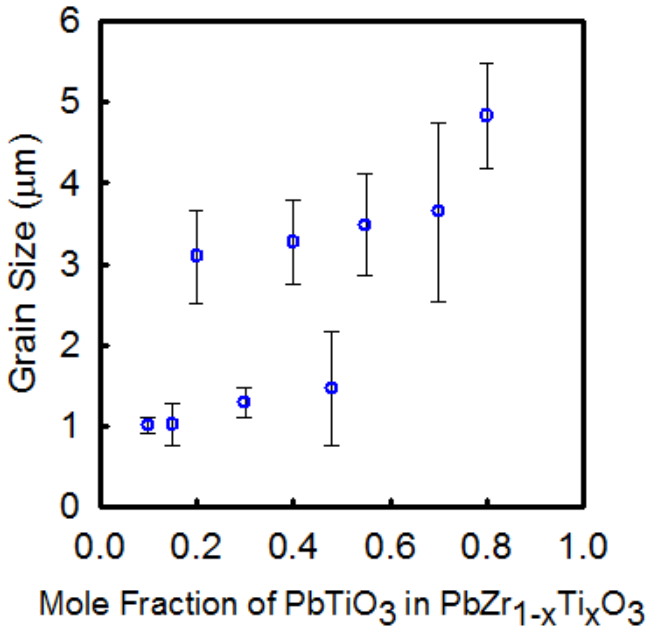

Figure 4. 7. Composition dependence of grain size of the PZT sintered disks ($0.10 \leq x \leq 0.80$).

x	*Grain Size* (μm)	*STDEVA*
0.00	-	-
0.10	1.01	0.10
0.15	1.02	0.25
0.20	3.10	0.57
0.30	1.29	0.19
0.40	3.27	0.52
0.48	1.46	0.70
0.55	3.48	0.63
0.70	3.64	1.10
0.80	4.83	0.66
1.00	-	-

Table 4. 2 Grain sizes of the PZT sintered disks ($0.10 \leq x \leq 0.80$).

4.3 Domain structure of MPB PZT Ceramics

As stated in the chapter 4.1.3, different phases coexist at the MPB region in the PZT solid solution. Presence of both tetragonal and rhombohedral domains enhanced dielectric, elastic, and piezoelectric properties at near the MPB. Domain structure of the PZT plays an important role to its electrical property, and it can be modified by different additives. In order to precisely control the domain structure, understanding the domain behavior of the PZT at near the MPB became a critical task. The most common and direct way to investigate the domain structure of the PZT is the transmission electron microscopy (TEM) measurement.

In this thesis work, the chemical profile, domain and more structural details were obtained by using a JEOL 2010 FasTEM. A FEI Strata 400S Dual-Beam FIB instrument was employed to prepare cross-sectional TEM samples. Domain configurations were studied using bright field imaging and selected area electron diffraction techniques. The TEM sample of PZT 52/48 prepared by focused ion beam (FIB) is shown in Fig. 4.8.

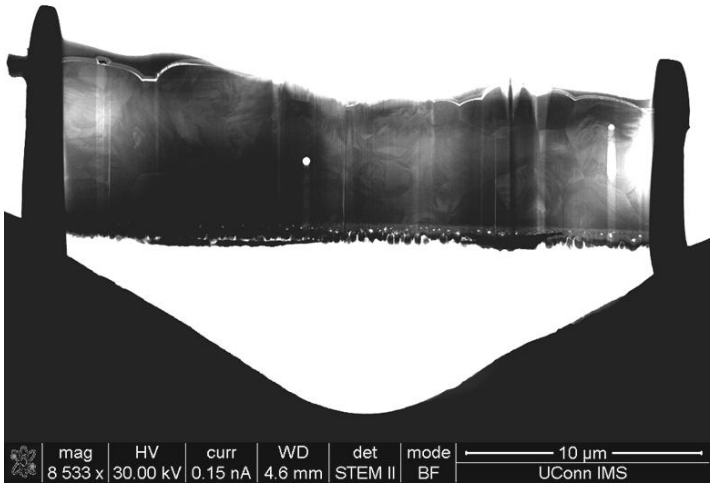

Figure 4.8 Cross-sectional TEM sample of the un-annealed PZT 52/48 sintered disk was prepared by focused ion beam.

An unique phenomenon has been observed by many authors that the domain (d) miniaturized due to the vanishing domain wall energy (γ) at near MPB ($d \propto \sqrt{\gamma}$) [26-31]. This special phenomenon was also observed in this thesis work. The Fig. 4.9 shows a bright field TEM image of the un-annealed PZT 52/48 with a curving domain structure in nanometer scale. The curving domain structure indicates that no preferred polarization direction at near the MPB region, and it would lead domain miniaturize to at around this region. The observed average domain width was around 20nm.

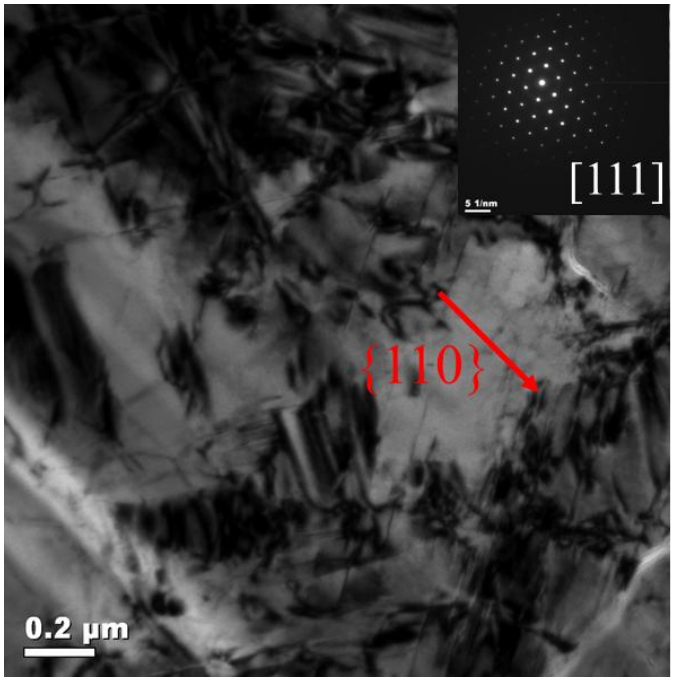

Figure 4.9 A bright field image of the domain structure of the un-annealed PZT 52/48 sintered disk.

As mentioned in the chapter 1.9, one or more extra diffraction peaks would be appeared when the nanodomains with different phases coexist within microdomains. Such a diffraction result can be easily misinterpreted as evidence of a new phase, which makes the average structure of the PZT at near the MPB still controversial. Another possible way to determine different phases in the PZT system is by analyzing the chemical composition of individual domain. The domain structure of tetragonal phase has higher titanium/zirconium ratio than the rhombohedral phase. However, to quantify the chemical analysis on PZT at MPB region is very difficult due to the limits of beam size. Also, the average structure and composition may be affected by a high energy focused beam [31].

4.4 Summary

This chapter is focused on the characterization of structure, microstructure, and domain structure of the dense PZT ceramics. The analysis of the structural properties was conducted by using XRD. The observations from XRD analysis are as follows,

1. Lattice parameters of the PZT powders (x = 0.00, 1.00) and sintered disks ($0.10 \leq x \leq 0.80$) were matching well with the literature data, which indicates that the compositions of samples in this work were very close to the desired composition.
2. The PZT powders and sintered disks with the rhombohedral phase has much smaller spontaneous strain than the ones with tetragonal phase.
3. {200} diffraction reflections of the un-annealed PZT 52/48 sintered disk show a two phase mixture of tetragonal (*P4mm*) and rhombohedral (*R3m*) phases.

4. FWHM of {200} reflections of the PZT sintered disks ($0.10 \leq x \leq 0.80$) show a jump at around the MPB region due to the combination effects of crystallite size and micro-strains. The peak width of the PZT sintered disks with compositions outside of the MPB region was sharing a close value.

Composition dependence of grain size of the PZT sintered disks ($0.10 \leq x \leq 0.80$) was examined by the SEM measurement. SEM images of surface morphology of the PZT sintered disks show dense and crackless morphology in every composition, and the PZT sintered disks with compositions at Ti-rich region show a larger averaged grain sizes than the ones at Zr-rich region. Domain structure of the PZT 52/48 sintered disk was carried out by TEM measurement. The bright field TEM image shows the un-annealed PZT 52/48 sintered disk has a curving domain structure in nanometer scale, which indicates no preferred polarization direction at near the MPB region.

4.5 References

1. A. Brown and J.W. Edmonds, *Advances in X-Ray Analysis* **23**, 361 (1980)
2. M.M. Hall, V.G. Veeraraghavan, H. Rubin, and P.G. Winchell, *J Appl Crystallogr* **10**, 66 (1977)
3. S. Enzo and W. Parrish, *Advances in X-Ray Analysis* **27**, 37 (1983)
4. G.A. Rossetti, A.G. Khachaturyan, G. Akcay, and Y. Ni, *J Appl Phys* **103**, 114113 (2008)
5. B. Noheda, D.E. Cox, G. Shirane, R. Guo, B. Jones, and L.E. Cross, *Physical Review B* **63**, 014103 (2000)
6. D.L. Corker, A.M. Glazer, R.W. Whatmore, A. Stallard, and F. Fauthx, *Journal of Physics: Condensed Matter* **10**, 6251 (1998)
7. J. Frantti, S. Ivanov, S. Eriksson, H. Rundlöf, V. Lantto, J. Lappalainen, and M. Kakihana, *Physical Review B* **66**, 064108 (2002)
8. D. Damjanovic, *Rep Prog Phys* **61**, 1267 (1998)
9. M.J. Haun, E. Furman, S.J. Jang, H.A. Mckinstry, and L.E. Cross, *J Appl Phys* **62**, 3331 (1987)
10. M.J. Haun, Z.Q. Zhuang, E. Furman, S.J. Jang, and L.E. Cross, *J Am Ceram Soc* **72**, 1140 (1989)
11. A. Pramanick, D. Damjanovic, J.C. Nino, and J.L. Jones, *J Am Ceram Soc* **92**, 2291 (2009)
12. G.A. Rossetti, W. Zhang, and A.G. Khachaturyan, *Appl Phys Lett* **88**, 072912 (2006)

13. P. Ari-gur and L. Benguigui, *Solid State Commun* **15**, 1077 (1974)

14. P. Arigur and L. Benguigui, *J Phys D Appl Phys* **8**, 1856 (1975)

15. H.W. Wang, D.A. Hall, and F.R. Sale, *J Am Ceram Soc* **75**, 124 (1992)

16. J.X. A. P. Wilkinson, S. Pattanaik, and S. J. L. Billinge, *Chemistry of Materials* **10**, (1998)

17. S.A. Mabud, *J Appl Crystallogr* **13**, 211 (1980)

18. B.D. Cullity, *Elements of x-ray diffraction.*, 1978, Addison-Wesley Pub: Reading, Mass.

19. D.L. HANKEY and J.V. BIGGERS, *Journal of the Amercan Ceramic Society*, C-172 (1981)

20. M.J. Hoffmann, M. Hammer, A. Endriss, and D.C. Lupascu, *Acta Mater* **49**, 1301 (2001)

21. Martiren.Ht and J.C. Burfoot, *J Phys C Solid State* **7**, 3182 (1974)

22. Martiren.Ht and J.C. Burfoot, *Ferroelectrics* **7**, 151 (1974)

23. B. Jaffe, W.R. Cook, and H.L. Jaffe, *Piezoelectric ceramics* 1971, London, New York,: Academic Press. 135.

24. C.A. Randall, N. Kim, J.P. Kucera, W.W. Cao, and T.R. Shrout, *J Am Ceram Soc* **81**, 677 (1998)

25. N. Ichinose and M. Kimura, *Jpn J Appl Phys 1* **30**, 2220 (1991)

26. G.A. Rossetti and A.G. Khachaturyan, *Appl Phys Lett* **91**, 072909 (2007)

27. Y.M. Jin, Y.U. Wang, A.G. Khachaturyan, J.F. Li, and D. Viehland, *J Appl Phys* **94**, 3629 (2003)

28. Y. Wang, *Physical Review B* **74**, 104109 (2006)

29. K.A. Schönau, L.A. Schmitt, M. Knapp, H. Fuess, R.-A. Eichel, H. Kungl, and M.J. Hoffmann, *Physical Review B* **75**, 184117 (2007)

30. D. Woodward, J. Knudsen, and I. Reaney, *Physical Review B* **72**, 104110 (2005)

31. L.A. Schmitt, K.A. Schönau, R. Theissmann, H. Fuess, H. Kungl, and M.J. Hoffmann, *J Appl Phys* **101**, 074107 (2007)

CHAPTER 5

PHASE TRANSITIONS IN PZT

5.1 Introduction

5.1.1 Thermal Properties of PZT

PZT is one of the most extensively studied piezoelectric materials, which has wide applications in the various fields. There has been a resurgence of interest for the nature of the phases and the phase diagram of this technologically important material. The symmetry and the phase transition sequence near the MPB were found to be much more complex than previously thought. Different methods were employed to investigate the phase transition behavior in the PZT system, especially at around the MPB region. However, the exact crystal symmetry and the nature of phase transition near MPB region over the whole composition in a wide temperature range remain still unclear and are currently under intense debate and investigation [1-3]. There are many different ways to study the behavior of paraelectric to ferroelectric phase transition in the PZT ceramic, such as temperature dependent structural [4, 5], thermal [6] and electrical properties [7].

In contrast to the studies on the dielectric, structural and electromechanical properties, there have been few reports on thermal behavior in the PZT systems. Not only knowledge of specific heat behavior of the ferroelectric materials is important for both scientific and technological purposes, but also is more suitable for studying the phase transition behavior than the structural properties test [8]. Because the specific heat (C_p) integrates over all possible temperature-dependent contributions to the free energy occurring on the time scale of the measurements. These contributions include the thermal

evolution of the primary order parameter as well as contributions arising from coupling with other possible relaxations of the structure. The specific heat is also very sensitive to the presence of lattice defects that influence the phase transition but may not be clearly revealed in X-ray diffraction or dielectric permittivity measurements [9].

In this chapter, the experimental results of the specific heat measurements of the PZT ceramics and the calculation results of the excess entropy and the excess enthalpy were reported. The specimens studied were well-crystallized, and were carefully prepared by a sol-gel method. The results showed the existence of two tricritical points in the PZT system, and provide the possible locations for them. The details of the tricritical points in the PZT will be carefully discussed in the following sections.

5.1.2 Tricritical Points in PZT

Tricritical behavior, where a phase transition changes from first to second order, has been observed in a number of ferroelectric materials [10, 11]. Among ferroelectric perovskites, PZT is of special interest not only because of its outstanding piezoelectric, elastic, and dielectric properties that occur near the (MPB) [12, 13], but its tricritical points appear as a consequence of composition variation while in other materials the tricritical point has been seen by the application of a hydrostatic pressure[14] or by a variation in chemical composition through ion substitution [15].

The appearance of two possible tricritical points (TCP) in the PZT system has been reported based on different methods, such as temperature dependence structural [4, 5], thermal and electrical properties [5, 16]. However, the locations of the tricritical points is still a subject of debate due to several obstacles are encountered in experimental

studies of tricritical phenomena in the PZT system. It is difficult to change the relevant thermodynamic variables continuously and accurately [7]. Also, the nature of the transition can be influenced by mircrocrystalline features of the sample [6, 17]. Therefore, there are distinct differences in the reported compositions at which the tricritical points occur. The location of one tricritical point on the rhombohedral ($PbZrO_3$-rich) side of the phase diagram has been variously reported as $x = 0.06$ [7, 18, 19], $x = 0.10$ [5], $x = 0.22$ [4], $x = 0.26$ [16] and $x = 0.45$ [20-22] which is close to the MPB. Similarly, a second tricritical point on the tetragonal ($PbTiO_3$-rich) side of the phase diagram has been reported as $x = 0.72$ [5], $x = 0.55$ [4], $x = 0.51$ [16] and $0.60 \leq x \leq 0.70$ [9]. A list of reported possible compositions for tricritical points in the PZT system is shown in table 5.1.

As mentioned in the previous section, an investigation of the specific heat should prove particularly advantageous in defining the tricritical behavior in the PZT system. The details of thermal properties and determination of phase transitions will be reported in the following sections of this chapter.

Year	Author	TCP at F_R	TCP at F_T	Sample type
1976	Clarke [23]	PZT 90/10	-	Single crystal
1978	Whatmore [7]	PZT 94/6	-	Single crystal
1982	Handerek [18]	PZT 94/6	-	Ceramic
1986	Haun [24]	PZT 94/6	~MPB	-
1989	Haun [5]	PZT 90/10	PZT 28/72	Powder
1990	Eremkin [4]	PZT 78/22	PZT 45/55	Single crystal
1995	Noheda [16]	PZT 74/26	PZT 49/51	Ceramic
1997	Pandey [20]	PZT 54.5/45.5	-	Ceramic
1999	Rossetti [9]	-	PZT 30/70-PZT40/60	Ceramic
2012	Kim [21]	PZT 58/42-PZT55/45	-	Single crystal

Table 5. 1 The reported tricritical points in the PZT system in the literature.

5.2 Specific Heat Measurement

A series of PZT ceramics were made to observe the first- and second-order transition behavior and to locate the tricritical point in the PZT solid solution. PZT powders with different compositions x = 0.00, 0.10, 0.15, 0.20, 0.30, 0.40, 0.48, 0.55, 0.70, 0.80, and 1.00 (labeled from 1 to 11) were prepared by a sol-gel method. The PZT powders (x = 0.10 - 0.80) were then pressed into dense pellet form and sintering at 1473K in a PbO-rich atmosphere for 2 hours. Because of the experimental difficulties, the PZ (x = 0.00) and the PT (x = 1.00) were not in ceramic form. PZ and PT powders were calcined at 1473K for two hours in a PbO-rich atmosphere, and then pressed into dense pellets form for measuring. More details of PZT synthesis can be found in chapter 3.

A calorimetric investigation was applied by using a Netzsch DSC 404 F1 Pegasus® high temperature differential scanning calorimeter was used for measuring specific heat (*Cp*) and Curie temperature (*Tc)*. Data were acquired at a scan rate of 10K/min with 1 points per degree Kelvin from 323K to 923K, under argon flow with a rate of 50 ml/min. The specimens were placed in good thermal contact within covered platinum crucibles and measured after careful calibration of the baseline (standard error~0.053%). Sample specific heat was computed by the ratio method using the NIST SRM data pertaining to single crystal sapphire. The measurements were repeated three times on each sample investigated and the heat capacity data from the three measurements were averaged.

5.3 Results and Discussions

5.3.1 Specific Heat (C_p) and Phase Transitions in the PZT System

The results of the temperature dependence of specific heat (C_p) of PZT ceramics (303K to 973K) can be divided into three distinct regions, which were shown in Fig. 5.1 (a) Zr-rich region ($0 \leq x \leq 0.30$), (b) near-morphotropic region ($0.30 < x < 0.55$) and (c) Ti-rich ($0.55 \leq x \leq 1$). In the Ti-rich region, the C_p shows an identical behavior at low temperature, far below the transition point, rising from 108 J/[mol-K] at 310K to 118 J/[mol-K] at around 450K. The C_p values measured at these temperatures were mainly contributed by lattice (hard mode). As closing to transition points, the C_p for various samples began to differ and to increase markedly as the transition temperature for each was approached. The C_p of each sample in Ti-rich region shows a distinct peak near the transition point. The peak values of C_p and transition temperatures were dropping with decreasing x, 286 to 138 [J/mol-K] and 750K to 665K respectively. In the Zr-rich region, two transition temperatures corresponding to the transition between two rhombohedral phases (*R3c* to *R3m*) and the transition between rhombohedral to cubic phases (*R3m* to *Pm3m*) can be observed in each composition except at $x = 0.00$. Near the MPB region, the behavior of phase transition between ferroelectric and paraelectric phases showed a step-like characteristic phase transition without any significant transition peaks. Lastly, it was noted that the heat capacity of the cubic phase showed a strong dependence on composition.

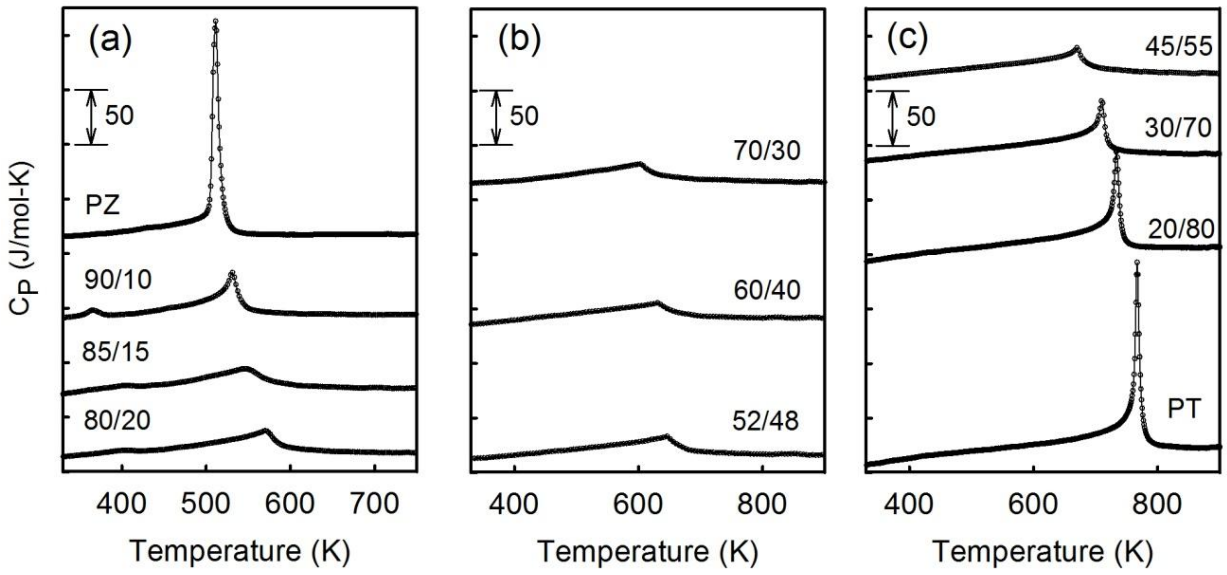

Figure 5. 1 Relative heat capacity *versus* temperature of un-annealed $PbZr_{1-x}Ti_xO_3$ powders (x = 0.00, 1.00) and sintered disks ($0.10 \leq x \leq 0.80$) in three ranges of composition (a) $0.00 \leq x \leq 0.20$ (b) $0.30 \leq x \leq 0.40$ and (c) $0.55 \leq x \leq 1.00$. The heat capacity data were collected on heating. The tick marks on the vertical axes represent intervals of 50 J/mol-K.

The order of the transition for each sample was characterized by first derivative of C_p curves, the transition enthalpy (ΔH_i), and the transition entropy (ΔS_i). The first derivative curve is useful for examining transitions. In general, sharper the transition peaks produce the better derivative curves with obvious maximum and minimum difference. As shown in Fig. 5.2 (a), the samples with strong or weak first-order transition characteristic ($0 \leq x \leq 0.30$ and $0.55 \leq x \leq 1$) show a strong and clear peak in their derivate curves. For the samples with second-order transition ($0.30 < x < 0.55$), their peaks in the derivative curves are very weak and unapparent. The first derivative curves showed sharp symmetric extrema that decreased markedly in intensity on moving away

from end member compounds with either increasing values of x from x = 0.00 or decreasing values of x from x = 1.00.

Fig. 5.2 (b) shows how the transition enthalpy (ΔH_i) in various situations was determined. For the compositions with the strong/weak first-order transition, a linear fit to C_p data at low temperatures (far below from transition temperature) was determined, and then this fitting-line was extrapolated to the region of the paraelectric to ferroelectric phase transition. The transition enthalpy (ΔH_i) then can be obtained by integrating the area of transition peak. For the compositions with second-order transition, this fitting-line goes all the way to the peak position leaves no area for integration. It means that there will be no transition enthalpy (ΔH_i) for the samples with second-order transition characteristic.

In the Ti-rich region, the behavior of phase transition change gradually from a sharp first-order transition at x = 1.00 to a weak first-order transition with decreasing titanium content. In the morphotropic region, the C_p at near the transition temperatures shows a step-like characteristic of a second-order phase transition without detectable transition enthalpy. The behavior of phase transition change gradually from a weak first-order transition at composition below x = 0.30 to a sharp first-order transition as titanium content toward to 0.

For the phase transition with first-order behavior, the transition temperatures were determined by the temperature at peak point of the phase transition (T_{peak}). The reported transition temperatures in this work were the averaged value of three individual measurements, and T_{peak} was used as phase transition temperature (T_t) for calculating. The blue circles in Fig. 5.3 represent the ferroelectric to paraelectric and the ferroelectric

to ferroelectric phase transition temperatures (T_{FP} and T_{RR}) of un-annealed PZT powders (x = 0.00, 1.00) and sintered disks ($0.10 \leq x \leq 0.80$) in present work. The ferroelectric to paraelectric phase transition temperatures (T_{FP}) increased from 504K to 760K which matches very well with the ferroelectric to paraelectric phase transition temperatures ($T_{FP\ (Jaffe)}$) in the conventional PZT phase diagram that assembled by Jaffe *et al*. [12]. The phase transition temperatures between R3c and R3m phases (T_{RR}) are also in a good agreement with literature data. This means that the quality of PZT ceramics in present work is good and very close to the desired compositions, and the composition assessment of the PZT ceramics will be discussed in the next section. The details of thermodynamic parameters are shown in Table 5. 2.

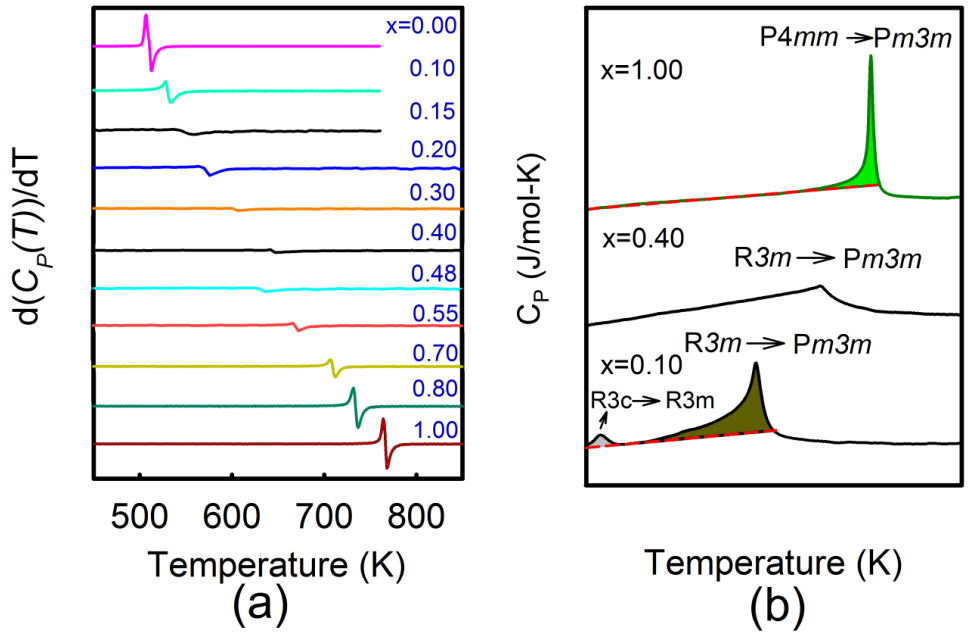

Figure 5. 2 (a) First derivative curves of heat capacity (C_p) *versus* temperature for un-annealed $PbZr_{1-x}Ti_xO_3$ powders (x = 0.00, 1.00) and sintered disks ($0.10 \leq x \leq 0.80$). (b) Heat capacity *versus* temperature for un-annealed $PbZr_{1-x}Ti_xO_3$ sintered disks with the compositions x = 0.10, 0.40 and 1.00 measured on heating.

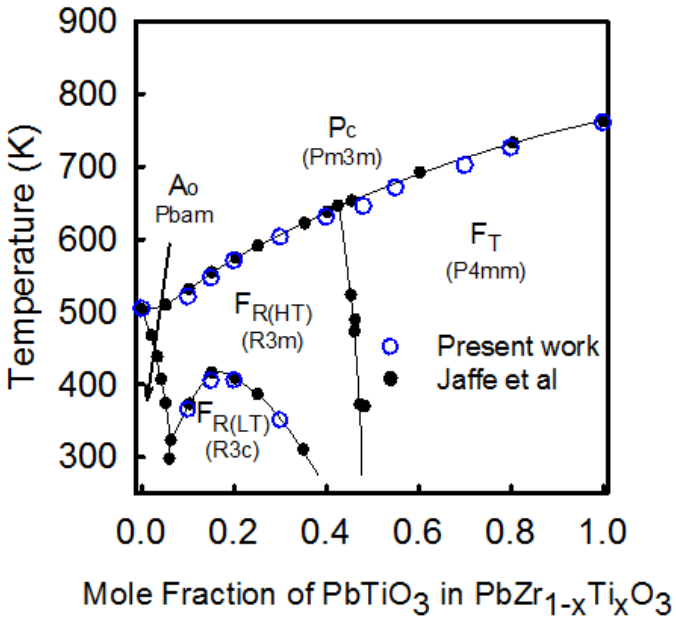

Figure 5. 3 Transition temperatures of the un-annealed PZT powders (x = 0.00, 1.00) and sintered disks ($0.10 \leq x \leq 0.80$) (blue circles) superimposed on the conventional phase diagram.

x	Form	T_{FP} (K)	T_{RR} (K)	ΔH_{FP} (kJ/mol)	ΔH_{RR} (J/mol)	ΔS_{FP} (J/mol-K)	ΔS_{RR} (J/mol-K)
0.00	P [a]	511 ±1[b]	-	1.72 ±0.09 [a]	-	3.37 ±0.58 [c]	-
0.10	SD	531 ±1	366 ±1[b]	0.86 ±0.08	72.2 ±4.4[b]	1.61 ±0.46	0.20 ±0.04 [c]
0.15	SD	547 ±1	406 ±2	0.36 ±0.05	60.7 ±3.0	0.66 ±0.26	0.15 ±0.02
0.20	SD	571 ±1	406 ±1	0.47 ±0.05	59.5 ±1.5	0.82 ±0.29	0.15 ±0.01
0.30	SD	603 ±1	351 ±4	0.04 ±0.01	6.5 ±4.0	0.08 ±0.03	0.03 ±0.03
0.40	SD	630 ±1	-	-	-	-	-
0.48	SD	646 ±1	-	-	-	-	-
0.55	SD	671 ±1	-	0.11 ±0.01	-	0.16 ±0.03	-
0.70	SD	710 ±1	-	0.65 ±0.05	-	0.91 ±0.25	-
0.80	SD	734 ±1	-	1.06 ±0.01	-	1.44 ±0.04	-
1.00	P	767 ±1	-	1.88 ±0.01	-	2.45 ±0.05	-

[a] P: Powder, SD: Sintered disk
[b] Standard deviation about the mean
[c] Error propagated using three times the standard deviation in ΔH_i and an estimated absolute error in Ti of ±3 K

Table 5. 2 Transition temperatures (T_i), transition enthalpies (ΔH_i) and transition entropies (ΔS_i) acquired on heating for the ferroelectric to paraelectric (FP) and rhombohedral cell doubling (RR) phase transitions in un-annealed $PbZr_{1-x}Ti_xO_3$ powders and sintered disks

5.3.2 Composition Assessment of the PZT Ceramics

Structural, electrical and thermal properties of the PZT solid solution are extremely sensitive to the compositional variation, especially at near the MPB region. To study the PZT solid solution, it is essential to have the samples with exceptionally high quality and accuracy in terms of chemical composition.

The composition assessment of the PZT solid solution was made by comparing the results of the crystal lattice parameters and the transition temperatures to the literatures, which were shown in Fig. 4.2 and Fig. 5.3, respectively. The combined measurements confirm that the composition of the PZT specimens was controlled to within ~1 mol% of the desired composition, and the result of composition assessment was shown in Fig. 5.4. The blue circles show the PZT samples' compositions (*x'*) were very close to the desired compositions (*x*). Thus, the prepared samples in this study were good quality and close to the desired compositions.

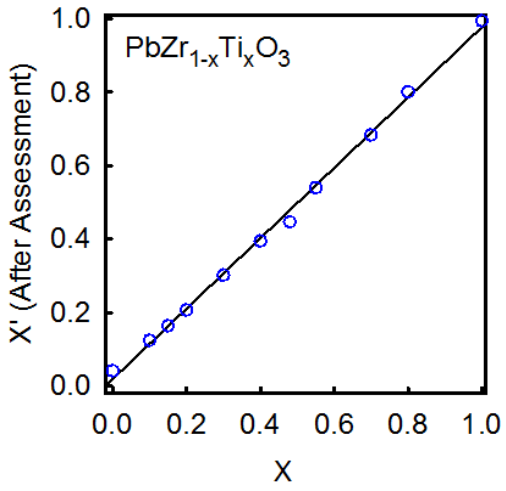

Figure 5. 4 Composition assessment of the un-annealed $PbZr_{1-x}Ti_xO_3$ powders (x = 0.00, 1.00) and sintered disks ($0.10 \leq x \leq 0.80$).

5.3.3 Tricritical Points in the PZT System

The data in Fig. 5.1 strongly support previous reports [1, 4, 16] that the PZT system exhibits two lines of first-order FP transitions separated by a line of second-order transitions. To further locate the positions of these two tricritical points, the transition enthalpy and the transition entropy were applied to determine where the order of the transition changes. The transition enthalpies, ΔH_{RR} and ΔH_{FP}, were determined by integrating the heat capacities [$C_P(T)$] relative to linear background function [$C_P^0(T)$] fitted to the data in ranges of temperature $T_1 < T_{FP}$ away from the transitions and extrapolated to temperatures $T_2 > T_{FP}$,

$$\Delta H_i = \int_{T_1}^{T_2} [C_P(T) - C_P^0(T)]dT \,. \qquad \text{Equation 5. 1}$$

The method of determining enthalpies is illustrated on Fig. 5. 2(b). Also, the transition entropies (ΔS_i) can be computed ($\Delta S_i = \Delta H_i / T_i$) after transition enthalpies were determined. The results of transition enthalpies collected on both heating and cooling measurements were shown in Fig. 5.5(a). From both Zr-rich ($0 \le x \le 0.30$) and Ti-rich regions ($0.55 \le x \le 1$) toward to MPB, the transition enthalpies decreases from 1.72 (x = 0) to 0.47 kJ/mol (x = 0.20) and 1.88 (x = 1.00) to 0.11kJ/mol (x = 0.55) respectively. The transition enthalpies remain 0 in the MPB region ($0.30 < x < 0.55$). The transition enthalpies of the PZT samples were listed in the table 5.2. . The errors for the transitions temperatures and enthalpies listed in Table 5.2 represent the standard deviations about the mean value of the three measurements preformed. From this experiment result, it is clear that two tricritical points exist in the PZT solid solution. The transition was first order from the end members to the tricritical points, and then a second order region occurs

across the phase diagram between the tricritical points. By extrapolating between the data points, two tricritical points were found to occur at around the MPB region ($0.30 < x < 0.55$). The results matches not only with other experiment observations [4, 16] by Eremkin *et al.* ($x = 0.22$ and $x = 0.55$) and Noheda *et al.* ($x = 0.26$ and $x = 0.51$)), but also match very well with predicted result from low order Landau theory for weak first-order transitions by Rossetti *et al*. [1].

The corresponding transition entropies are shown in Fig. 5.5(b). As seen in this figure, transition entropies decreases linearly with composition from two end compositions toward to MPB region and reach 0 at two tricritical points. However, the transition entropy for the composition $x = 0.00$ is far from the fitting line. This is due to lead Zirconate ($x = 0.00$) has an orthorhombic structure (Pbam) at room temperature, which is quite differ from rhombohedral phase (R3c). Thus, the phase transition was between orthorhombic phase (Pbam) and cubic phase (Pm3m), which is different from other compositions at Zr-rich region. The transition enthalpy of the lead Zirconate ($x = 0.00$) will not considered in the further analysis for the locations of the tricritical points described below.

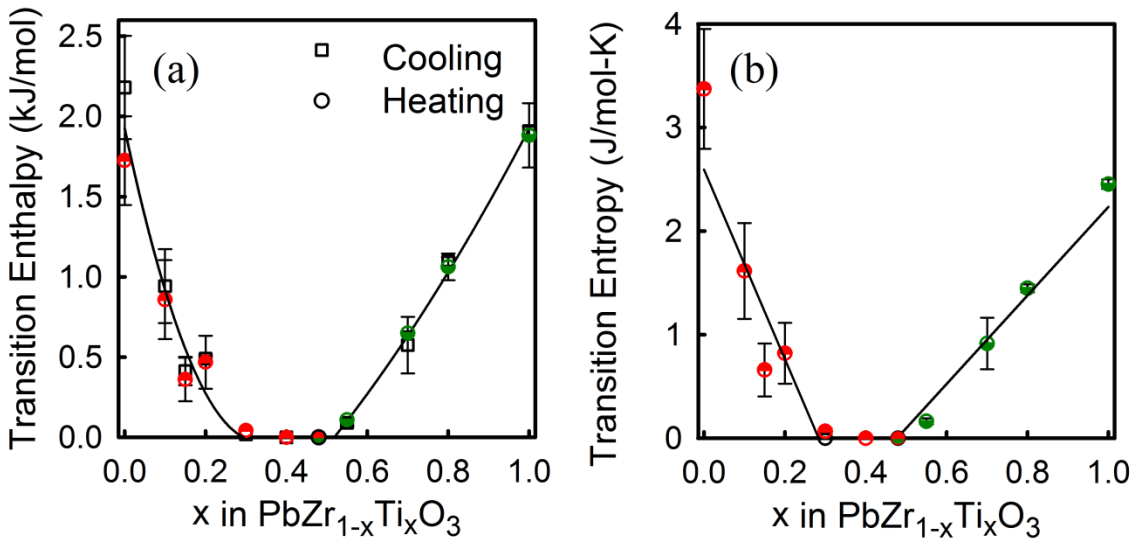

Figure 5. 5 (a) Transition enthalpies *versus* composition for the un-annealed PZT powders (x = 0.00, 1.00) and sintered disks ($0.10 \leq x \leq 0.80$) collected in both heating and cooling measurements. (b) Corresponding transition entropies *versus* composition collected in heating measurements. The solid lines shown are least-squares fits to both sets of data.

The experimental transition entropy data was analyzed using a Landau polynomial [1, 25]. At high temperatures near the line of Curie temperatures, $T_C(x)$, the truncated 2-4-6 Landau polynomial is asymptotically accurate. For this situation the excess non-equilibrium free energy, G^{XS}, for weak first-order transitions close to second order can be written

$$G^{XS} = G(x,T,\boldsymbol{n},P) = \frac{1}{2}A_0(x)[T - T_C(x)]P^2 + \frac{1}{4}B(x,\boldsymbol{n})P^4 + \frac{1}{6}C_0P^6, \qquad \text{Equation 5. 2}$$

where $\boldsymbol{n}$ is a unit vector in the direction of spontaneous polarization $\boldsymbol{P}$, and P is its absolute value. The dielectric stiffness is given by the Curie-Weiss law, $A_0(x) = 1/\varepsilon_0 C_{CW}(x)$, where $C_{CW}(x)$ is the Curie-Weiss constant and ε_0 is the permittivity of free space. The quartic term in Eq. 5.2 is assumed to have the following form,

$$B(x,\boldsymbol{n}) = B_0[(x-x_0) - \xi(x-x_m)(n_1^4 + n_2^4 + n_3^4)] \qquad \text{Equation 5. 3}$$

where B_0 and ξ are constants and x_0 and x_m are the compositions where the quartic isotropic and quartic anisotropic contributions to the free energy vanish, respectively. The coefficient of the sextic term, C_0, is taken to be a constant, independent of *x*, *T* and ***n***. After minimizing Eq. 5.2 with respect to ***n*** and *P*, below $T_C(x)$ the rhombohedral phase with $\boldsymbol{n}_{eq} = \{1/\sqrt{3}, 1/\sqrt{3}, 1/\sqrt{3}\}$ is stable for $x < x_m$ and the tetragonal phase with $\boldsymbol{n}_{eq} = \{0,0,1\}$ is stable for $x > x_m$. Hence, Eq. 5.3 becomes,

$$B(x,\boldsymbol{n}_{eq}) = \begin{cases} B_0[(x-x_0) - (x-x_m)\xi/3] & \text{if } x < x_m \\ B_0[(x-x_0) - (x-x_m)\xi] & \text{if } x > x_m \end{cases} \qquad \text{Equation 5. 4}$$

It is apparent from Eq. (4) that x_m is the composition where the morphotropic boundary line intersects the line of Curie temperatures, *i.e.*, a triple point with coordinates (x_m, $T_C(x_m)$). It is further evident that if the FP transitions for the two end members are both of first order, the constant ξ in Eq. 5.4 must adopt a value $1 \le \xi \le 3$.

A tricritical point is defined by the condition that the entire quartic term in by Eq. 5.2 turns out to be zero,

$$\min[B(x,\boldsymbol{n})] = 0 \qquad \text{Equation 5. 5}$$

It follows from Eqs. 5.4 and 5.5 that there is one such point in the rhombohedral phase having coordinates ($x_R^{CR}, T_C(x_R^{CR})$) with

$$x_R^{CR} = \frac{x_0 - x_m\xi/3}{1-\xi/3}, \qquad \text{Equation 5. 6}$$

and a second such point in the tetragonal phase having coordinates ($x_T^{CR}, T_C(x_T^{CR})$) with

$$x_T^{CR} = \frac{x_0 - x_m \xi}{1 - \xi}. \qquad \text{Equation 5. 7}$$

From Eqs. 5.6 and 5.7 there is one line of second-order FP transitions for $x_R^{CR} < x < x_T^{CR}$ and two lines of first-order FP transitions with $x < x_R^{CR}$ and $x > x_T^{CR}$. Along the two lines of first-order transitions, jumps in polarization $\Delta P(x)$ occur at the temperatures $T_0(x)$, where the ferroelectric and paraelectric phases are in equilibrium,

$$\Delta P^2(x, T_0) = -\frac{3}{4}\frac{B(x, \boldsymbol{n}_{eq})}{C_0}. \qquad \text{Equation 5. 8}$$

The jump in polarization can be related to the entropy change at $T_0(x)$ by taking the temperature derivative of Eq. 5.2,

$$\left.\frac{\partial G^{XS}}{\partial T}\right|_{T_0(x)} = -S^{XS}(x, T_0) = \frac{1}{2} A_0(x) \Delta P^2(x, T_0). \qquad \text{Equation 5. 9}$$

Equating the jumps in polarization in Eqs. 5.8 and 5.9, and associating the excess entropy with the experimentally measured values $-S^{XS}(x, T_0) \approx \Delta S(x, T_{FP})$ results in,

$$\frac{B(x, \boldsymbol{n}_{eq})}{C_0} = -\frac{8}{3}\frac{\Delta S(x, T_{FP})}{A_0(x)}. \qquad \text{Equation 5. 10}$$

In Eq. 5.10 $\Delta S(x, T_{FP}) = \Delta S_i(x) \rho_M(x)$ where $\Delta S_i(x)$ is the measured transition entropy reported in Table 5.2 in units of kJ/mol, and $\rho_M(x) = M(x)/\rho_X(x)$ is the molar density in which $M(x)$ is the molecular weight and $\rho_X(x)$ is the measured x-ray density. Using Eqs. 5.4 and 5.5 the LHS of Eq. 5.10 becomes

$$\frac{B(x,\boldsymbol{n}_{eq})}{C_0}=\begin{cases}\dfrac{B_0}{C_0}[(x-x_0)-(x-x_m)\xi/3] & \text{if } x<x_R^{CR}\\ \dfrac{B_0}{C_0}[(x-x_0)-(x-x_m)\xi] & \text{if } x>x_T^{CR}\end{cases}. \qquad \text{Equation 5. 11}$$

Eq. (11) predicts that the ratio $B(x,\boldsymbol{n}_{eq})/C_0$ is a linear function of composition. Further, from Eq. (10), if the transition entropy displays a linear dependence on composition as shown by the data in Fig. 5.5(b), then the dielectric stiffness $A_0(x)$ must also vary linearly with *x*. To compute values for the ratio $B(x,\boldsymbol{n}_{eq})/C_0$, the experimental transition entropies reported in Table 5.2 were inserted in Eq. (10), together with dielectric stiffnesses $A_0(x)$ taken as the linear interpolation between the measured values for single crystals of lead titanate [8] and zirconium-rich ($x \leq 0.06$) single crystals of $PbZr_{1-x}Ti_xO_3$ [7],

$$A_0(x)=5.66\times10^5(1-x)+8.70\times10^5 x \quad \text{(V-m/C-K)} \qquad \text{Equation 5. 12}$$

The variation of $B(x,\boldsymbol{n}_{eq})/C_0$ with composition is shown in Fig. 5.6(a). In this figure, the semi-filled circles are computed using Eq. 5.10 and the solid lines are the least-squares fits to the computed values. Two tricritical points, $x_R^{CR}=0.30$ and $x_T^{CR}=0.51$, can be found at the intersections of the fitted lines with the horizontal axis, and the triple point, $x_m=0.38$, can also be found at the intersection of the two fitting lines. Taking these values into Eqs. 5.6 and 5.7, the values of x_0 and ξ were then able to obtain. The calculated values of x_0 and ξ were 0.34 and 1.3, respectively. By substituting these parameters into Eq. 5.11 the scale factor $B_0/C_0=1.29$ ± 0.10 was found that best reproduced the fitted lines shown on Fig. 5.6(a). Using these parameters, the jumps in polarization along the lines for first-order transitions were predicted by inserting Eq. 5.11

into Eq. 5.8 and the results are shown on Fig. 5.6(b). For comparison, the jumps in polarization computed directly from Eq. 5.9 using the experimentally measured entropies and dielectric stiffnesses are also shown. As the latter computation makes no assumptions concerning the forms of the quartic and sextic terms, except that they are independent of temperature, the results shown on Fig. 5.6 verify that the truncated 2-4-6 Landau polynomial of Eq. 5.2 with quartic term given by Eq. 5.3 provides an excellent approximation for the PZT system at high temperatures near the Curie line.

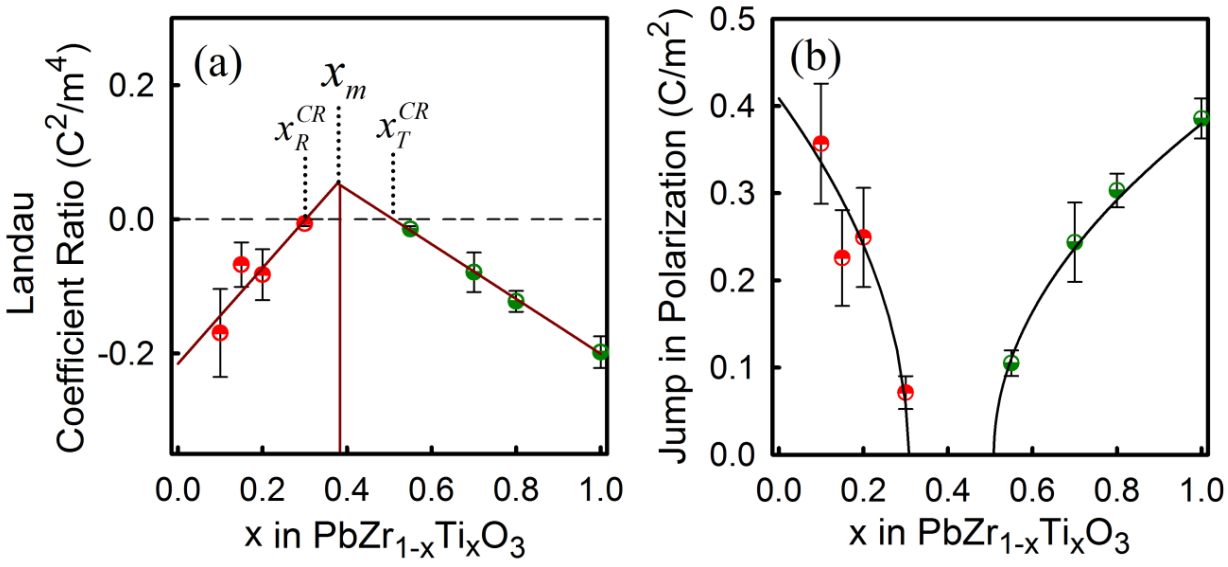

Figure 5. 6 (a) The Landau coefficient ratio $[B(x,\boldsymbol{n}_{eq})/C_0]$ of $PbZr_{1-x}Ti_xO_3$ powder (x = 1.00) and sintered disks ($0.10 \leq x \leq 0.80$) *versus* composition computed using Eq. 5.10. The solid lines shown represent linear least-squares fits to the data of un-annealed samples. (b) The jump in polarization at the ferroelectric to paraelectric transition for un-annealed $PbZr_{1-x}Ti_xO_3$ powders (x = 1.00) and sintered disks ($0.10 \leq x \leq 0.80$) *versus* composition computed using Eq. (9). The solid lines are computed from Eq. (8) and Eq. (11) using the Landau parameters of un-annealed samples given in the text.

5.4 Summary

This chapter was focused on the thermal parameters of the un-annealed PZT powders (x = 0.00, 1.00) and sintered disks ($0.10 \leq x \leq 0.80$). Thermal parameters of the PZT samples were studied by a differential scanning calorimeter measurement. The behavior of the temperature dependent specific heat is very sensitive to the composition in the PZT ceramics. Therefore, the phase transition behavior in the PZT ceramics can be tested by specific heat measurement. The observations from the specific heat measurement are as follows,

1. The Curie temperatures of the PZT powders (x = 0.00, 1.00) and sintered disks ($0.10 \leq x \leq 0.80$) were determined by the peak point of phase transition, and were in a good agreement with literature data.
2. The composition of the PZT specimens was controlled to within ~1 mol% of the desired composition.
3. The order of the transition for each sample was characterized by first derivative of C_p curves, the transition enthalpy (ΔH_i), and the transition entropy (ΔS_i). The phase transitions are the strong first order phase transition at two end members in the PZT system, and are the second order phase transition at the MPB region. The region between two end compositions and MPB area shows a weak first order phase transition behavior. There will be two tricritical points based on this observation.
4. Two tricritical points were found to occur at around $x_R^{CR} = 0.30$ and $x_T^{CR} = 0.51$. The results not only matches with the experimental observations by Eremkin *et al.* and Noheda *et al.*, but also match very well with predictions of a truncated 2-4-6

Landau polynomial describing a binary ferroelectric solid solution with two tricritical points.

5.5 References

1. G.A. Rossetti, A.G. Khachaturyan, G. Akcay, and Y. Ni, *J Appl Phys* **103**, 114113 (2008)
2. A.A. Heitmann and G.A. Rossetti, *Philos Mag* **90**, 71 (2010)
3. B. Noheda, J.A. Gonzalo, L.E. Cross, R. Guo, S.E. Park, D.E. Cox, and G. Shirane, *Physical Review B* **61**, 8687 (2000)
4. V.V. Eremkin, V.G. Smotrakov, and E.G. Fesenko, *Ferroelectrics* **110**, 137 (1990)
5. M.J. Haun, E. Furman, H.A. McKinstry, and L.E. Cross, *Ferroelectrics* **99**, 27 (1989)
6. G.A. Rossetti, P.F. Cahill, R.R. Biederman, and A. Sacco, *Mater Lett* **41**, 72 (1999)
7. R.W. Whatmore, R. Clarke, and A.M. Glazer, *Journal of Physics C: Solid State Physics* **11**, 3089 (1978)
8. G.A. Rossetti and N. Maffei, *Journal of Physics: Condensed Matter* **17**, 3953 (2005)
9. G.A. Rossetti and A. Navrotsky, *J Solid State Chem* **144**, 188 (1999)
10. E.K.H. Salje, *Phase Transitions* **34**, 25 (1991)
11. E.I. Gerzanich and V.M. Fridkin, *Ferroelectrics* **31**, 127 (1981)
12. B. Jaffe, W.R. Cook, and H.L. Jaffe, *Piezoelectric ceramics* 1971, London, New York,: Academic Press. 135.
13. S.A. Mabud, *J Appl Crystallogr* **13**, 211 (1980)
14. R. Clarke and L. Benguigui, *J Phys C Solid State* **10**, 1963 (1977)

15. L. Benguigui and Y. Beaucamps, *Ferroelectrics* **25**, 633 (1980)

16. B. Noheda, N. Cereceda, T. Iglesias, G. Lifante, J. Gonzalo, H. Chen, and Y. Wang, *Physical Review B* **51**, 16388 (1995)

17. K.S. Aleksandrov and I.N. Flerov, *Soviet Physics - Solid States* **21**, 195 (1979)

18. K. Roleder and J. Handerek, *Phase Transitions* **2**, 285 (1982)

19. R. Clarke and A.M. Glazer, *Ferroelectrics* **14**, 695 (1976)

20. S.K. Mishra and D. Pandey, *Philos Mag B* **76**, 227 (1997)

21. T.H. Kim, J.H. Ko, S. Kojima, A.A. Bokov, X.F. Long, and Z.G. Ye, *Appl Phys Lett* **100**, 082903 (2012)

22. D. Pandey, A.K. Singh, and S. Baik, *Acta crystallographica. Section A, Foundations of crystallography* **64**, 192 (2008)

23. R. Clarke, A.M. Glazer, F.W. Ainger, D. Appleby, N.J. Poole, and S.G. Porter, *Ferroelectrics* **11**, 359 (1976)

24. Z.Q. Zhuang, M.J. Haun, J. Jang, and L.E. Cross, *Ieee T Ultrason Ferr* **33**, 827 (1986)

25. G.A. Rossetti, W. Zhang, and A.G. Khachaturyan, *Appl Phys Lett* **88**, 072912 (2006)

CHAPTER 6

DIELECTRIC PROPERTIES IN PZT

6.1 Introduction

The dielectric property of the PZT ceramics has been extensively studied [1-3]. The dielectric properties can be modified over a wide range by using different dopants or by different processing conditions [4, 5]. High permittivity PZT-based ceramics are widely used in different types of capacitors. In order to optimize the performance of these ceramic devices, it is essential to understand the dielectric behavior of the PZT system at different conditions (i.e. temperature, composition, and electric field strength). The dielectric behavior can be varying in a wide range with different conditions. For example, the dielectric permittivity has a linear relation with the electric field at low level of applied field, which relation became nonlinear as the applied field increase. Such nonlinear behavior was so-called dielectric nonlinearity.

It is well understood that dielectric property of the PZT ceramics contains two mechanisms, which are the intrinsic and the extrinsic contributions [3, 6-8]. The intrinsic contributions were from the averaged unit cell deformation and single domain response under an external force. The extrinsic contributions were responsible for the origin of the nonlinear properties in ferroelectric ceramics, which is one of the limitations for practical use of these ceramic products. In literature, many ways to separate the intrinsic and the extrinsic contributions were reported. These techniques were discussed in details in the chapter 1. To have a better understanding of the different contributions to the dielectric properties and dielectric nonlinear is not only scientifically interesting, but also

technically important. For example, the nonlinear properties can be useful in some applications such as frequency mixers and nonlinear dielectric spectroscopy.

This chapter discusses the dielectric behavior of the PZT system. The temperature, frequency, and composition dependence of dielectric behavior were investigated at low electric field. These results were compared to the literature data to check the quality of the PZT sintered disks. Also, temperature dependence of dielectric behavior of the PZT sintered disks was used to determine the intrinsic and the extrinsic contributions to the dielectric permittivity. It offers an overview of the contribution mechanisms to dielectric properties in the un-doped PZT ceramics.

The field amplitude dependence of the real and imaginary part of the dielectric permittivity was measured at room temperature, and different types of the domain wall motions were quantified by using Rayleigh analysis. There were many reports of Rayleigh analysis on the PZT ceramics [9-13] and thin films [8, 14-16] in the past two decades. However, the systematically investigations on the composition dependence of Rayleigh analysis of the un-doped PZT ceramics has not been reported so far. The Rayleigh analysis of the un-doped PZT sintered disks with the compositions across whole phase diagram ($0.10 \leq x \leq 0.80$) was investigated, and different types of the domain wall motions in the PZT system can be quantified.

6.2 Dielectric Property Measurement

In this thesis work, electrical analysis of electrode PZT sintered disks was carried by a comprehensive dielectric and piezoelectric measurement system at the University of Connecticut (shown in Fig 6.1). This system consists of a HP Agilent 4282A LCR meter,

a Delta Design 9023 oven, a HP Agilent 4195A Network Spectrum Analyzer, an Agilent 34401A digital multimeter, a SR830 Lock-In amplifier, a Trek Precision High Voltage amplifier and a custom-built charge voltage converter. Custom designed software developed by Paul Moses at the Penn State MRL allows for the interconnection and data acquisition from the individual measurement systems listed above. The capacitance and loss were obtained as functions of frequency, ac and dc bias, temperature, and applied electrical field by this comprehensive system. In this thesis work, the dielectric properties at low field and strong field were investigated. The details of the dielectric measurement were discussed in the following sections.

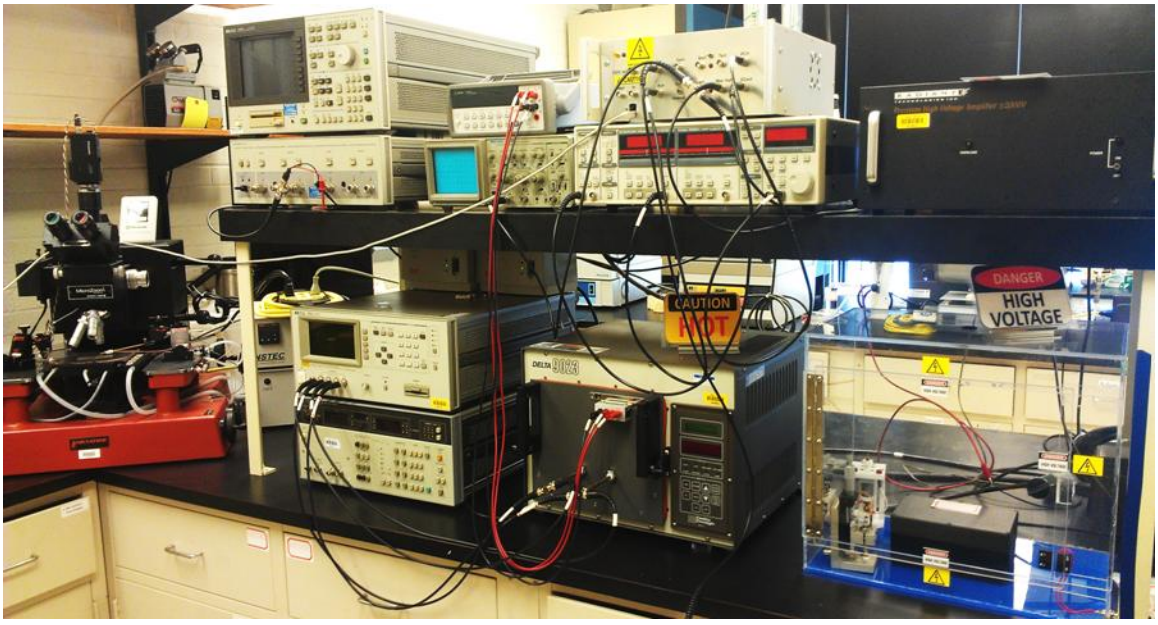

Figure 6.1 The Comprehensive dielectric and piezoelectric measurement system at the University of Connecticut

6.2.1 Low Field Dielectric Measurement

The dielectric properties of the PZT sintered disks as a function of composition, frequency and temperature were investigated at a low electric field (< 1V/cm). The composition and frequency dependent relative dielectric permittivity and loss tangent were obtained from capacitances and loss. The capacitances and loss of the dense PZT ceramics were determined by isothermal frequency sweeps from 100 Hz to 1 MHz under a field of 0.1 volts using a Hewlett-Packard Agilent 4282A LCR Meter at room temperature. A dielectric test fixture was used throughout this study for making contacts to the electrodes, which is shown in Fig. 6.2.

From the measured capacitance data, treatment of the 1mm thick silver paste electroded plate as a parallel plate capacitor, the relative dielectric permittivity (ε_r) was found using the following relation

$$\varepsilon_r = \frac{t_a \times C_p}{A \times \varepsilon_0} \qquad \text{Equation 6. 1}$$

where t_a is sample thickness, C_p is the capacitance, A is the sample area, and ε_0 is the permittivity of free space ($\varepsilon_0 = 8.854 \times 10^{-12}$ F/m).

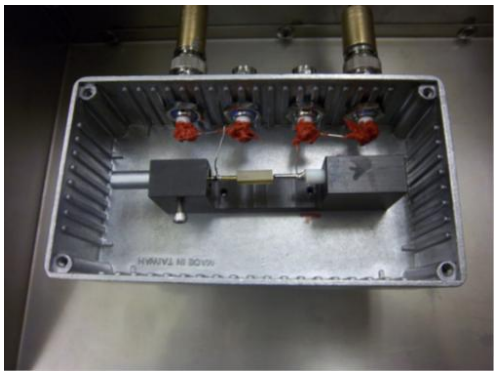

Figure 6.2 A picture of dielectric test fixture.

The temperature dependence dielectric measurement at low electric field were performed by placing the PZT sintered disk in a fixture and subsequently placed in a Delta Design 9023 Oven, capable of operating from liquid nitrogen temperatures up to 573K. Capacitance and loss measurements were obtained by isothermal frequency sweeps from 100Hz to 1 MHz under a field of 0.1 volts using a HP Agilent 4282A LCR meter in the temperature range of 173K to 473K. The PZT sintered disks were ramped in temperature at three degree increments and subsequently held at temperature for one and half minutes prior to each measurement in order to equilibrate the temperature of the sample with the desired temperature. At each temperature step, a complete frequency sweep was performed and at each frequency, capacitance and dielectric loss values were recorded. To accurately measure the sample temperature, the temperature in the oven was computer controlled via resistance temperature interfaced detector (RTD) connected to an Agilent 34401A multimeter. The RTD calibration range extended from liquid nitrogen temperature up to 573K. Fig. 6.3 presents the schematic of the electrical connections for temperature dependence dielectric measurements. Fig. 6.4 demonstrates an example result of the frequency and temperature dependence dielectric constant of the PZT 52/48 sintered disk. It shows that this setup could collect huge amount of data at one time, and provide a wider view to understand the dielectric behavior of the PZT.

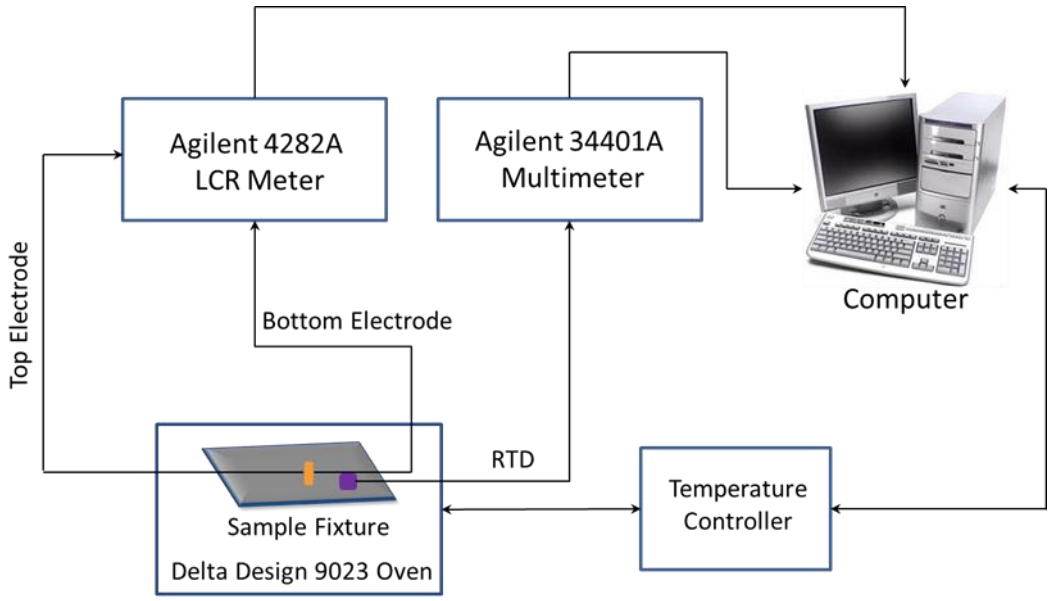

Figure 6.3 Setup of temperature dependence dielectric property measurement.

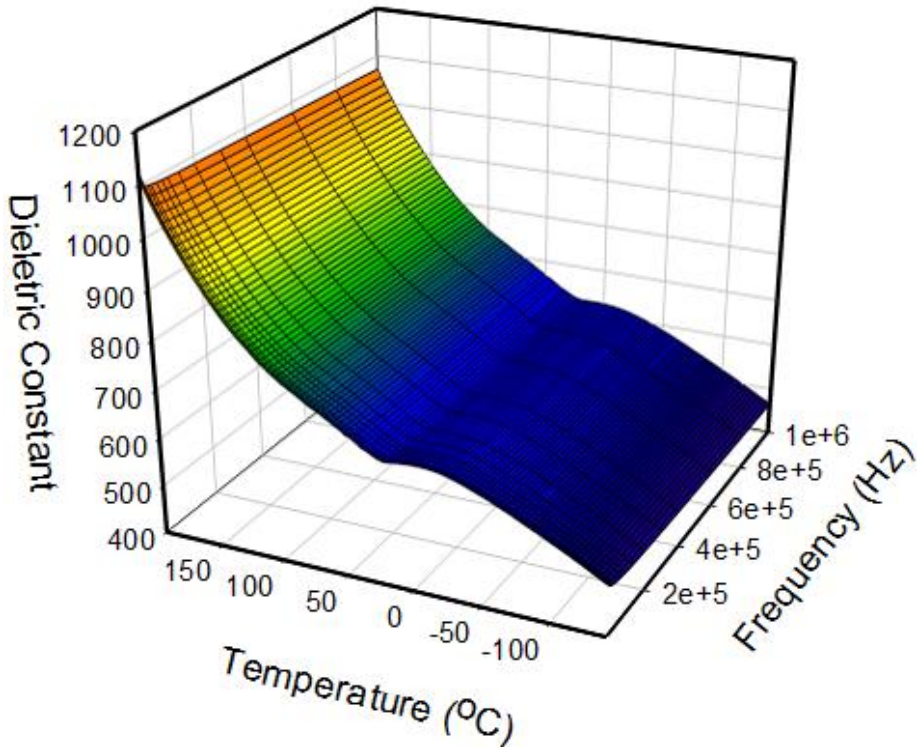

Figure 6.4 Temperature and frequency dependence of dielectric constant of the PZT 52/48 sintered disk.

6.2.2 Strong Field Dielectric Measurement

Rayleigh analysis on the ac field amplitude dependence of the dielectric and/or piezoelectric responses is another useful method to quantify the extrinsic contributions to their properties. Since the intrinsic response can be assumed to be independent of electric field [6, 17]. ac field dependence of dielectric constant of the PZT sintered disks was measured using a lock-in technique so that higher electric fields could be applied. In this approach, a lockin amplifier (SR830, Stanford Research), a custom made voltage amplifier, and a charge converter were used. The samples with different compositions were measured at their sub-switching field from 1 Hz to 1 kHz.

6.3 Results and Discussions

6.3.1 Low Field Dielectric Properties

6.3.1.1 Composition Dependence Dielectric Properties

As mentioned in the previous chapters, the PZT ceramics are very sensitive to composition variation and show pronounced extrema in piezoelectric, dielectric and elastic properties near their MPB region. Fig. 6.5(a) and 6.5(b) show composition dependence of dielectric constant of the PZT sintered disks at 1 kHz and 10 kHz, respectively. Similar to the earliest investigations [1, 18], the dielectric constants at both frequencies reach a maximum (~700) at around the MPB (x = 0.48). It is well known that the increased dielectric response in PZT materials near the MPB is due to the increased number of allowable domain states (six in tetragonal phase (*P4mm*, F_T), and eight in

rhombohedral phase (*R3m*, F_R)), low crystallographic anisotropy of polarization and extrinsic contributions (non-180 domain wall movements) [19] near the MPB. Comparison of the dielectric constant at two frequencies shows the dielectric constant decreases slightly with increased frequency at every composition. The details of dielectric properties were listed at the table 6.1.

Fig. 6.6(a) and Fig. 6.6(b) show the dielectric loss of the PZT sintered disks at 1 kHz and 10 kHz, respectively. A minimum of the dielectric loss was reached at the composition near the MPB region, and the PZT sintered disks with compositions at Ti-rich region (Ti-rich PZTs) have higher losses than the ones with compositions at Zr-rich region (Zr-rich PZTs) at 1 kHz. It is due to the as-synthesized Ti-rich PZTs have a much higher spontaneous strain than the Zr-rich PZTs. High spontaneous strain leads to create a higher defect concentrations. The losses of Ti-rich PZTs decrease drastically as the frequency increased to 10 kHz and/or higher.

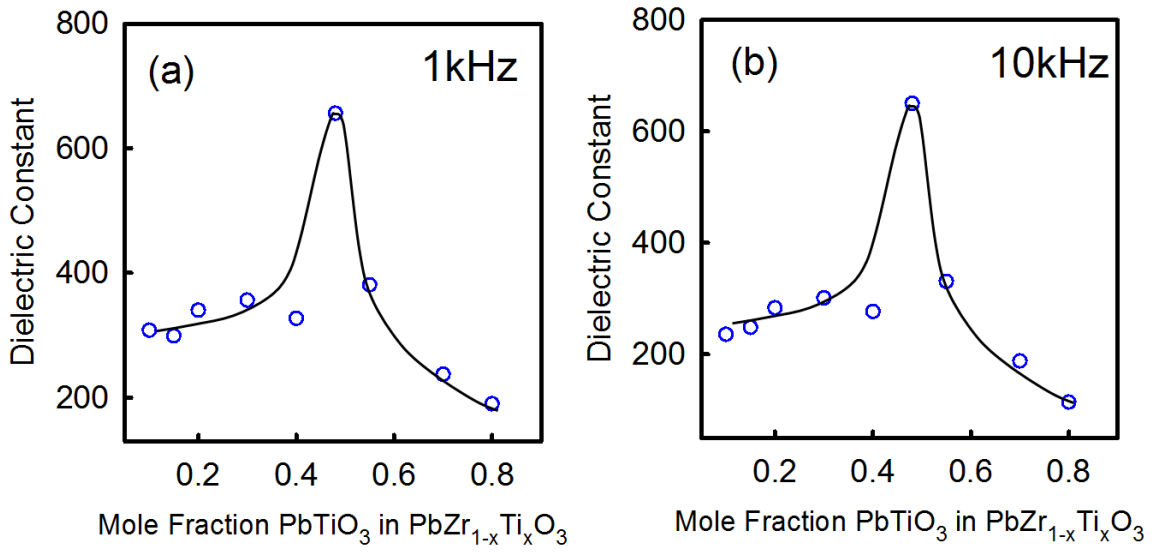

Figure 6.5 Dielectric constant of the PZT sintered disks at (a) 1kHz and (b) 10kHz. Open circles are the experimental data. Solid lines are guides to the eye

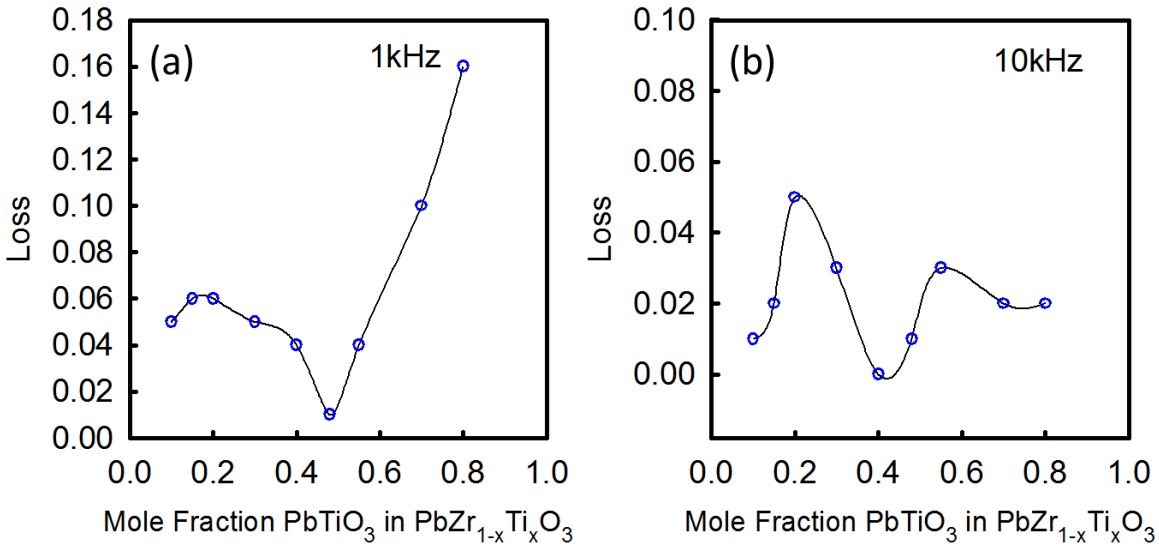

Figure 6.6 Dielectric loss of the PZT sintered disks at (a) 1 kHz and (b) 10 kHz. Open circles are the experimental data. Solid lines are guides to the eye

6.3.1.2 Frequency Dependence Dielectric Properties

Dielectric response of the PZT ceramics is frequency dependent. Generally, four different polarization mechanisms contribute to the dielectric response at frequencies from high to low are possible for a dielectric material: electronic, ionic, dipolar, and space charge or interfacial polarization. In this study, the frequency dependence dielectric properties were tested from the space charge region (1 kHz) to the edge of the ionic region (1 MHz).

Fig. 6.7 presents the frequency dependence of the dielectric constant of the PZT sintered disks with varying composition (x) showing (a) the tetragonal compositions with x = 0.55 – 0.80 and a two phase mixture of tetragonal and rhombohedral phases with x = 0.48 and (b) the rhombohedral compositions with x = 0.10 – 0.40 measured under the small ac signal of 100 mV. It can be seen that the dielectric constant decrease slightly

with frequency from 1 kHz to 1 MHz due to the reduced polarization mechanism with increased frequencies. Dielectric constant of the PZT sintered disks with tetragonal compositions (Ti-rich) is less frequency dependent with increased Zr content. The dielectric constant reduced 46% from 1 kHz to 1MHz [(ε_{1k}-ε_{1M})/ ε_{1k}] for the PZT 20/80 sintered disk, and reduced 21% for the PZT 45/55 sintered disk. Frequency dependence of dielectric constant of the PZT sintered disks with rhombohedral compositions (Zr-rich) show a similar behavior. The dielectric constant decreases with increased frequencies. However, dielectric constant of all PZT sintered disks with rhombohedral compositions show a similar reduction (~ 22%) from 1 kHz to 1 MHz.

Fig. 6.8 shows the frequency dependence of the dielectric loss of the PZT sintered disks with (a) the tetragonal compositions with x = 0.55 – 0.80 and a two phase mixture of tetragonal and rhombohedral phases with x = 0.48 and (b) the rhombohedral compositions with x = 0.10 – 0.40. It can be seen that the dielectric loss tend to rapidly increase as the frequency decreases close to 1 kHz. Practically, the dielectric properties are strongly influenced by the presence of moisture, the complexity of the grain boundaries, grain size and orientation, and ionic space-charge carriers. Thus, this high loss occurring at low frequency can be related to higher conductivity attributed by ionic space-charge carriers[20], such as the oxygen vacancies and defects generated during the ceramic sintering, interface polarization located at grain boundary[21]. At the Ti-rich region, the loss was less frequency dependent with increased Zr content, and a relaxation peak (jump) was observed. The relaxation peak move to lower frequency from 120 kHz (PZT 20/80) to 90 kHz (PZT 45/55) with increased Zr content. At Zr-rich region, the loss

behavior is very similar to each composition. The observed loss jump of each composition occurs at around 80 kHz.

Among all the samples, the dielectric constant and loss of the PZT sintered disk with composition at MPB (x = 0.48) are nearly frequency independent in this frequency range. There is no loss peak (jump) was observed in this frequency range.

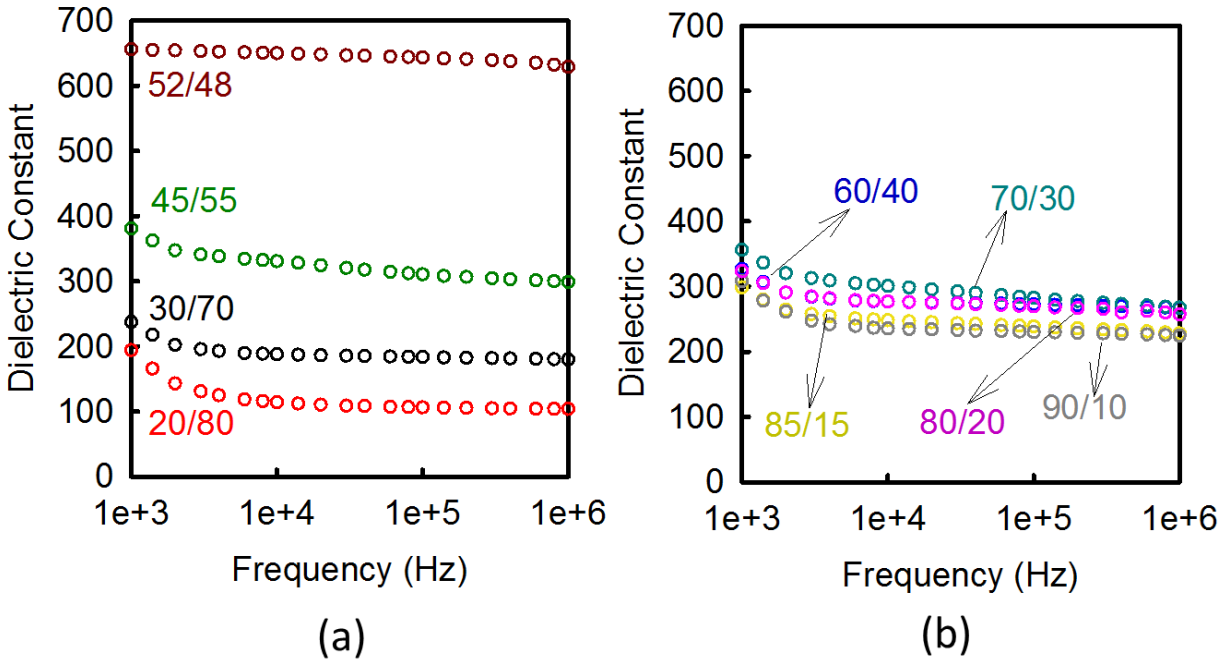

Figure 6.7 Frequency dependence of dielectric constant of the PZT sintered disks with (a) the tetragonal compositions with x = 0.55 – 0.80 and a two phase mixture of tetragonal and rhombohedral phases with x = 0.48 and (b) the rhombohedral compositions with x = 0.10 – 0.40.

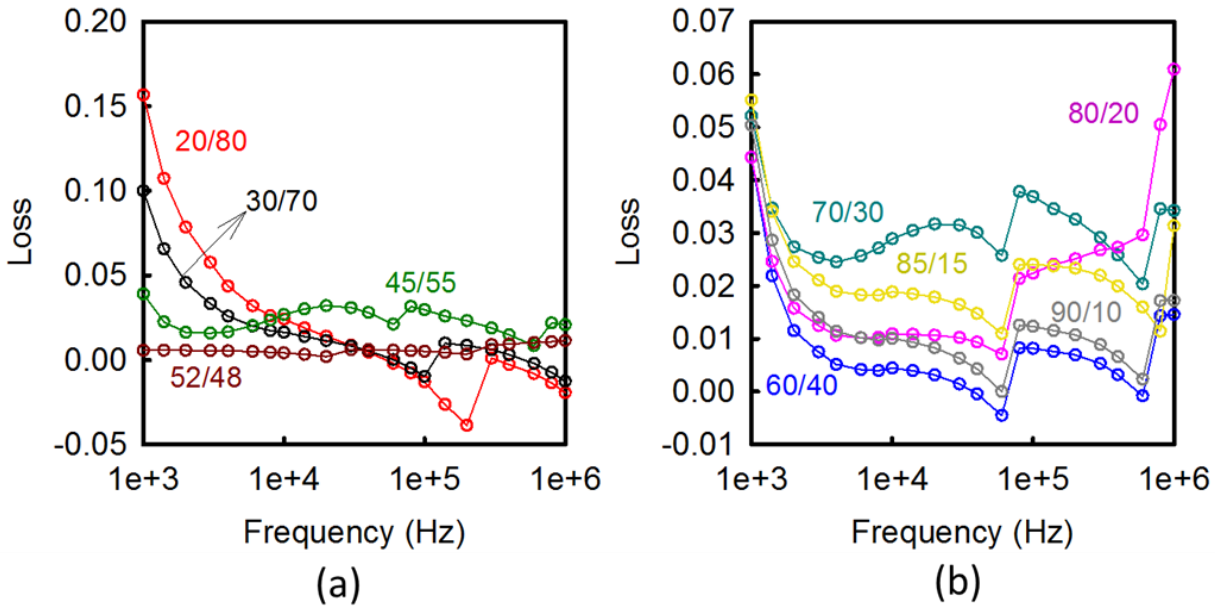

Figure 6.8 Frequency dependence of dielectric loss of the PZT sintered disks with (a) the tetragonal compositions with x = 0.55 – 0.80 and a two phase mixture of tetragonal and rhombohedral phases with x = 0.48 and (b) the rhombohedral compositions with x = 0.10 – 0.40.

Sample	x	1kHz		10kHz		100kHz		1MHz	
		ε	Loss	ε	Loss	ε	Loss	ε	Loss
1	0.00	-	-	-	-	-	-	-	-
2	0.10	308	0.05	236	0.01	230	0.01	225	0.02
3	0.15	299	0.06	248	0.02	239	0.02	228	0.03
4	0.20	340	0.06	283	0.05	249	0.09	222	0.07
5	0.30	342	0.05	301	0.03	283	0.04	268	0.03
6	0.40	327	0.04	277	0.00	273	0.01	267	0.01
7	0.48	656	0.01	650	0.01	643	0.01	629	0.01
8	0.55	381	0.04	331	0.03	311	0.03	299	0.02
9	0.70	237	0.10	188	0.02	184	0.01	180	0.01
10	0.80	190	0.16	112	0.02	107	0.01	105	0.02
11	1.00	-	-	-	-	-	-	-	-

Table 6. 1 Dielectric property of the PZT sintered disks at low electric field.

6.3.1.3 Temperature Dependence Dielectric Properties

In a polycrystalline system, dielectric constant is depending on both intrinsic and extrinsic mechanisms. The intrinsic part is mainly due to the lattice, and it is the average response of the single domains present in the ceramic. The extrinsic contribution is primarily associated with the motion of the domain walls, phase boundaries, and displacement of defects [19]. There have been many earlier attempts with different techniques to investigate the intrinsic and extrinsic contributions to PZT [3, 7, 15, 22, 23]. Among these techniques, the temperature dependence of the piezoelectric and dielectric properties has been used by several authors to separate the extrinsic and intrinsic contributions in the ferroelectrics [19, 22, 23]. Because of the extrinsic mechanisms are mainly attributed from the domain walls and defect dipoles movements, and they are thermally activated. Therefore, the extrinsic mechanisms can be frozen out at very low temperatures. The dielectric constant can be written as a summation of the intrinsic and extrinsic contributions.

$$\varepsilon_{total} = \varepsilon_{in} + \varepsilon_{ex} \qquad \text{Equation 6. 2}$$

where ε_{in} is the intrinsic contribution to the dielectric constant, and ε_{ex} is the extrinsic contribution to the dielectric constant

In this study, the frequency and temperature dependence dielectric constant was measured from 173K to 473K. Unfortunately, the temperature range in this measurement was not low enough to observe pure intrinsic contributed dielectric constant due to the limitation of the equipment. Several authors have been reported the dielectric constant of the PZT ceramic with composition near the MPB is around 350 at low temperature (10K <), and this value is equivalent to the intrinsic contribution and almost invariant with

temperature [3, 7]. The intrinsic contributed dielectric constants of Ti-rich (PZT 40/60) and Zr-rich PZTs (PZT 60/40 and PZT 70/30) were reported 220 and 180, respectively [3].

Fig. 6.9 presents the temperature dependence of (a) dielectric constant and (b) loss for the PZT sintered disks with different compositions (x = 0.30, 0.40, 0.48, 0.55 and 0.70) at 1kHz. The dielectric constants of the PZT sintered disk with the composition at MPB (x = 0.48) and at Zr-rich region (x = 0.30 and 0.40) show stronger temperature dependence than Ti-rich PZT sintered disks (x = 0.55 and 0.70) in this temperature region. Although the precise intrinsic dielectric constant (ε_{in}) cannot be direct measured by our current equipment setup, the estimate intrinsic dielectric constant can be obtained by extrapolating the curves in to 0K (shown in Fig. 6.10). The estimate intrinsic dielectric constants (at 0K) and measured temperature dependence of dielectric constant of the PZT were listed in table 6.2. The estimated intrinsic dielectric constant of the PZT sintered disk at MPB (x = 0.48) is in good agreement with the literature data [3, 7]. However, the estimated intrinsic dielectric constants of the PZT sinter disks with the composition at Zr-rich region (x = 0.30 and 0.40) were slightly lower than literature data. After knowing the intrinsic contribution part to the dielectric constant, the extrinsic contribution part to dielectric constant of the PZT with different compositions then can be determined from Eq. 6.3.

$$\varepsilon_{ex}(\%) = \frac{\varepsilon_{total} - \varepsilon_{in}}{\varepsilon_{total}} \times 100 \qquad \text{Equation 6. 3}$$

The extrinsic contribution to dielectric constant (ε_{ex}) at room temperature as a function of composition was shown in Fig. 6.11. It indicated that the PZT sintered disks with composition at MPB (x = 0.48) and Zr-rich regions (x = 0.30 and 0.40) have more

thermally activated extrinsic mechanisms than the compositions at Ti-rich Region (x = 0.55 and 0.70). There are two possible reasons can be explaining for this. First, the number of spontaneous polarization directions is larger in the rhombohedral phase (8) as compared to the tetragonal phase (6) which means that rhombohedral phase has more non-180 domains than tetragonal phase. Secondly, the higher extrinsic contributions for the rhombohedral phase are due to the smaller spontaneous strains, and it would lead to a higher domain wall mobility [9, 12, 24]. By contrast, the tetragonal phase has much higher spontaneous strain to restrict the domain wall motions. Table 6.3 shows details of the ε_{ex} as a function of composition and temperature. The ε_{ex} increased with rising temperature in every composition, especially in the MPB and Zr-rich regions. The extrinsic contribution part of the PZT sintered disks at the MPB and Zr-rich regions are around 70% in total dielectric constant at 473K, while the extrinsic contribution part of the PZT sintered disks with compositions at Ti-rich region has only 40%.

The temperature dependent dielectric property measurement have utilized the 'freezing out' of the domain wall contribution to dielectric constant at the low temperatures as a means of quantifying the intrinsic and extrinsic contributions to the low field dielectric properties. However, the extrinsic part is very complicated in the PZT system. It involves interactions between ions, domains, and even different phases. Therefore, it is very difficult to analysis and quantifies the factors that affect the extrinsic contributions by only applying the temperature dependent dielectric property measurement. The Rayleigh measurement can be used to separate different types of domain wall motion, which will be discussed in next section.

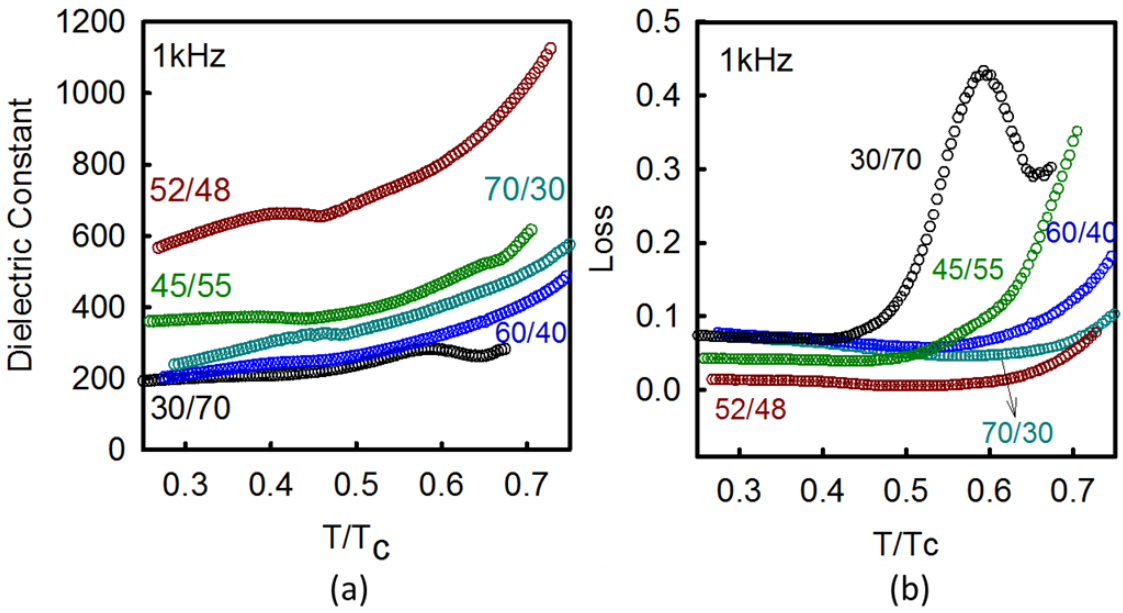

Figure 6.9 Temperature dependence of (a) dielectric constant and (b) loss of the PZT sintered disks with different compositions (x = 0.30, 0.40, 0.48, 0.55 and 0.70) measured at 1kHz.

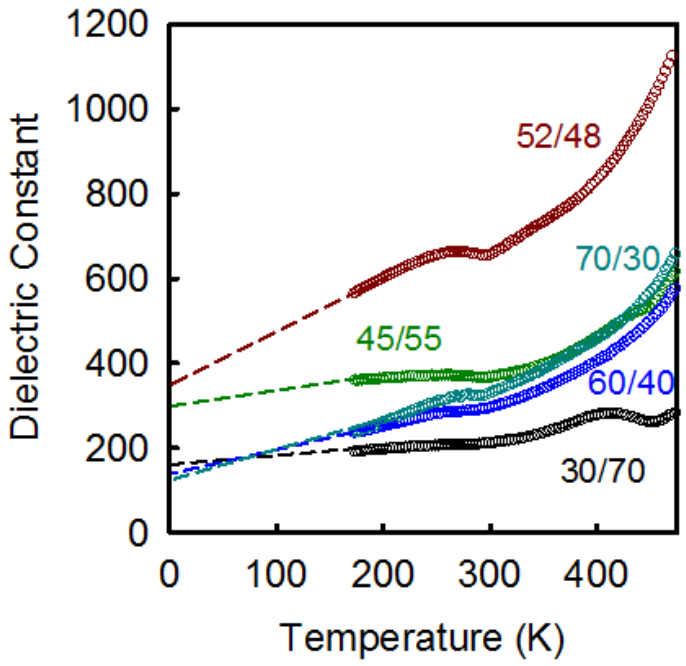

Figure 6. 10 Temperature dependence of dielectric constant of the PZT sintered disks with different compositions (x = 0.30, 0.40, 0.48, 0.55 and 0.70). The intrinsic dielectric constant can be obtained by extrapolating the curves to 0K.

Broad peaks in dielectric constant versus temperature were found to occur at around room 298 K for the compositions near the MPB (x = 0.40, 0.48, 0.55) and the PZT 70/30. This broad peak at the compositions near the MPB could be caused by internal stress field in the PZT ceramic [7] or effected by a possible low temperature monoclinic phase [25]. The broad peak in the PZT 70/30 could be the result of phase transition between two rhombohedral phases (*R3m* and *R3c*).

The dielectric losses start increasing rapidly at 350K for Ti-rich PZTs and at 430K for Zr-rich PZTs. The different activation energies for domain wall motion or defect induced space charge in the tetragonal and rhombohedral samples would possibly account for these high losses [3].

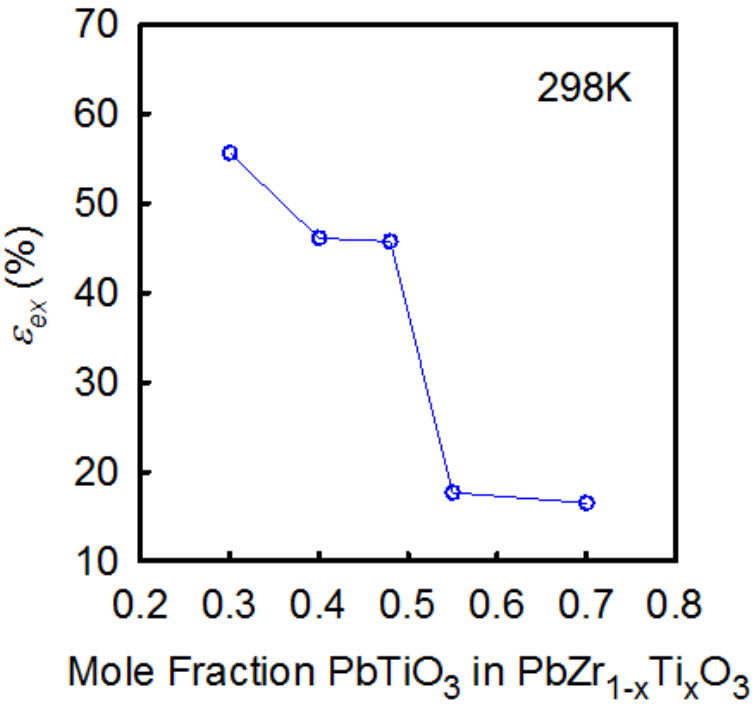

Figure 6.11 The extrinsic contribution to dielectric constant (ε_{ex}) of the PZT sintered disks (x = 0.30, 0.40, 0.48, 0.55 and 0.70) at room temperature.

x	0K	173K	298K	473K
0.70	177	192	212	282
0.55	303	360	368	616
0.48	356	566	656	1125
0.40	159	202	295	575
0.30	146	239	329	658

Table 6. 2 Temperature dependence of dielectric constant of the PZT sintered disks with different composition (x = 0.30, 0.40, 0.48, 0.55 and 0.70) at 1kHz.

x	173K	298K	473K
0.70	7.81	16.51	37.23
0.55	15.83	17.66	50.81
0.48	37.10	45.73	68.36
0.40	21.29	46.10	72.35
0.30	38.91	55.62	77.81

Table 6. 3 The extrinsic contribution to dielectric constant (ε_{ex}) of the PZT sintered disks with different composition (x = 0.30, 0.40, 0.48, 0.55 and 0.70) at 173K, 298K and 473K.

6.3.2 Strong Field Dielectric Properties

6.3.2.1 Frequency Dependence Dielectric Nonlinearities

In Figure 6.12 (a) the dielectric constant of the PZT sintered disk with composition (x = 0.48) was measured as a function of ac electric field at four frequencies ranging from 1 Hz to 1 kHz, and show linear increase with ac field amplitude. This indicates that Rayleigh relation Eq. 1.1 can be applied for dielectric constant versus ac field at every measured frequency. By fitting the data in Fig. 6.12 (a), the reversible (ε_{init}) and irreversible (α) Rayleigh parameters can be obtained as a function of frequency. The fitting results for the whole frequency range were plotted in Fig. 6.12 (b). The reversible and irreversible Rayleigh coefficients decrease linearly with the logarithm of the frequency, and can be fitted with logarithmic frequency dependence, express as [15]

$$\varepsilon_{init} = e_0 - e\ln(\omega) \qquad \text{Equation 6. 4}$$

$$\alpha = a_0 - a\ln(\omega) \qquad \text{Equation 6. 5}$$

where e_0, e, a_0 and a are fitting parameters, ω is equal to 2πf, ε_{in} is intrinsic dielectric constant and α is irreversible Rayleigh coefficient. The resulting parameters are e_0 = 684.68±8.14, e = 21.42±0.25, a_0 = 32.53±0.33 and a = 2.55±0.03 (standard error of 95% confidence). This result indicates that both reversible and irreversible Rayleigh parameters are frequency dependent. The irreversible Rayleigh parameters decreases with increasing frequency are due to some of the domain wall motions cannot keep up with higher frequency.

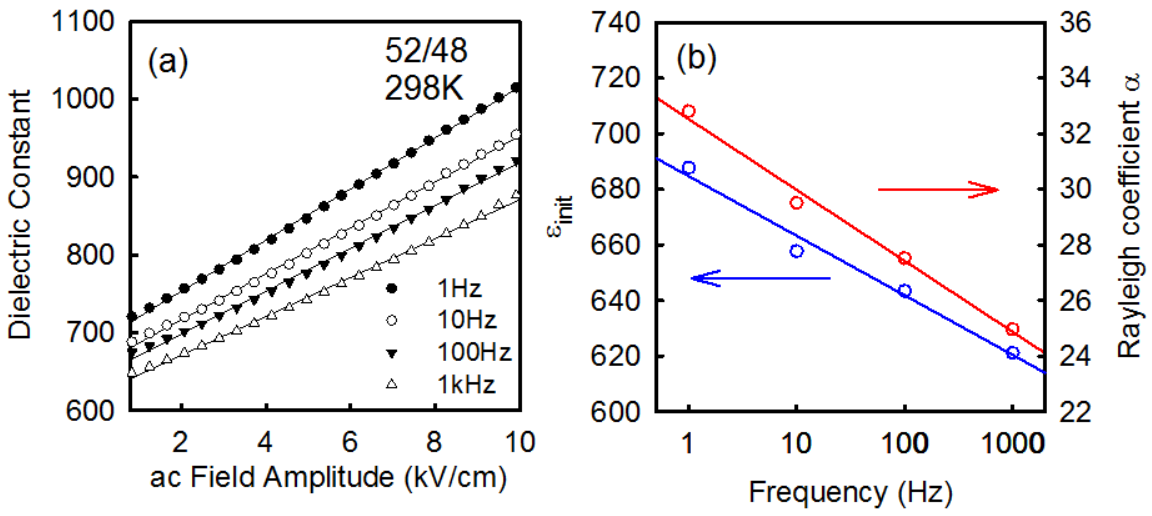

Figure 6.12 (a) Room temperature dielectric constant of PZT sintered disk (x = 0.48) *versus* ac field amplitude under four different frequencies (1 Hz, 10 Hz, 100 Hz, and 1 kHz) (b) Corresponding initial dielectric constant and Rayleigh coefficient *versus* frequency.

6.3.2.2 Composition dependence Rayleigh Coefficient

As shown in chapter 6.3.1.3, the extrinsic mechanisms can be very different between rhombohedral and tetragonal phases. Fig. 6.13 presents the ac field dependence of the dielectric constant of PZT sintered disks with different compositions, and all of them show a linear relationship with field amplitude. Therefore, the Rayleigh relation Eq. 1.3 can be applied for dielectric constant versus ac field at every composition. It is clear that the PZT sintered disks with the composition in the Zr-rich were much more sensitive to the ac field amplitude than the ones at the Ti-rich region. At the Ti-rich region, the extrinsic mechanisms were sensitive to the composition. The extrinsic contributed dielectric constant was decreasing with increased Ti content in tetragonal phase. It is because the higher Ti content leads to larger spontaneous strain at tetragonal phase, and more non-180^{o} domain wall motion would be restricted. In the other hand, the extrinsic

contributed dielectric constants of the PZT sintered disks at Zr-rich region were not composition sensitive due to the spontaneous strains at rhombohedral phase are much smaller.

The Rayleigh coefficient (α) and contribution of extrinsic part to dielectric constant can be obtained by fitting Fig. 6.13. The fitting results were shown in Fig. 6.14 and table 6.4. At Ti-rich region, the α decrease from 25.22 to 1.41 with increased Ti content (x = 0.55 to x = 0.8). At Zr-rich region, the α was less compositional sensitive and vary from 55 to 64. The reasons for rhombohedral phase has much higher extrinsic contribution to dielectric constant were mentioned in the previous section. It was because the rhombohedral phase has more domain directions lead to higher non-180^o domain wall concentration, and it has much less spontaneous strains lead to higher domain wall mobility.

The Rayleigh coefficient of the PZT sintered disks corresponds to their spontaneous strain was shown in the Fig. 6.15. The compositions in the Zr-rich region have lower spontaneous strains, and correspond to higher Rayleigh coefficient. Thus, the Rayleigh coefficient is strongly dependent on the crystal structure and spontaneous strains.

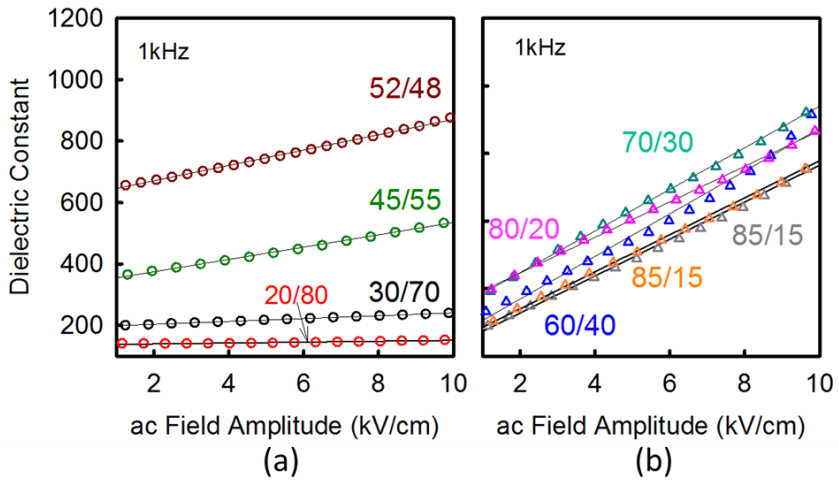

Figure 6.13 ac field dependence of dielectric constant of the PZT sintered disks with (a) the tetragonal compositions with x = 0.55 – 0.80 and a two phase mixture of tetragonal and rhombohedral phases with x = 0.48 and (b) the rhombohedral compositions with x = 0.10 – 0.40.

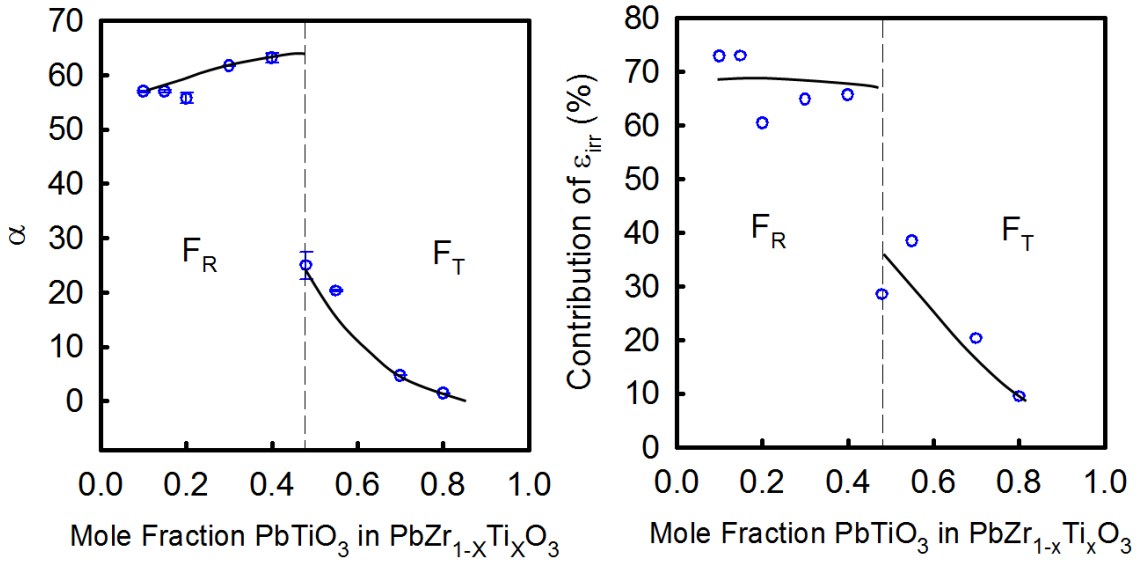

Figure 6.14 (a) Rayleigh coefficients and (b) percentage of irreversible contributed dielectric constant of the PZT sintered disks ($0.10 \leq x \leq 0.80$) at room temperature. The open circles are experimental data. The solid lines are guides to the eye.

Sample	*x*	*α*
1	0.00	-
2	0.10	56.94
3	0.15	56.98
4	0.20	55.69
5	0.30	64.30
6	0.40	60.64
7	0.48	24.97
8	0.55	25.22
9	0.70	4.69
10	0.80	1.41
11	1.00	-

Table 6. 4 Room temperature Rayleigh coefficient of the PZT sintered disks ($0.10 \leq x \leq 0.80$) at 1kHz

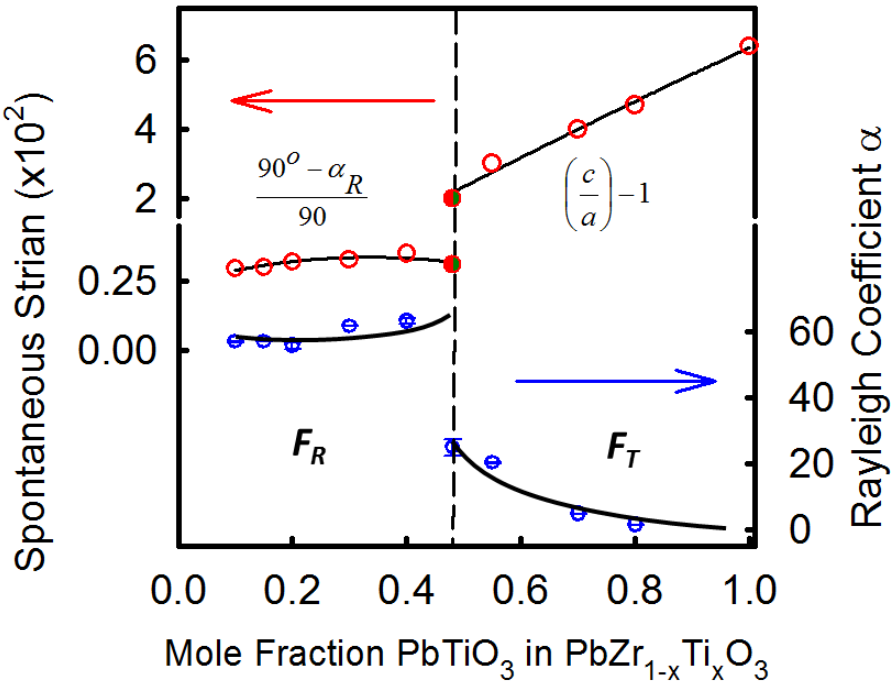

Figure 6.15 The relation between Rayleigh coefficient and spontaneous strain of the PZT sintered disks ($0.10 \leq x \leq 0.80$).

6.3.3 Intrinsic and Extrinsic Contributions to Dielectric Property

The combined results of the dielectric properties at low field and high field provide lots useful information for the investigation of the intrinsic and extrinsic contributions to dielectric properties. The intrinsic dielectric constant can be determined by the temperature dependence of the dielectric properties, and extrinsic contributions at different temperatures can be also obtained. However, the mechanisms of the domain wall motion in the extrinsic contributions to the dielectric properties are complicated. In order to separate different types of domain wall motions, the field dependence of the dielectric properties was carried out.

To combine the results of the temperature and field dependence of dielectric properties, the Eq 6.2 can be first rewritten into Eq. 6.6 and The Eq. 1.1 can be also rewritten into Eq. 6.7. The extrinsic contributions to the dielectric properties are majorly consisted with three parts at room temperature, which are thermally activated reversible domain wall motion, irreversible domain wall motion and defect dipoles.

$$\varepsilon_{total} = \varepsilon_{in} + \varepsilon_{rev} + \varepsilon_{irr} + \varepsilon_{def} \qquad \text{Equation 6. 6}$$

where ε_{total} is the total dielectric permittivity at room temperature, ε_{rev} is reversible domain wall motion contributed dielectric permittivity, ε_{irr} is irreversible domain wall motion contributed dielectric permittivity, and ε_{def} is dielectric permittivity from the defect dipoles.

$$\varepsilon = \varepsilon_{in} + \varepsilon_{rev} + \varepsilon_{def} + \alpha E_0 \qquad \text{Equation 6. 7}$$

The initial dielectric permittivity ε_{init} in Eq. 1.1 was consisted with the intrinsic dielectric permittivity, the reversible domain wall motion contributed dielectric permittivity, and the dielectric permittivity from the defect dipoles. The thermally activated ε_{irr} at zero field and can be obtained by subtracting the Eq. 6.6 to Eq. 6.7. And it gives Eq. 6.8,

$$Thermally\ activated\ \varepsilon_{irr} = \varepsilon - \varepsilon_{33} \qquad \text{Equation 6. 8}$$

The dielectric permittivity attributed from thermally activated irreversible domain wall motion can be determined by the Eq. 6.8. Fig.6.16 shows the ε_{33} is different from the ε_{init}, and the difference between these two is the thermally activated ε_{irr}, and the details of the thermally activated ε_{irr} were listed in table 6.5. The thermally activated ε_{irr} was almost composition independent at room temperature, which was attributed to the total dielectric permittivity around 7.5% in average.

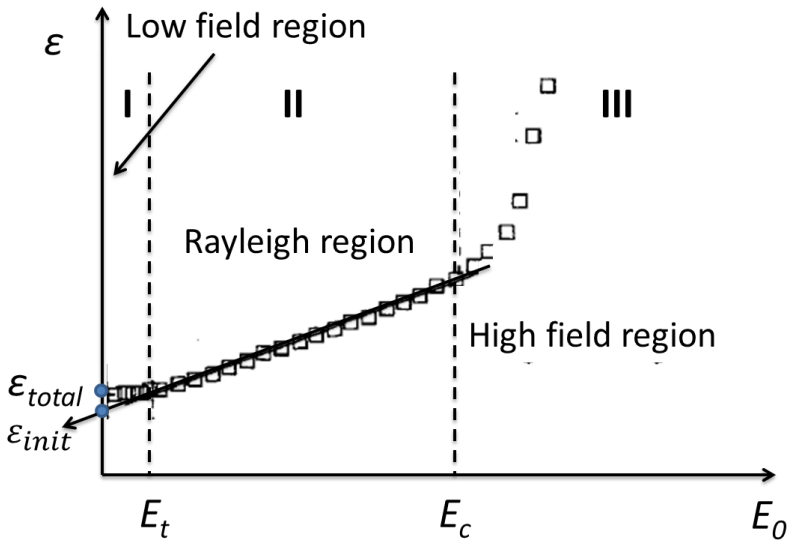

Figure 6.16 The field amplitude dependence of the dielectric permittivity behavior. Adapted from Hall [26].

x	ε_{RT}	ε_{init}	ε_{ex} (%)	Thermal Activated ε_{irr} (%)
0.70	212	194	16.51	8.49
0.55	368	334	17.66	9.24
0.48	656	621	45.73	5.34
0.40	295	269	46.10	8.81
0.30	329	313	55.62	4.86

Table 6. 5 Different contribution mechanisms to the dielectric permittivity of the PZT sintered disks ($0.30 \leq x \leq 0.70$).

6.4 Summary

The dielectric behaviors of the PZT sintered disks were characterized at low and strong field. The observations of temperature, composition, and frequency dependence of the dielectric behavior at low and strong field were listed as follows,

1. Composition and frequency dependence of dielectric constant of the PZT sintered disks has a good agreement with literature data, which indicates the quality of the PZT sintered disks is good.
2. The broad peaks in temperature dependent dielectric constant were observed at room around room temperature. It can be a result of the internal stress relaxation or the existence of a low temperature phase (monoclinic phase for the compositions near the MPB region, and low temperature rhombohedral phase, *R3c*, for the compositions at Zr-rich region).
3. The intrinsic and extrinsic contributions to the dielectric permittivity can be separated from temperature dependence of dielectric behavior measurement. The

PZT sintered disks with compositions at the MPB and Zr-rich regions have more thermally activated extrinsic mechanisms than the ones at the Ti-rich region. First possible reason is the number of spontaneous polarization directions is larger in the rhombohedral phase (8) as compared to the tetragonal phase (6). Secondly, the higher extrinsic contributions for the rhombohedral phase are due to the smaller spontaneous strains, and lead to higher domain wall mobility.

4. The ac field amplitude dependence of the dielectric behavior can be explained by the Rayleigh relation. The reversible (ε_{init}) and irreversible (α) Rayleigh parameters of the PZT were frequency dependent, which decrease linearly with the logarithm of the frequency.
5. The PZT sintered disks with compositions in the Zr-rich region were much more sensitive to the ac field amplitude than in the Ti-rich, which were also having higher extrinsic contributions to the dielectric permittivity. Therefore, the Rayleigh coefficients of the compositions with rhombohedral phase were much higher than the ones that with tetragonal phase.
6. The thermally activated ε_{irr} can be obtained from the combined results of the temperature and ac field amplitude dependence of dielectric behavior, which was composition independent.

6.5 References

1. B. Jaffe, W.R. Cook, and H.L. Jaffe, *Piezoelectric ceramics* 1971, London, New York,: Academic Press. 135.
2. S.A. Mabud, *J Appl Crystallogr* **13**, 211 (1980)
3. Z.Q. Zhuang, M.J. Haun, S.J. Jang, and L.E. Cross, *Ieee T Ultrason Ferr* **36**, 413 (1989)
4. Z.Q. Zhuang, M.J. Haun, J. Jang, and L.E. Cross, *Ieee T Ultrason Ferr* **33**, 827 (1986)
5. M.J. Haun, Z.Q. Zhuang, E. Furman, S.J. Jang, and L.E. Cross, *J Am Ceram Soc* **72**, 1140 (1989)
6. R.E. Eitel, *IEEE International Symposium on Applications of Ferroelectrics*, 319 (2007)
7. Q.M. Zhang, H. Wang, N. Kim, and L.E. Cross, *J Appl Phys* **75**, 454 (1994)
8. D.J. Kim, J.P. Maria, A.I. Kingon, and S.K. Streiffer, *J Appl Phys* **93**, 5568 (2003)
9. A. Pramanick, D. Damjanovic, J.C. Nino, and J.L. Jones, *J Am Ceram Soc* **92**, 2291 (2009)
10. J.E. Garcia, R. Perez, D.A. Ochoa, A. Albareda, M.H. Lente, and J.A. Eiras, *J Appl Phys* **103**, (2008)
11. D.A. Ochoa, J.E. Garcia, R. Perez, and A. Albareda, *Ieee T Ultrason Ferr* **55**, (2008)
12. D. Damjanovic and M. Demartin, *J Phys-Condens Mat* **9**, 4943 (1997)
13. D.A. Hall, *J Mater Sci* **36**, 4575 (2001)
14. D. Damjanovic and M. Demartin, *J Phys D Appl Phys* **29**, 2057 (1996)

15. D.V. Taylor and D. Damjanovic, *J Appl Phys* **82**, 1973 (1997)

16. D.V. Taylor and D. Damjanovic, *Appl Phys Lett* **73**, 2045 (1998)

17. D. Damjanovic, *Rep Prog Phys* **61**, 1267 (1998)

18. V.A. Isupov, *Soviet Physics - Solid States* **12**, 1084 (1970)

19. C.A. Randall, N. Kim, J.P. Kucera, W.W. Cao, and T.R. Shrout, *J Am Ceram Soc* **81**, 677 (1998)

20. M. Takahashi, *Japanese Journal of Applied Physics* **9**, 1236 (1970)

21. S.J. Lee, K.Y. Kang, and S.K. Han, *Appl Phys Lett* **75**, 1784 (1999)

22. X.L. Zhang, Z.X. Chen, L.E. Cross, and W.A. Schulze, *J Mater Sci* **18**, 968 (1983)

23. F. Xu, S. Trolier-McKinstry, W. Ren, B.M. Xu, Z.L. Xie, and K.J. Hemker, *J Appl Phys* **89**, 1336 (2001)

24. A. Pramanick and J.L. Jones, *Ieee T Ultrason Ferr* **56**, 1546 (2009)

25. B. Noheda, D.E. Cox, G. Shirane, R. Guo, B. Jones, and L.E. Cross, *Physical Review B* **63**, 014103 (2000)

26. D.A. Hall and P.J. Stevenson, *Ferroelectrics* **228**, 139 (1999)

CHAPTER 7

ANNEAL EXPERIEMENT

7.1 Introduction

In the last 40 years, the origin of two low temperature phases coexists and near the MPB in the PZT ceramics has been variously attributed to the metastable coexistence [1, 2], to the heterogeneity and/or the composition fluctuation [3, 4], to the thermal fluctuation with a statistical distribution model [5, 6], and to equilibrium coexistence [7-10]. Besides, the coexistence of tetragonal and rhombohedral phases around the MPB could be also affected by internal stress [11, 12]. Among these hypotheses, an equilibrium PZT phase diagram with two-phase regions replacing the line boundaries in the traditional phase diagram was reported by Rossetti *et al.* [9, 10]. This predicted equilibrium phase diagram can be obtained by considering PZT solutions as a regular solution and combines the conventional Landau-Ginzburg-Devonshire (LGD) free energy [13] function with a positive enthalpy of mixing [14]. It also suggests the decomposition occurs by a peritectoid reaction and the miscibility gaps can be extended to the cubic phase with a sufficient value of the atomic exchange interaction parameter. Based on this hypothesis, an equilibrium two-phase coexistence can be achieved with a normal material processing if the diffusional processes are sufficiently fast, and the ratio between two phases is determined by the lever law. Conversely, if diffusion processes are not sufficient fast enough, the ratio between the two ferroelectric phases would vary with different processing conditions and/or cooling rate.

In addition, a large tolerance (±20%) in piezoelectric and dielectric properties of the commercial PZT-based ceramic is usually observed. This, added to the fact that the ratio between two ferroelectric phases at near the MPB is not consistent with all literature data, would lead one to suspect that the PZT ceramics may not able to reach their equilibrium state after sintering at high-temperature and cooled by natural convection. A better understanding of the phase equilibria in the PZT ceramic is not only scientifically interesting, but also technically important. It could provide useful information for the processing, microstructure control, and structure-sensitive properties of PZT solid solutions.

In this work, an unusual annealing approach was used to investigate the influence of thermal history on domain structures and the irreversible domain wall contributions to the dielectric properties of un-doped PZT ceramics. Furthermore, it is of interest to see whether the equilibrium phase mixture can be established by accelerating the diffusional processes by applying a higher temperature at above Curie temperature (Tc) to allow for the atomic redistributions.

This chapter is focused on annealing procedures the PZT ceramics and the conditions of the ceramics after annealing. The lead loss, the phase purity, and grain size of the PZT ceramics will be discussed in this chapter.

7.2 Experimental Procedure

The PZT powders (x = 0.00 and 1.00) and sintered disks (x = 0.10 - 0.80) were obtained after sintering at 1473K for 2 hours (see details in Chapter 3.). The structure,

phase transition behavior, and dielectric property of as-synthesized PZT samples were characterized and shown in previous chapters. PZT powders and sintered disks were then annealing at 923K for 72h, 120h, and 240h in the air. The anneal temperature of the PZT samples was shown in Fig 7.1, the red crosses represent the anneal temperature correspond to the compositions of the PZT powders (x = 0.00 and 1.00) and sintered disks (x = 0.10 - 0.80) in the conventional phase diagram.

It should be noted that several additional anneal temperatures (below and above Curie temperature) were also applied on PZT powders, which were not discussed in this thesis work. If the anneal temperatures were too low, the diffusional process may too low to allow the atomic redistribution necessary to establish the equilibrium phase mixture. Thus, higher anneal temperature is needed to speed up the diffusional process. However, the severe lead loss in the PZT ceramics would occurs if the anneal temperatures were too high (> 1123K). Therefore, to choose a proper anneal temperature was critical in this study.

The properties of the PZT were very sensitive to the processing conditions. The thermal history of the PZT powders (x = 0.00 and 1.00) and sintered disks (x = 0.10 - 0.80) was shown in Fig 7.2. The PZT precursors were carefully pyrolysis, calcined and sintered into dense ceramics, and then were annealed at 923K up to 240 hours. The cooling processes in every step were natural convection cooling.

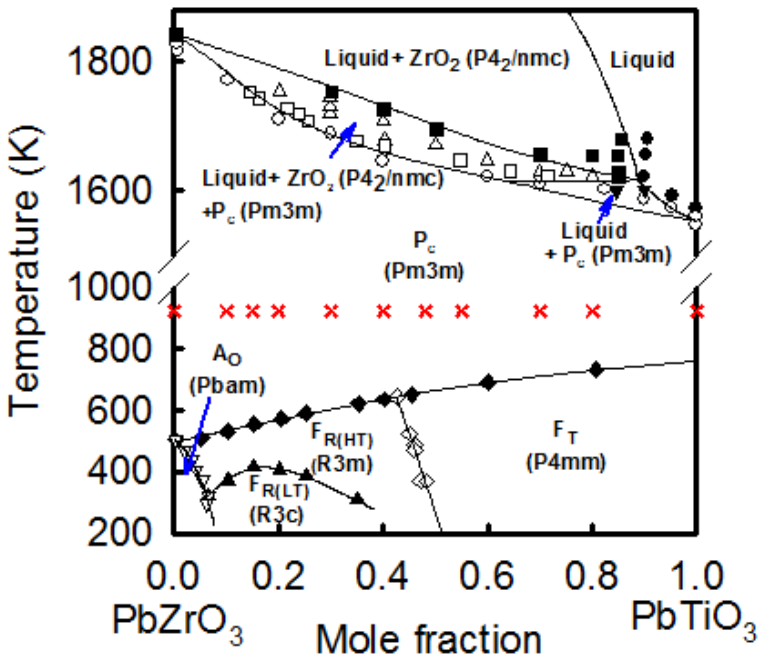

Figure 7.1 The anneal temperature of the PZT powders (x = 0.00 and 1.00) and sintered disks (x = 0.10 - 0.80) (red crosses) was superimposed on the conventional phase diagram.

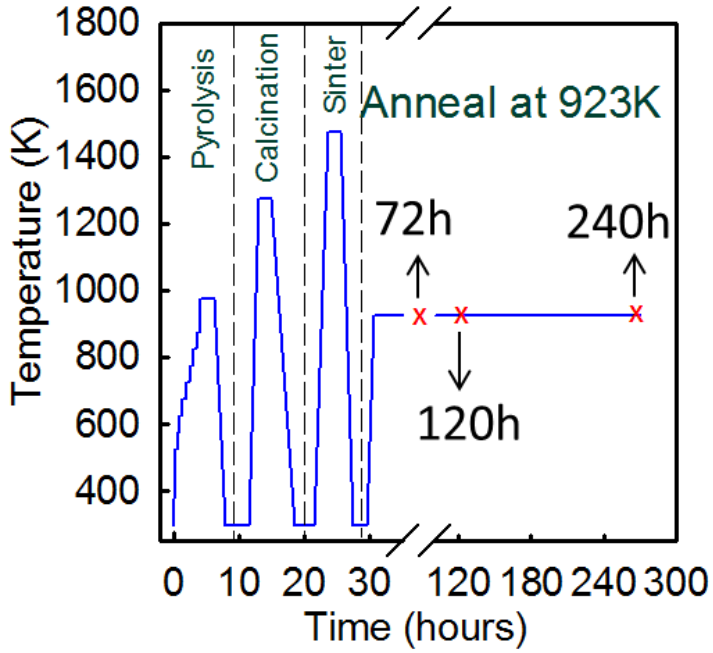

Figure 7.2 The thermal history of the PZT powders (x = 0.00 and 1.00) and sintered disks (x = 0.10 - 0.80) in this study.

7.3 Results and Discussions

7.3.1 Weight Loss Test

One of the major concerns in the anneal process is the lead loss from the PZT ceramics. PZT and other lead containing ferroelectric materials are prone to lead loss. This is due to the high vapor pressure of lead oxide above its melting point. Lead loss in the PZT ceramics will cause compositional non-stoichiometry, which is the primary technical challenge to produce quality piezoceramic PZT products in the industrial field.

The weight loss measurement of the PZT ceramics was used to determine the lead loss level. A Mettler Toledo XP105 analytical balance with 0.01mg readability was used to measure the weight of the annealed samples. The weights of PZT ceramics as a function of anneal time were shown in Fig. 7.3. The weight loss of all PZT ceramics was less than 0.01%. It indicates that there was no lead loss during the annealing process.

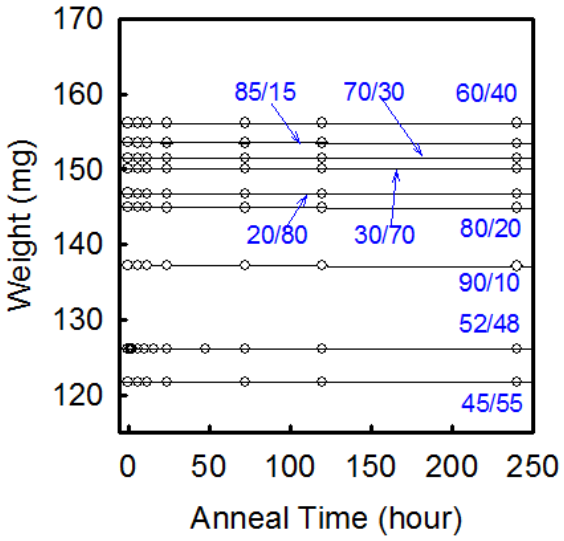

Figure 7.3 The sample weight of the PZT sintered disks (x = 0.10 - 0.80) *versus* anneal time.

7.3.2 Thermal effect on Grain Size of the PZT Sintered Disks

The grain size of PZT ceramics were mainly depends on the compositions and sintering conditions. In general, the grain size of PZT ceramics increases with the increasing sintering temperatures and sintering time, from submicron to about 10 μm [15, 16]. There were several reports indicate the properties of the PZT ceramics were depend on the grain sizes. However, compare to the mechanical property and piezoelectric property, the dielectric property of the unpoled PZT ceramic lightly dependent on the grain size within submicron region at room temperature [16, 17].

The grain sizes of the PZT sintered disks (x = 0.10 - 0.80) before annealing and after annealing at 923 K for 240 hours were listed in the table 7.1. The results show that the PZT ceramics were almost independent with anneal time. The grain sizes were stayed in the similar size after annealing at 923K for 240 hours. Surface SEM images of the annealed PZT 52/48 sintered disks are shown in Fig. 11. The surface shows a dense morphology without obvious grain growth as a function of annealing time, and the average grain size of each specimen is around 1.5μm with a standard deviation of 0.7μm.

x	Anneal Time		STDV
	0	240	
0.10	1.01	1.04	0.10
0.15	1.02	1.09	0.25
0.20	3.10	3.04	0.57
0.30	1.29	1.34	0.19
0.40	3.27	3.19	0.52
0.48	1.46	1.53	0.70
0.55	3.48	3.56	0.63
0.70	3.64	3.89	1.10
0.80	4.83	4.64	0.66

Table 7. 1 The grains size of the PZT sintered disks (x = 0.10 - 0.80) before annealing and after annealing at 923 K for 240 hours.

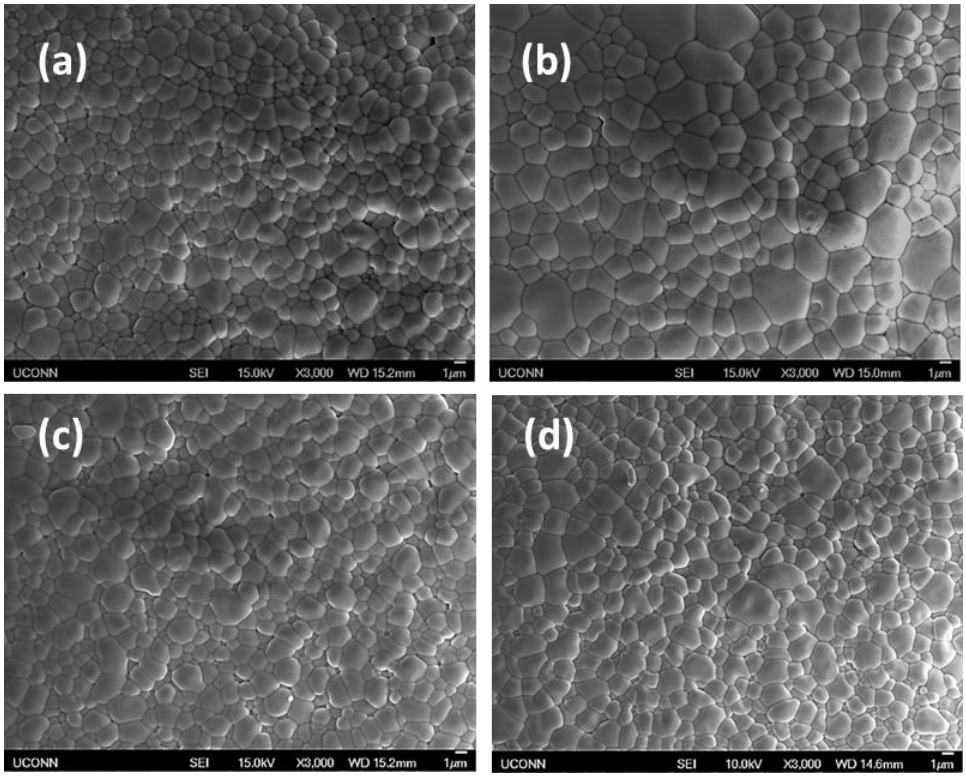

Figure 7.4. Surface SEM images of the PZT 52/48 sintered disks annealed at 923K for 0, 72, 120, and 240 hours.

7.3.3 Thermal Effect on the Phase Purity of the PZT Sintered Disks

The phase purity of the annealed PZT sintered disks was characterized by XRD. The details of XRD measurement were mentioned in the chapter 3. Fig. 7.5 shows the XRD patterns of the PZT sintered disks (x = 0.10 - 0.80), which were annealed at 923K for 240 hours. After annealing at 923K for 240 hours, the XRD patterns show no pyrochlore structure at any composition. It indicates that the PZT ceramics remain compositional stoichiometry and no lead loss during the anneal process. Structures of the PZT sintered disks with compositions at the Ti-rich region (x = 0.80 to x = 0.55) remain a pure ferroelectric tetragonal phase (F_T), and the ones at the Zr-rich region (x = 0.60 to x =

0.10) also remain a pure ferroelectric rhombohedral phase (F_R). The XRD patterns of as-synthesized and annealed PZT 52/48 sintered disks were shown in Fig. 7.6. There was also no pyrochlore phase appear in both as-synthesized and annealed sintered disks. The XRD patterns of the PZT 52/48 sintered disks as a function of anneal time were shown in Fig 7.6 (b). Two phase coexistence at the composition x = 0.52 which is near the MPB, and the volume ratio of these two phase was different with non-annealed sintered disks. The details of the thermal effect on the phase coexistence will be discussed in the next chapter.

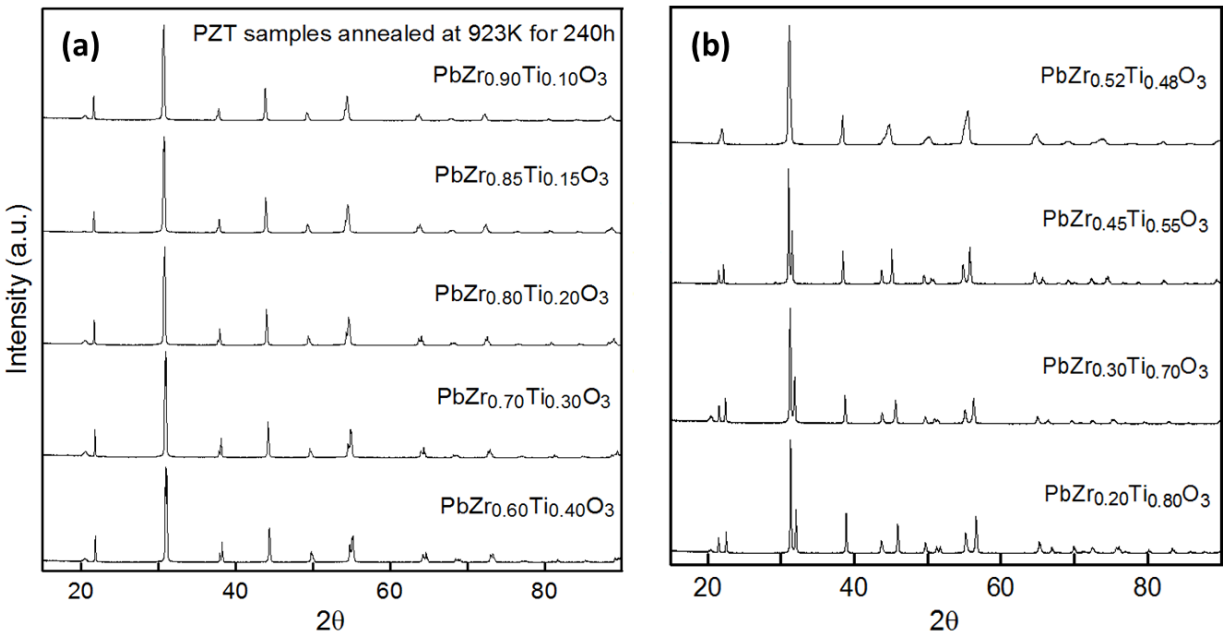

Figure 7.5. XRD patterns of the 240h-annealed PZT sintered disks with varying composition (x) showing (a) the rhombohedral compositions with x = 0.10 – 0.40 and (b) the tetragonal compositions with x = 0.55 – 0.80 and a two phase mixture of tetragonal and rhombohedral phases with x = 0.48.

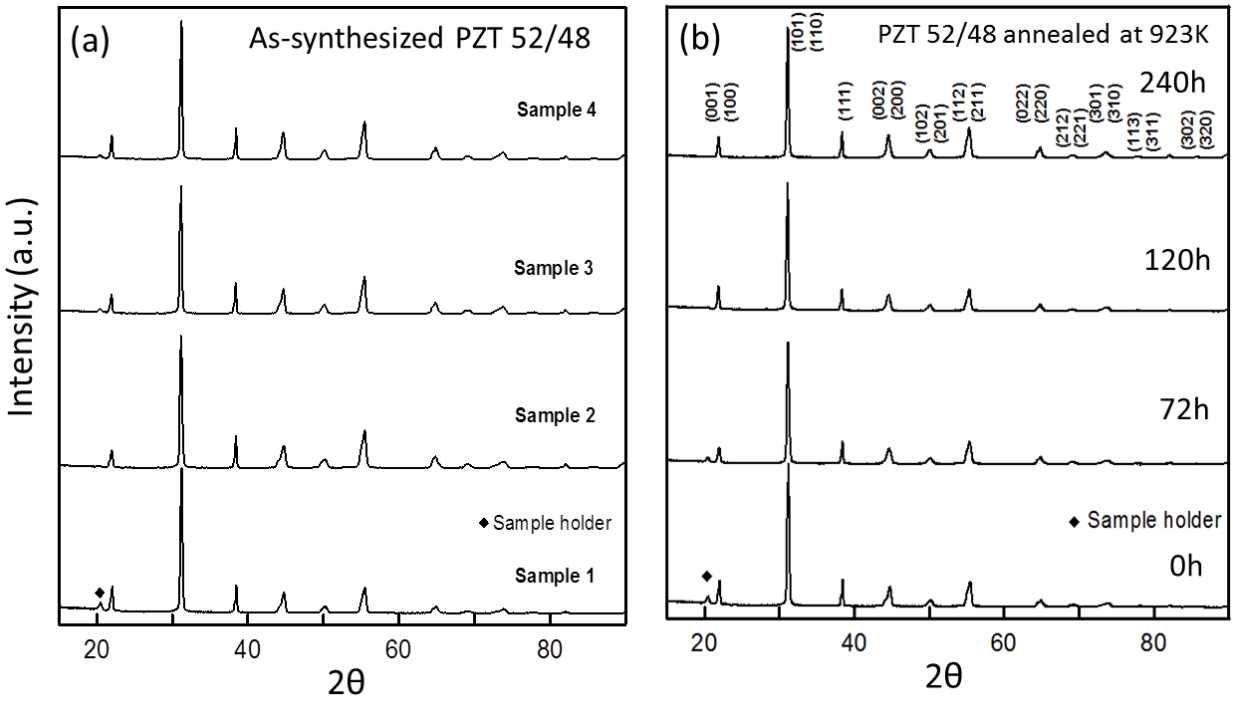

Figure 7.6. XRD patterns of the PZT 52/48 sintered disks (a) before and (b) after annealing at 923K for 240 hours.

7.4 Summary

The anneal process for the PZT powders (x = 0.00 and 1.00) and sintered disks (x = 0.10 - 0.80) in this thesis work was described. Also, the weight loss, grain size, and phase purity of the annealed PZT sintered disks (x = 0.10 - 0.80) were discussed in this chapter. The results of the weight loss test show that no lead loss during the anneal process. The grain sizes of the PZT sintered disks (x = 0.10 - 0.80) were not changed much after annealing at 923K for 240 hours. There was no pyrochlore phase appear after the long anneal process (240 hours), it indicates that the annealed PZT ceramics were still compositional stoichiometry.

7.5 References

1. V.A. Isupov, *Soviet Physics - Solid States* **19**, 783 (1977)
2. V.A. Isupov, *Physics of the Solid State* **43**, 2262 (2001)
3. K. Kakegawa, J. Mohri, T. Takahashi, H. Yamamura, and S. Shirasaki, *Solid State Commun* **24**, 769 (1977)
4. W. Wersing, *Ferroelectrics* **7**, (1974)
5. W. Cao and L.E. Cross, *J Appl Phys* **73**, 3250 (1993)
6. W.W. Cao and L.E. Cross, *Physical Review B* **47**, 4825 (1993)
7. P. Ari-gur and L. Benguigui, *Solid State Commun* **15**, 1077 (1974)
8. A. Barbulescu, E. Barbulescu, and D. Barb, *Ferroelectrics* **47**, 221 (1983)
9. G.A. Rossetti, W. Zhang, and A.G. Khachaturyan, *Appl Phys Lett* **88**, 072912 (2006)
10. G.A. Rossetti, A.G. Khachaturyan, G. Akcay, and Y. Ni, *J Appl Phys* **103**, 114113 (2008)
11. V.A. Isupov, *Soviet Physics - Solid States* **22**, 172 (1980)
12. T. Kala, *Phys Status Solidi A* **78**, (1983)
13. A.F. Devonshire, *Phil. Mag.* **42**, 1065 (1951)
14. M.V. Rane, A. Navrotsky, and G.A. Rossetti, *J Solid State Chem* **161**, 402 (2001)
15. G. Arlt, *Ferroelectrics* **104**, 217 (1990)
16. C.A. Randall, N. Kim, J.P. Kucera, W.W. Cao, and T.R. Shrout, *J Am Ceram Soc* **81**, 677 (1998)
17. Martiren.Ht and J.C. Burfoot, *J Phys C Solid State* **7**, 3182 (1974)

CHAPTER 8

INFLUENCE OF THERMAL HISTORY ON STRUCTURAL PROPERTY AND PARAELECTRIC TO FERROELECTRIC PHASE TRANSITION

8.1 Introduction

The morphotropic phase boundary (MPB) is a nearly vertical line in the traditional temperature-composition phase diagram [1], which separates the tetragonal F_T and the rhombohedral F_R ferroelectric phases. It was assumed the diffusional process is not fast enough to allow atomic redistribution to reach establish equilibrium with two-phase mixtures of rhombohedral and tetragonal phases at compositions located near the MPB [2, 3]. However, this boundary line should be replaced by a two-phase coexistence region otherwise it violets the Gibbs phase rule [4, 5]. In fact, the experimental observations commonly show the two-phase coexistence near at the MPB. The origin and width of the phase coexistence have been the topics of many investigations and remain subjects of debate [3, 5-10]. Besides the unclear issues with two-phase coexistence, a new intermediate monoclinic phase was reported by Noheda *et al.* [11]. This monoclinic phase not only renews the research interests in the PZT phase diagram, but also made the structures near at MPB complicated even more.

Many different hypotheses for two-phase coexistence were proposed in the past 40 years. These were diffusionless [1], metastable coexistence [7, 12-14], heterogeneity (composition fluctuation) [8, 15, 16], thermal fluctuation (statistical distribution model) [9, 10], and equilibrium coexistence [4, 5]. Among these hypotheses, Rossetti *et al.* predicts equilibrium (diffusional) PZT phase diagram with two-phase regions replacing

the line boundaries [4, 5]. This predicted equilibrium phase diagram can be obtained by considering PZT solutions as a regular solution and combines the conventional Landau-Ginzburg-Devonshire (LGD) free energy function with a positive enthalpy of mixing [17]. It also suggests the decomposition occurs by a peritectoid reaction and the miscibility gaps can be extended to the cubic phase with a sufficient value of the atomic exchange interaction parameter. The Diffusional processes are estimated to be sufficiently fast to achieve two-phase equilibria with a normal material processing. Later, a computer simulation of coherent domain structures of phase decomposition in PZT near MPB was proposed by Rao *et al.* [18]. This model was based on the equilibrium phase diagram and takes into account the coherency strain energy and electrostatic energy. It exhibits the domain morphologies with different phase decomposition stages in the PZT. If this equilibrium phase diagram is valid, then the structure and the properties of the PZT near at the MPB can be controlled by manipulating the process conditions.

The conditions of the PZT ceramic processing are extremely commercially important. The ferroelectric properties of the PZT can vary over a wide range of values with different processing conditions. In this chapter, the long anneal process was applied to accelerate the diffusional process to reach the phase equilibrium in the PZT system. It was also used to determine the influence of thermal history on the structure, microstructure and domain structure. To have a better understanding of the influence of the thermal history on the structures is essential for strategic processing of new and improved materials.

8.2 Experimental Procedure

The PZT ceramics were obtained after sintered at 1473 K for 2 hours. The processing details were described in chapter 3. The as-synthesized ceramics were then annealed at 923K for 72h, 120h, and 240h in air. The structure properties of the annealed ceramics were characterized by XRD measurement. The domain structure as a function of anneal time was carried out by TEM. The details of the characterization methods have been described in chapter 4.

8.3 Results and Discussions

8.3.1 Influence of Thermal History on Structure

The structural properties of un-annealed PZT powders (x = 0.00, 1.00) and sintered disks ($0.10 \leq x \leq 0.80$) were carefully characterized and discussed in chapter 4. In this chapter, four structural properties of annealed PZT ceramics will be comparing to those of as synthesized PZT samples. These are the influence of thermal history on the lattice parameters, ferroelectric elastic strain, phase coexistence, and peak width of the PZT. The results of annealed ceramics will be discussed in following sections.

The characterization techniques and data acquisition methods were mentioned in the chapter 4. Weight loss test, phase purity, and grain size of the annealed samples have been discussed in the previous chapter. These measurements show that there were no lead loss nor pyrochlore phase exist in the annealed samples.

8.3.1.1 Influence of Thermal History on Lattice Parameters

The lattice constant and the unit cell volume of PZT sintered disks ($0.10 \leq x \leq 0.80$) as functions of anneal time and composition were shown in Fig. 8.1. The results show that both the lattice constant and the unit cell volume of the annealed PZT sintered disks decrease with the anneal time. The red, dark cyan and orange circles in the Fig. 8.1 correspond to the lattice constants of PZT sintered disks after annealing for 72h, 120h and 240h. All lattice parameters show a marked decrease after annealing at 923K for 120h except for the PZT sintered disks with composition $x = 0.10$. It should be noted that the tetragonal phase of the PZT sintered disks with composition $x = 0.48$ became more difficult to resolve after annealing at 923K for 120h. Therefore, the lattice parameters of tetragonal phase were not able to obtain and to show in the Fig. 8.1(a). The changes in unit cell volume *versus* composition for the 120h- and 240h-annealed PZT sintered disks were shown in the Fig. 8.2. After annealing 240 hours, the change in volume of the PZT sintered disks with compositions near at MPB ($x = 0.30$ - 0.70) decrease around 0.6%. The level of volume decreasing became smaller with the compositions toward to two end members (~0.2%). The detail of the lattice parameters were listed in table 8.1 8.2 and 8.3.

There are two possible reasons for these dimensional changes. The first reason is the relaxation of the internal stress in the ceramic[19]. This internal stress relaxation could be caused by removing the oxygen vacancies at grain boundaries and lower the elastic energy. Result in change of the ratio of two different phases (*R3m/P4mm*, or F_R/F_T) and lower the number of domain walls. Indeed, the spontaneous strain of the annealed PZT sintered disks also show an increase with anneal time. This will be discussed in the next section. Another less likely reason is the composition changes with annealing time,

which is usually observed when the heat treatment is above 1073K. This composition change will accompany with the change in lattice parameters. The composition change in the PZT ceramics with anneal time is not very likely in this study. It is because the anneal temperature is 923K, which is almost 200K lower than the start temperature of PbO evaporation. Also, the weight loss measurement shows no evidence of lead loss during the anneal process.

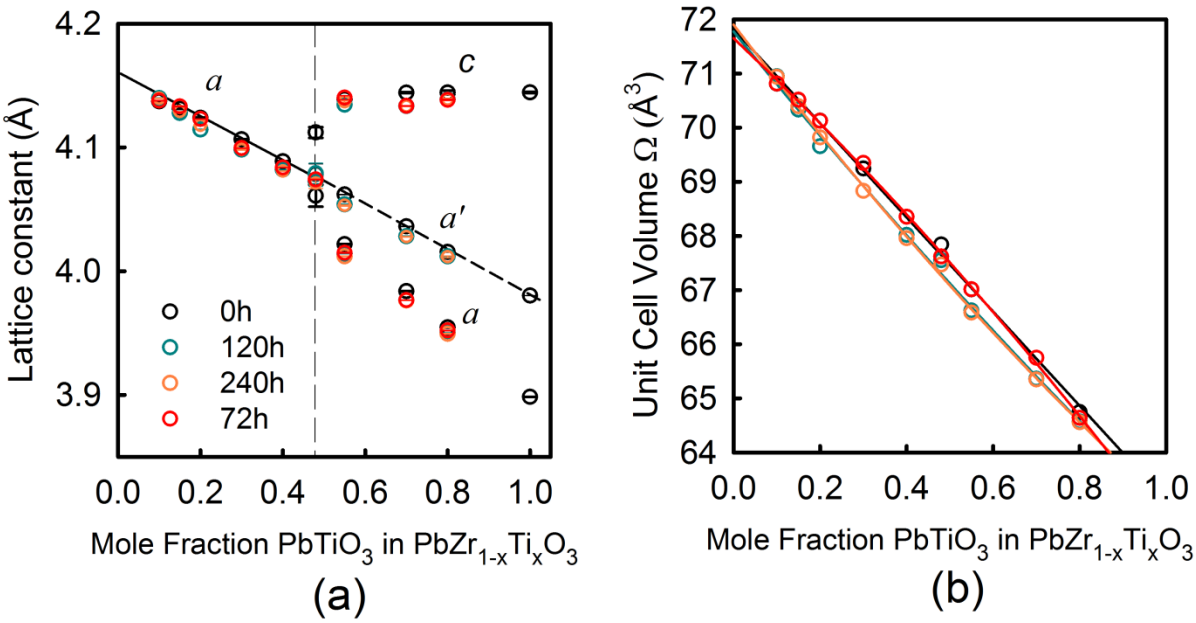

Figure 8.1 (a) Lattice constant and (b) unit cell volume of PZT sintered disks ($0.10 \leq x \leq 0.80$) as a function of anneal time (black circles: as synthesized, red circles: 72h dark cyan circles: 120h, and orange circles: 240h).

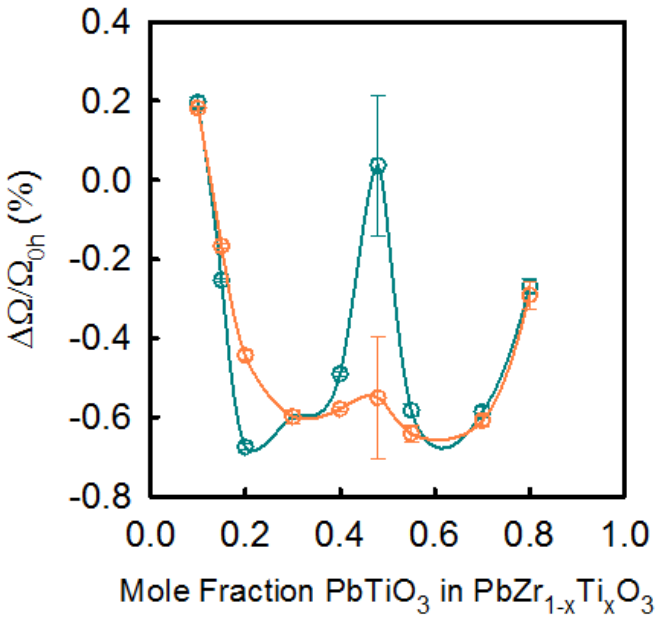

Figure 8.2. The changes in unit cell volume *versus* composition for the 120h- and 240h-annealed PZT sintered disks.

8.3.1.2 Influence of Thermal History on Spontaneous Strain

Composition and anneal time dependent of the lattice distortions of PZT sintered disks with tetragonal ($0.55 \leq x \leq 0.80$) and rhombohedral ($0.10 \leq x \leq 0.40$) compositions were shown in Fig. 8.3(a) and 8.3(b), respectively. There were not much change with anneal time in tetragonal distortions (*c/a*) of the ceramics with tetragonal phase. Only about 0.1% increase was observed in the PZT 45/55, which is close to the MPB region. Among the ceramics with rhombohedral phase, the lattice distortions increase around 5% with anneal time for the PZT sintered disks with compositions near at the MPB region. For those compositions away from the MPB region (x = 0.48 and x = 0.40), there were nearly no change in lattice distortion. The result indicates that the lattice distortion is more sensitive to thermal history for those compositions near at MPB region.

The spontaneous strains of the PZT sintered disks ($0.10 \leq x \leq 0.80$) as a function of anneal time were shown in the Fig. 8.4, which were determined by the lattice distortion of the samples. In order to have a better view of all the compositions, the spontaneous strains of the sintered disks of PZT with the compositions $x = 0.48$ and $x = 0.40$ (red symbols) were shifted 0.05 and 0.01, respectively. It is clear that the spontaneous strains were increased for the compositions near at the MPB region ($x = 0.40$, 0.48 and 0.55). More internal stress was relaxed after the long anneal process, especially in those compositions near at the MPB. The higher level of stress relaxation at MPB region is due to the fact that the high domain wall density at near the MPB, which is a distorted area in the crystal structure. The domains are generated during a structural phase transition (paraelectric to ferroelectric phase transition) to minimize the total free energy. When elastic energy was relieved by anneal process, the domain formation would favor to the rhombohedral phase. Because less distorted area was formed by elastic energy, and less tetragonal domain with high spontaneous strain was needed to compensate the distorted area. Hence, the spontaneous strains increased the most with anneal time at near the MPB.

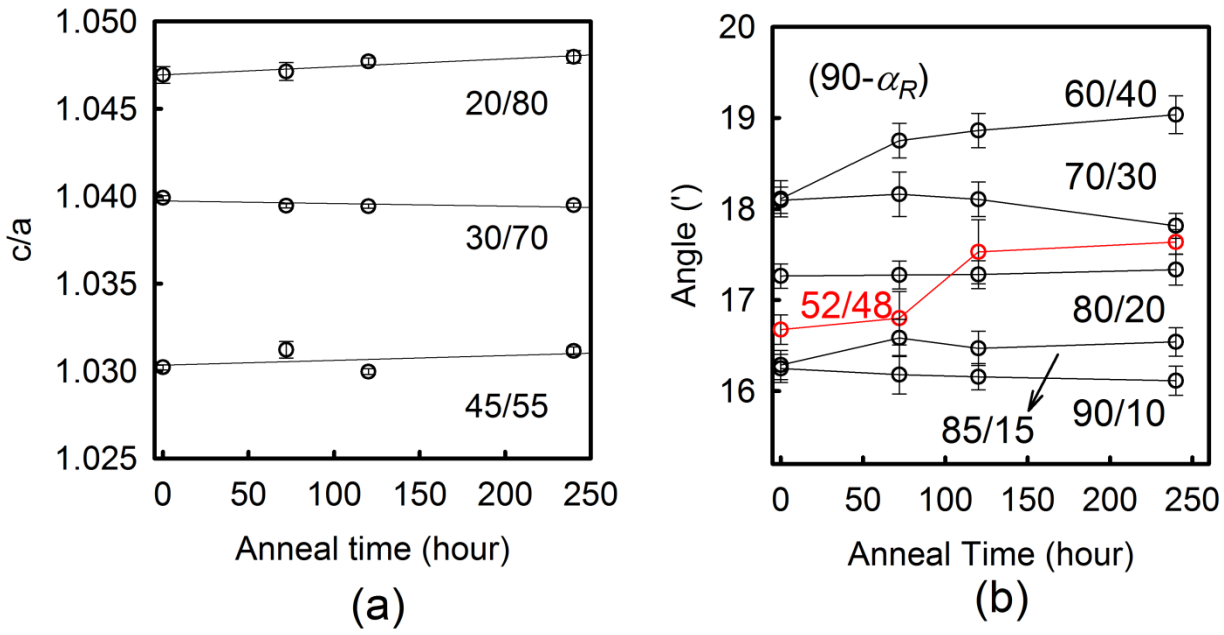

Figure 8.3. (a) Tetragonal distortion (c/a) and (b) rhombohedral distortion (90-α_R) of the PZT sintered disks ($0.10 \leq x \leq 0.80$) as a function of anneal time.

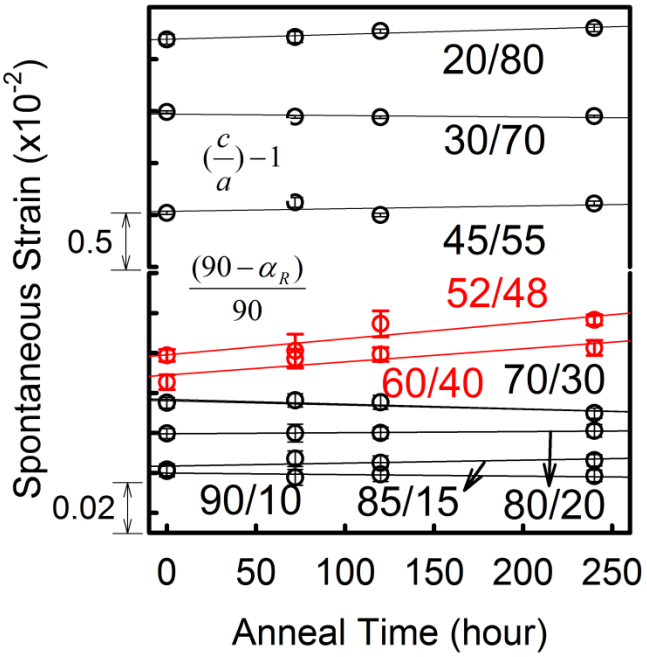

Figure 8.4. Spontaneous strains of the PZT sintered disks ($0.10 \leq x \leq 0.80$) as a function of anneal time.

Sample	*x*	*a(Å)*	α_R	*a (Å)*	*c (Å)*	*c/a*	*(c/a)-1*	$(90-\alpha_R)/90$
1	0.00	-	-	-	-	-	-	-
2	0.10	4.13(8)	89.72	-	-	-	-	0.003
3	0.15	4.13(3)	89.72	-	-	-	-	0.0031
4	0.20	4.12(3)	89.71	-	-	-	-	0.0032
5	0.30	4.09(8)	89.70	-	-	-	-	0.0033
6	0.40	4.08(4)	89.69	-	-	-	-	0.0035
7	0.48	4.07(4)	89.72	4.06(1)	4.11(2)	1.01	0.01	0.0031
8	0.55	-	-	4.01(5)	4.14(0)	1.03	0.03	-
9	0.70	-	-	3.97(67)	4.13(3)	1.04	0.04	-
10	0.80	-	-	3.95(2)	4.13(8)	1.05	0.05	-
11	1.00	-	-	-	-	-	-	-

Table 8. 1 Lattice parameters and spontaneous strains of the 72h-annealed PZT sintered disks ($0.10 \leq x \leq 0.80$).

Sample	*x*	*a(Å)*	α_R	*a (Å)*	*c (Å)*	*c/a*	*(c/a)-1*	$(90-\alpha_R)/90$
1	0.00	-	-	-	-	-		-
2	0.10	4.14(0)	89.73	-	-	-		0.0030
3	0.15	4.12(8)	89.73	-	-	-		0.0031
4	0.20	4.11(3)	89.71	-	-	-		0.0032
5	0.30	4.09(8)	89.70	-	-	-		0.0033
6	0.40	4.08(1)	89.69	-	-	-		0.0035
7	0.48	4.07(9)	89.71	4.06(1)	4.11(2)	1.02	0.020	0.0031
8	0.55	-	-	4.01(4)	4.13(4)	1.03	0.030	-
9	0.70	-	-	3.97(7)	4.13(3)	1.04	0.039	-
10	0.80	-	-	3.95(1)	4.13(9)	1.05	0.047	-
11	1.00	-	-	-	-	-	-	-

Table 8. 2 Lattice parameters and spontaneous strains of the 120h-annealed PZT sintered disks ($0.10 \leq x \leq 0.80$).

Sample	*x*	*a(Å)*	α_R	*a (Å)*	*c (Å)*	*c/a*	*(c/a)-1*	$(90-\alpha_R)/90$
1	0.00	-	-	-	-	-	-	-
2	0.10	4.12(9)	89.73	-	-	-	-	0.0030
3	0.15	4.12(9)	89.72	-	-	-	-	0.0030
4	0.20	4.11(8)	89.73	-	-	-	-	0.0032
5	0.30	4.09(8)	89.70	-	-	-	-	0.0033
6	0.40	4.08(1)	89.68	-	-	-	-	0.0035
7	0.48	4.07(1)	89.74	-	-	-	-	0.0033
8	0.55	-	-	4.01(2)	4.13(7)	1.03	0.031	-
9	0.70	-	-	3.97(6)	4.13(3)	1.04	0.040	-
10	0.80	-	-	3.94(9)	4.13(9)	1.05	0.048	-
11	1.00	-	-	-	-	-	-	-

Table 8. 3 Lattice parameters and spontaneous strains of the 240h-annealed PZT sintered disks ($0.10 \leq x \leq 0.80$).

8.3.1.3 Influence of Thermal History on Phase Coexistence at MPB

Among the un-annealed PZT sintered disks, two-phase coexistence of tetragonal and rhombohedral phases was observed in the composition of x = 0.48. This was discussed in the chapter 4. XRD {200} reflections of the PZT 52/48 as a function of anneal time were shown in Fig 8.5. It is clear that the {200} reflections of un-annealed sample (0h) shows an evidence of two phase coexistence. Green and red lines represent the peak fitting results for the tetragonal and rhombohedral phases, respectively. As the anneal time increased, the shoulder that contributed from $(002)_T$ reflection disappear gradually. After annealing for 120 hours, the shoulder was very difficult to recognize. The diffraction result shows that the volume fraction between two phases was obviously changed by the long anneal process. The volume fraction of F_R phase (I_R / I_T + I_R) was around 50% and increase with anneal time. It also indicates that the annealing process

was able to influence the volume fraction between two phases. This volume fraction between two phases changed by long anneal process was never reported in the literature.

The influence of anneal process on unit cell volume and spontaneous strain of the PZT 52/48 was shown in Fig 8.6. It shows that a decrease in the unit cell volume, and an increase in the spontaneous strain with anneal time. This indicates that the internal stresses were relieved during the annealing process, which leads to decrease the distorted area in the crystal. The volume fraction of F_R phase increases with anneal time was due to the spontaneous strain of rhombohedral phase is much smaller than the tetragonal phase. Therefore, the system tend to increase the volume fraction of the rhombohedral phase

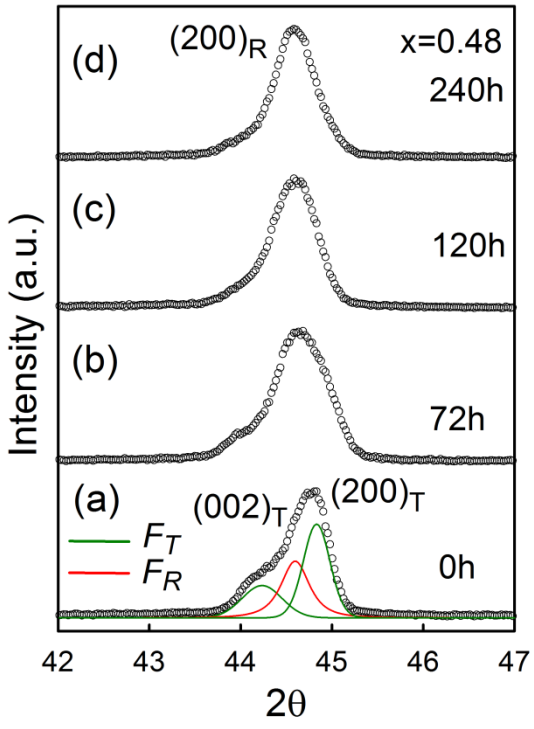

Figure 8.5. XRD {200} reflections of the PZT sintered disks with composition x = 0.48 *versus* anneal time.

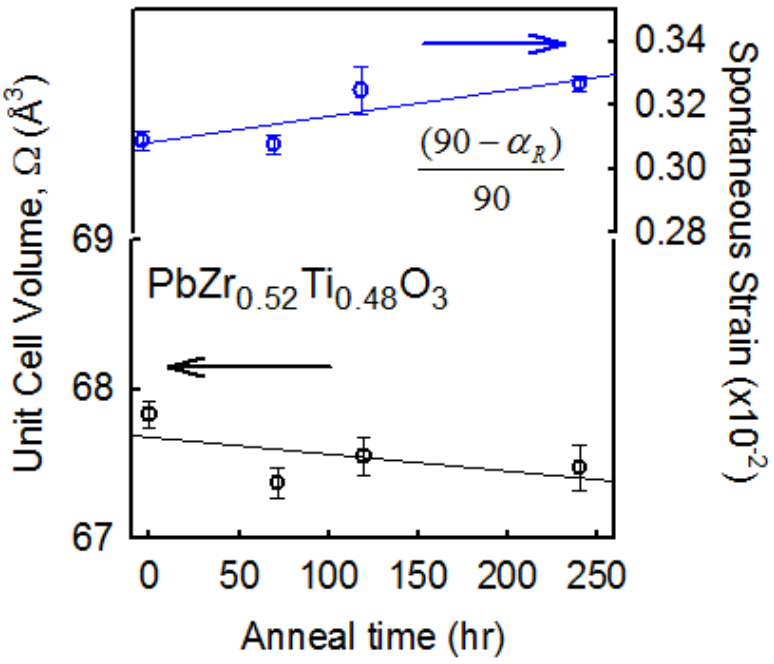

Figure 8.6. The unit cell volume (black circles) and spontaneous strain (blue circles) of the PZT sintered disks with composition $x = 0.48$ *versus* anneal time.

8.3.1.4 Influence of Thermal History on Peak Width

The peak widths of the PZT sintered disks with tetragonal compositions ($0.55 \leq x \leq 0.80$) were shown in Fig. 8.7. The peak widths of both (002) and (200) reflections of the PZT 20/80 and the PZT 45/55 decrease with anneal time, while it remained almost the same in the PZT 30/70. The (200) peak widths of the PZT sintered disks with rhombohedral compositions ($0.10 \leq x \leq 0.40$) as a function of anneal time were shown in Fig. 8.8. The peak width of the PZT 52/48 was increased with anneal time, and the peak widths of the other compositions were decreased with anneal time (except $x = 0.10$). The results show that the peak widths of most compositions were decreased after annealing process, except the PZT 52/48. The peak widths of the PZT 52/48 show a clear increase

with anneal time, and it can be caused by the phase decomposition or the stress-induced phase transformation. On the other hand, this result may be misinterpreted because the reflection peak of the PZT 52/48 after 120 hours was a broaden peak. It was not able to use two phases (three peaks) to do the peak fitting, only one rhombohedral phase (one peak) was applied to fit this broaden reflection.

As mentioned in the chapter 4, peak width of a XRD reflection is mainly affected by instrumental peak profile, crystallite size, domain size, different kind of micro-strains, and temperature. The peak profile of each sample was acquired under same condition, and the grain size of each composition was not change with anneal time. Therefore, the change in the peak width reveals the stress relaxation in the ceramic. The decrease in the peak width indicates that the non-uniform micro-strains in PZT ceramics were decreasing with the anneal time, and made the reflections became sharper. This stress relief can be cause by removing oxygen vacancies from the grain boundaries, reducing the distorted domain wall area, and the phase decomposition by the long annealing process. Consistent to the change in the structural properties (unit cell volume, spontaneous strains, and volume fraction of two ferroelectric phases), the results of peak widths indicate that a slow stress relaxation occurred during the annealing process.

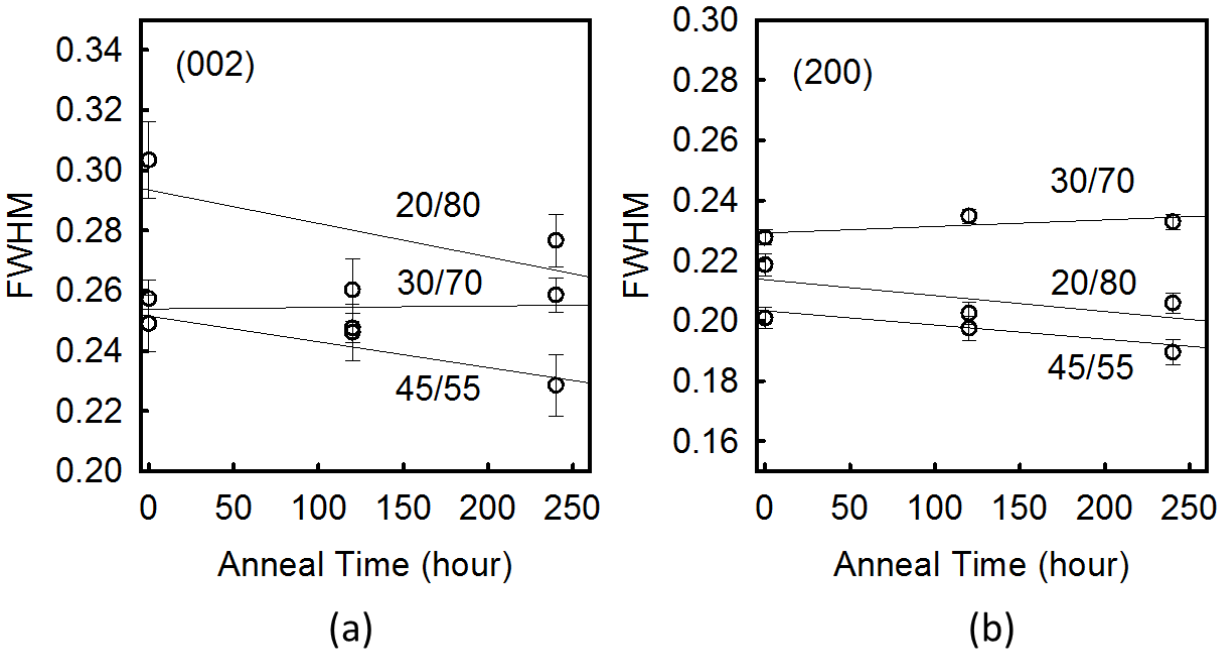

Figure 8.7. FWHM of (a) (002) and (b) (200) reflections of the PZT sintered disks with tetragonal compositions ($0.55 \leq x \leq 0.80$) *versus* anneal time.

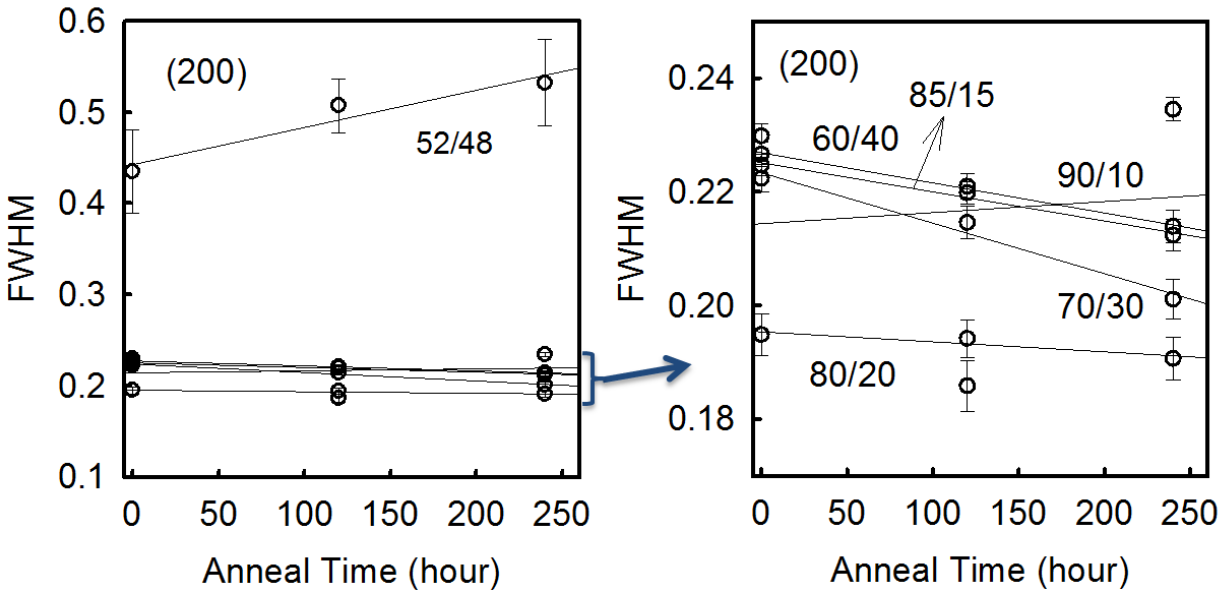

Figure 8.8. FWHM of (200) reflections of the annealed PZT ceramics with rhombohedral phase.

8.3.2 Influence of Thermal History on Domain Structure at near MPB

The investigation of the influence of thermal history on domain structure was carried out by TEM. Fig. 8.9 shows the domain structure evolution of the PZT 52/48 sintered disk along a [111] zone axis with increased anneal time. Different levels of domain curving were found in all annealed samples. High level of domain curving indicates that no preferred polarization direction at MPB, and it would lead domain miniaturize at around this region. This was domain miniaturize also reported by other authors [20, 21]. The domain size (thickness) of the un-annealed PZT 52/48 ceramic was around 10nm with high level of domain curving morphology. The TEM result shows the domain size increases, and the level of domain curving decreases with anneal time. This domain coarsening by different thermal histories has never been reported in literature.

In the literature, many authors relate grain size to the grain size [22], domain wall energy [23-25]. There was no obvious change in grain size of the PZT ceramic during the anneal process. Thus, the domain coarsening cannot be caused by grain growth during the annealing process. There are two possible reasons/mechanisms for the domains coarsening by anneal process. First possible reason is the internal stress relief of the system. The annealing process can reduce the internal stress by removing oxygen vacancies and relieving intergranular stress, the total elastic energy in the sintered disks were then lowered at above *Tc*. Thus, less domains need to be formed to relieve the elastic energy created during the paraelectric to ferroelectric phase transformation. This will lower the domain wall density and coarsen the domain structure. Also, the tetragonal phase has much higher spontaneous strain than rhombohedral phase. This explains the

observation of volume fraction of F_R phase increases with anneal time in XRD measurement.

The second possible reason is the phase decomposition occurs during the anneal process. The observation of domain coarsening match very well with the computer simulation result of phase decomposition of PZT which reported by Rao *et al*. [18]. Their simulation model demonstrates the different stages of phase decomposition in the PZT 50/50, which shows the evolution of the nanoscale domains of tetragonal and rhombohedral phases. The simulation results of phase decomposition at early stage and end stage were shown in Fig. 8.10 (a) and (b), respectively. At early stage of phase decomposition, the domain structures of both tetragonal and rhombohedral phases were randomly distributed in a nanoscale without fully decomposed. This simulated domain morphology was the result of considering the coherency strain and, in particular, the electrostatics of polarization at near the MPB region. Fig 8.10(b) shows the later stage of phase decomposition, the both tetragonal and rhombohedral domains coarsen with time. By comparing the experimental TEM results to the simulation results, the domain structure of un-annealed PZT 52/48 sintered disks has a good agreement with the simulation result of phase decomposition at early stage. The 240h-annealed PZT 52/48 sintered disks has similar domain structure with the simulation result of phase decomposition at end stage. The bright field TEM images have shown evolution of the domain structure with anneal time in the PZT 52/48 sintered disks, and the reason can be stress relief, phase decomposition or both.

The TEM results suggest that domain structures of PZT compositions near the MPB can be controlled without dopants by processing under different thermal histories.

As mentioned earlier, the ferroelectric properties of the PZT ceramics were strongly dependent on their domain structures. Therefore, this observation provides greatly useful information for the processing, microstructure control, and structure-sensitive properties of PZT solid solutions.

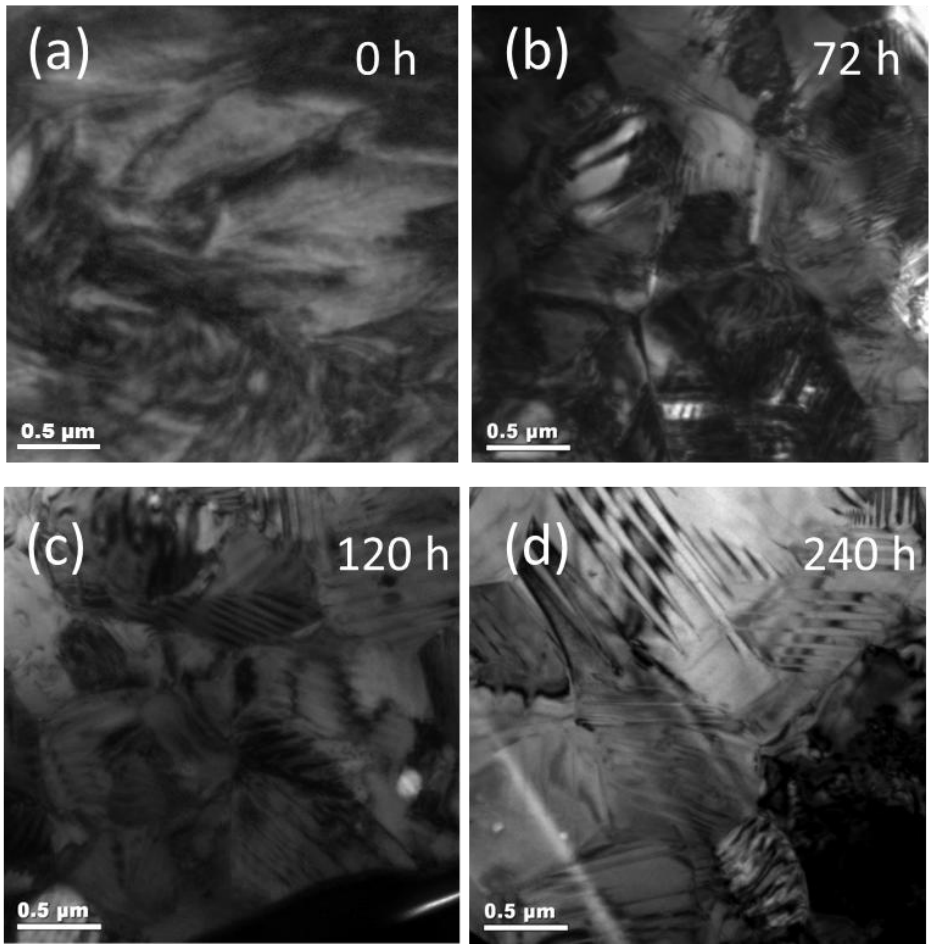

Figure 8.9. TEM bright field images of the sintered disks of $PbZr_{1-x}Ti_xO_3$ with the composition x = 0.48 as a function of anneal time (a) 0h, (b) 72h, (c) 120h, and (d) 240h.

Figure 8.10. Computer simulation of domain structures of phase decomposition in PZT near MPB. (a) Two-phase morphology at early stage of decomposition (simulation time t = 1), (b) coarsened morphology (t = 30), and 0 (c) Close-up look of a portion of the phase-coexisting multi domain microstructure shown in (b). Color scale shows the composition profile: tetragonal phase in red ($x \approx 0.77$) and rhombohedral phase in blue ($x \approx 0.38$), after Rao *et al*.

8.3.3 Influence of Thermal History on Paraelectric to Ferroelectric Phase Transition

Paraelectric to ferroelectric phase transition behavior of un-annealed PZT powders ($x = 0.00, 1.00$) and sintered disks ($0.10 \leq x \leq 0.80$) was discussed in chapter 5. The influence of thermal history on phase transition will be reviewed by comparing difference in phase transition behavior between as-synthesized and 240h-annealed PZT ceramics. As mentioned in chapter 5, specific heat measurement was applied to study the paraelectric to ferroelectric phase transition behavior. The influence of thermal history on specific heat, phase transition and latent heat of the PZT ceramics will be discussed in following sections.

It should be noted that the specific heat measurement is a very sensitive to the conditions of the samples. After measuring the specific heats of the as synthesized PZT ceramics, theses powders ($x = 0.00, 1.00$) and sintered disks ($0.10 \leq x \leq 0.80$) were

annealed at 923K for 240 hours. The purpose of using the same samples was to eliminate unnecessary complicating factors, such as different sample weight or vacancy concentration, which can be affecting the final results.

8.3.3.1 Influence of Thermal History on Specific Heat

Fig. 8.11 shows the specific heat of the PZT powders (x = 0.00, 1.00) and sintered disks ($0.10 \leq x \leq 0.80$) before (black) and after (orange) annealing at 923K for 240 hours as functions of composition and temperature. At the temperatures far away (below/above) from transition point, the specific heat behavior of the annealed samples was similar to those without annealing process. As closing to transition points, the phase transition peaks showed different level of change in shape between the as synthesized samples and annealed samples. After the anneal process, the phase transition peaks of the compositions that distance from MPB region only show a minor difference in shape. The phase transition peaks of most of compositions were sharpen after anneal process. There were two possible reasons for this peak sharpening. The first reason was the oxygen vacancies diffused to grain boundaries and reducing the internal stress during annealing process, the system with lower concentration of defects would show a stronger/sharper phase transition peak. The second reason that caused transition peak became shaper was a smaller distribution in composition about the mean value after anneal process. Among all compositions, the phase transition peak of PZT 52/48 showed a clear sharpening after the anneal process. The influence of thermal history on phase transition behavior of PZT 52/48 will be discussed in details at later section.

The phase transition temperatures of both un-annealed (blue circles) and 240h-annealed (orange circles) PZT powders (x = 0.00, 1.00) and sintered disks ($0.10 \leq x \leq$

0.80) were shown in Fig. 8.12. The paraelectric-ferroelectric phase transition temperatures of 240 hours annealed PZT ceramics increased from 503K to 760K which matches very well with phase transition temperatures before annealing and the ($T_{FP\ (Jaffe)}$) in the conventional PZT phase diagram that assembled by Jaffe *et al*. [1]. Also, the phase transition temperatures between *R3c* and *R3m* phases were unchanged with anneal time. The values of phase transition temperatures were listed in details at table 8.3 and 8.4. Phase transition temperatures of all samples were unchanged by annealing, indicating that the average composition does not change by annealing at 923K for 240 hours. The results show anneal process sharpen the phase transition peaks without changing their average compositions. This observation can be explained by the stress relief in the PZT ceramics during the anneal process. The sharpening of the phase transition became more obvious for those compositions near the MPB region. It could be the combined mechanisms of the stress relief and the redistribution of the zirconium and titanium atoms to a more uniform composition. However, the results indicate that the phase decomposition did not occur during the long annealing process. This is because the transition peak would broaden or split if the phase decomposition was occurred during the annealing process.

The method used to determine the order of phase transition between paraelectric and ferroelectric phase was mentioned in chapter 5. The order of phase transition of annealed sample showed a similar behavior to the as synthesized ceramics. The order of phase transition of samples with compositions away from the MPB region ($0 \leq x \leq 0.30$) and $0.55 \leq x \leq 1$) show strong or weak first-order transition characteristic, and the samples near at the MPB region have a step-like second-order transition characteristic. The order

of the phase transition of the PZT powders (x = 0.00, 1.00) and sintered disks ($0.10 \leq x \leq 0.80$) were not changed much with the anneal time.

The transition enthalpies measured on heating of the PZT samples before and after annealing were shown in Fig. 8.13 (a). Outside of MPB region, all latent heats of the annealed PZT samples were slightly decreased after annealing for 240 hours. However, the difference was within error. The transition entropies of the annealed also slightly lowered after anneal process (see Fig. 8.13 (b)). Although the second-order phase transition at MPB region became sharper after anneal process, the latent heat and excess entropy remains zero. Therefore, the locations of two tricritical points did not affected by the long annealing process. The values of these thermodynamic parameters were list in table 8.3 and 8.4.

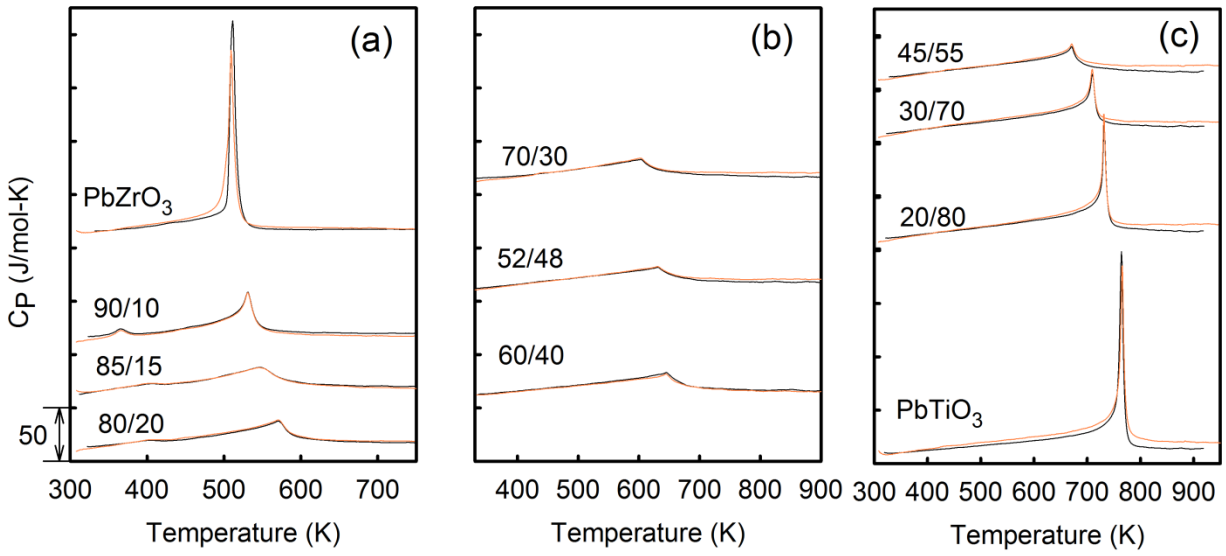

Figure 8.11. Relative heat capacity *versus* temperature of PZT powders (x = 0.00, 1.00) and sintered disks ($0.10 \leq x \leq 0.80$) before (black) and after (orange) in three ranges of composition (a) $0.00 \leq x \leq 0.20$ (b) $0.30 \leq x \leq 0.40$ and (c) $0.55 \leq x \leq 1.00$. The heat capacity data were collected on heating. The insets show the first derivative of the heat capacity *versus* temperature curves. The tick marks on the vertical axes represent intervals of 50 J/mol-K.

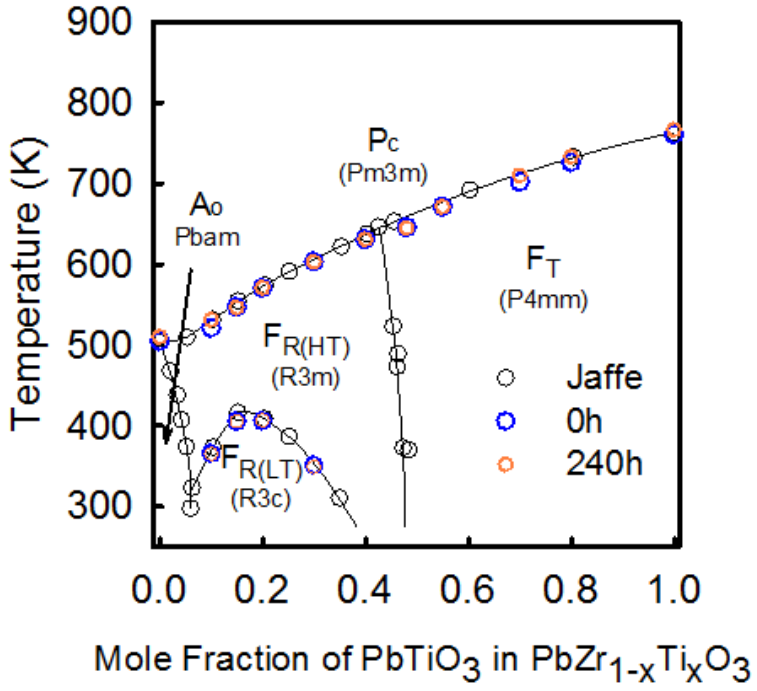

Figure 8.12. The Curie temperature of the PZT powders (x = 0.00, 1.00) and sintered disks ($0.10 \leq x \leq 0.80$) before (blue) and after (orange) annealing at 923K for 240 hours.

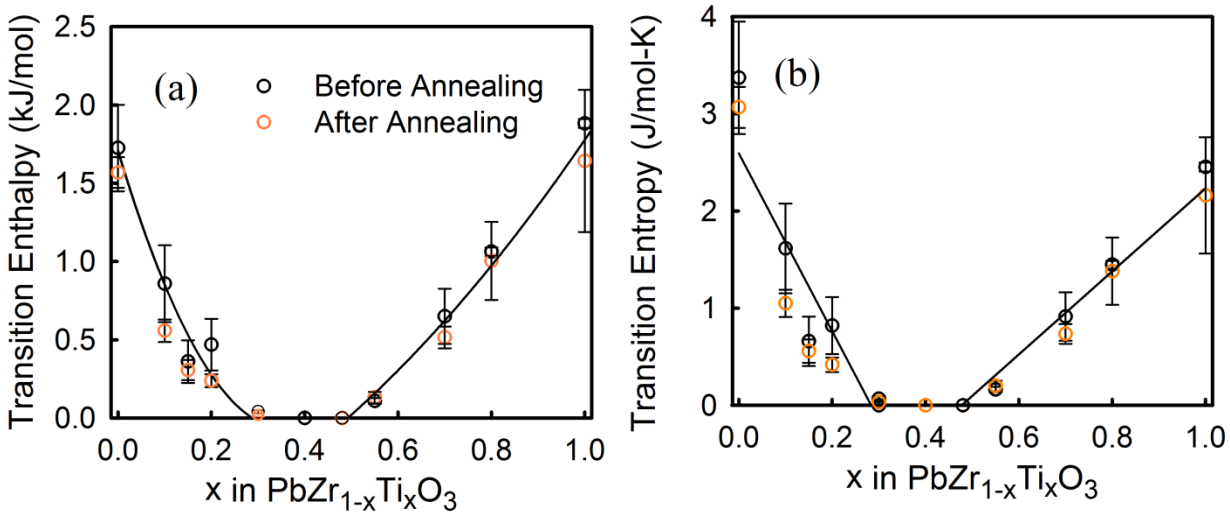

Figure 8.13. (a) Transition enthalpies and (b) transition entropies of PZT powders (x = 0.00, 1.00) and sintered disks ($0.10 \leq x \leq 0.80$) *versus* composition before annealing (black circles) and after (orange circles) annealing at 923 K for 240 hours. The heat capacity data were collected on heating. The solid lines are least-squares fits to the data collected in both heating and cooling measurements.

x	T_{onset}(K)	T_{peak}(K)	$F_{R(HT)}$-$F_{R(LT)}$ (K)	$L^{Heating}$ (kJ/mol)	$\Delta S^{XS(H)}$ (J/mol-K)
0.00	505	511	-	1.72 ± 0.184	3.37± 0.159
0.10	521	531	366	0.86 ± 0.164	1.61 ± 0.154
0.15	547	547	406	0.36 ± 0.091	0.66 ± 0.146
0.20	571	571	406	0.47 ± 0.110	0.82 ± 0.140
0.30	603	603	351	0	0
0.40	630	630	-	0	0
0.48	646	646	-	0	0
0.55	662	671	-	0.11 ± 0.013	0.16 ± 0.119
0.70	702	710	-	0.65 ± 0.118	0.91 ± 0.114
0.80	726	734	-	1.06 ± 0.018	1.45 ± 0.110
1.00	761	767	-	1.88± 0.019	2.45± 0.105

Table 8.4. Thermodynamic parameters of un-annealed PZT powders (x = 0.00, 1.00) and sintered disks ($0.10 \leq x \leq 0.80$).

x	T_{onset}(K)	T_{peak}(K)	$F_{R(HT)}$-$F_{R(LT)}$ (K)	$L^{Heating}$ (kJ/mol)	$\Delta S^{XS(H)}$ (J/mol-K)
0.00	503	510	-	1.57 ±0.032	3.115733598
0.10	520	531	365	0.56 ± 0.024	1.071651731
0.15	546	546	405	0.31 ± 0.022	0.559848901
0.20	571	571	406	0.24 ± 0.014	0.417209982
0.30	603	603	349	0.019 ± 0.005	0.031279104
0.40	630	630	-	0	0
0.48	645	645	-	0	0
0.55	661	671	-	0.13 ± 0.012	0.198718457
0.70	700	710	-	0.51 ± 0.023	0.735093857
0.80	727	733	-	1.00 ± 0.083	1.380302751
1.00	760	766	-	1.64 ± 0.151	2.160402895

Table 8.5. Thermodynamic parameters of 240h-annealed PZT powders (x = 0.00, 1.00) and sintered disks ($0.10 \leq x \leq 0.80$).

8.3.3.2 Influence of Thermal History on Phase Transition at MPB

Among all the compositions, the temperature dependence of specific heat behaviors of the 0h, 72h, 120h, 240h, and 360h-annealed PZT 52/48 sintered disks were carefully studied. The specific heat versus temperature for the PZT 52/48 ceramics with different anneal time (0-360 hours) was shown in Fig. 8.14. As synthesized and annealed PZT 52/48 ceramics showed different levels of sharpness of step-like second order phase transition behavior. To quantify the level (sharpness) of the second order transition, a method was applied by determining the difference between the Curie temperature (T_c) and the transition end temperature (T_{end}). The Curie temperature and the transition end temperature were determined by the onset temperature and end temperature of the specific heat curve, which were analyzed by NETZSCH Proteus® Software.

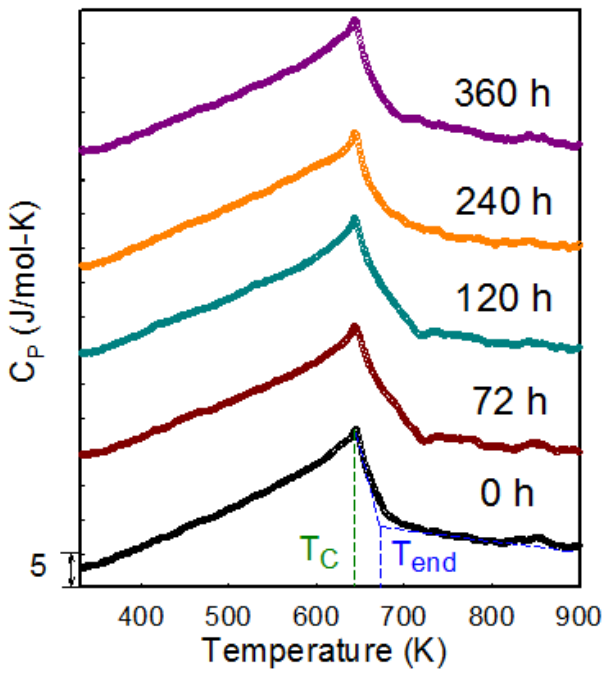

Figure 8.14. Specific heat versus temperature for the PZT 52/48 ceramics with different anneal time (0-360 hours)

Fig. 8.15 shows Curie temperature of the PZT 52/48 does not change with anneal time. It indicated that the average composition was not change by anneal process. The ΔT become higher after annealing for 72 hours and then declined with additional annealing (shown in upper part of Fig 8.15), which means that after annealing 72 hours the PZT tend to become a sharper second-order transition. As mentioned above, the peak sharpening in the PZT 52/48 was more obvious than other compositions. This is believed that the un-annealed (0h) PZT 52/48 contains two phases and phase rearrangement with anneal time occurred, which is also match with the observation in XRD analysis. Therefore, mechanisms of stress relief and two phases rearrangement by anneal process were attributed to larger level of transition peak sharpening in the PZT 52/48 ceramic.

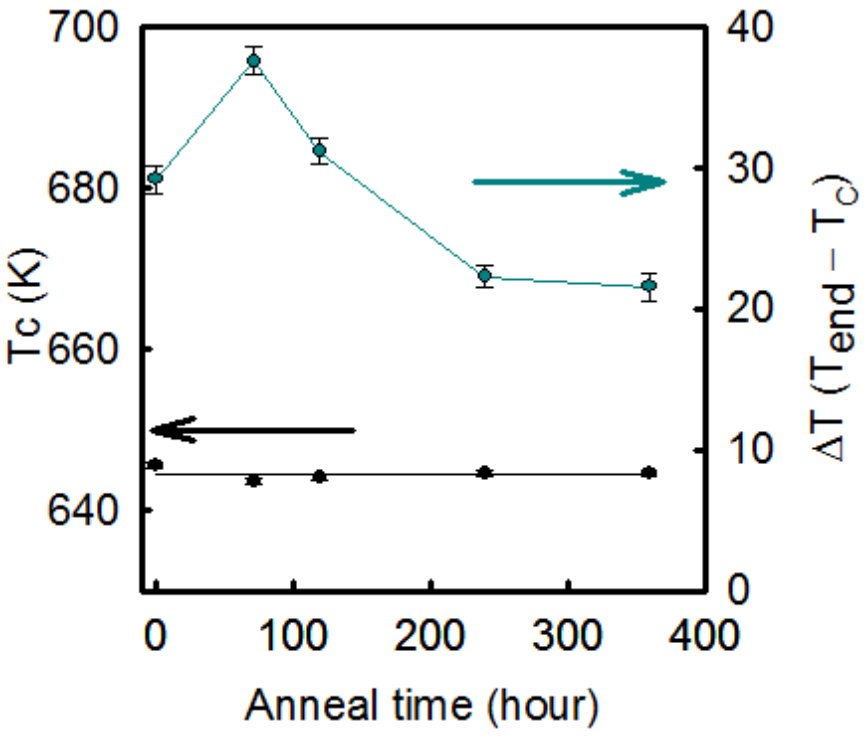

Figure 8.15. The Curie temperature and the ΔT (sharpness) of the PZT 52/48 ceramic as a function of anneal time.

8.4 Summary

Two hypotheses were proposed to explain the change in structural properties and domain structure, which were phase decomposition and stress relief. The first hypothesis is phase decomposition model, direct thermochemical studies of the equilibrium enthalpies of formation from the oxides have shown that the PZT system with a large positive mixing energy and exhibits a tendency towards phase decomposition. Therefore, an equilibrium two-phase coexistence can be observed if the diffusional process was fast enough. However, results of temperature dependence of specific heat of the annealed PZT samples were not support with the prediction of phase decomposition. The phase transition between paraelectric and ferroelectric phases was sharpening after long annealing process, which indicated that phase decomposition did not occur during the long annealing process.

The second hypothesis is stress relief. In this hypothesis, large elastic energy was accumulated during the normal ceramic processing. It is well known that the formation non-180^{o} domain wall can eliminate the elastic energy. Higher elastic energy leads to form more domain walls in the system. At near the MPB, the domain can be formed with either tetragonal or rhombohedral phases to compensate the elastic energy. More domain with tetragonal phase is expected if the PZT ceramic at MPB with a high elastic energy. The stress can be relieved at above *Tc* by annealing process and toward to an equilibrium state. Stress relief hypothesis has a good agreement with overall observations in this work.

The influence of thermal history on the structure, domain structure, and paraelectric to ferroelectric phase transition can be summarized as follows,

Influence of Thermal History on Structural Properties

- All lattice parameters decrease with anneal time at both tetragonal and rhombohedral phases except for the PZT 10/90. The volume change of the PZT shows a maximum at the compositions near at MPB.
- The maximum change of the spontaneous strains after the long anneal process occurs at the compositions near at the MPB increased.
- The volume fraction of F_R phase (I_R/I_T+I_R) in the PZT 52/48 was around 50% and increase with anneal time. It indicates that the diffusional process was fast enough to redistribute the atoms and influence the volume fraction between two phases.
- The maximum change of the diffractions peak width of PZT ceramics after the long anneal process occurs at the PZT 52/48. The diffractions peak widths of other compositions decrease with anneal time.

Influence of Thermal History on Domain Structure

- The TEM result shows the domain coarsens and the level of domain curving decreases with anneal time.
- The TEM results suggest that domain structures of PZT compositions near the MPB can be controlled without dopants by processing under different thermal histories.

Influence of Thermal History on Paraelectric to Ferroelectric Phase Transition

- Phase transition temperatures of all samples were unchanged by annealing, indicating that the average composition does not change by annealing at 923K for 240 hours.
- As closing to transition points, phase transition peaks of the annealed samples showed different level of sharpening in shape compare to the as synthesized samples. Among all compositions, a maximum change in transition peak occurred at the PZT 52/48.
- Phase transition temperature of the PZT 52/48 did not change with anneal time, and the second-order transition behavior became sharper as anneal time increases. This indicated that no phase decomposition was occurred during the long annealing process.
- The results of XRD analysis and specific behavior of PZT 52/48 show that two mechanisms attributed to the sharpening of the second-order transition behavior, these were stress relief and phase redistributions.

The combined results showed that PZT sintered disks made by a normal ceramic processing were not in their equilibrium state near the MPB. However, no clear evidence of phase decomposition into an equilibrium mixture of tetragonal and rhombohedral phases was found. Instead, the changes in structural and thermodynamical properties observed on annealing were most consistent with a stress relief mechanism.

8.5 References

1. B. Jaffe, W.R. Cook, and H.L. Jaffe, *Piezoelectric ceramics* 1971, London, New York,: Academic Press. 135.
2. W.W. Cao and L.E. Cross, *Physical Review B* **47**, 4825 (1993)
3. V.A. Isupov, *Ferroelectrics* **266**, 427 (2002)
4. G.A. Rossetti, W. Zhang, and A.G. Khachaturyan, *Appl Phys Lett* **88**, 072912 (2006)
5. G.A. Rossetti, A.G. Khachaturyan, G. Akcay, and Y. Ni, *J Appl Phys* **103**, 114113 (2008)
6. P. Arigur and L. Benguigui, *J Phys D Appl Phys* **8**, 1856 (1975)
7. V.A. Isupov, *Soviet Physics - Solid States* **18**, 529 (1975)
8. K. Kakegawa, J. Mohri, T. Takahashi, H. Yamamura, and S. Shirasaki, *Solid State Commun* **24**, 769 (1977)
9. W. Cao and L. Cross, *Physical Review B* **47**, 4825 (1993)
10. W. Cao and L.E. Cross, *J Appl Phys* **73**, 3250 (1993)
11. B. Noheda, D.E. Cox, G. Shirane, J.A. Gonzalo, L.E. Cross, and S.E. Park, *Appl Phys Lett* **74**, 2059 (1999)
12. V.A. Isupov, *Solid State Commun* **17**, 1331 (1975)
13. V.A. Isupov, *Soviet Physics - Solid States* **22**, 172 (1980)
14. V.A. Isupov, *Physics of the Solid State* **43**, 2262 (2001)
15. K. Kakegawa, J. Mohri, H. Ishiguro, K. Takahashi, and S. Shirasaki, *Chem Lett*, 1655 (1982)
16. K. Kakegawa, T. Kato, and Y. Sasaki, *J Eur Ceram Soc* **20**, 1599 (2000)

17. M.V. Rane, A. Navrotsky, and G.A. Rossetti, *J Solid State Chem* **161**, 402 (2001)

18. W.-F. Rao and Y.U. Wang, *Appl Phys Lett* **91**, 052901 (2007)

19. C.A. Randall, N. Kim, J.P. Kucera, W.W. Cao, and T.R. Shrout, *J Am Ceram Soc* **81**, 677 (1998)

20. D. Woodward, J. Knudsen, and I. Reaney, *Physical Review B* **72**, 104110 (2005)

21. K.A. Schönau, L.A. Schmitt, M. Knapp, H. Fuess, R.-A. Eichel, H. Kungl, and M.J. Hoffmann, *Physical Review B* **75**, 184117 (2007)

22. W.W. Cao and C.A. Randall, *J Phys Chem Solids* **57**, (1996)

23. A.G. Khachaturyan, *Theory of Structural Transformation in Solids* 1983, New York: John Wiley & Sons Inc.

24. Y.M. Jin, Y.U. Wang, A.G. Khachaturyan, J.F. Li, and D. Viehland, *Phys Rev Lett* **91**, 197601 (2003)

25. Y. Wang, *Physical Review B* **74**, 104109 (2006)

CHAPTER 9

INFLUENCE OF THERMAL HISTORY ON DIELECTRIC PROPERTY

9.1 Introduction

The dielectric properties of the PZT ceramics were extremely sensitive to their structure, microstructure, domain structure and defects concentration. The influence of thermal history on structure, microstructure and domain structure was discussed on the previous chapters. This chapter is focus on the influence of structural change on dielectric properties.

Temperature, frequency, and composition dependence of dielectric behavior of 72h-, 120h-, and 240h-annealed PZT sintered disks ($0.10 \leq x \leq 0.80$) were investigated at low electric field (0.1V). These results were compared to the low field dielectric properties of the un-annealed PZT sintered disks, and provided the information of how thermal history affects the low field dielectric behaviors of the PZT ceramics. The field amplitude dependence of dielectric behavior of annealed PZT sintered disks ($0.10 \leq x \leq 0.80$) were measured at room temperature, and the influence of thermal history on different types of domain wall motion was quantified by using Rayleigh analysis.

The influence of thermal history on dielectric behavior of the PZT sintered disks will be discussed at following sections. The results provide not only scientifically important, but also industrially valuable for properties control during the ceramic processing.

9.2 Experimental Procedure

Methods of dielectric characterization at low and strong field were mentioned in the chapter 6. All dielectric tests on the annealed PZT sintered disks were operated under same condition as the un-annealed PZT ceramics.

9.3 Results and Discussions

9.3.1 Influence of Thermal History on Low Field Dielectric Property

In this section, the influence of thermal history on composition, frequency, and temperature dependence of low field dielectric behavior of annealed PZT sintered disks will be discussed and compared to the result of the un-annealed samples.

9.3.1.1 Influence of Thermal History on Composition Dependence of Dielectric Property

The composition dependence of dielectric constants of annealed PZT sintered disks at different anneal time (0h, 72h, 120h, and 240h) were shown in Fig. 9.1, and the values of dielectric properties of annealed PZT sintered disks were listed in table 9.1 and 9.2. All PZT sintered disks (except x = 0.10) showed different levels of increase in dielectric constant after annealing process. In order to simplify the discussion, only 240h-annealed PZT sintered disks were used to compare to un-annealed samples in the following discussion.

Fig. 9.2 shows composition dependence of dielectric constant of un-annealed and 240h-annealed PZT sintered disks at (a) 1k and (b) 10 kHz. The comparison between all the compositions, the dielectric constant of the annealed PZT sintered disks with

compositions near at the MPB region (x = 0.40, 0.48 and 0.55) increased most after annealed at 923K for 240 hours. The increased value and percentage in dielectric constant were shown in Fig. 9.3, and the values were listed in table 9.3. For the compositions close to MPB region (x = 0.40, 0.48 and 0.55), their dielectric constant increased 11% to 36% after 240 hours annealing process. For the compositions away from the MPB region (x = 0.15, 0.20, 0.30 and 0.70), their dielectric constant increased 1.2% to 6.5% after 240 hours annealing process. To be noted that dielectric constant of the PZT 20/80 sintered disks (x = 0.80) increased 14% after annealing at 923K for 240 hours. At the same time, the dielectric loss of PZT 20/80 sintered disks reached an unacceptable high value of 0.44. This high loss was because of reduced density in annealed PZT 20/80 sintered disks. Small cracks were formed after this ceramic, which has high spontaneous, experienced few times of phase transitions. Therefore, the dielectric behavior of the annealed PZT 20/80 sintered disks was not included in discussion.

Dielectric properties of the PZT ceramics enhanced after anneal process (from 15 minutes up to 8 hours) in ferroelectric ceramics [1-3] and thin films [4-6] were reported in literature. Most accepted explanations for the enhancements in the properties were the elimination of the excess PbO at grain boundaries by lead evaporation and the removal oxygen vacancies in the grains that formed during the sintering. The dielectric constant was then increased by reducing undesirable second phase or by increasing the domain wall mobility (removing the defects). However, these explanations were not enough to interpret the fact that the dielectric constant increased most at the MPB region. Thus, the mechanisms of stress relief must be taken into account to proper explain this unique observation.

Composition dependence of dielectric loss of un-annealed and 240h-annealed PZT sintered disks ($0.10 \leq x \leq 0.80$) at 1k and 10 kHz were shown in Fig. 9.4. The loss decreases with anneal time was found in most of the compositions, except for three end members (x = 0.10, 0.15 and 0.80). The loss was lower after long anneal process can be explained by a reduction in concentration of oxygen vacancy, and the stress relief in the PZT sintered disks. For the compositions close to pure PZ, the loss increased after anneal process might due to the vaporization of very little lead (Pb). For the PZT 20/80 sintered disks, the reason was mentioned above.

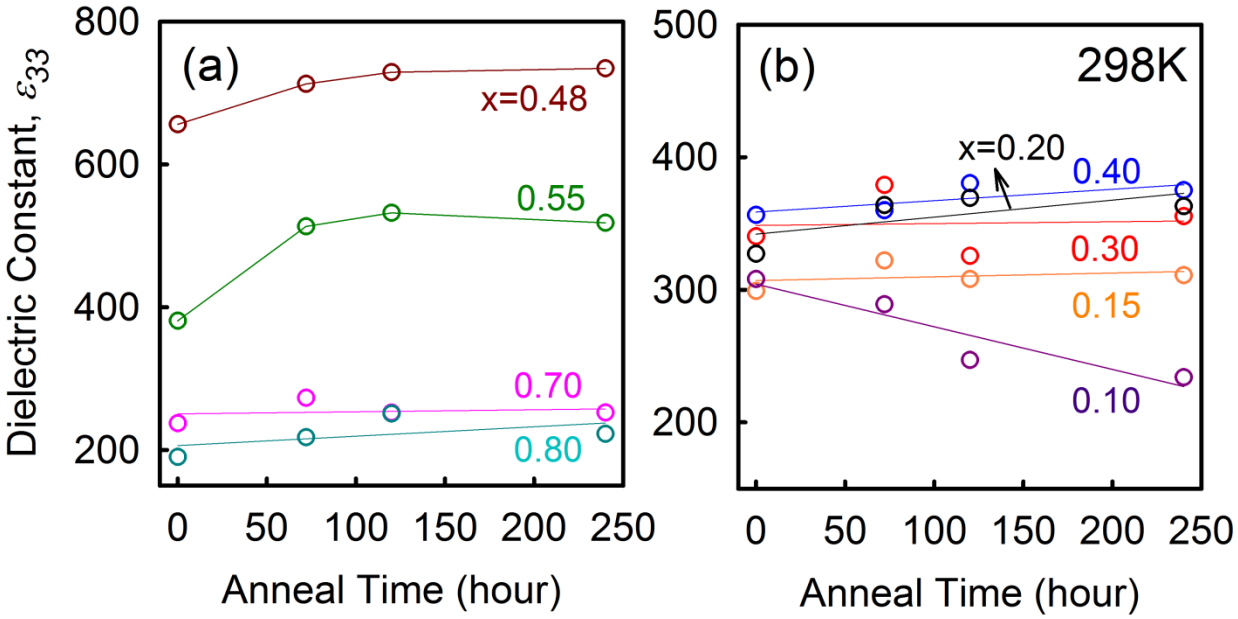

Figure 9.1. Room-temperature dielectric constant *versus* anneal time for the sintered disks of PZT in two ranges of composition (a) $0.48 \leq x \leq 0.80$ and (b) $0.10 \leq x \leq 0.40$ at 1 kHz.

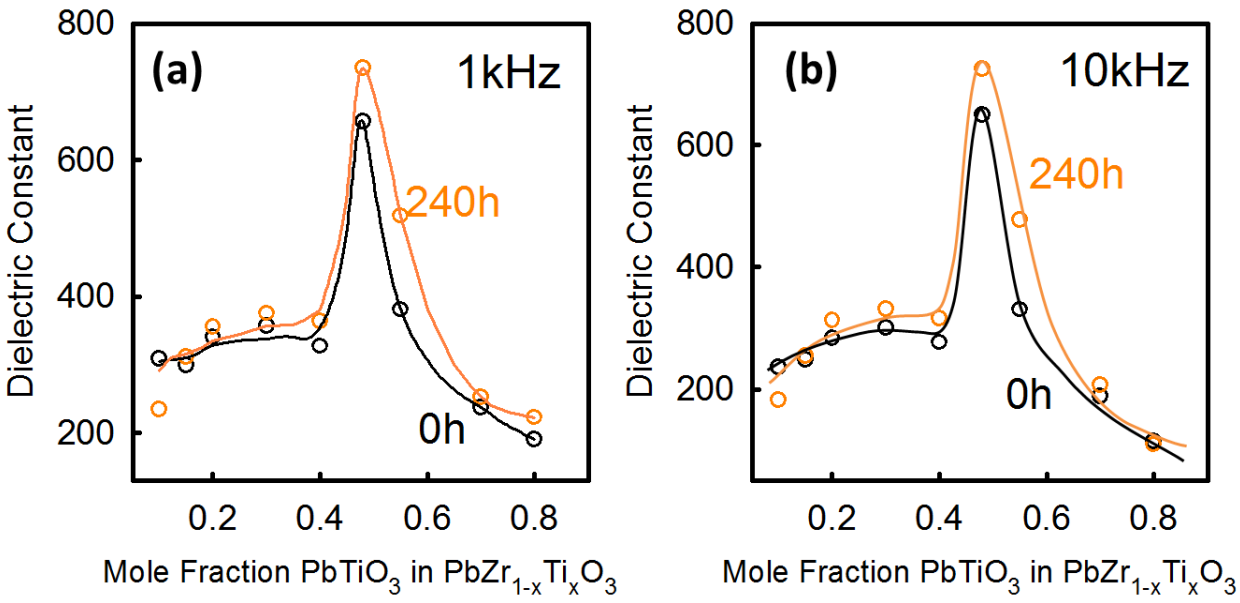

Figure 9.2. Composition dependence of dielectric constant of un-annealed sintered disks of PZT ($0.10 \leq x \leq 0.80$) (black circles) and change in the dielectric constant after annealing at 923K for 240 hours (orange circles) at (a) 1 kHz and (b) 10 kHz.

Sample	x	0h		72h		120h		240h	
		ε	Loss	ε	Loss	ε	Loss	ε	Loss
1	0.00	-	-	-	-	-	-	-	-
2	0.10	308	0.05	289	0.06	247	0.08	234	0.08
3	0.15	299	0.06	322	0.05	308	0.06	311	0.08
4	0.20	340	0.06	381	0.04	326	0.04	355	0.04
5	0.30	342	0.05	366	0.05	380	0.04	375	0.03
6	0.40	327	0.04	366	0.04	369	0.04	363	0.04
7	0.48	656	0.01	713	0.01	729	0.01	734	0.01
8	0.55	381	0.04	521	0.03	532	0.03	518	0.03
9	0.70	237	0.10	276	0.08	252	0.08	252	0.11
10	0.80	194	0.16	223	0.36	251	0.48	223	0.44
11	1.00	-	-	-	-	-	-	-	-

Table 9.1. Low field dielectric property of PZT sintered disks with different annealing time (0h, 72h, 120h, and 240h) at 1 kHz.

Sample	x	0h		72h		120h		240h	
		ε	Loss	ε	Loss	ε	Loss	ε	Loss
1	0.00	-	-	-	-	-	-	-	-
2	0.10	236	0.010	240	0.024	192	0.022	183	0.025
3	0.15	248	0.019	264	0.014	259	0.014	254	0.022
4	0.20	283	0.048	335	0.010	283	0.007	313	0.005
5	0.30	301	0.029	313	0.012	334	0.005	331	0.006
6	0.40	277	0.004	317	0.006	323	0.009	316	0.006
7	0.48	650	0.004	704	0.006	721	0.006	725	0.007
8	0.55	331	0.027	476	0.002	485	0.002	478	0.002
9	0.70	188	0.016	228	0.004	204	0.007	206	0.012
10	0.80	114	0.024	138	0.113	127	0.238	109	0.230
11	1.00	-	-	-	-	-	-	-	-

Table 9.2. Low field dielectric property of PZT sintered disks with different annealing time (0h, 72h, 120h, and 240h) at 10 kHz.

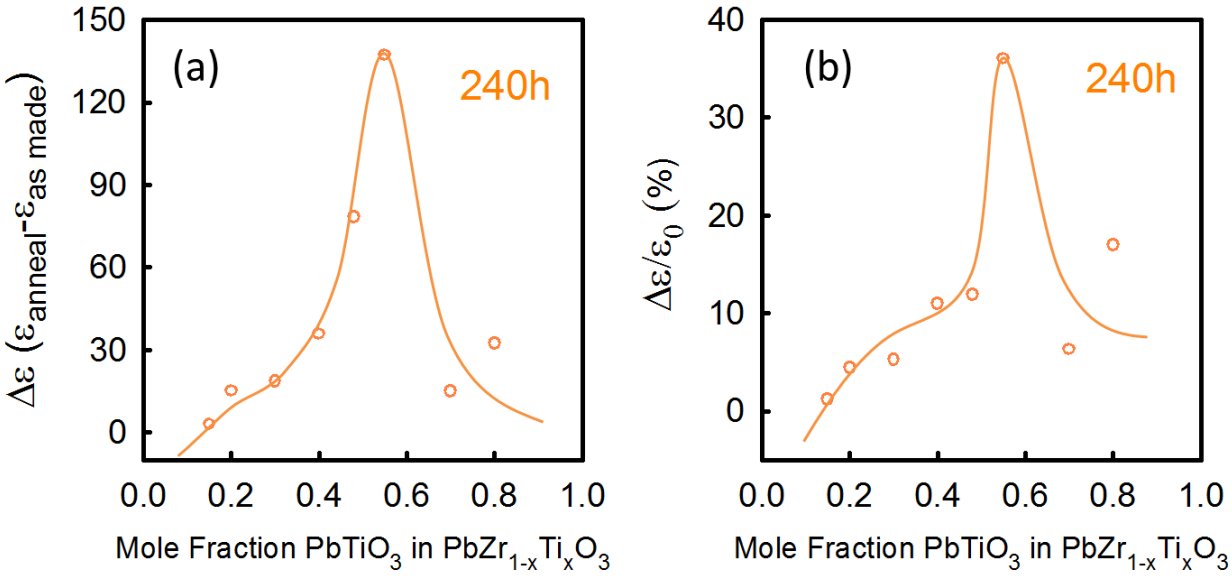

Figure 9.3. (a) Increased dielectric constant and (b) increased dielectric constant in percentage of the PZT sintered disks of ($0.10 \leq x \leq 0.80$) after annealing at 923K for 240h.

Sample	x	72h		120h		240h	
		$\Delta\varepsilon$	$\Delta\varepsilon/\varepsilon_{0h}$ (%)	$\Delta\varepsilon$	$\Delta\varepsilon/\varepsilon_{0h}$ (%)	$\Delta\varepsilon$	$\Delta\varepsilon/\varepsilon_{0h}$ (%)
1	0.00	-	-	-	-	-	-
2	0.10	-9	-3.82	-52	-22.06	-65	-27.58
3	0.15	14	5.64	0	0.00	3	1.21
4	0.20	39	11.47	-14	-4.26	15	4.54
5	0.30	4	1.01	24	6.72	19	5.25
6	0.40	39	11.86	42	12.91	36	11.01
7	0.48	57	8.64	73	11.14	78	11.96
8	0.55	140	36.62	151	39.68	137	35.98
9	0.70	39	16.48	15	6.36	15	6.48
10	0.80	29	15.13	57	29.34	29	14.70
11	1.00	-	-	-	-	-	-

Table 9.3. Increase in dielectric constant of the PZT sintered disks of ($0.10 \leq x \leq 0.80$) after annealing at 923K for 72h, 120h, and 240h.

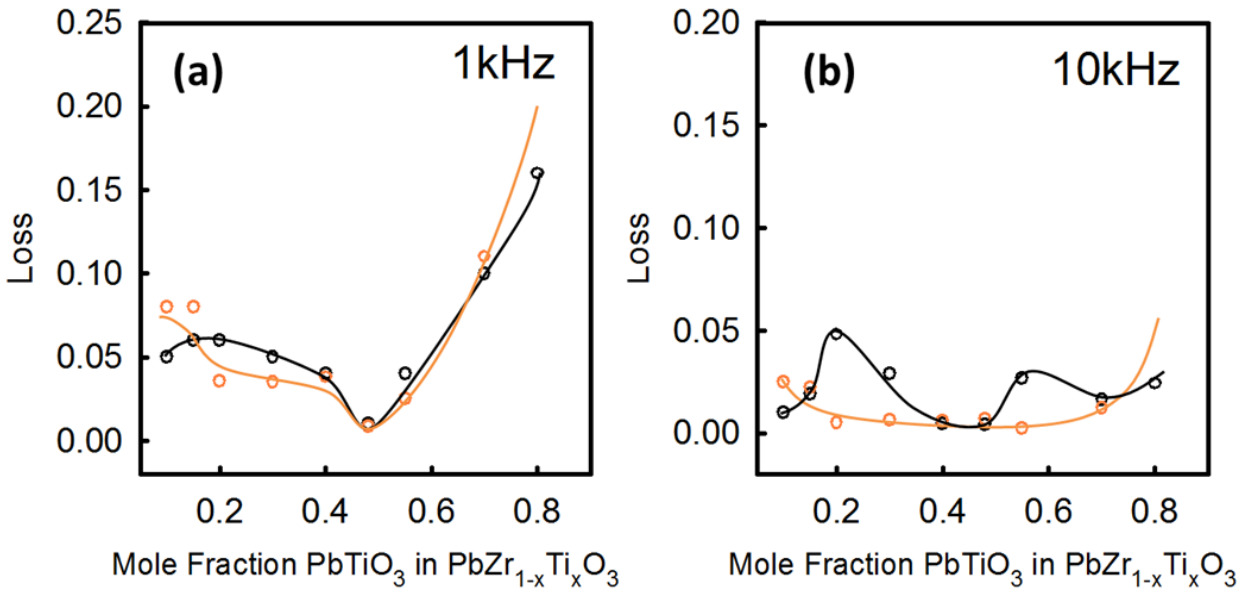

Figure 9.4. Composition dependence of dielectric loss of un-annealed sintered disks of PZT ($0.10 \leq x \leq 0.80$) (black circles) and change in the dielectric constant after annealing at 923K for 240 hours (orange circles) at (a) 1 kHz and (b) 10 kHz.

9.3.1.2 Influence of Thermal History on Frequency Dependence of Dielectric Property

Frequency dependence of dielectric constant of un-annealed and 240h-annealed PZT sintered disks ($0.10 \leq x \leq 0.80$) was shown in Fig. 9.5 (a) and (b), respectively. The dielectric constants of all PZT sintered disks were decreased slightly with frequency from 1 kHz to 1 MHz due to the reduced polarization mechanism with increased frequency. PZT sintered disks with composition of x = 0.48 were most frequency independent among all compositions before annealing process, the dielectric constant only decreased 4.1% from 1k to 1MHz. The other compositions showed 18%~44% decrease in dielectric constant from 1k to 1MHz. The dielectric constant of most PZT sintered disks became less frequency sensitive in this frequency range (1 kHz to 1 MHz) after annealing at 923K for 240 hours, except three end members (x = 0.10, 0.15 and 0.80). The difference in dielectric constant between 1 kHz and 1 MHz of un-annealed and 240h-annealed PZT sintered disks were shown in Fig. 9.6, and the values were listed in table 9.4. Compare Fig. 9.6 to Fig 9.4 (a), both plots showed a similar behavior. It implies that the frequency dependence of dielectric behavior of PZT ceramics was close related to their loss mechanism. For those compositions with lower dielectric loss after anneal process (x = 0.20 to 0.70), their dielectric constant also became less sensitive to the frequency. Conversely, the dielectric constant became more sensitive to the frequency for those compositions with higher dielectric loss after anneal process (x = 0.10, 0.15 and 0.80). The dielectric constant became less sensitive to the frequency was due to the lower concentration of defects after annealing for a long period of time, and lead to a lower amount of ionic space-charge carriers [7].

Frequency dependence of dielectric loss of un-annealed and 240h-annealed PZT sintered disks ($0.10 \leq x \leq 0.80$) were shown in Fig. 9.7 (a) and (b), respectively. The dielectric loss of all PZT c sintered disks, both before and after anneal process, tends to rapidly increase as the frequency decreases close to 1 kHz. The reason for this phenomenon has been mentioned in chapter 6.3.1.2. Therefore, the loss usually increases more rapidly at low frequency for those ceramics contain higher concentration of defects. The behaviors of dielectric loss were similar to their behaviors of dielectric constant. Comparison between un-annealed and 240h-annealed PZT sintered disks, the dielectric loss of most PZT sintered disks became less frequency sensitive in this frequency range (1 kHz to 1 MHz) after annealing at 923K for 240hours. This means that the long annealing process lower the concentration of defects (i.e. oxygen vacancy, distorted area/domain walls and defects generated during the ceramic sintering) in most of the compositions. The frequency dependence of dielectric properties of 240 hours annealed PZT sintered disks were list in table 9.5.

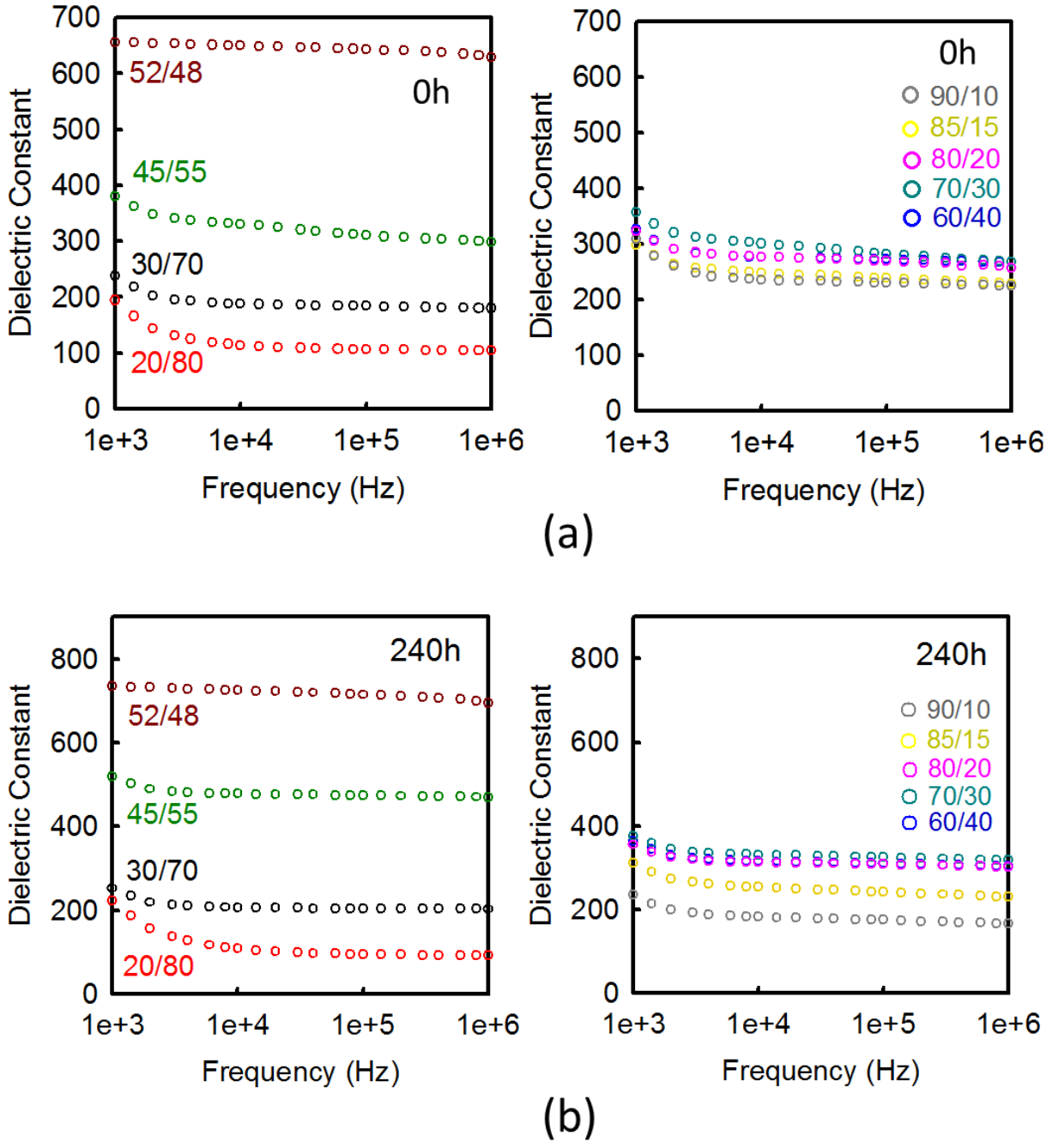

Figure 9.5. Frequency dependence of dielectric constant of (a) un-annealed and (b) 240h-annealed PZT sintered disks ($0.10 \leq x \leq 0.80$).

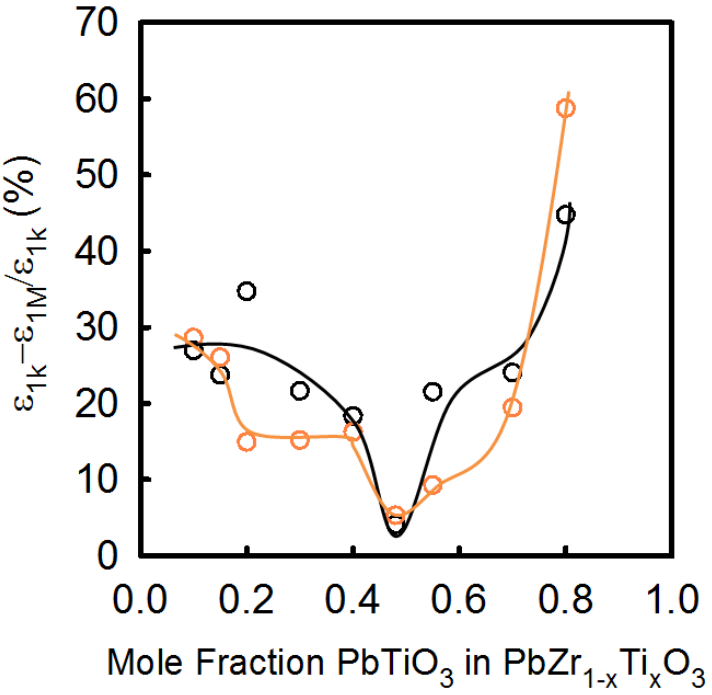

Figure 9.6. Dielectric constant difference between 1 kHz and 1 MHz *versus* composition for the sintered disks of PZT ($0.10 \leq x \leq 0.80$) before (black circles) and after annealing at 923K for 240 hours (orange circles) at room temperature.

x	0h	240h
0.10	26.95	28.63
0.15	23.75	26.05
0.20	34.71	14.93
0.30	21.64	15.20
0.40	18.35	16.25
0.48	4.12	5.31
0.55	21.52	9.27
0.70	24.05	19.44
0.80	44.74	58.74

Table 9.4. Dielectric constant difference $(\varepsilon_{1k}-\varepsilon_{1M})/\varepsilon_{1k}$ (%) between 1 kHz and 1 MHz of un-annealed (0h) and 240h-annealed PZT sintered disks ($0.10 \leq x \leq 0.80$).

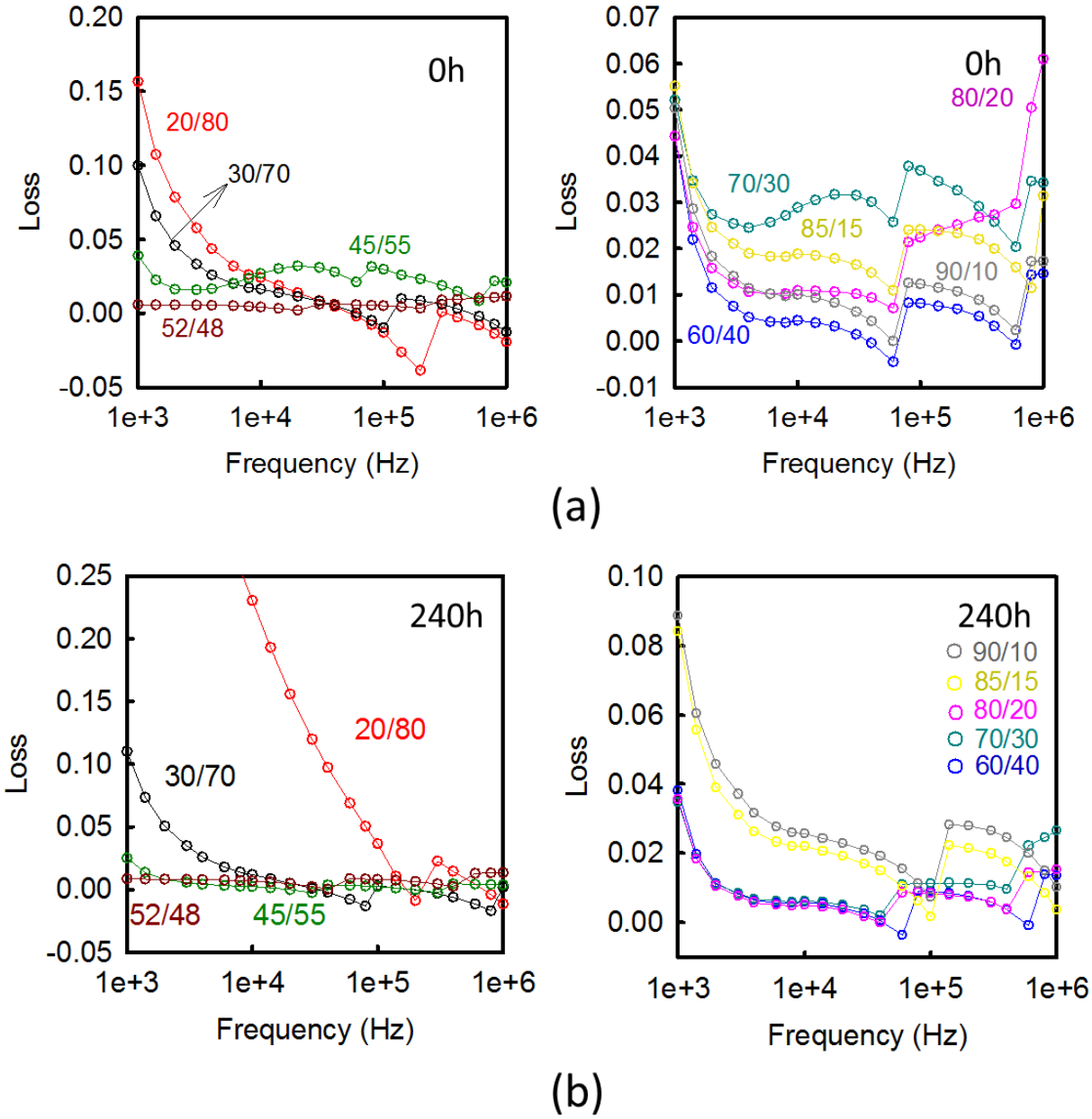

Figure 9.7. Frequency dependence of dielectric constant of (a) un-annealed and (b) 240h-annealed PZT sintered disks ($0.10 \leq x \leq 0.80$).

Sample	x	1 kHz		10 kHz		100 kHz		1 MHz	
		ε	Loss	ε	Loss	ε	Loss	ε	Loss
1	0.00	-	-	-	-	-	-	-	-
2	0.10	234	0.09	183	0.03	175	0.01	167	0.01
3	0.15	311	0.08	254	0.02	242	0.002	230	0.004
4	0.20	355	0.04	313	0.01	308	0.01	302	0.02
5	0.30	375	0.03	331	0.01	325	0.01	318	0.03
6	0.40	363	0.04	316	0.01	310	0.01	304	0.01
7	0.48	734	0.01	725	0.01	715	0.01	695	0.01
8	0.55	518	0.03	478	0.002	474	0.002	470	0.02
9	0.70	252	0.11	206	0.01	204	0.003	203	0.002
10	0.80	223	0.44	109	0.23	95	0.04	92	0.01
11	1.00	-	-	-	-	-	-	-	-

Table 9.5. Frequency dependence of dielectric properties of 240h-annealed PZT sintered disks ($0.10 \leq x \leq 0.80$).

9.3.1.3 Influence of Thermal History on Temperature Dependence of Dielectric Property

The frequency and temperature dependence dielectric properties of 240h-annealed PZT sintered disks (x = 0.30, 0.40, 0.48, 0.55 and 0.70) was measured from 173K to 473K. The results were compared to the dielectric properties of un-annealed PZT sintered disks. Temperature dependence of dielectric constants of un-annealed and 240h-annealed PZT sintered disks at 1 kHz were shown in Fig. 9.8 (a) and (b), respectively. The dielectric constants of the PZT sintered disks with composition at MPB (x = 0.48) and Zr-rich region (x = 0.30 and 0.40) show a stronger temperature dependence than the compositions at Ti-rich region x = 0.55 and 0.70) with or without annealing in this temperature region.

The estimate intrinsic dielectric constants of the PZT sintered disks were obtained by extrapolating the curves to 0K. The intrinsic dielectric constants of un-annealed and 240h-annealed PZT sintered disks at 1 kHz were list in the table 6.2 and 9.6, respectively. The intrinsic dielectric constant of each composition did not significantly change after annealing at 923K for 240 hours. However, the dielectric constants of annealed ceramics were higher than the as synthesized ceramics at elevated temperatures. This means that the influence of anneal process was mainly on the extrinsic contribution to dielectric properties, which is primarily associated with the motion of the domain walls and phase boundaries and displacement of defects [1]. This result matches with the alteration of domain morphology that was observed in TEM.

Broad peaks in temperature dependence of dielectric constant curves were found to occur at around 298 K for both un-annealed and 240h-annealed PZT sintered disks. The broad peaks in the PZT sintered disks with composition x = 0.48 and 0.70 were faded after annealing at 923K for 240 hours. Conversely, the broad peaks in the PZT sintered disks with composition x = 0.30, 0.40 and 0.55 were sharpen after long anneal period. It is still not clear that the broad peaks of the compositions close to the MPB observed were caused by the low temperature monoclinic phase (M_A) [8] or simply by the stress relief mechanism [9]. But the broad peaks in the PZT 60/40 and the PZT 70/30 sharpening with anneal time were match with the specific heat results. The long anneal process also sharps the phase transition peaks in the specific heat measurement.

The ε_{ex} of the un-annealed and 240h-annealed PZT sintered disks (x = 0.30, 0.40, 0.48, 0.55 and 0.70) at room temperature was shown in Fig. 9.9. The extrinsic contribution to dielectric constant of all compositions had different level of increasing after annealing for 240 hours. The combined results of the influence of thermal history on structural properties and phase transitions implied the increase in extrinsic contribution was due to the stress relief (i.e. defects,

distorted area, and internal stress between different phases). For all compositions, the long anneal process allowed the oxygen vacancies diffuse to the grain boundaries or out of the ceramic, and lead to an increasing in domain wall mobility. At the MPB (x = 0.48), the {200} diffraction results indicate that phase tend to transform into rhombohedral phase during the anneal process. The increase in phase fraction of rombohedral phase would also lead to a higher extrinsic contribution. Because of the rhombohedral phase have more polarization states than the tetragonal phase. Among all compositions at room temperature, the PZT 45/55 had largest increase in extrinsic contribution. It increased from 17.6% to 36.5% after annealed at 923K for 240hours. The values of intrinsic (ε_{in}) and extrinsic contributions (ε_{ex} in %) to dielectric constant at room temperature (ε_{RT}) were listed in table 9.7.

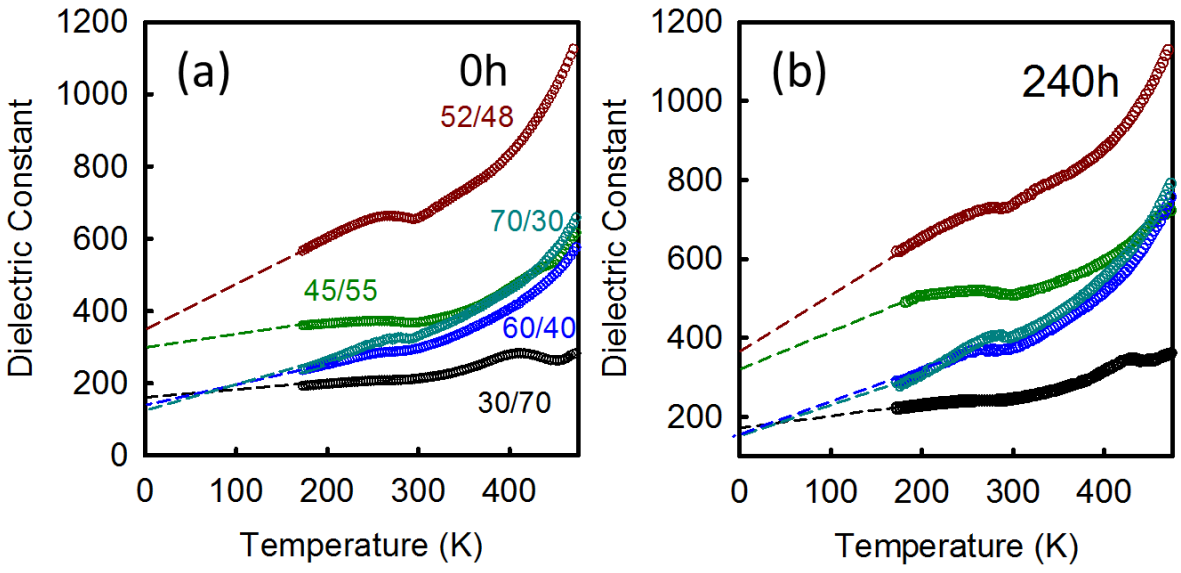

Figure 9.8. Temperature dependence of dielectric constant of (a) un-annealed and (b) 240h-annealed PZT sintered disks (x = 0.30, 0.40, 0.48, 0.55 and 0.70).

x	0 K	173 K	298 K	473 K
0.70	174	221	244	356
0.55	322	485	507	726
0.48	362	618	734	1128
0.40	161	290	371	737
0.30	152	286	401	775

Table 9.6. Temperature dependence of dielectric constant of the 240h-annealed PZT sintered disks (x = 0.30, 0.40, 0.48, 0.55 and 0.70).

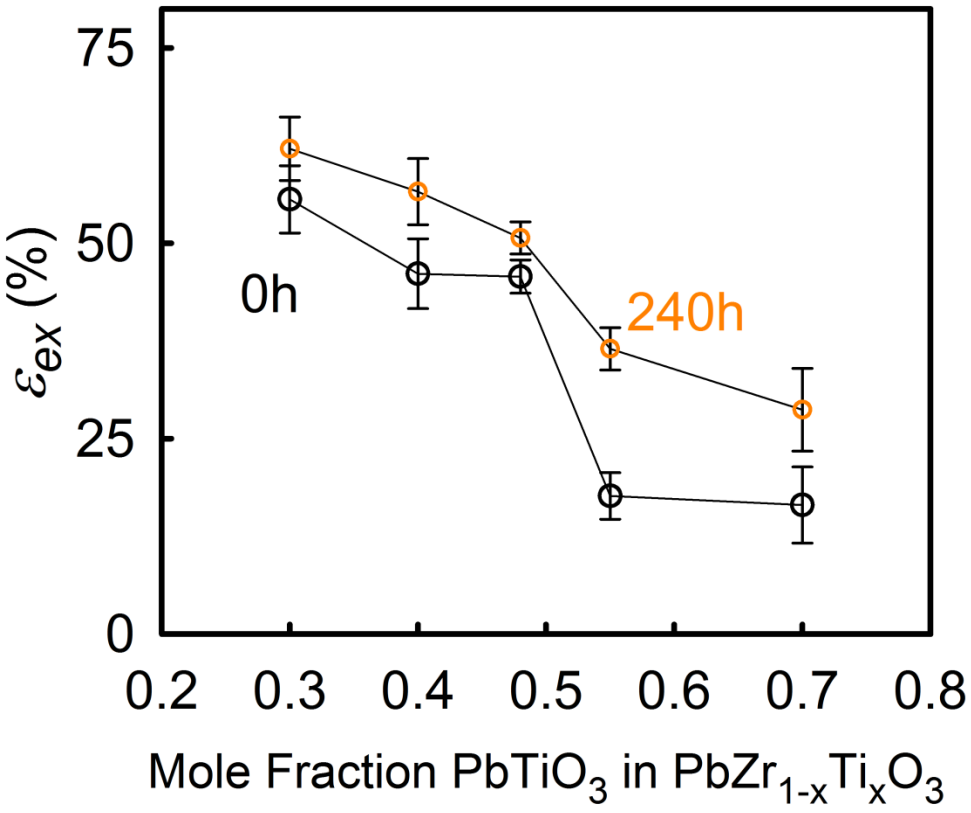

Figure 9.9. Extrinsic contributions to the dielectric constant *versus* composition for the PZT sintered disks ($0.10 \leq x \leq 0.80$) before (black circles) and after (orange circles) annealing at 923K for 240h. Errors were standard propagated errors by using an estimated uncertainty in the dielectric constant of ±10.

x	0h			240h		
	ε_{in}	ε_{RT}	ε_{ex} (%)	ε_{in}	ε_{RT}	ε_{ex} (%)
0.70	177	212	16.51	174	244	28.69
0.55	303	368	17.66	322	507	36.49
0.48	356	656	45.73	362	734	50.68
0.40	159	295	46.10	161	371	56.60
0.30	146	329	55.62	152	401	62.09

Table 9.7. The intrinsic (ε_{in}) and extrinsic contributions (ε_{ex} in %) to room temperature dielectric constant (ε_{RT}) of PZT sintered disks ($0.30 \leq x \leq 0.70$) before and after annealing at 923K for 240h..

9.3.2 Influence of Thermal History on Strong Field Dielectric Property

9.3.2.1 Influence of Thermal History on Frequency Dependence of Dielectric Nonlinearities

The PZT sintered disks with composition at the MPB (x = 0.48, or PZT 52/48) was selected for investigating the frequency and ac field amplitude dependence of dielectric behavior. Fig. 9.10 shows the dielectric constants of the PZT 52/48 sintered disks with different anneal time (0-240 hours) were measured as a function of ac electric field at four different frequencies (1, 10, 100 and 1kHz). The dielectric constant of the annealed PZT 52/48 sintered disks became more sensitive to the ac field amplitude, and reaches a maximum after annealed for 120 hours. A higher sensitivity to ac field amplitude indicates a higher domain wall mobility or larger number of polarization directions or both. Fig. 9.10 also shows the ac field dependence of dielectric constants

decrease with increasing frequency. This is because of some of the domain wall motions cannot keep up with higher frequency.

Fig. 9.11 shows the initial dielectric constant and irreversible Rayleigh coefficients of the annealed PZT 52/48 sintered disks decrease linearly with the logarithm of the frequency, which matches with the Rayleigh law [10]. The frequency dependence of initial dielectric constant and Rayleigh coefficients follows the Eq. 6.4 and 6.5, which are expressed as

$$\varepsilon_{init} = e_0 - e\ln(\omega) \qquad \text{Equation 6. 9}$$

$$\alpha = a_0 - a\ln(\omega) \qquad \text{Equation 6. 10}$$

The fitting parameters e_0, e, a_0 and a of the PZT 52/48 sintered disks with different anneal time were listed in table 9.8. The 120h-annealed PZT 52/48 sintered disk has highest fitting parameters, which was the most sensitive to the frequency. The frequency dependence dielectric behavior was changed by anneal process. It indicates that the domain morphology of the PZT 52/48 sintered disks was changed after a long period of anneal treatment, which was also match the observed domain revolution in TEM images.

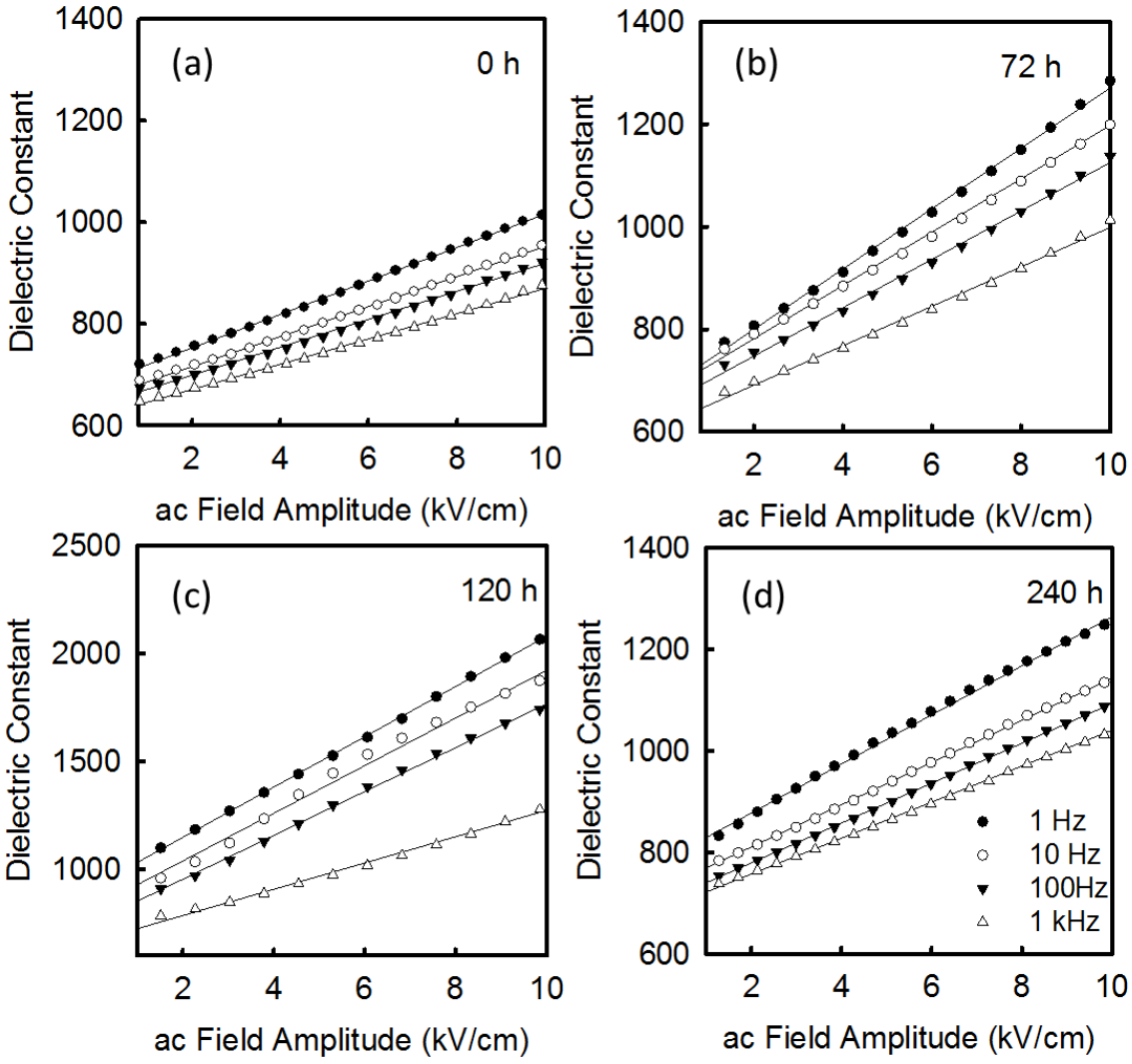

Figure 9.10. ac field amplitude dependence of dielectric constant of the PZT 52/48 sintered disks that annealed at 923K for (a) 0h, (b) 72h, (c) 120h, and (d) 240h under four frequencies (1 Hz, 10 Hz, 100Hz and 1 kHz).

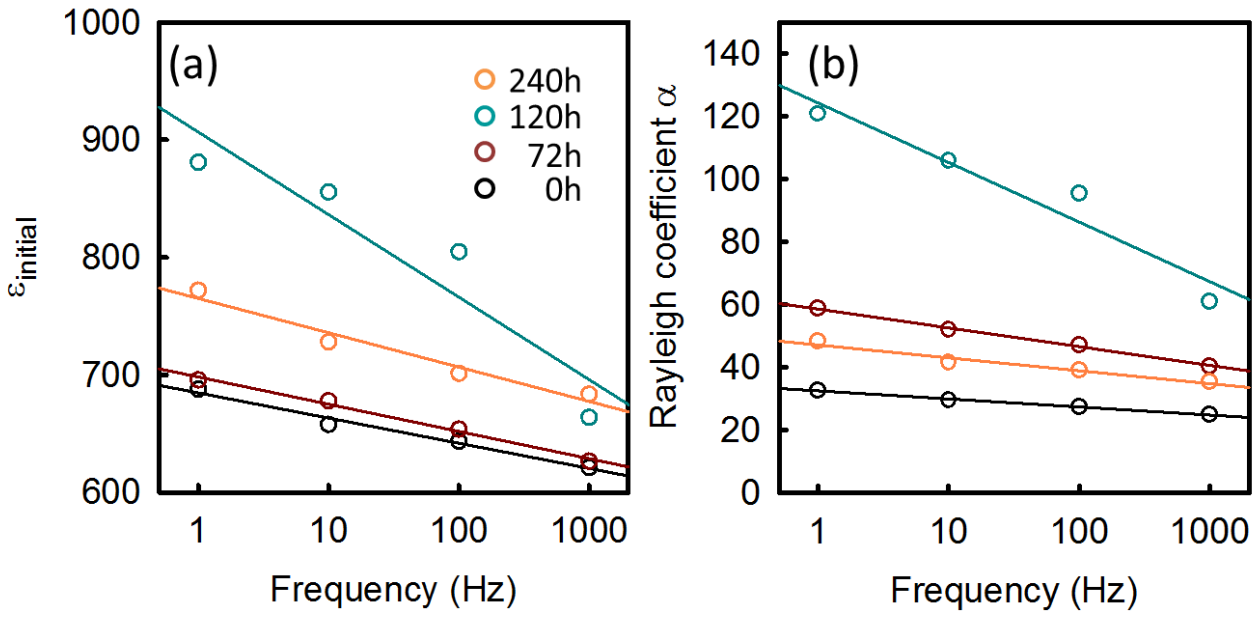

Figure 9.11. (a) The initial dielectric constant (reversible) and (b) Rayleigh coefficient (irreversible) of the PZT 52/48 sintered disks with different anneal time (0h, 72h, 120h, and 240h).

Anneal Time (h)	e_0	e	a_0	a
0	684.68	21.42	32.53	2.55
72	698.14	23.15	58.63	6.00
120	906.60	70.22	124.17	18.98
240	765.03	29.22	47.28	4.09

Table 9.8. Fitting parameters in Eq. 6.4 and 6.5 of the PZT 52/48 sintered disks with different anneal time (0h, 72h, 120h, and 240h).

9.3.2.2 Influence of Thermal History on Composition Dependence of Rayleigh Coefficient

It was found in the temperature dependence of dielectric constant that the intrinsic dielectric constant did not change much with the long anneal process. This means that the enhanced dielectric constant after anneal process was mainly contributed from the extrinsic part, which is close associated with the motion of the domain walls. The temperature dependence of dielectric constant measurement can only separate out the intrinsic and extrinsic contributions to dielectric constant. To further investigate the mechanisms in the extrinsic contributions to dielectric constant, Rayleigh analysis is needed.

Fig. 9.12 shows the ac field dependence of dielectric constant of un-annealed (0h-), 72h-, 120h- and 240h-annealed PZT sintered disks (x = 0.30, 0.40, 0.48, 0.55 and 0.70) at 1 kHz. It is clear that PZT sintered disks with compositions at Zr-rich region (x = 0.30 and 0.40) were more sensitive to the ac field amplitude than the ones with compositions at Ti-rich region (x = 0.55 and 0.70) with or without anneal treatment. This is because the sintered disks with compositions at Ti-rich region has much higher spontaneous strains than the ones with compositions at Zr-rich region (x = 0.30 and 0.40), and their high spontaneous strains obstruct the domain wall motions.

Dielectric constants of the PZT sintered disks were enhanced after the long annealing process. The Rayleigh coefficients of all samples were obtained by fitting the ac field dependent dielectric constant curves in Fig. 9.12. The Rayleigh coefficient of all annealed PZT sintered disks were shown in Fig. 9. 13(a) and listed in table 9.9. It shows that Rayleigh coefficients were slightly change with anneal time in most of compositions, except PZT 52/48. Rayleigh coefficient is an indicator of the irreversible domain wall

motions, and the higher value means the domain wall is easier move to next position (to overcome the potential energy around it). Fig. 9.13 (b) shows the difference in Rayleigh coefficient of PZT sintered disks with different anneal time. Only the PZT sintered disks with composition x = 0.55 and 0.48 have shown an increase in Rayleigh coefficient after long annealing process (240h). The other compositions barely changed the value. The initial dielectric constants ($\boldsymbol{\varepsilon_{init}}$) of the PZT ceramics as function of anneal time were shown in Fig. 9. 14. The initial dielectric constants of PZT sintered disks increase with anneal time. This is because the extrinsic contributions to dielectric constant increases with anneal time. To be noted that the initial dielectric constant is not the same as the intrinsic dielectric constant.

Among all the compositions, Rayleigh coefficient of the PZT 52/48 sintered disks had a significant change with anneal time (seen Fig. 9.15). It reached a maximum after annealing for 120 hours, and this value is close to the ones at single rhombohedral phase. The increase in Rayleigh coefficient of the PZT 52/48 sintered disks with anneal time was due to the phase fraction rearrangement between tetragonal and rhombohedral phases through phase decomposition. The previous XRD results also reveal the volume fraction of rhombohedral in the PZT 52/48 sintered disks increase with anneal time. The Rayleigh coefficient of the PZT 52/48 sintered disks declined after 240 hours annealing process. The initial dielectric constant of the PZT 52/48 sintered disks also increases with anneal time (seen Fig. 9.15). Around 12% increase in initial dielectric constant after 240 hours annealing. Because the overall extrinsic contribution to dielectric constant was increased with anneal time. The Rayleigh analysis shows both initial dielectric constants (reversible domain wall motion) and Rayleigh coefficients (irreversible domain wall motion) of the

PZT ceramics were affected by anneal process. The Rayleigh coefficient reach a maximum at 120 hours and start to decline, it point out that the proper thermal history can enhance the dielectric property of the PZT, over or less heat treatment can hugely effect on the final results.

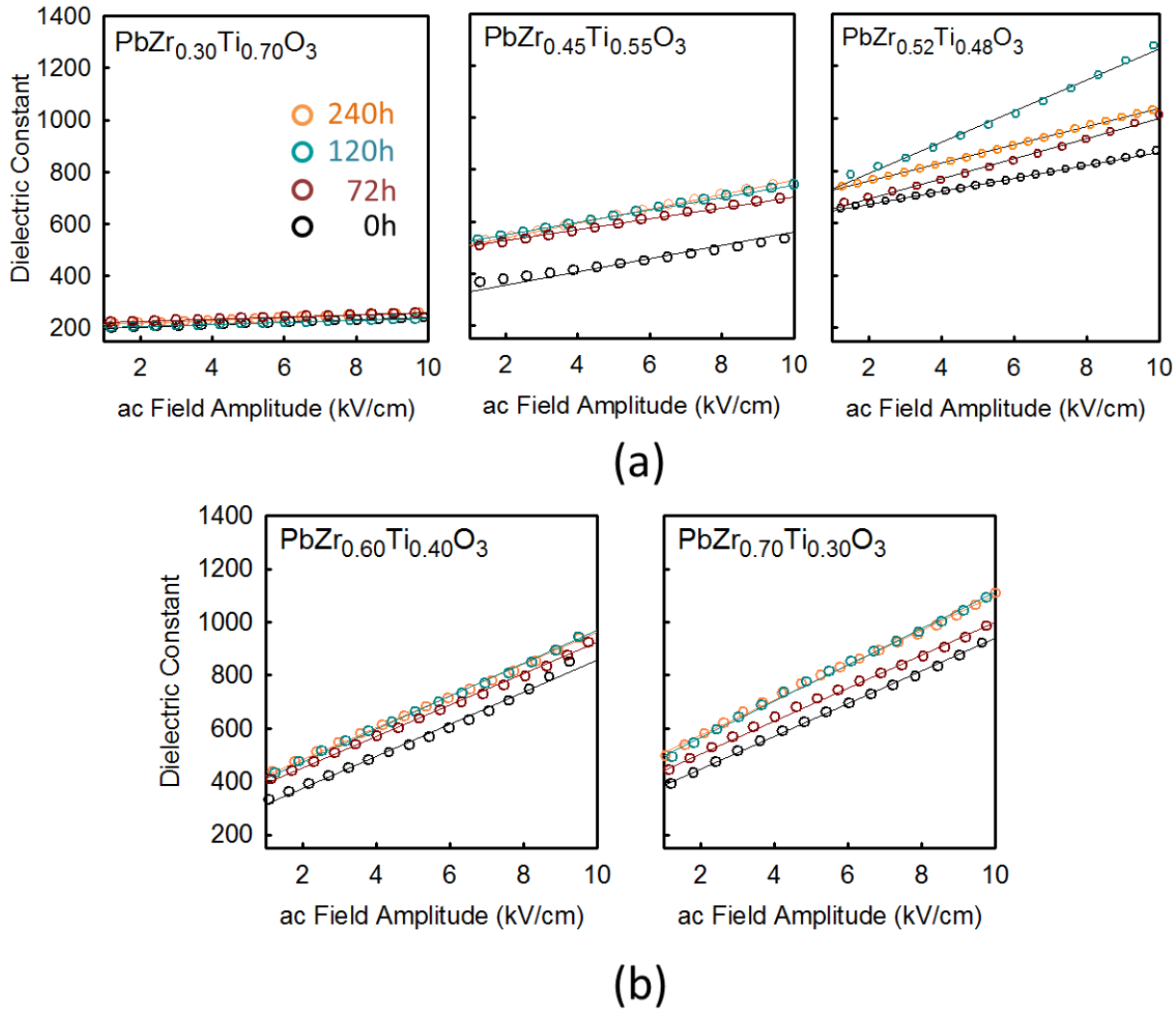

Figure 9.12. ac field amplitude dependence of dielectric constant of the 0h-, 72h-, 120h-, and 240h-annealed PZT sintered disks in two ranges of composition (a) $0.30 \leq x \leq 0.48$ and (b) $0.60 \leq x \leq 0.70$ at room temperature

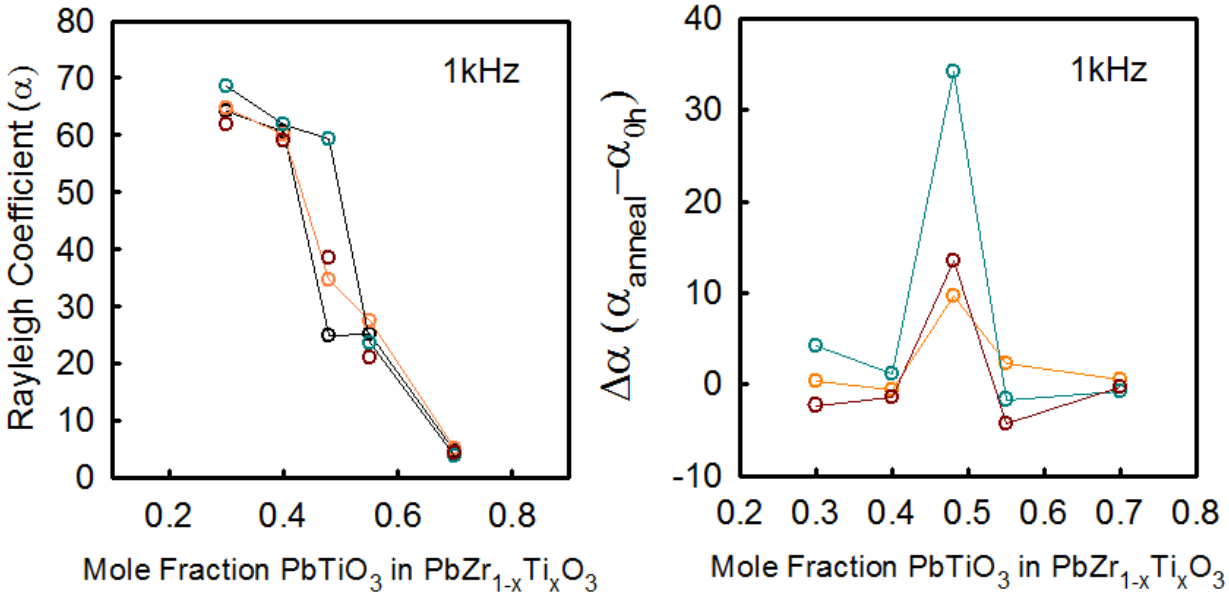

Figure 9.13. (a) The Rayleigh coefficients (α) and (b) $\Delta\alpha$ (α_{anneal}-α_{0h}) of the 0h-, 72h-, 120h-, and 240h-annealed PZT sintered disks at room temperature.

x	0h	72h		120h		240h	
	α	***α***	**Δ*α***	***α***	**Δ*α***	***α***	**Δ*α***
0.30	64.3	62.01	-2.3	68.48	4.18	64.59	0.29
0.40	60.64	59.15	-1.49	61.8	1.16	60.09	-0.55
0.48	24.97	38.45	13.48	59.22	34.25	34.62	9.65
0.55	25.22	20.97	-4.24	23.56	-1.66	27.49	2.28
0.70	4.69	4.39	-0.3	3.89	-0.8	5.14	0.45

Table 9.9. Room temperature Rayleigh coefficient of the 0h-, 72h-, 120h-, and 240h-annealed PZT sintered disks at 1 kHz

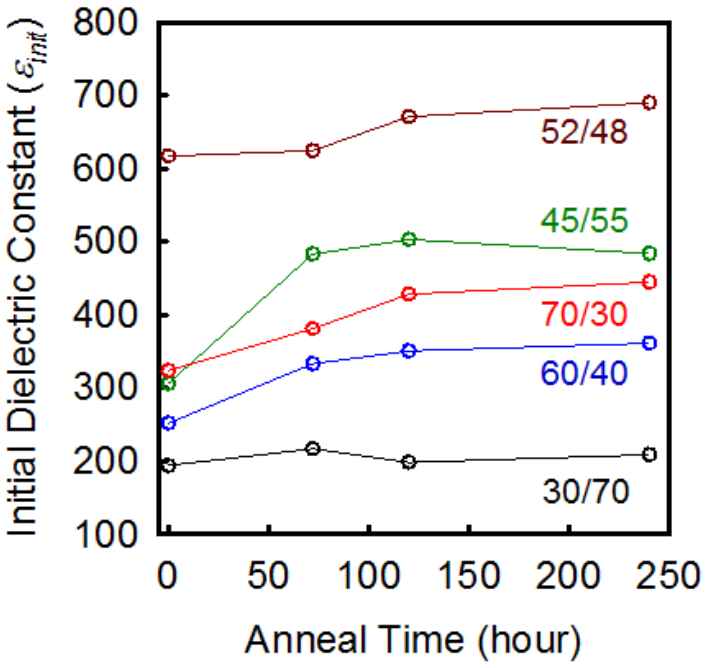

Figure 9.14. The initial dielectric constants (ε_{init}) of the PZT sintered disks as function of anneal time.

x	0h	72h		120h		240	
	$\varepsilon_{initial}$	$\varepsilon_{initial}$	$\Delta\varepsilon$ (%)	$\varepsilon_{initial}$	$\Delta\varepsilon$ (%)	$\varepsilon_{initial}$	$\Delta\varepsilon$ (%)
0.30	324	381	18	428	32	445	37
0.40	252	333	32	350	39	361	43
0.48	617	624	1	671	9	690	12
0.55	306	483	58	503	64	484	58
0.70	194	217	12	198	2	209	8

Table 9.10. Initial dielectric constant of the 0h-, 72h-, 120h-, and 240h-annealed PZT sintered disks at 1 kHz.

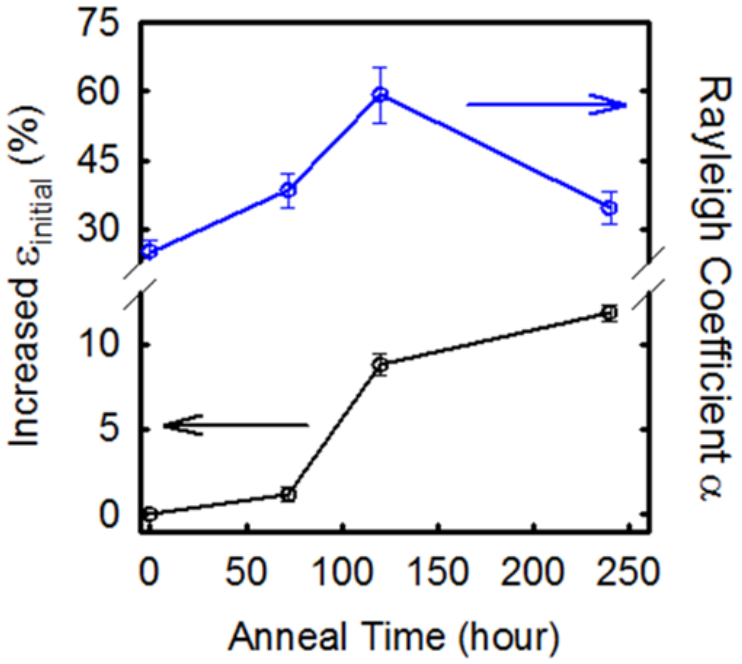

Figure 9.15. Rayeligh coefficient and increased initial dielectric constant of the PZT 52/48 sintered disks as a function of anneal time.

9.4 Summary

The observations of the influence of thermal history on temperature, composition, and frequency dependence of the dielectric behavior at low and strong field were listed as follows,

1. The dielectric constant of all PZT sintered disks (except x = 0.10) at low field (0.1V) increases with anneal time, and increase most for those compositions near the MPB region (x = 0.40, 0.48, and 0.55).
2. The dielectric loss decreases with anneal time was found in most of the compositions, except for three end members (x = 0.10, 0.15, and 0.80).

3. The dielectric constant of most PZT sintered disks became less frequency sensitive in this frequency range (1 kHz to 1 MHz) after annealing at 923K for 240 hours, except three end members (x = 0.10, 0.15, and 0.80).
4. The intrinsic dielectric constant of each composition did not significantly change after annealing at 923K for 240 hours.
5. The extrinsic contribution to dielectric constant of all compositions had different level of increasing after annealing for 240 hours. Among all compositions at room temperature, the PZT sintered disks with composition x = 0.55 had largest increase in extrinsic contribution. It increased from 17.6% to 36.5% after annealed at 923K for 240hours.
6. The initial dielectric constant and irreversible Rayleigh coefficients of the annealed PZT 52/48 sintered disks decrease linearly with the logarithm of the frequency, which matches with the Rayleigh law.
7. PZT sintered disks with composition at Zr-rich region were more sensitive to the ac field amplitude than the ones at Ti-rich region with or without anneal treatment.
8. The initial dielectric constants of PZT sintered disks increase with anneal time.
9. The PZT sintered disks with composition x = 0.48 and 0.55 have shown an increase in Rayleigh coefficient after 240 hours anneal process. It had a significant increase from 25 (0h) to 59 (120h) in PZT 52/48 sintered disks. The other compositions were barely changed the value.

9.5 References

1. C.A. Randall, N. Kim, J.P. Kucera, W.W. Cao, and T.R. Shrout, *J Am Ceram Soc* **81**, 677 (1998)
2. H.Q. Fan, G.T. Park, J.J. Choi, J. Ryu, and H.E. Kim, *J Mater Res* **17**, (2002)
3. M. Hammer and M.J. Hoffmann, *J Am Ceram Soc* **81**, (1998)
4. C.V.R.V. Kumar, R. Pascual, and M. Sayer, *J Appl Phys* **71**, (1992)
5. G.A.C.M. Spierings, G.J.M. Dormans, W.G.J. Moors, M.J.E. Ulenaers, and P.K. Larsen, *J Appl Phys* **78**, (1995)
6. P.K. Larsen, G.J.M. Dormans, D.J. Taylor, and P.J. Vanveldhoven, *J Appl Phys* **76**, (1994)
7. M. Takahashi, *Japanese Journal of Applied Physics* **9**, 1236 (1970)
8. B. Noheda, D.E. Cox, G. Shirane, J.A. Gonzalo, L.E. Cross, and S.E. Park, *Appl Phys Lett* **74**, 2059 (1999)
9. Q.M. Zhang, H. Wang, N. Kim, and L.E. Cross, *J Appl Phys* **75**, 454 (1994)
10. D.V. Taylor and D. Damjanovic, *J Appl Phys* **82**, 1973 (1997)

CHAPTER 10

CONCLUSIONS AND FUTURE WORK

10.1 Summary of Key Observations

This thesis intended to study the influence of thermal history on structure, microstructure, domain structure, phase transitions, and dielectric behavior of PZT sintered disks across whole system. The characterization results of the un-annealed PZT sintered disks were not only used as references for those after annealed, but also provided new information about the tricritical behavior and the dielectric properties in the PZT solid solution.. The properties of annealed PZT sintered disks were used to study the influence of thermal history on PZT ceramics. The key observations in this thesis study were divided into following categories,

Preparation and structural characterization of PZT powder and ceramics

The PZT powder and ceramics with different compositions (x = 0.00 - 1.00) were successfully synthesized by an alkoxide-derived sol–gel method. The structural properties of PZT sintered disks ($0.10 \leq x \leq 0.80$) were characterized by x-ray diffraction, and the reflections were carefully analyzed by peak fitting software. The key observations in the structural characterization of PZT powder and sintered disks are listed as follows,

1. Lattice parameters and unit cell volumes of the un-annealed PZT powders (x = 0.00, 1.00) and sintered disks ($0.10 \leq x \leq 0.80$) have a good agreement with the literature data. The unit-cell volume (Ω) has increased with zirconium content from around 63 $Å^3$ to 71 $Å^3$ and shows an essentially linear behavior with

composition. This means the composition of PZT specimens were very close to desired composition.

2. Spontaneous strain of the PZT sintered disks ($0.10 \leq x \leq 0.80$) with tetragonal phase ($0.55 \leq x \leq 0.80$) is an order larger than those with rhombohedral phase ($0.10 \leq x \leq 0.40$) due to the larger tetragonal distortion. The spontaneous strain of the PZT sintered disks with rhombohedral phase $[(90^o\text{-}\alpha_R)/90^o]$ is increased slightly with decrease zirconium content from 0.0030 to 0.0035. The spontaneous strain of the PZT sintered disks with tetragonal phase $[(c/a) - 1]$ is depending on the tetragonal distortion (c/a), which is decreased linearly with increase zirconium content from 0.064 to 0.020.
3. {200} XRD reflections of the PZT 52/48 ($x = 0.48$) sintered disks show the evidence of the two-phase coexistence of tetragonal and rhombohedral phases (F_T and F_R).
4. The XRD peak width (FWHM) of PZT 52/48 sintered disks was almost double the size than the rest of the compositions.
5. TEM bright field image of as synthesized PZT 52/48 sintered disks shows a curving domain structure in nanometer scale (~20nm).

Paraelectric to ferroelectric phase transition behavior in the PZT ceramics

The temperature dependence of specific heat behavior was used to study the paraelectric to ferroelectric phase transition behavior in the as-synthesized PZT sintered disks. The order of the transition for each sample was determined by first derivative of C_p curves, the transition enthalpy (ΔH_i), and the transition entropy ((ΔS_i). The key

observations in the paraelectric to ferroelectric phase transition behavior in the un-annealed PZT sintered disks are listed as follows,

1. The Curie temperatures of the PZT sintered disks were in a good agreement of the literature data. The ferroelectric to paraelectric phase transition temperatures increased from 504K to 760K with increase titanium content. Besides lattice parameters, thermodynamic parameters also show the composition of the PZT specimens is controlled to within ~1 mol% of the desired composition.
2. The PZT sintered disks near at MPB region ($0.30 \leq x \leq 0.48$) have a second-order phase transition behavior, while those outside the MPB region have either a weak or a strong first-order phase transition behavior.
3. Two tricritical points were found to occur at around $x_R^{CR} = 0.30$ and $x_T^{CR} = 0.51$. The results match with the experimental observations and prediction based on Landau theory in the literature.

Dielectric behavior in the PZT ceramics

Dielectric behavior of the as-synthesized PZT sintered disks was characterized by a comprehensive dielectric and piezoelectric measurement system at the University of Connecticut. The results have provided new information about contribution mechanisms to dielectric constant, especially in irreversible Rayleigh coefficient. The key observations in the dielectric behavior of PZT sintered disks are listed as follows,

1. Composition dependence of dielectric constant of PZT sintered disks was in a good agreement with literature data, which reached a maximum at near MPB.

2. Among all the samples, the dielectric behavior of the PZT sintered disks at MPB (x = 0.48) was nearly frequency independent in the frequency range from 1 kHz to 1 MHz.
3. Intrinsic and extrinsic contributions to dielectric constant were determined by extrapolating the temperature dependence of dielectric constant to 0K. The intrinsic constant reach the maximum at MPB (x = 0.48). The PZT sintered disks with composition at MPB (x = 0.48) and Zr-rich region (x = 0.30 and 0.40) have higher thermally activated extrinsic mechanisms than the ones with composition at Ti-rich region (x = 0.55 and 0.70), which were around 49% and 17%, respectively.
4. All PZT sintered disks show a linear relationship with ac field amplitude at an intermediate field. PZT sintered disks with rhombohedral phase have higher Rayleigh coefficient (α) and irreversible extrinsic contribution to dielectric constant than those with tetragonal phase. At Zr-rich region ($0.10 \leq x \leq 0.40$), α was less compositional sensitive and vary from 55 to 64. At Ti-rich region ($0.55 \leq x \leq 0.70$), α decrease from 25.22 to 1.41 with increased Ti content
5. Rayleigh coefficient of the PZT sintered disks was strongly correlated with their crystal structure and spontaneous strains.
6. The dielectric permittivity attributed from thermally activated irreversible domain wall motion (ε_{irr}) was determined by the combined result of the temperature and ac field amplitude dependence of dielectric behavior. The thermally activated ε_{irr} was almost composition independence, which attributed to the total dielectric permittivity around 7.5% in average.

Influence of thermal history on structure

To test whether or not the un-annealed PZT sintered disks are at their equilibrium states, PZT sintered disks were annealed at 923K for 72h, 120h, and 240h. The structure properties of annealed ceramics were then characterized by XRD. The key observations in the thermal effect to structure property are listed as follows,

1. Lattice parameters and unit cell volume of all annealed PZT sintered disks decrease with anneal time. The maximum change in unit cell volume after annealing for 240 hours was occurred at the composition x = 0.48, which was around 0.6%.
2. The maximum change in the spontaneous strains after the long anneal process was also occurred at the compositions near at the MPB (x = 0.40 and 0.48), which was increased around 5%.
3. Volume fraction of rhombohedral ($F_{R)}$ phase (I_R/I_T+I_R) of the un-annealed PZT 52/48 sintered disks was around 50%, and it was increased with anneal time.
4. The maximum change of the diffractions peak width of PZT sintered disks after the long anneal process occurs at the composition x = 0.48, which was increased from 0.43 to 0.53.

Influence of thermal history on domain structure

Domain structure has significant influence on electrical properties of the PZT sintered disks. In the industry, electrical property of a ferroelectric is usually controlled by modifying its domain structure through different additives. In this study, the domain structure evolution as a function of anneal time was investigated by TEM. The key observation in the thermal effect to domain structure are listed as follows,

1. TEM bright field images show the domain structure of PZT 52/48 sintered disks coarsens from 15nm (0h) to 100nm (240h), and the level of domain curving decreases with anneal time.
2. The observation of domain coarsening match very well with the computer simulation result of phase decomposition of PZT ceramics which reported by Rao *et al*.

Influence of thermal history on paraelectric to ferroelectric phase transition behavior

The phase transition behavior between paraelectric and ferroelectric phases of annealed PZT powders (x = 0.00, 1.00) and sintered disks ($0.10 \leq x \leq 0.80$) was investigated by specific heat measurement. Thermodynamic parameters of annealed ceramics, such as phase transition temperatures, transition enthalpies, and transition entropies, were compared to un-annealed powders and sintered disks. Also, influence of thermal history on the order parameter was studied. The key observation in the thermal effect to phase transition behavior between paraelectric and ferroelectric phases are listed as follows,

1. Phase transition temperatures of all samples were unchanged by annealing, indicating that the average composition does not change (within 0.4%) by annealing at 923K for 240 hour.
2. Phase transition peaks were sharpening with anneal time. Among all compositions, a maximum change in transition peak occurred at the composition $x = 0.48$, which is right on the MPB.
3. Outside of MPB region, latent heats and excess entropies of all annealed PZT ceramics were slightly decreased after annealing for 240 hours. However, the decrease amounts were within error.
4. At phase transition region, temperature dependent specific heat curves were sharpen after long annealing process.
5. Long annealing process did not change the locations of two tricritical points.

Influence of thermal history on Dielectric behavior

Influence of thermal history on structure, microstructure, and domain structure were discussed. The processing-structure-property relation can be built by investigating the dielectric property of annealed PZT sintered disks ($0.10 \leq x \leq 0.80$), since they are very sensitive to their structural properties. The key observations in thermal effect to dielectric properties are listed as follows,

10. The dielectric constant of all PZT sintered disks increases with anneal time, and increase most for those compositions near the MPB region ($x = 0.40$, 0.48 and 0.55), their dielectric constant increased 11% to 36% after 240 hours annealing process.

11. The intrinsic dielectric constant all PZT sintered disks did not significantly change (within 6.5%) after annealing at 923K for 240 hours.
12. The extrinsic contribution to dielectric constant of all PZT sintered disks had different level of increasing after annealing for 240 hours. Among all compositions at room temperature, the PZT sintered disks with composition x = 0.55 had largest increase in extrinsic contribution. It increased from 17.6% to 36.5% after annealed at 923K for 240 hours.
13. PZT sintered disks with compositions at the Zr-rich region ($0.10 \leq x \leq 0.40$) were more sensitive to the ac field amplitude than the ones with composition at Ti-rich region ($0.55 \leq x \leq 0.80$) with or without anneal treatment, which means that their Rayleigh coefficients would be higher.
14. The PZT sintered disks with composition x = 0.48 and 0.55 have shown an increase in Rayleigh coefficient after 240 hours anneal process. It had a significant increase from 25 (0h) to 59 (120h) in PZT 52/48 sinter disks. The other compositions (x = 0.30, 0.40, and 0.70) were barely changed the value.

10.2 Conclusions

Conclusions were made based on the key experimental observations listed above. Conclusions can be divided into two major parts. The first part of conclusions is focus on the sample preparation and characterization results of un-annealed PZT ceramics. The second part is focus on the influence of thermal history on PZT ceramics.

Preparation of Un-annealed PZT Powders and Ceramics

To investigate phase equilibria in the PZT system and thermal effect on their properties, PZT powders (x = 0.00, 1.00) and sintered disks ($0.10 \leq x \leq 0.80$) were successfully synthesized using an alkoxide-derived sol–gel method. Comprehensive characterization results of crystal structure, domain structure, paraelectric to ferroelectric phase transition, and dielectric behavior of the un-annealed PZT powders (x = 0.00, 1.00) and sintered disks ($0.10 \leq x \leq 0.80$) were reported in this thesis. These characterization results of the un-annealed PZT powders and sintered disks were not only used as a baseline to investigate the influence of thermal history on PZT ceramics, but also provide new findings about the location of tricritical points and dielectric properties in the PZT solid solution.

Tricritical Behavior in the PZT Solid Solution

The nature of phase transition is unclear in the PZT solid solution. The locations of the tricritical points is still a subject of debate due to several obstacles are encountered in experimental studies of tricritical phenomena in the PZT solid solution. There are distinct differences in the reported compositions at which the tricritical points occur. In this thesis work, the order parameter of paraelectric to ferroelectric phase transition of un-

annealed PZT solid solution across whole phase diagram was determined by its specific heat behavior. The specific heat results clearly revealed two tricritical points located at around x = 0.30 and x = 0.51. Finding two tricritical points in the PZT system by analyzing their specific heat behaviors has never been reported.

Intrinsic and Extrinsic Contributions to Dielectric Permittivity in the PZT ceramics

Intrinsic and extrinsic contributions to dielectric permittivity of un-annealed PZT sintered disks were separated by measuring temperature dependence of dielectric permittivity. Spontaneous strain is much smaller in the PZT sintered disks with rhombohedral phase than the ones with tetragonal phase. Also, there are more polarization directions in rhombohedral phase than tetragonal phase. This means the domain wall mobility of a PZT sintered disk with rhombohedral phase would be much higher than a PZT sintered disk with tetragonal phase. Consequently, the fraction of extrinsic contributions is greater in the rhombohedral phase than in the tetragonal phase. PZT sintered disks with rhombohedral phase showed an averaged 49 % extrinsic contribution to total dielectric constant at room temperature, while PZT sintered disks with tetragonal phase only showed 17% extrinsic contribution to total dielectric constant.

The amount irreversible extrinsic mechanism was calculated by application of Rayleigh law. Comprehensive Rayleigh coefficients were collected and showed strong correlation with the crystal structure and spontaneous strains. PZT sintered disks with rhombohedral phase also have higher Rayleigh coefficient (α) and irreversible extrinsic contribution to dielectric constant than those with tetragonal phase. This can be interpreted as a result of greater non-180° domain wall mobility in the rhombohedral

phase. Similar variations in extrinsic contributions with different crystallographic phases were reported earlier for dielectric response in PZT ceramics and thin films. However, systematic studies on the correlation between Rayleigh coefficients and spontaneous strains of PZT ceramics across whole system have never been reported.

Influence of Thermal History on PZT Ceramics

To test the hypothesis of phase decomposition phase and thermal effect on properties in the PZT system, the PZT powders (x = 0.00, 1.00) and sintered disks ($0.10 \leq x \leq 0.80$) were then annealed at 923K for 72h, 120h and 240h. The influence of thermal history on properties of PZT powders and sintered disks were observed and carefully analyzed. X-ray diffraction studies showed that long (10 days) annealing at temperatures above the Curie line resulted in changes in the unit cell volume, the spontaneous strain, the volume fractions of ferroelectric rhombohedral (F_R) and tetragonal (F_T) phases, and the peak width of {200} reflections. These changes were highest at around MPB. Based on the observations, there was no clear evidence of phase decomposition in the PZT solid solution during the long annealing process. The phase decomposition model was failed to explain the sharpening of specific heat curves at transition after annealing process. On the other hand, the stress relief mechanism was able to interpret all observation results. The decrease in unit cell volume with anneal time was due to less distorted domain wall area were formed after annealing, which was also shown in the TEM images. The increase in spontaneous strain was due to lower internal stress in the annealed ceramics. The elastic energy was relived after annealing process, it lead to the change in the phase fraction of ferroelectric phases in the XRD results.

This special stress relief mechanism can be explained as follows. Large elastic energy was accumulated during the normal ceramic processing. It is well known that the formation non-180^{o} domain wall can eliminate the elastic energy. Higher elastic energy leads to form more domain walls in the system. At near the MPB, the domain can be formed with either tetragonal or rhombohedral phases to compensate the elastic energy. More domain with tetragonal phase is expected if the PZT sintered disks at MPB with a high elastic energy. In the annealed PZT sintered disks, some elastic energy was relieved by anneal process at 923K. Consequently, less distorted domain wall area and more domains with rhombohedral phase were formed.

The changes in structural properties and domain structure were accompanied by changes in the paraelectric to ferroelectric phase transition and dielectric properties. The long anneal process also affected on the nature of the paraelectric to ferroelectric phase transition. The phase transition temperature of annealed PZT samples were remain the same, but the reduced distorted domain wall area resulted in phase transition peaks sharpening and latent heats reducing after annealing at 923K for 240 hours.

Systematic changes in relative dielectric permittivity, extrinsic contribution mechanism to dielectric constant and Rayleigh coefficent were observed. The dielectric constant of all PZT sintered disks increases the most for those compositions (x = 0.40, 0.48 and 0.55) near the MPB region. This was due to stress relieved by the annealing process changed the volume fractions of the ferroelectric phases and the domain wall mobility. A quantitative determination of thermal effects on Rayleigh coefficient, which is an indicator to irreversible domain wall motion, was carried out. It was observed a significant increase from 25 (0h) to 59 (120h) in PZT 52/48 sintered disks after annealing

at 923K for 240 hours, because of phase redistribution and increase in domain wall mobility.

Based on overall observations, the un-annealed PZT sintered disks at around MPB were not in their equilibrium state. The volume fractions of ferroelectric phases and domain morphologies of the PZT sintered disks were changed by a stress relief mechanism. These changes accompanied by changes in the domain structure, the paraelectric to ferroelectric phase transition, and electrical properties. In particular, systematic changes in extrinsic contributions to dielectric constant were observed. This means that structure, domain structure and dielectric property of the PZT sintered disks at near the MPB were extremely sensitive to their thermal history. These results suggest that domain structures and dielectric properties of the PZT ceramics with compositions near the MPB can be controlled without dopants by processing under different thermal histories. The reported results in this thesis study developed a very useful processing-structure-property relaiton for PZT ceramic processing.

10.3 Future Plan

In addition to the work in this study, the work list as follows would provid more informationto allow to fully understand the influence of thermal history on PZT, especially in relation of elastic energy and formation of the phase coexistence. The suggestions for future research are listed as follows,

Further studies of current observed phenomenon:

1. Synchrotron diffraction: Synchrotron diffraction concentrates the intensity into a fine well-defined near-parallel x-ray beam, which offers better resolved diffraction pattern. It can be useful for separating out the diffraction peaks that contributed from two ferroelectric phases, and provide a better way to determine volume fractions of two ferroelectric phases.
2. TEM: Domain structure evolution of PZT 52/48 sintered disks (MPB) as a function of anneal time had been observed by TEM measurement. If possible, to obtain the domain structure evolution of PZT sintered disks outside of MPB region (with pure tetragonal phase and pure rhombohedral phase) as a function of anneal time, this would provide enough information to help developing processing-domain structure relation across PZT system.
3. Piezoelectric property: Influence of thermal history on piezoelectric property was not discussed in this thesis study. A certain change in piezoelectric property with anneal time is expected, since it is highly dependent on domain structure.
4. Defects study: By annealing the specimens at 923K in oxygen flow to investigate how the system behaves under a different atmosphere. Electrical measurements

would be applied on this study to show the loss or the conductivity of the PZT specimens with different heat treatments under oxygen atmosphere

5. Investigation of internal stress effects on the volume fraction of the two ferroelectric phases (tetragonal and rhombohedral) in the PZT with compositions at near the MPB: Influence of the internal stress on the structural properties can be investigated by pulverizing a PZT sintered disk into powder form. The diffraction results of the PZT powder can be treated as stress-free condition, and then comparing to the diffraction results of the PZT sintered disk (stressed condition).

The influence of thermal histories on PZT with different anneal temperatures

The observations in this thesis were only a slice of the phase diagram of PZT solid solution. Annealing ceramics at different temperatures provide useful information for testing the phase equilibria and establishing a comprehensive processing-structure-property relation.

1. Anneal at a higher temperature (T > 923K): The observations in this thesis study suggest the dielectric property was enhanced by a very slow (up to 10 days) relaxation mechanism at 923K in PZT system. However, to enhance dielectric property by annealing for a long time is not practical in industry. To accelerate this relaxation process a higher anneal temperature is needed.
2. Anneal at a lower temperature ($T < Tc$): Although a slower relaxation rate at lower anneal temperature is expected, but it is useful for studying the kinetics of this relaxation mechanism.